Lifetime prediction methods for un- and low-alloyed steels based on the combination of non-destructive and destructive materials testing

Dissertation

zur Erlangung des akademischen Grades
Doktor der Ingenieurwissenschaften
der Naturwissenschaftlich-Technischen Fakultät
der Universität des Saarlandes

vorgelegt von
M. Sc. Fabian Weber
November 19, 2024

Tag des Kolloquiums:	16.05.2025
Dekan:	Prof. Dr.-Ing. Dirk Bähre
Berichterstatter:	Prof. Dr.-Ing. Peter Starke Prof. Dr.-Ing. Dirk Bähre Prof. Dr.-Ing. Tobias Melz
Akad. Mitarbeiter:	Dr. Michael Roland
Vorsitz:	Prof. Dr. Martin Müser

"You can't start a fire without a spark"

– Bruce Springsteen

Acknowledgements

The main part of the experimental data and the proposed lifetime prediction methods presented within this thesis as well as the attached journal contributions originate from the research project EKusaP (Entwicklung eines Kurzzeitverfahrens zur Bewertung schadensrelevanter Parameter von in der Kernenergietechnik eingesetzten ferritischen Werkstoffen und Bauteilen / Development of a short-term procedure for the evaluation of damage-relevant parameters of ferritic materials and components used in nuclear technology) which was funded by the BMUV (Bundesministerium für Umwelt, Naturschutz, nukleare Sicherheit und Verbraucherschutz / Federal Ministry for the Environment, Nature Conservation, Nuclear Safety and Consumer Protection) with the grant number 1501623. Since this thesis would not have been possible without this funding, special thanks to the funding organisation as well as the GRS (Gesellschaft für Anlagen- und Reaktorsicherheit) as the project management agency.
Besides the results of EKusaP, the developed methods were validated using further materials. These investigations are based on experimental results of DFG (Deutsche Forschungsgemeinschaft / German Research Foundation)-funded research projects with the grant numbers STA 1133/6-1, STA 1133/10 and STA 1133/20-1. Accordingly, further thanks go to the DFG.
Foremost, I would like to thank my doctoral supervisor Prof. Dr.-Ing. habil. Peter Starke. His passion for the subject of fatigue of metallic materials ultimately led to my decision to start as scientific researcher at his chair and to do a doctorate in this field of material science. Besides his professional expertise, I particularly appreciate his manner as a leader who is always solution-orientated and willing to help. As a result of the countless discussions and suggestions, he made a significant contribution to the generation of the presented research. The unconditional will to provide employees with the best possible personal development is a special characteristic of Prof. Dr. Starke. All those qualities make him an admirable person and mentor who I could always look up to. Thank you.
I would also like to thank Prof. Dr.-Ing. Dirk Bähre who agreed to supervise the thesis as co-supervisor. I am particularly pleased that a proven specialist in the field of manufacturing has taken on the role as co-supervisor, especially because of the thematic overlaps caused by the investigations of the influence of surface integrity on fatigue behaviour. Further thanks goes to Priv. Doz. Dr.-Ing. habil. Michael Marx, since he agreed to be the academic supervisor.
During my doctorate, I was allowed to work at the Department of Materials Science & Materials Testing WWHK (Fachgebiet für Werkstoffkunde & Werkstoffprüfung) under the guidance of Prof. Starke at University of Applied Sciences Kaiserslautern. Therefore, i would like to thank the University of Applied Sciences Kaiserslautern for the opportunity to use its extensive infrastructure.
An important aspect for the success of this doctoral thesis is a functioning team. I am happy and proud to be able to work in a team like the WWHK. I would like to thank all the staff at the WWHK, as well as the staff of the University of Applied Sciences that I have had the pleasure of getting to know during the course of my work as scientific researcher.
I would particularly like to mention Haoran Wu, who helped to ignite my passion for the subject of fatigue by supervising my Master's thesis, and Florian Juner, who was always available to help me as research assistant. Apart from that I would like to thank Janina Koziol, with whom I also had many scientific discussion, as well as conversations regarding our activities as group leaders.
Last but not least, I would explicitly like to acknowledge my whole family, especially my parents and sisters, my best friend Vincent and my girlfriend Miriam for their comprehension and support during this time. None of this would have been possible without you.

List of Publications

Journal contributions as corresponding author:

- **F. Weber**, J. Koziol, P. Starke
  StressLife: A Short-Time Approach for the Determination of a Trend S-N Curve in and beyond the HCF Regime for the Steels 20MnMoNi5-5 and SAE 1045.
  Materials, 2023, 16(11), 1–19.
- **F. Weber**, H. Wu, P. Starke
  A new short-time procedure for fatigue life evaluation based on the linear damage accumulation by Palmgren–Miner.
  International Journal of Fatigue, 2023, 172, 1–8.
- **F. Weber**, M. Maul, F. Juner, P. Starke
  A nonlinear lifetime prediction method for un- and low alloyed steels by damage determination based on nondestructive measurement techniques.
  Fatigue & Fracture of Engineering Materials & Structures, 2024, 47(5), 1566–1583.
- **F. Weber**, P. Starke
  Implementation of modelled surface roughness in the accelerated lifetime prediction of a 20MnMoNi5-5 steel.
  International Journal of Fatigue, 2024, 186, 1–9.
- **F. Weber**, T. Eyrisch, T. Hielscher
  Tool Wear Influence on the Fatigue Life of Lathe Processed Specimens of 1.6310 Steel.
  Modern Concepts in Material Science, 2024 1–9.

Conference contributions as corresponding author:

- **F. Weber**, P. Starke
  MiDAcLife - Ein neues Kurzzeitverfahren zur Lebensdauerberechnung basierend auf dem Ansatz von Palmgren Miner
  Werkstoffe und Bauteile auf dem Prüfstand, Tagung Werkstoffprüfung, 2023, 296–301.
- **F. Weber**, P. Starke
  MiDAcLife - Ein neues Lebensdauerprognoseverfahren basierend auf der Kombination zerstörungsfreier Messverfahren und (nicht)linearer Schadensakkumulationsansätzen
  DGZfP-Berichtsband BB 182, 2024.
- **F. Weber**, P. Starke
  Beschleunigte Bestimmung virtueller Wöhlerkurven unter Berücksichtigung modellierter Rauheitswerte
  Werkstoffe und Bauteile auf dem Prüfstand, Tagung Werkstoffprüfung, 2024.
- **F. Weber**, F. Juner, P. Starke, T. Hielscher
  Bewertung des Einflusses spanender Bearbeitungsparameter auf das mechanische Verhalten am Beispiel niedriglegierter Stähle
  Werkstoffe und Bauteile auf dem Prüfstand, Tagung Werkstoffprüfung, 2024.
- **F. Weber**, F. Weber, A. Bezold, C. Broeckmann, P. Starke
  MiDAcLifecast – A lifetime prediction method for heavy-section castings based on non-

destructive measurements
InCeight Casting C8, 2025 (submitted).

Journal contributions as co-author:

- R. Acosta, **F. Weber**, T. Eyrisch, T. Hielscher, M. Magin, P. Starke
  Influences through processing parameters on the lifetime of quenched and tempered SAE 4140H specimens.
  MP Materials Testing, 2019, 61(9), 842–850.
- R. Acosta, H. Wu, R.S. Venkat, **F. Weber**, J. Tenkamp, F. Walther, P. Starke
  SteBLife, a New Approach for the Accelerated Generation of Metallic Material's Fatigue Data.
  Metals, 2020, 10, 1–17.
- R. Acosta, C. Boller, M. Doktor, H. Wu, H. Jost, **F. Weber**, P. Starke
  Evaluation of S-N curves including failure probabilities using short-time procedures.
  Materials Testing, 2021, 63(8), 705–713.
- H. Wu, J.A. Ziman, S.R. Raghuraman, J.-E. Nebel, **F. Weber**, P. Starke
  Short-Time Fatigue Life Estimation for Heat Treated Low Carbon Steels by Applying Electrical Resistance and Magnetic Barkhausen Noise.
  Materials, 2022, 16(1), 1–21.
- H. Wu, S.R. Raghuraman, J.A. Ziman, **F. Weber**, T. Hielscher, P. Starke
  Characterization of the Fatigue Behaviour of Low Carbon Steels by Means of Temperature and Micromagnetic Measurements.
  Metals, 2022, 12(11), 1–15.

Conference contributions as co-author:

- S.R. Raghuraman, A. Shrivastava, **F. Weber**, U. Krupp, P. Starke
  Bewertung von Volumen- und Oberflächenschäden bei HCF- und VHCF-Beanspruchung von Vergütungsstählen
  Werkstoffe und Bauteile auf dem Prüfstand, Tagung Werkstoffprüfung, 2023, 256–261.
- J. Koziol, M. Maul, **F. Weber**, P. Starke
  Temperaturbasierte Analyse des Frequenzeinflusses auf die Ermüdungseigenschaften des Stahles C45E
  Werkstoffe und Bauteile auf dem Prüfstand, Tagung Werkstoffprüfung, 2023, 270–275.
- S.R. Raghuraman, A. Shrivastava, **F. Weber**, U. Krupp, P. Starke
  Assessment of volume and surface damage in mixed HCF and VHCF loading of quenched and tempered steels
  Proceedings EUROMAT, 2023.
- J.A. Ziman, J.L. Otto, **F. Weber**, L.M.Sauer, F. Walther, P. Starke
  Einsatz des temperaturkorrigierten elektrischen Widerstands in Lebensdauerprognoseverfahren bei erhöhten Prüffrequenzen
  Werkstoffe und Bauteile auf dem Prüfstand, Tagung Werkstoffprüfung, 2024.

- S.R. Raghuraman, A. Shrivastava, **F. Weber**, U. Krupp, P. Starke
  Influence of reconditioning on the re-use potential considering HCF and VHCF loading of quenched and tempered steels
  Werkstoffe und Bauteile auf dem Prüfstand, Tagung Werkstoffprüfung, 2024.
- F. Weber, **F. Weber**, A. Bezold, P. Starke, C. Broeckmann
  Kurzzeitverfahren zur Ermittlung lokaler Festigkeiten in Großgussbauteilen aus EN-GJS-500-14 und EN-GJS-1050-6
  Werkstoffe und Bauteile auf dem Prüfstand, Tagung Werkstoffprüfung, 2024.
- J.A. Ziman, M. Maul, J.L. Otto, **F. Weber**, F. Walther, P. Starke
  Temperature-corrected electrical resistance in fatigue life prediction methods for higher testing frequencies
  European Conference on Fracture, 2024.

Abstract / Kurzfassung

Abstract

Within the dissertation, a new lifetime prediction method called MiDAcLife is developed, enabling a significant reduction in the required number of fatigue specimens. By combining non-destructively determined signals and damage accumulation models, virtual S-N curves are obtained based on only one fatigue test. This process-oriented assessment of fatigue behaviour demonstrably reduces incurred costs. Since crack initiation from the surface is one of the most dominant failure mechanisms considering a High Cycle Fatigue loading, a key focus is on the assessment of the surface influence on the fatigue behaviour of a 20MnMoNi5-5 steel, which was mainly used in German nuclear power plants. The effect of increased surface roughness is demonstrated on five differently manufactured surface conditions. Besides that, a method is developed by which the roughness is modelled and directly integrated into MiDAcLife. As a consequence, conclusions regarding the fatigue behaviour of different surface conditions can be drawn based on only one reference surface. Another important aspect is the provision of individualised S-N curves. Therefore, additional parameters such as carbon content and different heat treatment for instance are considered while the applicability of MiDAcLife is examined. Apart from that, new methods are presented that enable the integration of statistical approaches, as well as the consideration of different damage mechanisms in case of further material groups.

Kurzfassung

Im Rahmen dieser Dissertation wird das neu entwickelte Lebensdauerprognoseverfahren MiDAcLife präsentiert, welches die benötigte Probenanzahl durch eine Kombination aus zerstörungsfreier Prüfung mit der linearen Schadensakkumulation deutlich reduziert. Infolge dieser vorgangsorientierten Bewertung des Ermüdungsverhalten können auftretende Kosten signifikant verringert werden. Insbesondere im Falle einer High Cycle Fatigue Beanspruchung ist die Rissinitiierung an der Oberfläche einer der wichtigsten Versagensmechanismen. Folglich besteht ein zentraler Aspekt in der Untersuchung des Oberflächeneinflusses auf das Ermüdungsverhalten eines 20MnMoNi5-5 Stahls, welcher in der deutschen Kernenergietechnik Anwendung fand. Die Auswirkung der Rauheit wird an fünf Oberflächenzuständen untersucht. Durch eine Modellierung der Daten wird eine Integration in MiDAcLife zugänglich. Darauf aufbauend können Rückschlüsse auf das Ermüdungsverhalten unterschiedlicher Oberflächenzustände basierend auf lediglich einer Referenzoberfläche gezogen werden.

Ein weiterer zentraler Aspekt besteht in der Bereitstellung individualisierter Wöhlerkurven. Daher werden zusätzliche Parameter wie beispielsweise der Kohlenstoffgehalt oder verschiedene Wärmebehandlungen in die Betrachtung integriert und die Anwendbarkeit von MiDAcLife validiert. Darüber hinaus werden neue Methoden vorgestellt, welche die Erweiterung um statistische Ansätze, sowie die Berücksichtigung variierender Schadensmechanismen ermöglichen.

Contents

List of Symbols

Abbreviations

AM	Additive manufacturing
CAT	Constant amplitude test
EBSD	Electron backscatter diffraction
FKM	Forschungskuratorium Maschinenbau
GL	Gauge length
HCF	High Cycle Fatigue
HV	Vickers hardness
KTA	Kerntechnischer Ausschuss
LCF	Low Cycle Fatigue
LIT	Load increase test
LPM	Lifetime prediction method
MiDAcLife	Miner Damage Accumulation Lifetime Prediction
NDT	Non-destructive testing
OECD	Organisation for Economic Cooperation and Development
PSB	Persistent Slip Bands
SEM	Scanning electron microscopy
SLM	Selective laser melting
VHCF	Very High Cycle Fatigue

Greek Symbols

ΔE_f	Total plastic strain energy $[\mathrm{J} \cdot \mathrm{m}^{-3}]$
ΔE_i	Dissipated plastic strain energy $[\mathrm{J} \cdot \mathrm{m}^{-3}]$
ΔR	Change in electrical resistance [µΩ]
ΔR_{exp}	Sum of the variation induced by temperature change [%]
δ_i	Damage index [−]
δ_i	Deviation of the calculated parameters from conventional data [%]
δ_m	Maximum deformation peak under cyclic loading [m]
δ_u	Ultimate displacement under monotonic loading [m]
γ	Material constant depending on tensile strength [mm]
γ_{FF}	Fatigue fracture entropy $[\mathrm{MJ} \cdot (\mathrm{m}^3\mathrm{K})^{-1}]$
λ	Ratio roughness spacing and height [−]
λ_i	Wavelength i^{th} wave [µm]
ω_h	Heat source combining dissipation and thermoelasticity $[\mathrm{kW} \cdot \mathrm{m}^{-3}]$
ω_{thc}	Thermomechanical coupling source $[\mathrm{kW} \cdot \mathrm{m}^{-3}]$
ω_{the}	Thermoelastic heat source $[\mathrm{kW} \cdot \mathrm{m}^{-3}]$
$\overline{\rho}$	Effective profile valley radius [µm]
ρ	Profile valley radius [µm]
ρ'	Resistivity of damaged specimen [Ωm]
ρ_{heq}	Material constant heat equation $[\mathrm{kg} \cdot \mathrm{m}^{-3}]$
σ_a	Stress amplitude [MPa]
σ_D^{load}	Permitted load amplitude [MPa]
σ_e	Fatigue strength [MPa]

σ'_f	Fatigue strength coefficient [MPa]
σ_l	Lower stress [MPa]
σ_u	Upper stress [MPa]
$\sigma_{a,eff}$	Effective stress amplitude [MPa]
σ_{axial}^{RS}	Axial residual stresses [MPa]
σ_{eq}^{i}	Equivalent stress [MPa]
$\sigma_{eq}^{i,max}$	Maximum equivalent stress [MPa]
$\sigma_{RS}(x)$	Distribution of residual stresses [MPa]
$\sum_i^{eq}$	Damage stress amplitude at i$^{\text{th}}$ load level [−]
τ_u	Ultimate stress in torsion test [MPa]
τ_{eq}	Heat loss to environment $[\mathrm{W} \cdot \mathrm{K}^{-1}]$
θ	Temperature variation with respect to initial equilibrium [K]
ε_0	Strain at fatigue strength [%]
ε'_f	Fatigue ductility coefficient [−]
ε_R	Maximum reversed strain [%]
$\varepsilon_{a,p}$	Plastic strain amplitude [%]
$\varepsilon_{a,t}$	Total strain amplitude [%]
φ_i	Phase i$^{\text{th}}$ wave [µm]
$tan(\theta)$	Slope iso-damage line [−]
σ_m	Mean stress [MPa]

Other symbols

$2b$	Surface pitch [µm]
$\int dE$	Incremental absorbed plastic strain energy $[\mathrm{J} \cdot \mathrm{m}^{-3}]$

Roman Symbols

$\overline{K_f}$	Effective fatigue stress concentration [−]
$\overline{K_t}$	Effective stress concentration [−]
a	Crack length [µm]
a	Surface depth [µm]
A_i	Amplitude i$^{\text{th}}$ wave [µm]
a_R	Material specific constant FKM [−]
A_{el}	Resistance temperature coefficient $\left[\mathrm{m}\Omega \cdot^{\circ} \mathrm{C}^{-1}\right]$
B	Basquin coefficient StressLife [K]
b	Fatigue strength exponent [−]
C	Manson & Coffin coefficient StressLife [K]
c	Fatigue ductility exponent [−]
c	Heat capacity $[\mathrm{J} \cdot \mathrm{K}^{-1}]$
$C_{\varepsilon,\alpha}$	Material constant heat equation $[\mathrm{J} \cdot (\mathrm{kg} \cdot^{\circ} \mathrm{C})^{-1}]$
D	Total damage [−]
D_i	Partial damage [−]
D_{N_f}	Critical cummulative damage [−]
E_f	Total plastic strain energy $[\mathrm{J} \cdot \mathrm{m}^{-3}]$
h_{el}	Material constant electrical resistance measurement [−]
$J_{1,max}$	Maximum hydrostatic-stress [MPa]
$J_{2,a}$	Second invariant deviatoric stress amplitude [MPa]
k	Slope S-N curve [−]
K'	Cyclic hardening coefficient $[\mathrm{MPa} \cdot \mathrm{K}^{-1}]$
K_R	Surface factor FKM [−]
K_t	Stress concentration factor [−]

K_{el}	Material constant electrical resistance measurement [−]
K_{max}	Maximum stress concentration factor [−]
K_{res}	Stress concentration factor as a result of residual stresses [−]
k_{th}	Thermal conductivity $[\mathrm{W \cdot mK^{-1}}]$
M_{RS}	Mean stress sensitivity [−]
m_{RS}	Residual stress sensitivity [−]
n	Stress state [−]
n'	Cyclic hardening exponent [−]
N_e	Limiting number of cycles [−]
N_f	Number of cycles to failure [−]
n_i	Number of applied cycles [−]
N_k	Number of cycles at the knee point [−]
n_{el}	Slope of the elastic range Morrow-equivalent plot [−]
$N_{fictitious}$	Fictive limiting number of cycles [−]
$N_{P10\%}$	Cycle number with a failure probability of 10 % [−]
$N_{P90\%}$	Cycle number with a failure probability of 90 % [−]
n_{pl}	Slope of the plastic range Morrow-equivalent plot [−]
P	Experimentally determined material-specific constant [−]
q	Notch sensitivity [−]
R	Load ratio [−]
R_0	Initial resistance [µΩ]
R_e	Yield strength [MPa]
r_e	External heat supply $[\mathrm{kW \cdot m^{-3}}]$
R_m	Tensile strength [MPa]
$R_{m,N,min}$	Material specific constant FKM [MPa]
S_f	Maximum entropy generation $[\mathrm{J \cdot K^{-1}}]$
S_{N_f}	Critical entropy generation $[\mathrm{J \cdot K^{-1}}]$
T_d	Temperature due to dissipation [K]
T_N	Range of scatter [−]
T_{amb}	Environmental temperature [K]
x_σ	Stress-dependent exponent for damage parameter evaluation [−]

PART I

1 Motivation & Objectives

1.1 Motivation

Since fatigue of materials is one of the most common failure mechanism in engineering applications, a profound understanding of ongoing microstructural processes is essential when it comes to future research. Because of material degradation as a result of fatigue processes, specimen-, or component-failure can occur at load levels well below statically determined strength values, which is why an appropriate design of dynamically loaded components is quite challenging. However, overdimensioning of components must be avoided, particularly in reference to energy policy requirements and economic efficiency. Therefore, the microstructure, as well as the mechanisms involved, need to be detected and understood.
In the past, serious accidents have reoccurred, caused by the sudden failure of components which were subjected to dynamic loads. Only a small percentage of many damage cases are given in the literature [1, 2].
To estimate the lifetime of a specimen, which is subjected to dynamic loading, the so-called S-N curve (Wöhler curve) is used. It displays the relation between the loading amplitude and the corresponding number of cycles to failure. According to literature, first systematical investigations regarding this relation were performed by the German engineer August Wöhler in 1860 on railway axles [3]. However, the generation of such curves is connected to an increased testing effort of about 20 specimens and consequently to an increased amount of time and costs.
Apart from that, fatigue of metals is a multi-parameter phenomenon affected by a high amount of influencing factors. These factors can be material-dependent as well as caused by environmental influences. Since cracks mostly initiate at the surface, especially in the High Cycle Fatigue (HCF) regime, roughness is of great importance and needs to be considered within the calculations. Moreover, residual stresses can result from the manufacturing process and increase or decrease the lifetime of metallic components. In addition to the influencing factors mentioned, the ambient temperature is a distinct factor leading to a lifetime reduction in most cases, with the exception of phenomena such as dynamic strain aging.
A very important engineering field in which new material science methods are investigated, is the field of nuclear energy. The reactor accident in Fukushima in 2011 has led to a worldwide review of the design concepts and operating conditions of nuclear power plants used in Germany and internationally. Particularly in view of the fact that nuclear power plants currently in operation outside of Germany still continue to be the largest source of low carbon electricity generation in OECD (Organisation for Economic Co-operation and Development) countries, the technical and scientific validation of long-term operation conditions is essential in order to achieve the decarbonisation targets that have been set.
Components and structures of nuclear power plants are subjected to mechanical as well as thermal loads. The aging of those components causes a need to develop new methods in order to enable a reasonable prediction of the integrity. Even if certain information can be covered by simulations, these simulations must be extended and improved on the basis of experimental data, which again highlights the importance of an accelerated provision of fatigue data. In addition to the experimental tests with constant load amplitude, a further test form, the so-called load increase test (LIT), is used for this purpose, which serves as an input for the new developed lifetime prediction method (LPM) and for the estimation of other important characteristic values, such as the fatigue strength σ_e of the material.

The Department of Materials Science & Materials Testing (WWHK) at the University of Applied Sciences Kaiserslautern intensively deals with the provision of fatigue data based on physical measurement methods. In recent years, different lifetime prediction methods, such as SteBLife, StrainLife and StressLife have been developed.

1.2 Objectives and Scope

The goal of this doctoral thesis is to enable a provision of reasonable and accelerated fatigue data and to develop models in order to calculate the lifetime of metallic specimens with a highly reduced amount of specimens, resulting in time- and cost savings. To reach this aim, new approaches are used, combining conventional fatigue testing and NDT (non-destructive testing)-related methods. As a result, a process-orientated determination of fatigue behaviour is enabled. This research uses different measurement techniques to monitor the material response to dynamic loading. In addition to conventional strain measurements, thermography and resistometric measurement techniques are applied on the testing system as part of this work. Both techniques are considered as sensitive devices for the evaluation of microstructural changes as a result of dynamic loading.
The existing LPMs generally enable a global assessment of fatigue properties. Within the scope of this research, a newly developed procedure is applied to enable a local assessment. Very common approaches to describe fatigue behaviour of metallic materials are damage accumulation models, which are based on the calculation of a partial damage, induced per load cycle. A very simple and frequently used method is the linear damage accumulation model according to Palmgren Miner, in which the partial damage results from the relation between the applied load cycles and the number of cycles to failure. However, the assumption of linearity sometimes leads to large deviations from real applications. Therefore, the development of new methods with increased prediction quality is of great importance. Within this thesis, a new LPM is developed, which considers a non-linear damage behaviour by correlating the partial damage with the material response.
Most investigations are performed on a ferritic-bainitic 20MnMoNi5-5 steel which was used in spraylines of German nuclear power plants. As certain factors can have a significant influence on the lifetime of materials, a key objective of the presented work is to investigate the influence of damage-relevant parameters on fatigue behaviour. Since the experiments are carried out in the HCF regime of S-N curves, where crack initiation from the surface is the dominant failure mechanism, the focus is on the determination of surface integrity influence. For this purpose, five different surface topographies need to be manufactured and characterised using analytical methods. The aim is not only to eliminate the dependence of fatigue lifetime on defined roughness parameters, but also to develop and calculate damage factors that can be directly included in the lifetime prediction. Therefore, the overall aim of the thesis is to make a virtual estimation of S-N curves accessible, using conversion factors from an output variable such as surface roughness.

2 State of the Art

2.1 Fatigue of Metallic Materials

Because of the wide range of possible applications as a result of various properties, metallic materials are mainly used as construction materials. Most operation conditions are dominated by dynamic load sequences, which lead to a change in the mechanical properties of metallic materials. This degradation is called fatigue of metals and effects damage within the material, leading to a reduced load capacity. Since fatigue failure can occur at load levels evidently below static strength values, serious cases of damage can be the result. The following chapter aims to give a brief introduction regarding the phenomenon of fatigue.

2.1.1 Historical Overview

With the beginning of the industrial revolution in the first half of the 19^{th} century, fatigue of components and structures came into focus of science and engineering and is therefore closely connected to the industrial revolution [4]. The development and utilization of steam engines, locomotive axles and pumps led to increased loading of structural components causing unexplainable fractures and failures at that time [5,6]. Despite usage of ductile materials, component failures were characterised as processes without any visible indication of plastic deformation such as in a brittle material behaviour [4, 5]. Apart from that, failure occurred after large amount of load cycles although the materials were designed to withstand much higher static loads [4, 7]. In order to prevent these unexpected failures, detailed investigations of the affected components became necessary, attracting the attention of researchers [4].
Even though fatigue research is very often associated with the well-known engineer August Wöhler, first investigations date back to an earlier time. The very first fatigue testing machine was developed by "Oberbergrat" Albert in 1837 in Clausthal. The goal was the investigation of conveyor chains from mines, since there were numerous rope breaks every quarter of the year [8]. Albert became particularly well-known for the resulting invention of the wire rope [9].
Since a very common issue at this time was the failure of axles, several researchers, for example Rankine [7], devoted themselves to this matter. A more detailed description of the investigations before 1858 is given by Schütz [9].
First systematic fatigue experiments were then performed by August Wöhler in 1858, who investigated the operational loads of railway axles. He was able to prove that the strength of railway axles, which were subjected to dynamic loading, was evidently lower compared to static values. To achieve these insights, Wöhler constructed not only axial testing machines but also bending and torsion testing machines [3]. Because of this ground-breaking research, the relation between the stress amplitude and associated number of cycles to failure is still referred to today as the Wöhler curve (S-N curve), even though this type of illustration was introduced later on.
An important step in the clarification of microstructural fatigue mechanism was achieved by Ewing & Rosenhain as well as Ewing & Humfrey in 1900 / 1903, as they were able to evidently display cyclic damage on the surface using optical micrographs. Therefore, slip bands within different grains, which are one of the main fatigue mechanism, could be detected [10].
Basquin was the first person to propose an empirical law, which characterises the progression of an S-N curve [11]. Using a double-logarithmic scale, a linear relationship between the stress amplitude

and the number of cycles to failure could be found.
A widely exerted model for assessing the damage state of fatigue specimens was given between 1924 and 1945 by Palmgren and Miner [12, 13] by the linear damage accumulation model. It defines the partial damage as the relation between the applied load cycles and the number of cycles to failure. From 1960 on, the research results in the field of fatigue have been increasing enormously, which is mainly caused by improved testing systems, improved sensor technology and new analytical methods. A compact overview of further evolution can be found in literature [3, 9, 14].

2.1.2 Introduction to Fatigue

In many engineering applications, components or structures are subjected to dynamic loading. Therefore, the sub-field of materials science, labelled as fatigue of materials, is assigned a decisive role. In order to understand the process of fatigue and the involved mechanisms, a generalised definition is required first, which was established in 1964 by the Organization for Standardization. Within this report, fatigue is assigned to *"changes in the properties of metallic materials because of the repeated application of stress- or strain amplitudes. Usually this term applies specially to those changes which lead to cracking or failure"* [3]. The previously mentioned definition shows demonstrably that all changes in properties are summarised under the term fatigue. However, particularly for the design of dynamically loaded components, changes in mechanical properties are usually in the focus of research. Within this thesis, it will be shown that various property changes can be used beneficially to infer mechanical changes.
Fatigue damage is further characterised by the fact that it already occurs at load amplitudes evidently below statically determined strength values such as the yield strength. Especially the failure without macroscopic plastic deformation is challenging. At this point it should be noted that loading in a fatigue test can be applied in a stress-controlled or strain-controlled manner. For reasons of clarity and since only stress-controlled tests are carried out as part of this research, the focus is on a consideration of the applied stress amplitude.

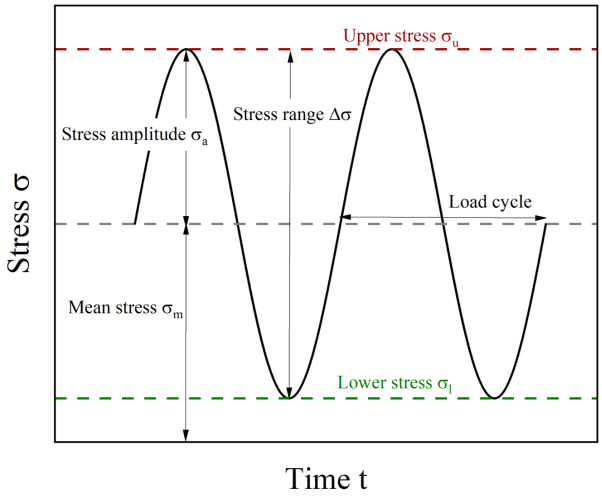

Figure 2.1: Schematic representation of important parameters describing a fatigue test

Basic terms describing fatigue properties of materials are summarised in DIN 50100 [15]. The most important parameters defining dynamic loading are the stress amplitude σ_a, the mean stress σ_m, the upper and lower stress σ_u and σ_l, as well as the stress range $\Delta\sigma$, which are given schematically in figure 2.1. Besides that, the relation between the lower and the upper stress is defined by the load ratio R, which is displayed in equation 2.1.

$$R = \frac{\sigma_l}{\sigma_u} \tag{2.1}$$

It can be stated that the so-called S-N curve is the most frequently used representation in order to assess fatigue behaviour. It displays the relation between the applied load amplitude σ_a and the corresponding number of cycles to failure N_f and can be divided in mainly three regimes.
In case of high load amplitudes and therefore lower numbers of cycles to failure, the term LCF (Low Cycle Fatigue) is used. The limits of the different regimes highly depend on which literature is considered. Within this thesis, the transition point to the LCF regime is set to 10^4 cycles. The range between 10^4-10^7 is characterised by the HCF regime, which is the most important part for the presented research. A further increase of N_f leads to the transition to the VHCF regime (Very High Cycle Fatigue) in which damage mechanisms change and inhomogenities in the bulk material become more important.
In case of an HCF loading, fatigue tests are usually carried out stress-controlled, and the elastic approach according to Basquin, given in equation 2.2, is used [16].

$$\sigma_a = \sigma'_f \cdot (N_f)^b \tag{2.2}$$

In equation 2.2, σ'_f is defined as the fatigue strength coefficient, whereas b displays the fatigue strength exponent.
Unlike in the HCF regime, fatigue experiments in the LCF regime are conventionally strain-controlled. To describe fatigue behaviour mathematically, an approach according to Manson & Coffin is used [17–19]. It describes the plastic strain amplitude $\varepsilon_{a,p}$ as a function of the fatigue ductility coefficient ε'_f, the number of cycles to failure N_f and the fatigue ductility exponent c.

$$\varepsilon_{a,p} = \varepsilon'_f \cdot (N_f)^c \tag{2.3}$$

2.1.3 Stages of Fatigue

Fatigue behaviour of metallic materials can essentially be divided into four different phases, which are displayed in figure 2.2. In the first stage of the fatigue process, dislocation reactions take place. Depending on the material and the applied load, different dislocation structures such as vein structures, persistent slip bands (PSB), forming a ladder-like structure, or dislocation cells can occur [3, 20, 21]. In the second stage, micro-cracks are initiated at locations with increased stress concentration, for example extrusions and intrusions. Micro-cracks are usually initiated at several starting points and combine to form an effective macro-crack. The propagation of the macro-crack is represented by stage III. Because of the reduced cross-section of the specimen as a result of the macro-crack, the yield point of the material is exceeded at a certain point and final fracture occurs. This final fracture is assigned to stage IV of the fatigue process.

As the 20MnMoNi5-5 (1.6310) steel, examined within this thesis, is characterised by an increased strength and therefore a consequently more brittle material behaviour, stages III and IV are of minor importance. Especially stage I and II of figure 2.2, determine the majority of fatigue life. For this reason, only these two aspects are explained in more detail within this section.

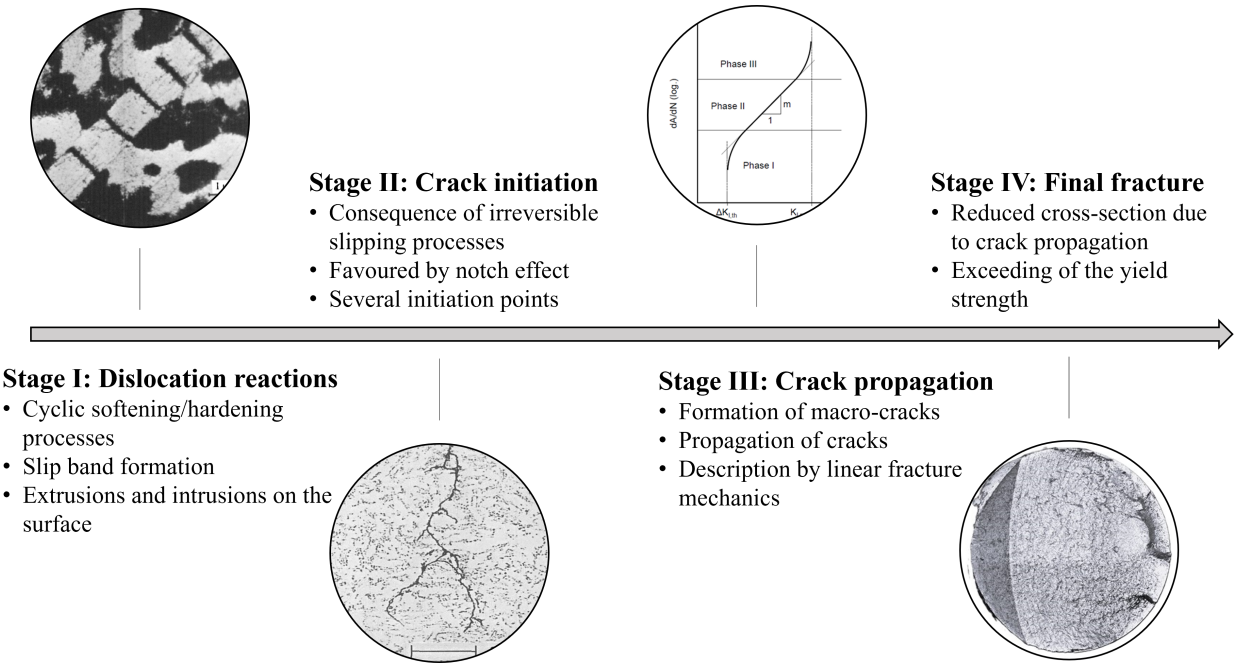

Figure 2.2: Schematic representation of different stages regarding a fatigue process; Stage I: dislocation reactions in the volume of the material [3], stage II: crack initiation at locations with increased stress concentration, stage III: formation of macroscopic cracks and crack propagation, which is described by fracture mechanics [22], stage IV: final fracture of the specimen

Stage I and II: Dislocation Reactions and Crack Initiation

Especially since the fundamental research of Manson & Coffin, it is well-known that the phenomenon of material fatigue is always a consequence of plastic strain. Even for stress amplitudes that are evidently below the macroscopic yield strength R_e, failure of the material can occur as a result of dynamic loading, leading to localised micro-plastic deformations. The irreversible deformation of components resulting from the loading causes damage in each load cycle, which accumulates over a large number of cycles to a critical damage value [3, 23].
The driving force of plastic deformation in metals are the so-called dislocations in the lattice structure, which interact with each other. As a result of shear stress, dislocation movements occur in terms of slipping processes along defined crystallographic planes and directions. This dislocation movement results in different dislocation structures, which in turn have influence on the mechanical properties. The type of dislocation structure highly depends on the characteristic slipping behaviour of the material, which represents a benchmark for the formation of three-dimensional dislocation structures, such as cell structures. In literature, a distinction is made between planar and wavy slipping material behaviour [20].

Since there is no parameter that enables a direct quantification of slipping behaviour, the stacking fault energy is used for an indirect assessment. The stacking fault energy describes the energy stored in the lattice due to a displacement of atoms or atomic layers in relation to their idealised lattice position. It is initially assumed that an increased stacking fault energy results in a decreased splitting distance of partial dislocations and therefore facilitates the recombination of the splitted screw dislocations.

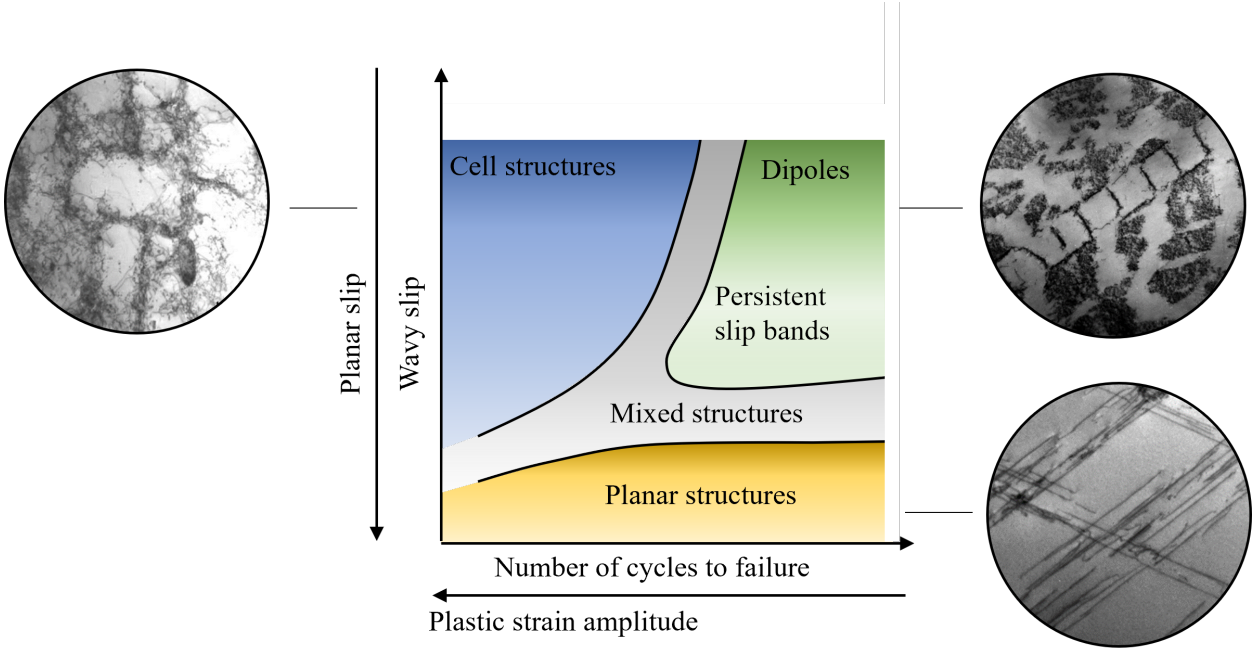

Figure 2.3: Schematic representation of different dislocation structures as a function of the plastic strain amplitude and number of cycles to failure according to [24] with micrographs of the different dislocation structures from [25–27]

Figure 2.3 provides an overview of the different dislocations structures as a function of the load amplitude and the number of cycles to failure. In case of planar sliping behaviour, which is shown in the lower part of figure 2.3, edge dislocations are arranged parallel to each other over the entire volume of the material. Besides that, an independence of the planar structure from the respective load amplitude can be determined. In contrast, wavy slipping behaviour is characterised by a strong dependence on the load amplitude. For moderate load amplitudes, usually only one sliding system is actuated, which leads to the formation of dislocation bundles or vein structures, that are essential for the formation of PSB. If the load amplitude is increased, several slip systems are activated and thus enable multiple slip, resulting in cell- or labyrinth structures [3, 21].
Because of the localised high concentration of plastic deformation, PSB are highly important in terms of fatigue damage in the HCF regime and are characterised by their ladder structure. The term persistent goes back to the work of Thompson [28], who was able to prove that PSB reappear in the same places even after a polishing process. Due to the high slipping activity within PSB, surface roughness is formed in terms of extrusions and intrusions. These areas of increased stress concentrations represent starting points for crack initiation.
The second stage of the fatigue process is characterised by crack initiation, following the dislocation

reactions. Because of the uncertain definition of a crack, a quantitative statement about when and where a micro-crack is initiated is challenging. Technically, a crack is already present if local interatomic forces are exceeded [29]. Furthermore, the differentiation between crack initiation and propagation is demanding due to the dependency on the resolution of measurement devices. A possible demarcation is given by Mughrabi. In his work, he suggested to define the crack initiation process up to the point at which the crack has reached a size at which it can be described in terms of the rules of fracture mechanics. As a result of this definition, early slow crack growth is also included in the initiation stage [30].
According to Suresh [3], micro-cracks can emerge along PSBs, as well as along grain boundaries and near inclusions or pores. Considering an HCF loading, crack initiation along PSBs is probably the most important mechanism. The fact that the material surface usually serves as a starting point for crack initiation can be explained by an increased plastic activity, which has two main reasons. On the one hand, notch effects due to extrusions and intrusions or, more general, surface roughness lead to local increased stress concentration. On the other hand, multiple slip is necessary in polycrystalline materials to ensure compatibility of the deformation, which is associated with higher shear stresses.
A method to describe the formation of surface protrusion is given by the EGM model according to Eßman, Gösele and Mughrabi [31–34]. The model considers that dislocations can be newly formed or annihilated as a result of dynamic loading. In case of annihilation of vacancy dislocation dipoles, vacancies are formed causing material to emerge from the surface in form of extrusions.
For further crack initiation mechanisms such as crack initiation at grain boundaries, inclusions or pores, additional literature can be taken into account [35–46].

2.2 Influencing Factors on the Fatigue Behaviour

The phenomenon of materials fatigue as a result of dynamic loading is a multi-parametric process. The complexity of this material degradation is essentially caused by the large amount of influencing factors. For a reliable lifetime prediction, it is therefore crucial to include these factors into the different evaluations and calculation methods. However, this is only possible if the effects on fatigue behaviour are sufficiently understood. Figure 2.4 divides influencing factors in three clusters: load parameters, structural parameters and geometry parameters.
The presented research results mainly focus on the influence of surface integrity on fatigue behaviour, which is why surface roughness and residual stresses are of high importance. For this reason, theoretical explanations in this chapter are limited to these two aspects, which is graphically illustrated by the green font in figure 2.4. Since the results of this doctoral thesis are not only based on the ferritic-bainitic 20MnMoNi5-5 steel, but also further materials, such as normalised and quenched-tempered un- and low alloyed steels and cast iron, additional parameters, as for instance heat treatment and microstructure are investigated (blue font in figure 2.4).

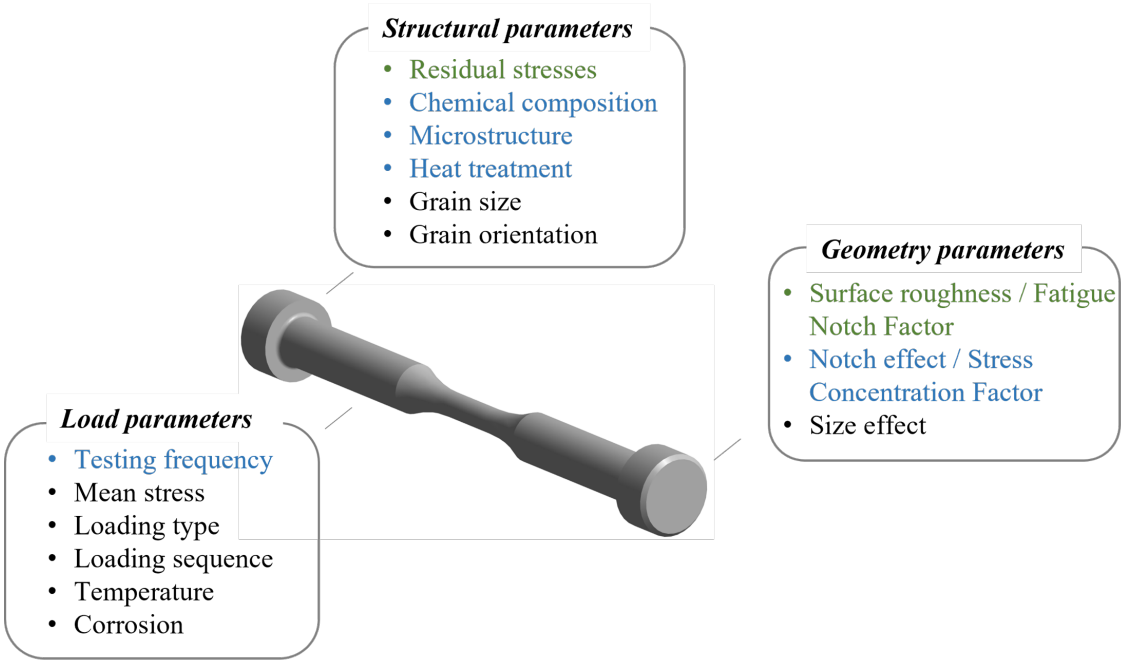

Figure 2.4: Schematic representation of the subdivision of influencing factors regarding fatigue behaviour of metallic materials (green: directly investigated parameters, blue: indirectly investigated parameters, black: not considered within this work)

2.2.1 Surface Roughness

Considering an HCF loading, crack initiation from the specimen surface is proven to be most prominent compared to other initiation mechanisms. Therefore, it can be concluded that the fatigue behaviour of a material is highly influenced by the surface condition as a result of the manufacturing process. Since different surface topographies lead to high variations regarding the numbers of cycles to failure, parameters describing the surface must be integrated into lifetime prediction. This chapter is intended to provide an overview of the possibilities to integrate surface roughness values into the evaluation of fatigue behaviour, leading to a reliable assessment.

In previous research, it has been shown that cracks mostly initiate at locations with increased stress concentration. Based on this finding, models were developed that describe the stress concentration mathematically as a function of different surface parameters. Neuber [47, 48] provided a semi-empirical relation, given in equation 2.4. Within this approach, the stress concentration factor K_t is a function of the surface height R_z and the notch radius ρ. Furthermore, n represents the stress state, whereas λ is defined as the ratio of the spacing and the height, enabling an estimation of surface irregularities.

$$K_t = 1 + n \cdot \sqrt{\lambda \frac{R_z}{\rho}} \tag{2.4}$$

It should be noted that approaches using standard roughness parameters to calculate the stress

concentration factor have the disadvantage of being insensitive to surface height distribution. To ensure an improved estimation of the stress concentration factor, Arola & Ramulu [49,50] extended the method proposed by Neuber. While investigating the influence of surface roughness on a high strength low alloyed SAE 4130 steel, the authors defined an effective stress concentration factor $\overline{K_t}$, which is displayed in equation 2.5.

$$\overline{K_t} = 1 + n \left(\frac{R_a}{\overline{\rho}} \right) \left(\frac{R_y}{R_z} \right) \tag{2.5}$$

Within this equation, R_a, R_y and R_z represent the standard roughness parameters. The effective profile valley radius is given by $\overline{\rho}$ and n is the differentiation between tension and shear loads according to Neuber. The stress concentration factor, calculated in equation 2.5 can subsequently be used to derive the effective fatigue stress concentration $\overline{K_f}$ (equation 2.6), which is also dependent on the notch sensitivity q (equation 2.7). In addition to the effective profile valley radius, the notch sensitivity is determined by a material-specific constant γ, which is influenced by the tensile strength R_m.

$$\overline{K_f} = 1 + q \left(\overline{K_t} - 1 \right) \tag{2.6}$$

$$q = \frac{1}{(1 + \gamma/\overline{\rho})} \tag{2.7}$$

The approach according to Arola & Ramulu is still subject of current research. Quan et al. [51] used the correlation of equation 2.5 to investigate the roughness influence on a GH4169, which is mainly applied in aerospace industry. In order to ensure a separate consideration of surface roughness, a vacuum annealing process was carried out to reduce the effect of residual stresses, originating from the manufacturing process. Apart from that, Starke et al. [52] explored the influence of different processing parameters on the fatigue behaviour of a quenched-tempered SAE 4140 steel implementing the Arola & Ramulu method. Within this research, different variations of feed rate, depth of cut, cooling and polishing were considered. Based on the obtained data, conclusions could be drawn about how changes in process parameters might effect changes in surface integrity and therefore have an impact on the fatigue behaviour. A comparable study was carried out by Javidi [53] on an SAE 4340 steel. Fatigue tests at specimens, manufactured with different feed rates and nose radii of the cutting tool, were selected to assess the influence of the manufacturing influence.

Another very common approach to consider the surface condition is given in the FKM guideline (Forschungskuratorium Maschinenbau), which introduced a surface-factor K_R on the basis of equation 2.8. It uses material-specific constants such as a_R and $R_{m,N,min}$, as well as static values like the tensile strength R_m to predict the change in fatigue strength [54, 55].

$$K_R = 1 - a_R \cdot log \left(\frac{R_z}{\mu m} \right) \cdot \left(\frac{2R_m}{R_{m,N,min}} \right) \tag{2.8}$$

Under the assumption of periodic surface notches simulating surface roughness, Murakami [56–58] developed the well known $\sqrt{area}$-method. According to Murakami, the stress concentration factor depends not only on the depth a, but also on the pitch $2b$ of cracks, since a decreased pitch leads to decreased stress concentration factors as a result of crack interference. The maximum value for the stress concentration factor is given by equation 2.9.

$$K_{tmax} = 0.65 \cdot \sigma_a \sqrt{\pi \sqrt{area}} \tag{2.9}$$

Depending on a and $2b$, there are two definitions for $\sqrt{area}$, given in equation 2.10 and 2.11.

$$\sqrt{area}/2b \cong 2.97 \cdot (a/2b) - 3.51 \cdot (a/2b)^2 - 9.74 \cdot (a/2b)^3 \tag{2.10}$$

$$\sqrt{area}/2b \cong 0.38 \tag{2.11}$$

A very frequently used parameter for the evaluation of fatigue behaviour, which considers influencing factors, is the fatigue strength σ_e. In their work, Murakami and Endo [58] proposed a relation between the fatigue strength, the Vickers hardness (HV) of the material and $\sqrt{area}$, depending on the load ratio R, which is given in equation 2.12.

$$\sigma_e = \frac{1.43 \cdot (HV + 120)}{(\sqrt{area})^{1/6}} \cdot \left(\frac{1-R}{2}\right)^{\alpha} \tag{2.12}$$

Itoga et al. [59] used the aforementioned approach to investigate the effect of different surface conditions on fatigue behaviour of high strength steels. Since crack initiation has a very prominent influence on the fatigue process, especially in case of high strength materials, the objective of the authors was to evaluate crack initiation mechanism-based. Therefore, additional SEM (Scanning electron microscopy) micrographs were applied in order to validate the results. It could be shown that the the influence is highly pronounced in terms of cycles lower than 10^5, whereas higher numbers of cycles lead to a damage shift into the volume.
Similar results were achieved by Lai et al. [60]. Here, a model was presented, which, in addition to various roughness values, also considered different microstructures. In order to realise this model, a comparison between a high carbon steel (100CrMnMoSi8) and a medium carbon steel (SAE 4147) was put into practice. It could be shown, that the high carbon steel tended to fail because of inclusions in case of smooth surface condition, whereas higher surface roughness favored crack formation at the surface. The result of the carbon content comparison showed a significantly reduced sensitivity to surface influences in case of lower carbon contents.
The damage transfer into the bulk was investigated by Bayraktar et al. [61] on a Ti-Al alloy, which is typically used in aerospace applications. Based on ultrasonic fatigue tests, it was demonstrated that the surface roughness has no significant influence on the lifetime, considering VHCF loading. The reason for this is given by low load amplitudes which lead to very high numbers of cycles in the VHCF regime. The dominant damage mechanisms are transferred from the surface into the volume of the material.
While investigating the influence of the surface finish effect on fatigue behaviour of forged steels

with different hardness, McKelvey and Fatemi [62] used both the approach of Murakami to estimate the fatigue limit of the materials and equation 2.6 (proposed by Arola & Ramulu) to calculate the Fatigue Notch Factor. The authors concluded, that in case of higher hardness values, polished surfaces lead to an improvement of the fatigue strength because of reduced critical stress locations.

Some of the previous presented research explored the integration of damage-relevant influencing factors in fatigue assessment of conventionally manufactured specimens or components. In recent years, additive manufacturing (AM) has become a significant alternative to subtractive machining. Caused by the layer by layer manufacturing process in case of an SLM (Selective Laser Melting) process, highly complex structures, for example in the aerospace, or nuclear energy industry, can be produced. However, the manufacturing process can also lead to material inhomogenities, which have a negative impact on fatigue behaviour. In particular, pores, unmelted powder nests, residual stresses and increased surface roughness should be mentioned at this point. Even a polishing process to reduce surface roughness might be challenging to attain due to the complexity of AM-components. For this reason, the investigation of the influence of these damage relevant parameters is of great interest in recent research. A selection of references is given in [63–78].

Based on the experimental results of recent research, various models have been developed, allowing the surface condition to be simulated and therefore lead to cost and time savings. Stopka et al. [79] presented a microstructure sensitive model, which aimed to correlate the microstructure and the surface condition with fatigue behaviour. To achieve this objective, a synthetic microstructure was simulated, using the simulation software DREAM 3D, which included realistic roughness profiles. Afterwards, a finite element method, called crystal plasticity was used to generate results.
A model for a relation between the surface roughness and fatigue behaviour of AM Ti-alloys was given by Hu et al. [80]. In order to quantify the roughness influence, a parameter G, considering surface height and correlation length was introduced. The basic idea of this research was, that parameters like laser power, scanning speed or the diameter of particles lead to unmelted/partially melted powder particles and therefore decrease the surface quality. The research provided a numerical simulation model, in which material degradation is applied by continuum damage mechanics. Additional research dealing with the simulation of different surface conditions is given in [81–89].

Apart from simulation models, Zhu et al. [90] provided analytical equations to estimate the stress concentration factor, as well as the Fatigue Notch Factor for an SAE 4140 steel. Within this study, experimentally determined roughness values were evaluated using a Fourier transformation. According to [91, 92], the surface height $Z(x)$ can be modelled by the sum of cos-functions and expressed as a function of the amplitude A_i of the i^{th} wave, the wavelength λ_i and the phase φ_i of the i$^{\text{th}}$ wave. The relation is given in equation 2.13.

$$Z(x) = -\sum_{i=1}^{n} A_i \cdot cos\left(\frac{2\pi \cdot x}{\lambda_i + \varphi_i}\right) \tag{2.13}$$

Considering surface grooves as multi-notches, the stress concentration factor is defined by equation 2.14.

$$K_t(x) = 1 + 4\pi \sum_{i=1}^{n} \frac{A_i}{\lambda_i} \cdot cos\left(\frac{2\pi \cdot x}{\lambda_i} + \varphi_i\right) \tag{2.14}$$

By including the theory of critical distance, a relation for the Fatigue Notch Factor can be obtained, which is shown in equation 2.15. The basic idea is, that the fatigue limit of specimens or components is reached, when the effective stress amplitude, which is not in the notch root but $\frac{a_0}{2}$ ahead, equals the fatigue limit [90, 93].

$$K_f(x) = 1 + 4\pi \sum_{i=1}^{n} \frac{A_i}{\lambda_i} \left(1 - \frac{\pi a_0}{2\lambda_i}\right) \cdot e^{\frac{\pi a_0}{\lambda_i}} \cdot cos\left(\frac{2\pi \cdot x}{\lambda_i} + \varphi_i\right) \tag{2.15}$$

2.2.2 Residual Stresses

Macroscopic residual stresses are internal forces, occurring without the effect of external forces, which are in equilibrium with themselves in the volume of the component. In general, loading a component leads to a superposition of external loads with residual stresses. A distinction is made between residual stresses of type I, II and III, which differ in their effective range. While residual stresses of type I act over a macroscopic range, residual stresses of type II are only significant over a range of several grains. Type III only occurs at an atomic level and extend over a small range of atomic distances [94–96]. Because of the given definitions, type I residual stresses in particular need to be considered in the design of dynamically loaded components. A schematic representation of the different types of residual stresses mentioned and their effective zone within the microstructure is shown in figure 2.5.

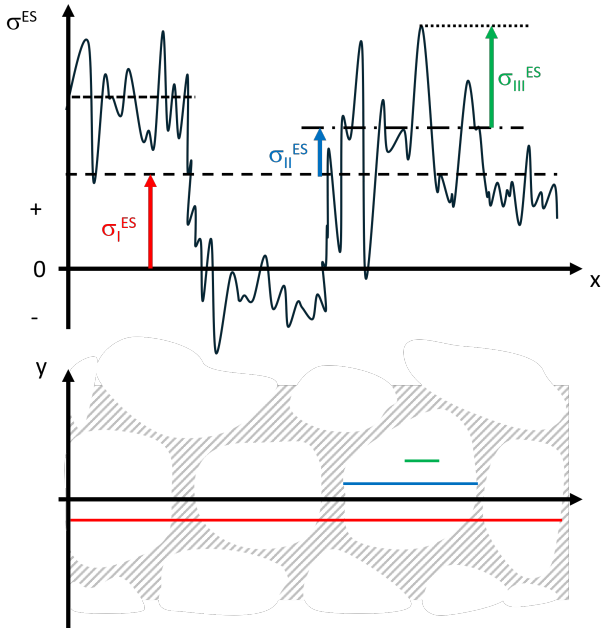

Figure 2.5: Schematic representation of different residual stress components regarding type I, II and III according to [96]

Depending on their origin, residual stresses can be roughly categorised into thermal and mechanical residual stresses. For instance, cooling parameters of a heat treatment are crucial for thermal residual stresses, whereas mechanical residual stresses can occur due to plastic deformation as a result of a machining process.
In addition to the general perception that the influence of residual stresses is very large and the fact that compressive residual stresses lead to an increased fatigue lifetime, there are many studies on the influence of residual stresses on fatigue behaviour.
Since the evolution of residual stresses strongly depends on the manufacturing method, research regarding the influence of manufacturing parameters has been carried out in recent years. El-Helieby [97] investigated the influence of different grinding parameters on residual stresses and consequently on fatigue behaviour of a ferritic-pearlitic steel. It was shown that a gentle grinding process evidently increased the fatigue strength, compared to conventional and abusive grinding methods. The acting forces during a grinding process caused the material to become more elongated at the surface than in subsurface layers, resulting in high compressive residual stresses. In case of more abuse grinding parameters, thermal induced residual stresses were predominant compared to mechanical induced stresses, leading to tensile residual stresses, which significantly reduced the fatigue resistant of the steel. The reduction in fatigue life due to residual tensile stresses could be explained by the fact that residual tensile stresses favour crack initiation and promote the propagation of an existing crack, whereas compressive residual stresses greatly reduce crack propagation [98]. Based on these insights, Webster [98] investigated the influence of residual stresses on the stress intensity factor K_t, which mainly affects the crack propagation according to equation 2.16, where C and m describe materials parameter and a the crack length.

$$\frac{da}{dN} = C\Delta K_{eff}^{m} \tag{2.16}$$

The stress intensity factor given in equation 2.17 consists of two parts: the maximum value for the stress concentration facotr K_{max} and the stress concentration factor as a result of residual stresses K_{res} [98, 99].

$$\Delta K_{eff} = K_{max} + K_{res} \tag{2.17}$$

Similar results were presented by Okamoto in his investigations about the influence of residual stresses on growth behaviour of fatigue cracks [100]. In the work of Morikage et al. [101], a peening process was used to induce compressive residual stresses in welded specimens, resulting in a reduced crack growth rate and therefore in an increased lifetime. Since distribution and the magnitude of residual stresses change during a fatigue process, Zhu [102] provided an approach considering the distribution of residual stresses based on the diffusion theory of cavity.
A mathematical description regarding the consideration of mean stress effects as well as the influence of residual stresses, was presented by Krug et al. [103] and is shown in equation 2.18.

$$\sigma_D^{load}(x) = \sigma_a(x) + M \cdot \sigma_m(x) + m \cdot \sigma_{RS}(x) \tag{2.18}$$

In the approach of equation 2.18, M displays the mean stress sensitivity and m the residual stress sensitivity. In addition to that, the permitted load amplitude $\sigma_D^{load}(x)$ is characterised by the

nominal stress amplitude $\sigma_a(x)$, the mean stress σ_m(x) and the distribution of the residual stresses $\sigma_{RS}(x)$. A comparable approach was chosen in the work of Starke et al. [52], in which the influence of the damage-relevant parameters roughness and residual stresses on the fatigue behaviour of a quenched-tempered SAE 4140 steel was investigated. Residual stresses were integrated into the calculations, using an approach of Sines, which is specified in equation 2.19.

$$\sigma_{a,eff} = K_t \cdot \sigma_a - m \cdot \Delta\sigma_{axial}^{RS}. \tag{2.19}$$

Within this approach, the effective stress amplitude $\sigma_{a,eff}$ is given as a function of the stress concentration factor and the change of axial residual stresses $\Delta\sigma_{axial}^{RS}$. Ghanem et al. [104] compared the effect of electro-discharge machining and milling processes regarding the microstructure and near-surface residual stresses. The results of these investigations revealed a sharp drop in fatigue strength in case of the electro-discharge, which can be attributed to a combination of phase transformations, hydrogen embrittlement and tensile stresses.
Further results and approaches regarding the influence of residual stresses on fatigue life can be found in the literature references [105–119].

2.3 Damage Accumulation Models

The main idea of damage accumulation models is to enable a lifetime prediction of structures or components that are subjected to variable amplitude loading. In contrast to dynamic loading with constant amplitudes, it is not possible to extract the lifetime directly from the S-N curve. Therefore, the partial damage of each load step needs to be determined and accumulated. The results presented in this doctoral thesis are based on the newly developed LPM MiDAcLife, which is based on the the damage accumulation model according to Palmgren and Miner. Because of this, the following chapter should give detailed insights of the state of the art with respect to existing damage accumulation models. In a first step, the basics and developments will be explained in detail, followed by a presentation of selected recent research results.

2.3.1 Basics of the Damage Accumulation in Fatigue

According to Fatemi and Yang [120], damage theories, especially before 1970, originated from three basic concepts: linear summation, change in fatigue limit and the two stage damage process. One of the most common method is the linear damage accumulation according to Palmgren and Miner [12, 13], in which Palmgren proposed a linear summation of all the emerging damage and Miner summarised this approach mathematically. The partial damage D_i of each load step is defined as the relation of the number of applied cycles n_i and the number of cycles to failure $N_{f,i}$ of the i$^{\text{th}}$ load step.

$$D_i = \frac{n_i}{N_i} \tag{2.20}$$

To ensure the validity of equation 2.20, a constant load ratio is assumed [2]. The partial damage is accumulated until a critical threshold value is reached. In terms of steels, this threshold is given

by the value 1.

$$D = \sum D_i = \sum \frac{n_i}{N_i} = 1 \tag{2.21}$$

In general, there are three different main approaches of Miner's rule in literature, which distinguish the original, the elementary Miner rule and the Haibach rule [121]. In case of the elementary Miner rule, it is assumed that there is no fatigue strength within the S-N curve. However, if there is a pronounced fatigue strength, this means that damage below the fatigue strength is included in the same proportions as damage above fatigue strength. This leads to a significant overestimation of the total damage and consequently to a reduced number of cycles to failure [2]. As a result, the original Miner rule differentiates two different settings. If the stress amplitude is greater than the fatigue strength, damage contributions must be taken into account within the calculation and a corresponding number of cycles to failure can be determined. Otherwise, the number of cycles are regarded as infinite.

$$\sigma_a \geq \sigma_e : N = N_e \cdot \left(\frac{\sigma_a}{\sigma_e}\right)^{-k} \tag{2.22}$$

$$\sigma_a < \sigma_e : N = \infty \tag{2.23}$$

Within equation 2.22, the parameter k indicates the slope of the S-N curve, whereas the limiting number of cycles is displayed by N_e. Haibach [2] introduced a modified version of the original Miner rule, which enables a consideration of fatigue strength as a function of progressive damage. Within this approach, the S-N curve is expanded by a fictitious area, characterised with a lower slope. The change in slope is expressed in a new exponent, which can be seen in equation 2.24.

$$N_{fictitious} = N_e \cdot \left(\frac{\sigma_a}{\sigma_e}\right)^{-(2k-1)} \tag{2.24}$$

Even if the above approach according to equation 2.21 is characterised by its great simplicity, it also contains a number of disadvantages, leading to inapplicable lifetime predictions [122]. Because of the linearity of the approach, load sequences and interactions between these loads are not considered [123]. A remarkable increase of failure of the linear damage accumulation model can be noted if the load increases from a very low to a high load level. Since decreased load levels at the beginning result in a strengthening of the material, lifetime prediction according to Palmgren Miner is to conservative. More critical is a reverse load sequence, as in this case the linear approach leads to an underestimation of the residual life [123, 124].

Additional to that, the stochastic character of materials due to natural scattering as a result of microstructural inhomogenities is not considered in terms of the limitation of equation 2.21. It has already been proven, that, depending on the material group, failure can occur at an earlier state [125].

A possible solution could be found by methods basing on a change of fatigue strength. The two-level step loading method according to Kommers and Bennett investigated the influence of pre-stressing on fatigue strength [126]. The goal was to use the reduction of the fatigue strength because of pre-stressing as a damage parameter. Additional models with respect to a change in fatigue strength, which were able to integrate load sequence effects, are summarised in [120].

In 1966, Manson [17] proposed a method that differs from the initial linear approach by separating the fatigue process into two phases: crack initiation and crack propagation. The linear damage rule is than applied on both phases. Crack propagation is therefore empirically described by equation 2.25.

$$(\Delta N)_f = P \cdot N_f^{0.6} \tag{2.25}$$

P is a specific material constant, that needs to be estimated experimentally, testing the first part of fatigue life at high load amplitudes and the remaining part at lower amplitudes. As a result, some kind of knee-point can be obtained. Since fatigue life is determined by the summation of both phases, crack initiation can be expressed by the following equation:

$$N_0 = N_f - P \cdot N_f^{0.6} \tag{2.26}$$

Combining equation 2.25 and 2.26 and transferring it into the approach according to Palmgren Miner, the double linear damage rule for crack initiation (equation 2.27) as well as for crack propagation (equation 2.28) can be derived.

$$\sum \frac{n}{N_0} = \sum \frac{n}{N_f - P \cdot N_f^{0.6}} \tag{2.27}$$

$$\sum \frac{n}{(\Delta N)_f} = \sum \frac{n}{P \cdot N_f^{0.6}} \tag{2.28}$$

Even if Manson's model was able to reduce the amount of deficiencies while maintaining simplicity, the determination of the knee-point is among further aspects a weakness of the double linear approach [127].

According to literature [120, 128], Marco and Starkey were the first researchers to introduce a nonlinear load depended damage theory. The damage parameter D_i of the fatigue damage process was described using a stress-depended exponent x_σ in equation 2.29.

$$D_i = \left(\frac{n}{N_f} \right)^{x_\sigma} \tag{2.29}$$

Because of the evidently increased accuracy in case of nonlinear damage accumulation models compared to linear models, subsequent research focused on the development of new nonlinear models.

In 1976, Subramanyan [129] introduced a cumulative damage rule based on the knee-point of an S-N curve. He proposed that microstructural changes and therefore, the damage induced into the material are continuous but still can be divided in a certain number of stages. The iso-damage curve displays the cycles required in order to reach a defined stage of damage plotted against the corresponding stress amplitudes. The damage is then given as the ratio of the slopes $tan(\theta)$ and $tan(\theta_k)$ obtained from the iso-damage lines and the S-N curve.

$$D = \frac{tan(\theta)}{tan(\theta_k)} = \frac{\frac{\sigma-\sigma_e}{log(N_k)-log(n)}}{\frac{\sigma-\sigma_e}{log(N_k)-log(n)}} = \frac{log(N_k) - log(N)}{log(N_k) - log(n)} \tag{2.30}$$

The number of cycles at the knee-point is defined as N_k in equation 2.30, whereas σ_e represents the fatigue strength of the material.
Under the assumption of pre-stressing with one amplitude and a substitution of the cycle ratio C_i, which is given in equation 2.31, Subramanyan's equation 2.32, considering pre-stressing conditions, can be obtained.

$$C_i = \frac{n_i}{N_i} \tag{2.31}$$

$$C_2 = 1 - C_1^{\alpha} \tag{2.32}$$

The exponent of equation 2.32 shows a dependency of the fatigue strength σ_e, that is given by equation 2.33.

$$\alpha = \frac{\sigma_2 - \sigma_e}{\sigma_1 - \sigma_e} \tag{2.33}$$

In case of multilevel stressing instead of just two different load levels, equation 2.32 can be generalized by equation 2.34 [129, 130].

$$C_i = 1 - [C_{i-1} + [C_{i-2} + ... + (C_2 + C_1^{\alpha_1})^{\alpha_2}]^{\alpha_{i-2}}]^{\alpha_{i-1}} \tag{2.34}$$

Based on the fundamentals of the damage accumulation and the different approaches that have been described, a large number of additional nonlinear methods have been developed recently. A condensed summary is given by Hectors in [124].

2.3.2 Nonlinear Damage Accumulation - Recent Developments

Because of a very high deviation of lifetime prediction based on the linear damage accumulation according to Palmgren and Miner, a large number of nonlinear damage accumulation models, based on different physical approaches have been developed in recent years. The aim of this chapter is to provide an overview of current research results in the field of nonlinear damage accumulation models. However, because of the large number of existing publications, it should be noted at this point, that only a representative selection is collected here without any claim to completeness.

According to [131], nonlinear damage accumulation models can be divided into the following groups:

- Damage accumulation models based on static toughness exhaustion
- Damage curve approaches
- Damage accumulation models based on memory effect
- Damage accumulation based on S-N curve
- Mesmacque's damage indicator

Ye et al. [132] were able to show that the static toughness, representing the strength, as well as plasticity of metals, is a useful tool that can be correlated with the fatigue damage process. The approach is based on the idea that a reduction of static toughness indicates the ability to absorb energy inherently, which happens due to increasing fatigue damage and therefore can be used as an indicator. In order to investigate static parameters after a fatigue process, specimens were cyclically loaded up to a specific number of cycles, followed by a static load until failure. The damage parameter D can be calculated using equation 2.35.

$$D = -\frac{D_{N_f} - 1}{ln(N_f)} \cdot ln\left[1 - \frac{N}{N_f}\right] \tag{2.35}$$

D_{N_f-1} represents the critical cumulative damage after a total of N_f-1 cycles.

A very common method using damage curve approaches was given by Manson and Halford [133], which uses the crack length to determine the damage parameter. However, even if the effect of load sequence can be considered within the model, load interactions are not included. As a result, further developments had to be initiated.
Benkabouche et al. [134] developed a finite element based method, which enables an estimation of damage evolution and residual life, while considering multiaxial loading and load sequence effects. In order to calculate the damage as a result of cyclic loading, the block loading data had to be transformed into equivalent constant amplitude data by means of the Crossland criterion, given in equation 2.36 [135].

$$\sigma_{eq}^{i} = \sqrt{J_{2,a}} + \rho \cdot J_{1,max} \leq A \tag{2.36}$$

It uses the second invariant of the deviatoric stress amplitude $J_{2,a}$ and the maximum hydrostatic stress $J_{1,max}$. In addition, fatigue strength in terms of pure tension ρ, as well as in pure torsion A, is considered. Based on equation 2.36 and the model according to Mesmacque et al. [136], the damage parameter can be mathematically formulated by equation 2.37.

$$D_i = \frac{\sum_i^{eq} - \sigma_{eq}^{i,max}}{\tau_u - \sigma_{eq}^{i,max}} \tag{2.37}$$

Within equation 2.37, $\sum_i^{eq}$ represents the damage stress amplitude at the i^{th} load level. Besides that, D_i is described by the ultimate stress in torsion tests τ_u and the maximum equivalent stress $\sigma_{eq}^{i,max}$.

Yu et al. [137] also focused on the integration of load sequence as well es load interactions, since high load amplitudes favour crack initiation processes and therefore enable crack propagation under lower amplitude conditions. The proposed model is based on the approach according to Aeran, introducing a damage index δ_i [138] and aiming to predict fatigue life of roller bearings under variable loading conditions.

$$\delta_i = \frac{-1.25}{ln(N_i)} \tag{2.38}$$

Applying the damage index of equation 2.38, the damage parameter at the i$^{\text{th}}$ load step is given as:

$$D_i = abs\left[1 - \left(1 - \frac{n_i}{N_{fi}}\right)^{\delta_i}\right] = \left(1 - \frac{n_i}{N_{fi}}\right)^{\delta_i} - 1 \tag{2.39}$$

Compared to the model according to equation 2.37, the advantage in this case is that no additional parameters need to be determined apart from the S-N curve itself. Apart from that, the applicability to LCF as well as HCF has been proven by the authors.
Further methods dealing intensively with the integration of load sequence and load interaction effects can be found in [123, 138–150].

A model based on isodamage curves was proposed by Bjørheim et al. [151]. Due to the finding, that an increased number of cycles caused an increased damage in the material, the following differential equation can be derived.

$$\frac{dD}{D} = q(\sigma, m)\frac{dn}{n} \tag{2.40}$$

Derived from equation 2.40, q is a parameter depending on the stress amplitude σ_a and a material constant m. The solution of the differential equation is given by equation 2.41.

$$D = \left(\frac{n}{N_f}\right)^{q(\sigma,m)} \tag{2.41}$$

Additional literature focusing on isodamage curve-based accumulation models are compiled in [124, 130, 152–154].
Within MiDAcLife, which is described in chapter 3, the nonlinearity is ensured by the integration of the material response as a result of dynamic loading. This process-orientated, instead of lifetime-orientated approach significantly differs from the aforementioned models.

2.4 Fatigue Characterisation Methods

2.4.1 Strain-Based Fatigue Characterisation

The plastic strain amplitude is an important indicator to determine plastic deformation during a fatigue process. Therefore, especially in the LCF regime with significantly localised plastic defor-

mation processes, strain measurements have established as state of the art and therefore require a brief explanation.

The total strain amplitude $\varepsilon_{a,t}$ during a fatigue test is divided in the elastic $\varepsilon_{a,e}$ and plastic strain amplitude $\varepsilon_{a,p}$. The elastic portion can be described in a linear way using Hookes law, whereas the relation between the stress amplitude and plastic strain amplitude is given by a power law, which is presented in equation 2.42 [155, 156].

$$\sigma_a = K' \cdot (\varepsilon_{a,p})^{n'} \tag{2.42}$$

In this term, K' is defined as the cyclic hardening coefficient and n' represents the cyclic hardening exponent. Since the total strain amplitude results from the summation of both portions, the relation according to equation 2.43 arises, which is called the Ramberg-Osgood relationship [157–159].

$$\varepsilon_{a,t} = \varepsilon_{a,e} + \varepsilon_{a,p} = \frac{\sigma_a}{E} + \left(\frac{\sigma_a}{K'}\right)^{1/n'} \tag{2.43}$$

Important characteristics of the stress-strain hysteresis are given in figure 2.6. The area enclosed by the hysteresis loop that can be described using the integral of equation 2.44, is linked to the energy per unit volume dissipating during a load cycle [155]. Since the main part of the mechanically induced energy dissipates as heat, this determination becomes important for temperature-based fatigue testing in the following chapter.

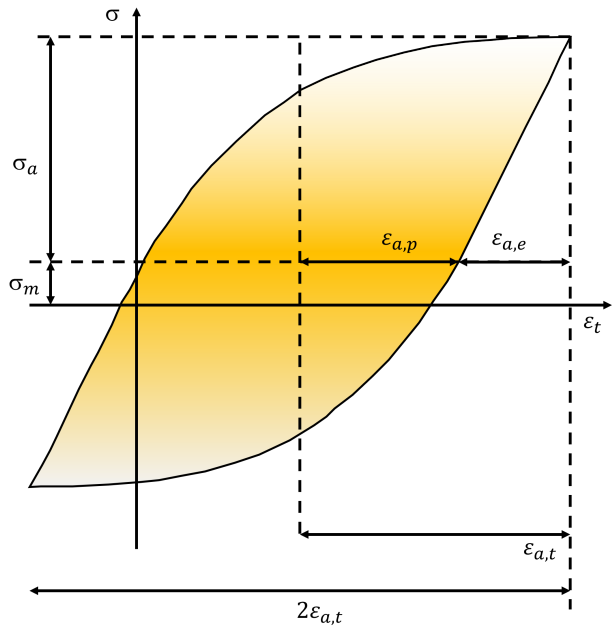

Figure 2.6: Schematic representation of a generalised stress-strain hysteresis loop including important parameters

$$E = \oint_0^{2\pi} \sigma d\varepsilon_t \tag{2.44}$$

Based on the shape of the hysteresis in figure 2.6, conclusions can be drawn about microstructural processes such as dislocation reactions. An increasing area thus indicates cyclic softening of the material as a result of dynamic loading, whereas a decrease refers to cyclic hardening processes. These effects in cyclic deformation behaviour are called cyclic transient behaviour.
In order to enable a lifetime estimation, especially in the LCF regime, a strain based approach based on the work of Manson & Coffin can be used. It describes the total strain amplitude $\varepsilon_{a,t}$ as a function of the fatigue strength coefficient σ'_f, the fatigue strength exponent b, the fatigue ductility coefficient ε_f and exponent c. Furthermore, it depends on the Young's Modulus E and the number of cycles to failure [160, 161].

$$\varepsilon_{a,t} = \frac{\sigma'_f}{E} \cdot (2N_f)^b + \varepsilon'_f \cdot (2N_f)^c \tag{2.45}$$

Since the LPM MiDAcLife, which is discussed later on within this thesis, is based on the damage accumulation model according to Palmgren and Miner, correlations between the damage parameter and parameters resulting from strain measurements need to be analysed.
In the work of Park and Ang in 1985 [162], a model considering the plastic strain energy in the evaluation of the partial damage was presented.

$$D_i = \frac{\delta_m}{\delta_u} + \beta \cdot \frac{\int dE}{R_e \cdot \delta_u} \tag{2.46}$$

In equation 2.46, the partial damage D_i consists of the relation between the maximum deformation peak under cyclic loading δ_m and the ultimate displacement under monotonic loading δ_u, the yield strength R_e, and the incremental absorbed plastic strain energy $\int dE$ [163, 164], as well as a non-negative material constant β.
Since the dissipated energy during fatigue is linked to plastic deformation and therefore to microstructural changes such as phase changes, residual stress evolution or the reaction and translation of dislocations, Duyi [132] proposed that fatigue damage can be defined as the relation between dissipated plastic strain energy ΔE_i and the total plastic strain energy E_f, given in equation 2.47.

$$D_i = \sum_{i=1}^{N} \frac{\Delta E_i}{E_f} \tag{2.47}$$

2.4.2 Temperature-Based Fatigue Characterisation

In recent years, temperature measurements have emerged to be a suitable tool for the evaluation of fatigue behaviour of metallic materials. Especially the wide range of possible applications, the possibility of accelerated non-destructive materials testing and the potential for increased information content regarding microstructural changes as a result of the degradation process are the reasons motivating research in the field of thermography. The first part of this chapter explores

thermodynamic theories, which enable a correlation of the fatigue process and temperature. Specific application examples are given later on.

Considering mechanical loading of a specimen, energy induced in the material, leads to irreversible plastic deformations. From a graphical point of view, this energy absorption can be monitored with a stress-strain-hysteresis curve [3,165]. The main concept of temperature measurements in fatigue testing is that the enclosed area of the hysteresis curve can be correlated with the dissipated energy. A defined portion of this energy dissipates in terms of heat, whereas the other portion remains within the material as stored energy [166,167].

In case of dynamic loading, the mechanical energy, which is induced into the specimen, dissipates to a large extend in terms of heat. According to Chrysochoos et al. [168], two different types of dissipation can be distinguished: intrinsic and thermal dissipation. While intrinsic dissipation is linked to material degradation processes, thermal dissipation is induced by heat diffusion. Furthermore, [168] proposed that applied mechanical loads lead to two inner heat sources, which are represented by the thermoelastic source ω_{the} as a result of thermoelasticity and the thermomechanical coupling source ω_{thc}, for example as a consequence of latent heat rate of phase change. Assuming defined boundary conditions, the heat equation can be postulated.

$$\rho_{heq} \cdot C_{\varepsilon,\alpha} \frac{\partial T}{\partial t} - k\Delta T = \omega_h + r_e \tag{2.48}$$

While ρ_{heq} and $C_{\varepsilon,\alpha}$ from equation 2.48 are material constants, r_e displays a possible external heat supply. The parameter ω_h combines effects due to dissipation d_1 as well as thermoelasticity ω_{the} as an overall heat source.
Based on these insights, Boulanger et al. [169] presented a method dealing with the separation of thermoelastic and dissipative heat sources. This approach was driven by the urgent need to distinguish between dissipated energy as a result of microstructural changes, which are mainly responsible for occurring fatigue damage, and thermoelastic sources, characterised by reversible thermal expansion. The required data was provided using an infrared camera system.
Assuming a homogeneous, uniaxial testing condition, Boulanger et al. [169] proposed a simplified version of the heat equation, shown in equation 2.49.

$$\rho_{heq} \cdot C_{\varepsilon,\alpha} \left(\frac{d\theta}{dt} + \frac{\theta}{\tau_{eq}} \right) = w_{the} + d_1 \tag{2.49}$$

The heat equation according to equation 2.49 consists of material parameters, such as the density ρ_{heq} and the heat capacity $C_{\varepsilon,\alpha}$ of the material. Apart from that, equation 2.49 is characterised by the temperature variation θ with respect to the initial equilibrium state, as well as the heat loss to the environment, which is displayed as τ_{eq}. Considering the strain rate dependency of the thermoelastic part of equation 2.49, the energy induced into the specimen can be formulated using an integral representation, displayed in equation 2.50.

$$\omega_h = \int \omega_{the}(\dot{\varepsilon}) + d_1 dN \tag{2.50}$$

Pioneering work in the field of thermography in combination with fatigue behaviour of materials was carried out by La Rosa and Risitano [170]. In their work, they were able to develop a method (Risitano method) that enables a short-time estimation of the fatigue strength of a material. In general, the authors proposed that if the applied stress amplitude is beneath the fatigue strength, there is nearly no increase within the change in temperature. If the stress amplitude exceeds the fatigue strength, the material response can be divided into three main regions. In the first part, the material response shows a great increase as a result of the dynamic loading. This part is followed by a phase where the change in temperature and thus material response remains approximately constant. This condition lasts until shortly before final fracture of the specimen occurs (phase 3). To summarise the Risitano method, fatigue strength values can be estimated by establishing a relationship between the change in temperature and the corresponding stress amplitude. As a result, the fatigue strength calculation is highly accelerated by the specimen reduction.

In addition to Risitano, Luong [171, 172] provided important research results regarding IR thermography. In his work, he used IR thermography in rotating bending tests as well as tension-compression tests on connecting rods to observe the fatigue behaviour of materials. In order to ensure comparability with conventional fatigue methods, a large number of experiments were carried out, using the staircase-method. According to Luong, fatigue strength is determined graphically, using an intrinsic dissipation - stress amplitude plot. The experimental effort could therefore be significantly reduced.

Since temperature measurements are extremely sensitive to external noise, an extension of the already existing methods was presented by De Finis [173]. In addition to previous research, this research focused on a martensitic steel, which is characterised by a brittle behaviour and therefore exhibits small deformations and decreased values for the change in temperature. According to De Finis, temperature is a function of three different terms, which are given in equation 2.51. It consists of the temperature due to dissipation T_d, the temperature transferred from the servo-hydraulic testing machine into the specimen T_{lm} and the environmental temperature T_{amb}.

$$T(x, y, t) = f[T_d(x, y, t), T_{amb}(t), T_{lm}(x, y, t)] \tag{2.51}$$

The goal of the proposed research was to separate each part of equation 2.51 to correctly estimate the dissipative source as a fatigue damage indicator. To determine the influence of environmental heat sources, a reference measurement was made on a black body, which was then considered as T_{amb}. The influence of the environmental temperature could therefore be eliminated, subtracting it from the measured temperature data. The determination of the machine contribution was based on the assumption of a linear temperature increase and is estimated using fitting procedures.
In addition to previous considerations, entropy can also be applied as a thermodynamic parameter to characterise fatigue behaviour. One approach is carried out by Liakat [174, 175]. Within this research, the fatigue fracture entropy was used to describe fatigue degradation processes, deploying equation 2.52.

$$\gamma_{FF} = \int_0^{N_f} \left(\frac{\Delta E_i}{T} \right) dN + \int_0^{N_f} \left(\frac{k_{th}}{T^2} \cdot (gradT)^2 \right) dN \tag{2.52}$$

In equation 2.52, the fatigue fracture entropy γ_{FF} is a function of ΔE_i, the temperature T, the thermal conductivity k_{th} and the number of cylces N. It can be concluded that the fatigue fracture entropy is given by the summation of the entropy generation as a result of plastic strain energy generation and heat conduction [174].
Teng et al. [176] also utilised entropy as a parameter to describe the damage accumulation process in the HCF regime of a normalised SAE 1045 steel. According to Teng, the damage parameter D, given in equation 2.53, is a function of the critical Damage D_{N_f}, the critical entropy generation s_c and the maximum entropy generation s_f.

$$D = \frac{D_{N_f}}{ln\left(1 - \frac{s_c}{s_f}\right)} \cdot ln\left(1 - \frac{s}{s_f}\right) \tag{2.53}$$

Further research characterising the fatigue behavior and the fatigue strength of metallic materials is assembled in [177–188].

2.4.3 Electrical Resistance-Based Fatigue Characterisation

Besides temperature measurement using IR camera systems or thermistors as described in chapter 2.4.2, electrically based measurements represent a powerful tool to investigate material degradation due to dynamic loading. Electrical resistance in particular is highly influenced by the microstructure, since electrons are scattered by inhomogeneities, such as dislocations, inclusions and grain boundaries [189].
In 1966, Harting [190] established a relation between the change in electrical resistance and fatigue parameters, which is shown in equation 2.54.

$$\Delta R = K_{el} \cdot (\varepsilon_R - \varepsilon_0) \cdot n^{h_{el}} \tag{2.54}$$

In equation 2.54, ΔR displays the change in electrical resistance, ε_R the maximum reversed strain and ε_0 the strain at fatigue strength. The parameters K_{el} and h_{el} are material constants, and n represents the number of applied load cycles.

Charsley [191] investigated the change in the electrical resistance during dynamic loading of copper foil. Apart from that, the dependency of parameters like different strain amplitudes, the grain size and testing frequency were determined. According to Charsley, the obtained plot consisting of the change in electrical resistance and numbers of cycles can be separated into two main portions. In the first part, the change in temperature increases steadily. This can be traced back to accumulation processes of defects like dislocations and point defects. In the second part, an extremely fast increase can be observed, which is caused by macro-cracks within the material.
A method to enable a real-time monitoring of fatigue damage evolution in an SAE 316 L steel was presented by Nobile [192]. Within this approach, change in electrical resistance ΔR is measured via four-wire configuration. This technique is characterised by two external electrodes, through which current is applied into the specimen. The resistance calculation is based on the determination of the voltage drop, which is measured via two internal electrodes. Since the electrical resistance is highly influenced by temperature, equations 2.55 and 2.56 take the change in resistance because of temperature effects into account [192–194].

$$\Delta R = R - R_0 = A_{el} \cdot \Delta T \tag{2.55}$$

$$\Delta R_{damage} = \Delta R_{exp} - \Delta R_{th} \tag{2.56}$$

While the change in the electrical resistance ΔR is influenced by the initial resistance R_0 and the resistance temperature coefficient A_{el}, the sum of the variations induced by temperature changes can be used to calculate variations induced by fatigue damage ΔR_{damage}.

The mechanical properties of cast materials are characterised by different influencing factors compared to steels. In particular, parameters like the shape of graphite precipitate, micro-cracks and composition of the matrix play a distinctive role. Therefore, Germann et al. [195] used the electrical resistance to obtain detailed information regarding defect density and cyclic deformation behaviour. According to the authors, electrical resistance measurements are very well suited in case of small plastic deformations. In order to correlate the measured signals with defined fatigue stages, SEM micrographs were used as reference. In addition to the in-situ measurement of the electrical resistance, the initial resistance R_0 already provides important information. It can therefore generally be stated that an increased initial value of the electrical resistance leads to a reduced lifetime.

Starke et al. [196] investigated the cyclic deformation behaviour of a quenched and tempered SAE 4140 steel and an EN-GJS-600 cast iron, using a conventional stress-strain hysteresis, temperature measurements as well as the change in electrical resistance. Within this research, the authors were able to provide insights about the progression of the electrical resistance in terms of dynamic loading. At the beginning, a decrease was detected, which was explained by the closing of micro-cracks during compression half cycles. After reaching a saturation state, the change in electrical resistance increased because of graphite-matrix debonding and micro-crack initiation and growth.

Since the evaluation of fatigue damage evolution is often correlated with the damage parameter D, Sun et al. [197] proposed a method, combining the change in electrical resistance and the damage parameter.

$$D = 1 - \frac{(1 + \varepsilon_{a,p}) \cdot \rho' \cdot R}{(1 - \varepsilon_{a,p}) \cdot \rho \cdot R'} \tag{2.57}$$

In case of equation 2.57, ρ and ρ' represent the electrical resistivity and the resistivity of the damaged specimen, whereas ε_p is the plastic strain amplitude. At this point, it should be noted that the resistivity is highly influenced by an increased defect density (e.g. dislocations, vacancies, or inclusions).
A more microstructure-based method was proposed by Omari [198, 199], analysing the dislocation density by electrical resistance measurements and SEM analysis. Starke et al. [200] presented a correlation between the change in electrical resistance and change in dislocation density. Therefore, ICE R7 wheel steel specimens were used. Furthermore, the authors also used load free sequences to enable an estimation of the fatigue damage process. By inserting load-free sequences,

a temperature-unaffected value for the electrical resistance can be obtained. In addition to NDT-measurements, a transmission electron microscope was exerted to characterise the microstructure resulting from cyclic loading. Starke et al. concluded, that the change in dislocation density over the entire fatigue test is relatively small. Rearrangement processes of dislocations offer an explanation for the, nevertheless, increasing material response.
Further research focusing on the evaluation of fatigue behaviour using electrical resistance measurements to detect microstructural changes is compiled in [201–212].

2.5 Fatigue Evaluation Methods

2.5.1 Conventional Characterisation of Fatigue Behaviour

When it comes to designing dynamically loaded components, fatigue strength is often defined as a decisive parameter for assessing fatigue properties. In this case, a very frequently used method is the staircase method, which is characterised by the sequential execution of follow-up tests. Each experiment is dependent on the result of the previous one, leading to a clustering of data points around the fatigue strength [1]. The schematic procedure of the staircase method is given in figure 2.7.

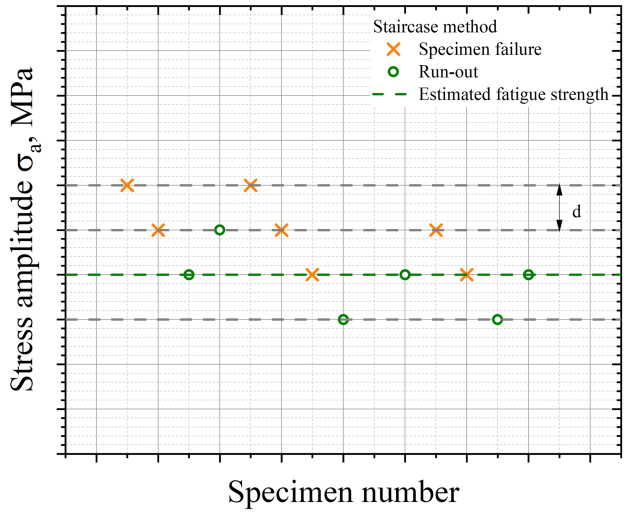

Figure 2.7: Schematic representation of the staircase procedure to estimate the fatigue strength of metallic materials

As a first step of the staircase method, a critical stress amplitude for the first specimen has to be estimated. If the specimen breaks before reaching a defined number of cycles to failure, the following specimen is loaded with a decreased stress amplitude. Otherwise, the stress amplitude is increased [2]. As shown in figure 2.7, equidistant load levels are selected for these experiments. In order to avoid high scattering of the fatigue strength estimation, the step increase or decrease must be selected sufficiently precise [1]. Even if the method is a reliable approach to estimate fatigue strength, the high number of specimens required with approximately 40-50 specimens according to Maenning [213] is a disadvantage.
Although the method was already developed by Dixon and Mood in 1948 [214] and further modified

by Ransom and Hück [215,216], the staircase method is still subject of current research concerning fatigue strength estimation. According to the work of Thompson et al. [217], another disadvantage of the staircase method is the assumption of a normal distribution, which means that a bimodal behaviour of components as a result of material inhomogenities from manufacturing is not taken into account. Therefore, the staircase method tends to overestimate the fatigue strength. Within his research, Thompson compared the results of the staircase method with fatigue strength estimation according to step loading, with the outcome that the fatigue strength is significantly lower using step loading for estimation.
Pollak et al. [218] analysed the effect of step size and specimen size on the prediction accuracy of the staircase method using numerical simulation models, whereas Müller et al. [219] provided a comparison of the accuracy of different evaluation models using Monte Carlo simulations. Further research results regarding the staircase method are given in [220–224].
Since the previously presented staircase method only estimates the fatigue strength of materials, additional approaches must be used to determine the S-N curve. A recognised method, especially for small amounts of specimens, is the step-down approach. Within this approach, fatigue tests are carried out on different load levels, with the 50 % S-N curve resulting from the regression of all data points. In order to enable a statistical evaluation of fatigue behaviour, all data points are transferred parallel to the regression line on a common virtual load level. Therefore, different distribution models can be used to generate scatter bands, which display different failure probabilities [225]. Figure 2.8 provides an overview of the step-down method including the translation of CAT data points on one load level.

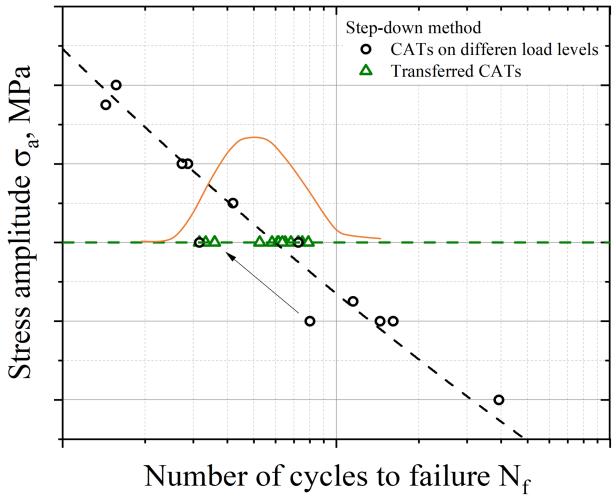

Figure 2.8: Schematic representation of the step-down procedure to estimate the S-N curve of metallic materials including scatter bands

Although the proposed method offers the advantage of a reduced number of specimens (approximately 8-12), one disadvantage is the generalisation of the scattering caused by the shift of the CAT data points on one common load level. This means that the increased scattering in case of lower stress amplitudes cannot be taken into account [22, 225].

Since microstructural inhomogenities cause scattering in fatigue life even on one load level, it is

highly eminent to carry out statistical evaluations regarding lifetime on different load levels, which is shown in figure 2.9. Within this method, approximately 2-5 load levels, that are located within the HCF regime, are defined. At least 6-10 specimens should be tested on each load level. In contrast to the step-down method that was described previously, statistical evaluations are carried out independently for each load level in a probability plot.

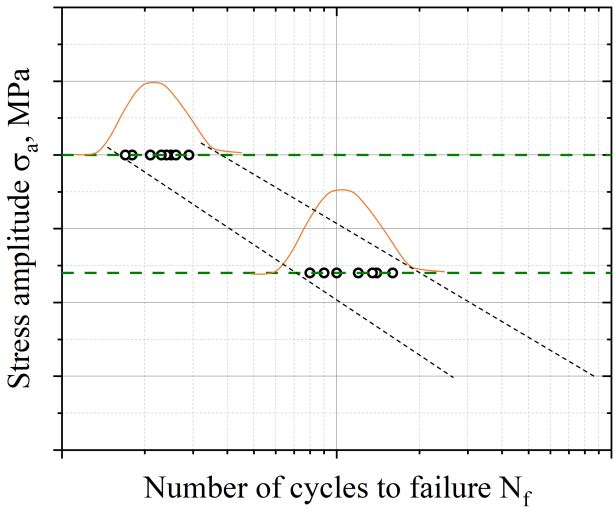

Figure 2.9: Schematic representation of the statistical evaluation on different load levels

2.5.2 Accelerated Lifetime Prediction Methods

Conventional methods to analyse fatigue behaviour of metallic materials are usually characterised by a high level of statistical reliability. However, a large number of specimens are mostly required to generate an S-N curve, which is very time-consuming and expensive. In addition, these S-N curves are only valid for given environmental conditions and influencing factors. If one parameter changes, a new S-N curve needs to be estimated.
Furthermore, the lifetime-orientated assessment of the fatigue process results in high safety-factors, which lead to an over-dimensioning of components and therefore counteract the lightweight construction potential. For these reasons, there is great interest in the accelerated provision of fatigue data, using LPMs, which are based on different physical approaches.
In order to reduce the amount of specimens required to generate an S-N curve, the information content from an experiment must be increased. This can be achieved through a process-orientated evaluation of the fatigue process using NDT-related measurement methods, which are sensitive to microstructural changes and therefore provide a good possibility to monitor material degradation. By combining fracture mechanics parameters and temperature measurements, Kim [226] developed a method to determine the lifetime of three different materials (steels for welded structures and cast iron). In previous research, the author was able to show a correlation between the logarithmic lifetime and the J-integral J_c under consideration of the strain amplitude. Since the relation of the strain amplitude and the change in temperature ΔT could be proven to be linear, equation 2.58 was developed to describe the number of cycles to failure as a function of the change in temperature. The parameters of the linear regression are represented by α' and β'.

$$log(N_f) = \alpha' \sqrt{J_c \cdot \Delta T} + \beta' \tag{2.58}$$

In their investigations regarding the LCF regime of Cr-alloyed steels, Wang et al. [227] proposed a new approach, which enables the consideration of different parameters, such as temperature, strain amplitude and holding time as well as the holding direction. Therefore, a combined approach according to Manson & Coffin and Basquin, displayed in equation 2.59, was modified by the integration of temperature dependency of the involved parameters, using the homologous temperature and the integration of the damage coefficients D_t for tensile hold and D_c for compressive hold.

$$\varepsilon_a = \varepsilon_{a,e} + \varepsilon_{a,p} = \left(\frac{\sigma'_f}{E}\right) \cdot (2N_f)^b + \varepsilon'_f \cdot (2N_f)^c \tag{2.59}$$

$$\varepsilon_a = \varepsilon_{a,e} + \varepsilon_{a,p} = \left(\frac{\sigma'_f(T)}{E}\right) \cdot \left(\frac{2N_f}{D_t D_c}\right)^{b(T)} + \varepsilon'_f(T) \cdot \left(\frac{2N_f}{D_t D_c}\right)^{c(T)} \tag{2.60}$$

Especially in case of structures or components that are designed for long-term use application, such as wind turbines (20-25 years), or components applicated in nuclear energy technology, accelerated testing is becoming increasingly important as a result of the reduced costs. As an example, methods that offer a possibility to determine the lifetime of offshore wind turbines under given environmental conditions have been developed in literature [228, 229]. In this work, a high focus had to be placed on integrating the influence of corrosion on fatigue behaviour into the calculations.
In order to enable a rapid lifetime determination of aluminium and stainless steels, Amiri [230] used the slopes of cyclic deformation curves as an index for the lifetime prediction. Within their work, Fargione et al. [231] applied temperature measurements not only to estimate the fatigue strength, but also to implement this on an entire S-N curve. For this purpose, the authors used the fact that plastic deformation energy is nearly proportional to the dissipated heat during a fatigue test and introduced the parameter Φ, which is defined as the integral of the temperature function $\Delta T = f(N)$ and is shown in equation 2.61.

$$\Phi = \int_0^{N_f} \Delta T dN \tag{2.61}$$

A wide-ranging overview of further thermo-based LPMs was provided by Teng [232].

A physically based short-time procedure was proposed by Starke et al. [233], where the authors used a combination of the approaches according to Morrow and Basquin. Since the proposed method only requires data from one LIT and two CATs (constant amplitude tests), the experimental effort could be highly reduced. Based on the pioneering work by Starke et al., several LPMs have been developed at Saarland University and University of Applied Sciences Kaiserslautern in recent years. All methods combine non-destructive testing techniques and destructive testing, as well as a combination of different empirical approaches, such as Basquin, Manson & Coffin or the approach according to Palmgren and Miner. The short-time procedure SteBLife [234–236] uses a stepped shape specimen geometry, resulting in different values of the stress amplitude depending on the corresponding diameter. The method is based on the material response, which is measured

using NDT-methods during constant amplitude loading. The monitored data serves as input for the Morrow-equivalent-plot which is defined as the relation between the material response and the corresponding stress amplitude. The trend S-N curve regarding the HCF-regime is then calculated using generalised Morrow and Basquin approaches. In addition to SteBlife, further methods have been developed that enable a reliable lifetime prediction under strain-controlled testing conditions (StrainLife) [237, 238] or differentiate between a global or local assessment of fatigue properties.
In particular, the further development and modification of the LPM StressLife and the new development of the MiDAcLife method, which is based on the linear damage accumulation model according to Palmgren and Miner and thus significantly differs from the previously mentioned models, are part of the presented doctoral thesis. For this reason, the procedure of both methods will be explained in detail in the following chapter.

3 Materials and Methods

3.1 Material

Because of the extremely high safety requirements of components used in nuclear energy technology, the right material selection is of crucial importance to avoid critical failure during operation. The aim is to use as few different materials as possible, which are nevertheless characterised by their high qualification with regards to respective demands. The basis for this is a profound understanding of the microstructural composition of each material and the resulting physical and, in particular, mechanical properties. Especially fatigue properties are highly dependent on the respective microstructure of the material. The influence of different microstructural parameters such as carbon content, alloying elements or microstructural changes as a result of heat treatment is a major part of chapter 4.
In nuclear power plants, reactor pressure vessels and spraylines are mainly made of low alloy ferritic fine-grained steels, whereas austenitic materials are used for smaller connecting pipes. Until the 1970s, the 22NiMoCr3-7 steel was mainly used [239]. Even though the steel was considered qualified for the application, it was replaced by the 20MnMoNi5-5 (similar grades: 16MND5 and SA 533B1) steel due to its improved properties. Compared to the 22NiMoCr3-7 steel, 20MnMoNi5-5 is characterised in particular by improved toughness properties and reduced affinity for cracking during welding and heat treatment.
In order to be able to reliably evaluate the mechanical properties of the 20MnMoNi5-5 steel considering dynamic loading, a basic characterisation of the material is required. In the following chapter, the material is analysed regarding its microstructural composition and resulting mechanical properties. Apart from that, focus is on the investigation of different machined surface conditions, resulting in various residual stresses and roughness conditions. Both parameters are significantly relevant regarding the damage assessment. In particular, the influence of surface roughness on the fatigue behaviour as well as the integration of roughness parameters into the newly developed lifetime prediction method MiDAcLife is a key objective of the presented research. Therefore, precise information concerning the surface condition is of crucial importance.
The investigations presented within this chapter span from a macroscopic assessment of damage-relevant factors (e.g. roughness influence) to microscopic investigations regarding phase distributions, grain size and occurring precipitates, based on different analytical methods such as light microscopy, digital microscopy, laser-scanning microscopy and scanning electron microscopy.

3.1.1 Microstructural Characterisation

In a first step of the microstructure evaluation, micrographs were taken using a light optical microscope type Axioplan 2 by the company Carl Zeiss Microscopy Deutschland GmbH. In addition to that, the microstructure was examined regarding grain size and phase distribution, using a digital microscope type DSX1000 of the company EVIDENT Europe GmbH. The results are given in figures 3.1 and 3.2.

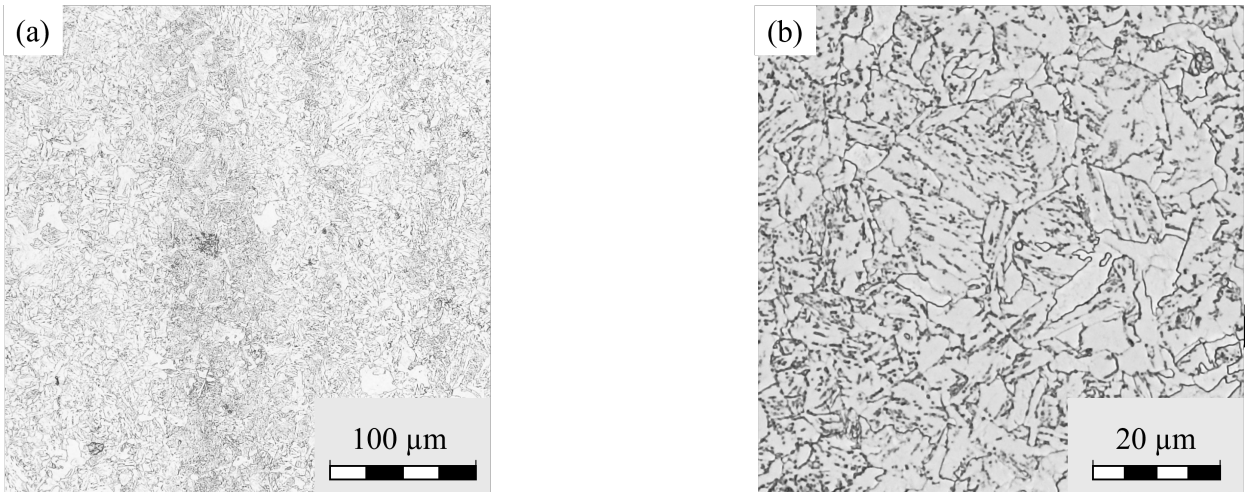

Figure 3.1: Microstructural investigation based on light microscopy (a) Overview of the microstructure (b) Detailed consideration of the microstructure regarding a 20MnMoNi5-5 steel

In addition to an overview micrograph, figure 3.1(b) contains a more detailed examination regarding the microstructure of the 20MnMoNi5-5 steel. It can be observed that the majority of the structure consists of more whitish ferrite areas. An accurate quantification of the bainite components is difficult due to the low magnification in case of light microscopy. Despite the comparatively low magnification, the carbide structure of the material can already be identified. In particular, an increased occurrence of carbides can be observed at grain boundaries. However, it is not possible to provide information regarding the type of carbides based on figure 3.1. Nevertheless, considering the chemical composition of the steel, Mn-carbides can be assumed.

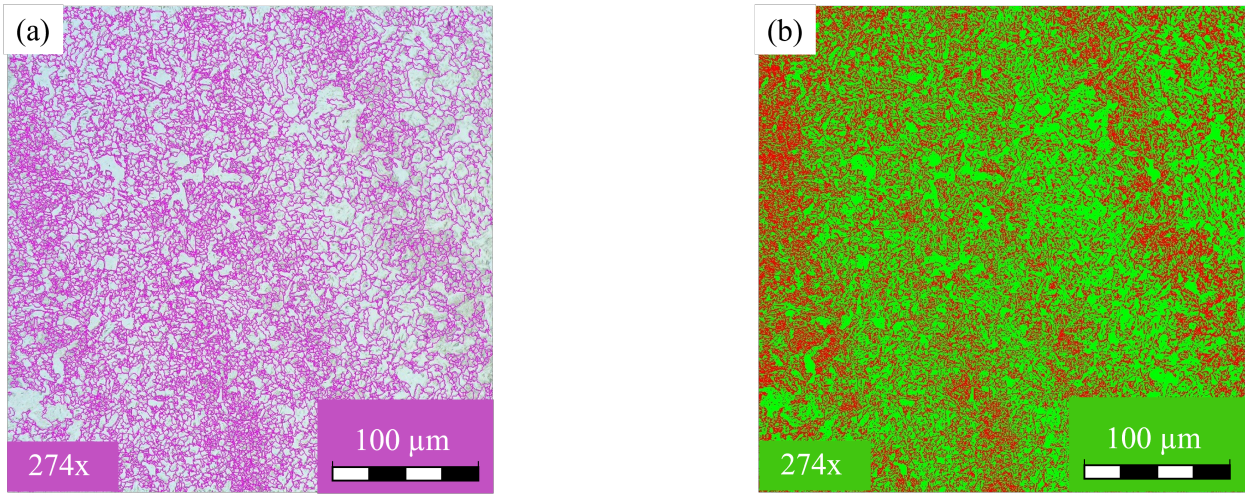

Figure 3.2: Microstructural investigation based on digital microscopy (a) Grain size determination (b) Phase fraction determination regarding a 20MnMoNi5-5 steel

A more precise investigation regarding the microstructure is given in figure 3.2, displaying the grain size distribution and an analysis of the phase fraction. Based on the results of figure 3.2(a), a grain size number of G = 14.11 can be found, which corresponds to an average grain area of 7.28 μm^2. The comparatively small grain size is a result of the heat treatment process of the material. As a result of the carbide structure, a precise phase analysis becomes challenging. Nevertheless, figure 3.2(b) leads to the insight that ferrite portions, shown as green grains, represent the majority of the microstructure.
Since an important aspect of this research is to investigate the influence of different surface conditions on fatigue behaviour of metallic materials, the microstructure in near-surface regions are of great interest. In order to assess the influence of manufacturing parameters on the respective microstructure, cross-sections of the 20MnMoNi5-5 specimens, taken with a laser-scanning microscope type OLS5100 of the company EVIDENT Europe GmbH, are summarised in figure 3.3, considering machining processes with different feed rates of 0.05 mm/min and 0.4 mm/min. Based on this, two important differences can be highlighted from the illustration. On the one hand, an increase in feed rate demonstrably leads to an increase in surface roughness, which can be observed in figure 3.3(b). Apart from that, a significant deformation of the grains located near the surface can be seen in case of figure 3.3(b), whereas a reduced feed rate in terms of figure 3.3(a) does not cause any noticeable changes within the grains.

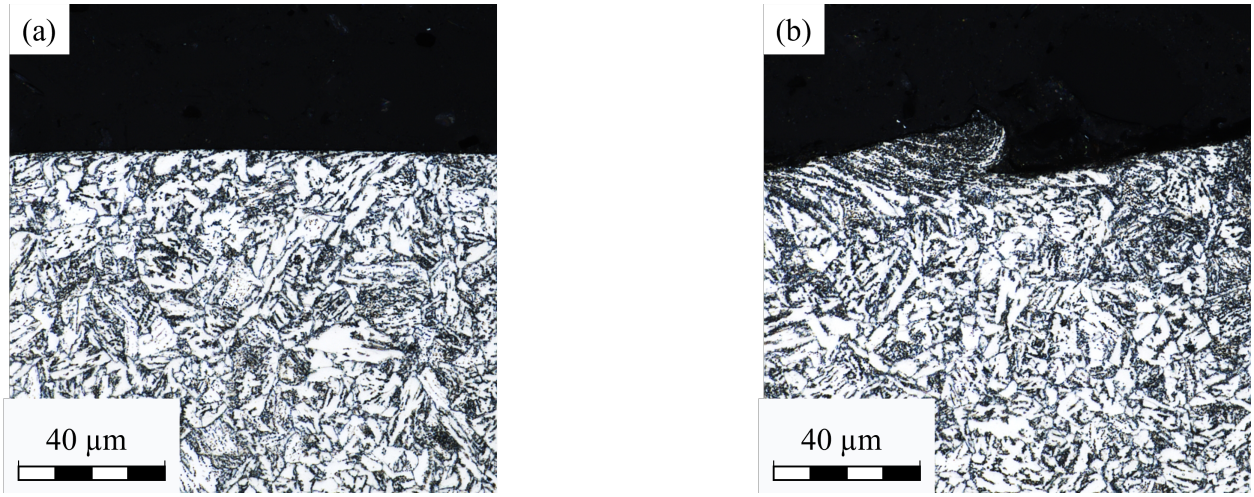

Figure 3.3: Microstructural investigation based on laser-scanning-microscopy concerning the surface area as a result of different feed rates (a) f = 0.05 mm/min (b) f = 0.4 mm/min regarding a 20MnMoNi5-5 steel

In order to provide more detailed insights regarding the microstructure of the 20MnMoNi5-5 steel, scanning electron microscopy was used in addition to light microscopic investigations. These results are presented within the following section of this chapter.
The results provided within figures 3.4, 3.5 and 3.6 were obtained using a scanning electron microscope (SEM) type Clara by the company TESCAN.

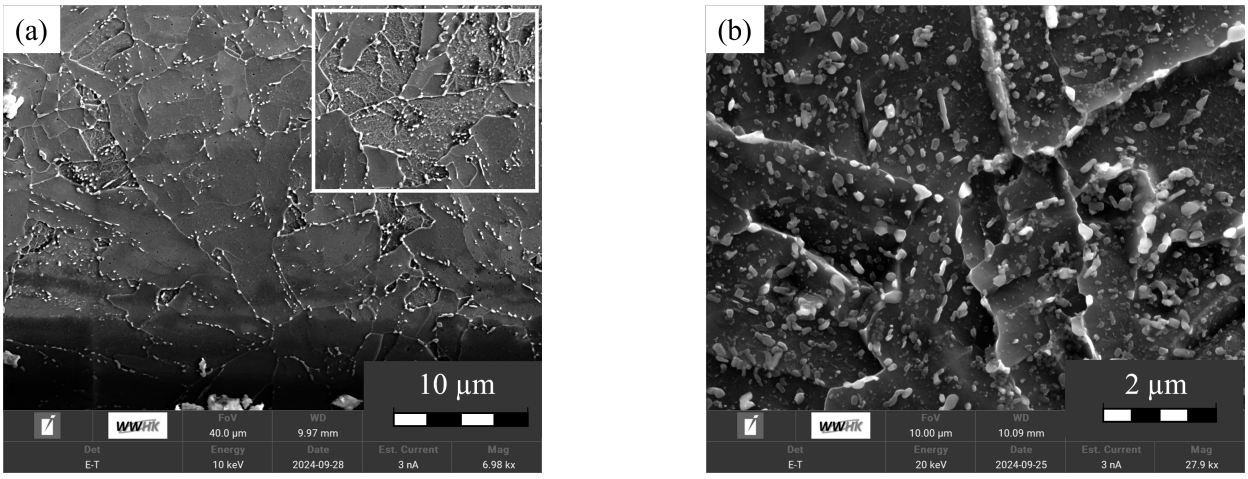

Figure 3.4: Microstructural investigation based on scanning electron microscopy regarding phases and precipitates (a) Overview of the microstructure including ferrite and bainite content as well as carbides (b) Detailed illustration concerning carbides within the volume of a 20MnMoNi5-5 steel

An investigation of the base material, shown in figure 3.4(a), leads to the insight that the microstructure of the 20MnMoNi5-5 steel can be divided into three main components. While the majority of the microstructure consists of ferritic grains, additional areas, characterised by an increased degree of inhomogeneity, can be observed. These grains might indicate the bainitic structure of the material. A selection of those regions is marked within figure 3.4(a). A striking attribute regarding the microstructure is the pronounced number of precipitates. Apart from that it can be stated that especially along grain boundaries, an increased occurrence of those precipitates is detectable. Figure 3.4(b) displays a more detailed consideration of the precipitates. Based on previous research, it has already been shown that these are mainly Fe_3C and M_2C carbides [240, 241].

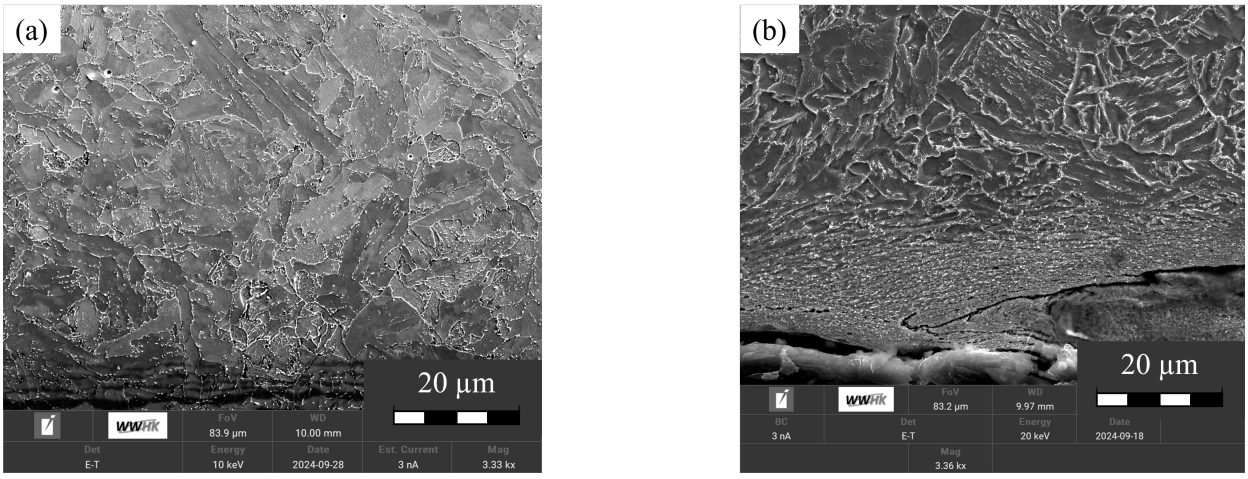

Figure 3.5: Microstructural investigation based on scanning electron microscopy regarding the surface area of different batches (a) Near-surface microstructure of the batch N3 (b) Near-surface microstructure of the batch N8 regarding a 20MnMoNi5-5 steel

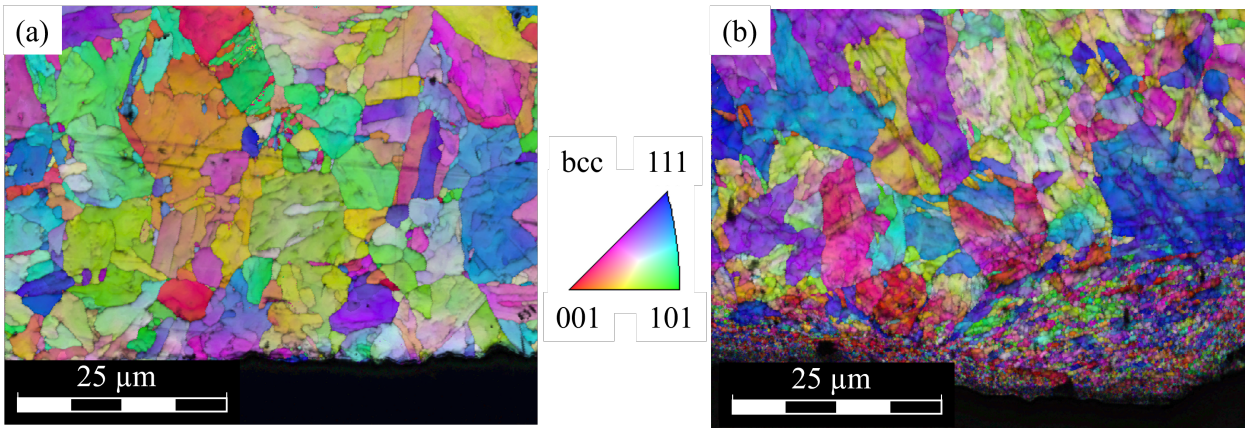

Figure 3.6: Microstructural investigation based on EBSD analysis in order to illustrate grain refinement of different surface finishes (a) Near-surface microstructure of the batch N3 (b) Near-surface microstructure of the batch N8 regarding a 20MnMoNi5-5 steel

Since previous investigations (figure 3.3) have already demonstrated the deformation of near-surface grains as a function of manufacturing parameters, figures 3.5 and 3.6 serve to provide more detailed insights regarding this influence. Within the presented SEM examinations, N3 and N8 are compared with each other as these batches illustrate the most distinctive differences. While figure 3.5(a) reveals almost no deformation of near-surface areas in terms of N3, the microstructure of N8, which is given in figure 3.5(b) is highly dependent on the distance to surface. Considering near-surface grains, a pronounced grain refinement of the microstructure can demonstrably be shown. Apart from that, the specimen assigned to N8 exhibits micro-cracks at the surface, which significantly affects the later discussed fatigue behaviour. In order to evidently visualise grain refinement concerning N3 and N8, additional EBSD (electron backscatter diffraction) measurements were performed (Figure 3.6).

3.1.2 Mechanical Characterisation

The mechanical characterisation includes hardness measurements of the 20MnMoNi5-5 steel, as well as the determination of mechanical parameters from tensile tests. The macro-hardness of the steel was measured on the basis of ten HV50 measurements. With an average value of 211.36 HV, it is evidently lower than the micro-hardness with 250.95 HV (HV0.05). This can be attributed to the increased proportion of the elastic component in case of the decreased testing force. Based on empirical relationships, the tensile strength of the material can be estimated from the hardness values. The experimental measured data results in an estimated tensile strength of 679.06 MPa. To verify this derived value, as well as to determine additional significant mechanical parameters, four experimental tensile tests were carried out as part of the presented research project. The results are summarised in figure 3.7.

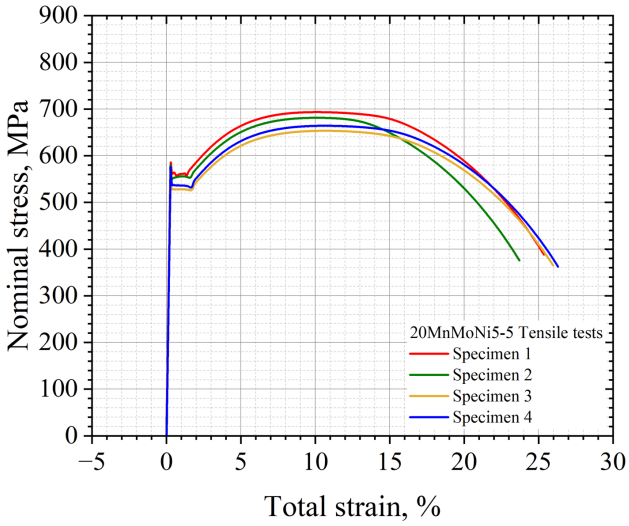

Figure 3.7: Investigation of the mechanical properties based on tensile tests regarding a 20MnMoNi5-5 steel

Based on this outcome, a pronounced yield point can be derived from the curve progressions. This indicates that after reaching the higher yield point R_{eh}, the required stress initially decreases to a lower value. The reason for this is given by the presence of alloy atoms, settling on dislocations and therefore accumulating to Cottrell Clouds. To enable dislocation movements, an initial increase in the applied load is needed. Assuming an average maximum tensile strength of 673.2 MPa and a yield strength of 577.6 MPa, the yield point ratio is approximately 0.86. Since this ratio is defined by the correlation of the yield strength and tensile strength, it is well suited to provide information regarding the material behaviour. Higher values indicate a more brittle behaviour, whereas lower values suggest ductile behaviour. The most important parameters describing the mechanical properties of the 20MnMoNi5-5 steel under static loading are summarised in table 3.1.

Table 3.1: Mechanical properties considering static loading of a 20MnMoNi5-5 steel

E [GPa]	R_{eh} [MPa]	R_{el} [MPa]	$R_{p\,0.2}$ [MPa]	R_m [MPa]	A_t [%]
198.2	586.3	557.2	563.8	693.6	25.36
266.4	580.3	552.8	551.5	681.3	23.73
194.5	576.4	532.1	537.2	664.3	26.32
218.1	567.4	525.8	528.3	653.5	25.99
219.3	577.6	541.9	545.2	673.2	25.35

3.1.3 Surface Conditions

As already described in chapter 2.2.1, the fatigue behaviour of metallic materials is highly influenced by the surface condition. The reason for this are localised increased stress concentrations, which promote crack initiation from the surface, especially in the HCF regime. Consequently, an

overarching objective of the presented research is the scientific quantification of this influence.
A total of five different surface topographies are analysed with regard to their fatigue properties. Prior to specimens manufacturing, a universally valid classification of different surface qualities needs to be introduced. The standard DIN EN ISO 1302 [242] divides surface conditions into the groups N1-N12 regarding their roughness value R_a, which covers a roughness range of 0.025 µm - 50 µm. A combination of several factors is used in order to machine the specimens (table 3.2). In addition to varying turning parameters such as feed rate and cutting speed, tool wear is simulated by mechanically modified cutting tools, leading to an increased surface roughness. Besides that, two batches are subjected to mechanical polishing, that effects not only surface roughness but also residual stresses.

Table 3.2: Summary of the machining parameters regarding the different batches N3-N9 of a 20MnMoNi5-5 steel

Batch	Feed Rate [mm/rev]	Rotational Speed [rpm]	Cooling
N3	0.05	600	✓
N5	0.05	600	✓
N7	0.20	600	✓
N8	0.20	600	✓
N9	0.20	600	✓
Batch	Pre-Grinding	Polishing	Mod. tools
N3	✓	✓	x
N5	x	✓	x
N7	x	x	x
N8	x	x	✓
N9	x	x	✓

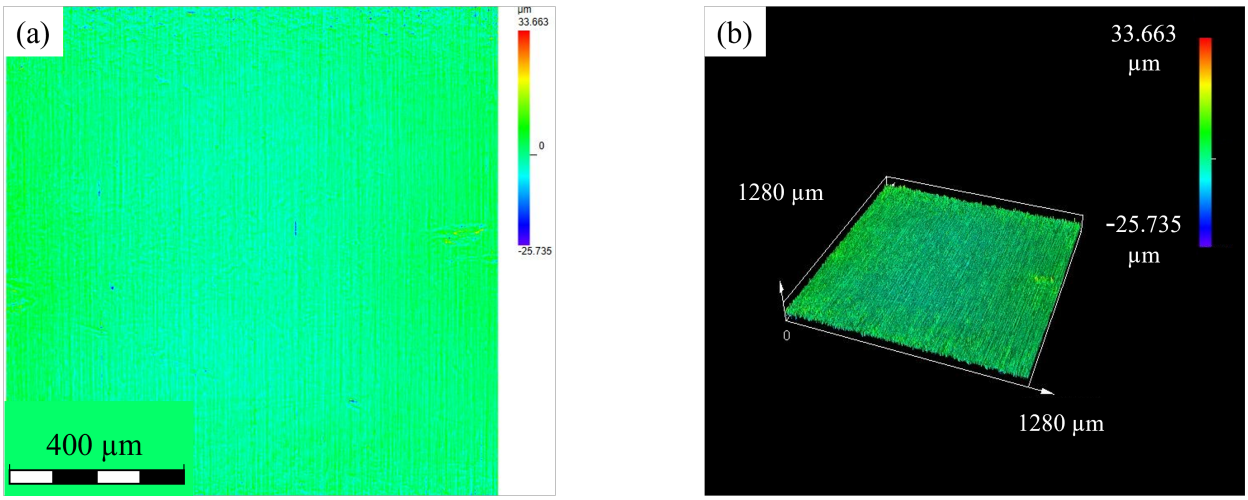

Figure 3.8: Investigations based on laser-scanning-microscopy concerning surface roughness of the mechanically polished batch N3 machined with unworn cutting tools (a) 2D-mapping of the surface (b) 3D-mapping of the surface regarding a 20MnMoNi5-5 steel

The machining parameters summarised in table 3.2 can therefore be used to manufacture specimens from batches N3, N5 and N7-N9. The defined machining parameters result in different surface conditions which are illustrated in figures 3.8, 3.9, 3.10, 3.11 and 3.12. All conditions were investigated using a laser-scanning-microscope type LEXT OLS5100 by the company EVIDENT Europe GmbH. Figure 3.8 and figure 3.9 provide information regarding the two mechanically polished batches N3 and N5, which differ only in the preliminary grinding process in terms of N3.

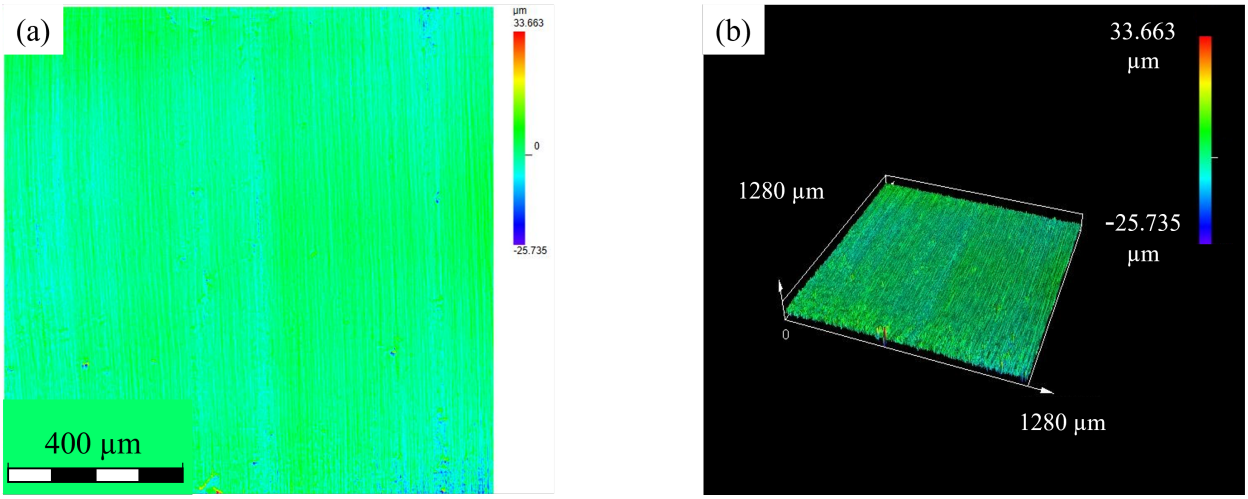

Figure 3.9: Investigations based on laser-scanning-microscopy concerning surface roughness of the mechanically polished batch N5 machined with unworn cutting tools (a) 2D-mapping of the surface (b) 3D-mapping of the surface regarding a 20MnMoNi5-5 steel

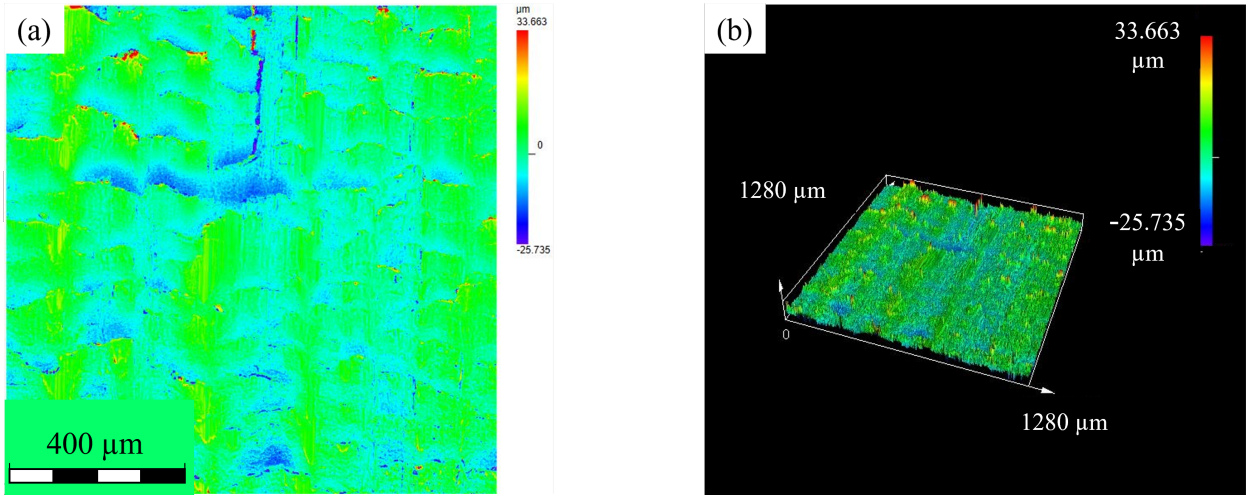

Figure 3.10: Investigations based on laser-scanning-microscopy concerning surface roughness of the batch N7 machined with unworn cutting tools (a) 2D-mapping of the surface (b) 3D-mapping of the surface regarding a 20MnMoNi5-5 steel

In addition to the homogeneity of the surfaces, that can be attributed to the polishing process, almost no difference between N3 and N5 can be monitored as a result of the comparable manufacturing process parameters. Nevertheless, table 9.3 of journal contribution 4 in part II of this thesis shows that the grinding process has a significant influence on surface integrity since the residual stresses are highly reduced.
The evidently increased surface roughness of the batch N7 compared to N3 and N5, which is shown in figure 3.10, can be explained on the one hand by the lack of polishing process, but also the increased feed rate. Despite higher surface roughness, a certain homogeneity in form of recurring grooves can still be assumed. The previous illustrations (figures 3.8, 3.9 and 3.10) refer to surface conditions, that are machined using non-worn cutting tools. In addition to process parameters, however, tool wear and its influence on surface integrity is an important factor, which also needs to be considered for real manufacturing applications.
Based on this finding, the cutting tools for the machining of batches N8 and N9 are mechanically pre-processed in order to simulate different tool wear conditions and therefore generate significantly increased roughness values. Figures 3.11 and 3.12 show the 2D-, as well as the 3D-mapping of those surface conditions. In Particular, in case of batch N9, which represents the most critical tool wear condition, the inhomogeneity of the surface compared to the other conditions becomes apparent.

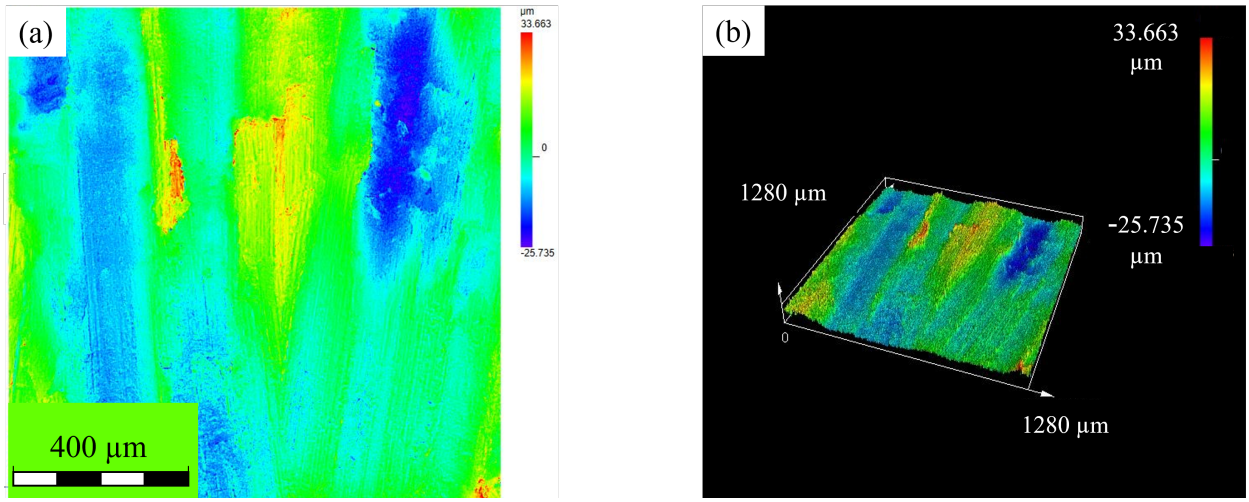

Figure 3.11: Investigations based on laser-scanning-microscopy concerning surface roughness of the batch N8 machined with worn cutting tools (a) 2D-mapping of the surface (b) 3D-mapping of the surface regarding a 20MnMoNi5-5 steel

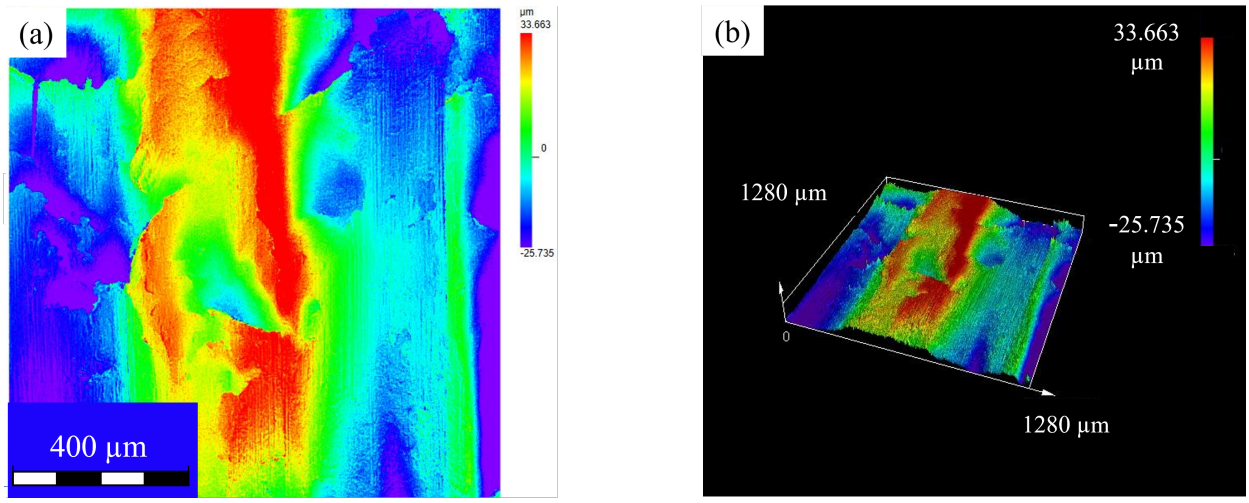

Figure 3.12: Investigations based on laser-scanning-microscopy concerning surface roughness of the batch N9 machined with worn cutting tools (a) 2D-mapping of the surface (b) 3D-mapping of the surface regarding a 20MnMoNi5-5 steel

A general overview of the manufactured surfaces is given in figure 3.13, in which the periodic peaks in terms of the N7 surface are particular striking. In order to enable a more detailed examination of the N7 surface topography, a detailed illustration is shown in figure 3.14.

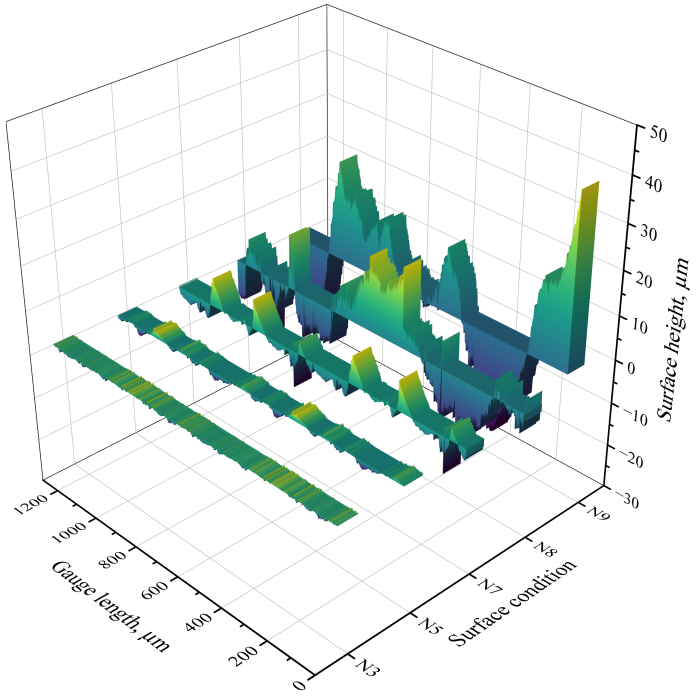

Figure 3.13: Comparison of the surface roughness based on the results of the laser-scanning-microscopy regarding surface batches N3-N9 of a 20MnMoNi5-5 steel

While the peaks in terms of N5 can still be roughly recognised, surface N3 exhibit no pronounced roughness peaks as a consequence of the grinding process. Therefore, it can be concluded that although the mechanical polishing process leads to significantly improved surface conditions, kinematic roughness cannot be completely removed. Considering the harsh manufacturing conditions of N8 and N9, kinematic roughness is superimposed by vibration processes of the machine. This is a consequence of the increased feed rate as well as the wear condition of the cutting tool. Within figure 3.14, the measured surface height (ΔR) is given as a function of the gauge length (GL). The distance between the roughness peaks is equal to 200 µm and therefore corresponds to the machining feed rate of 0.2 mm $\cdot$ rev^{-1}. The theoretical surface roughness R_{max} consists of geometric contribution of the tool tip radius r_ε and the feed rate f. The relation between those parameters is given in equation 3.1.

$$R_{max} = \frac{f^2}{8 \cdot r_\varepsilon} \tag{3.1}$$

Assuming a feed rate of 0.2 mm $\cdot$ rev^{-1} and a tool tip radius of 0.8 mm, the theoretical surface roughness can be calculated as $R_{max} = 6.25$ µm , which is in high agreement with the experimental data.

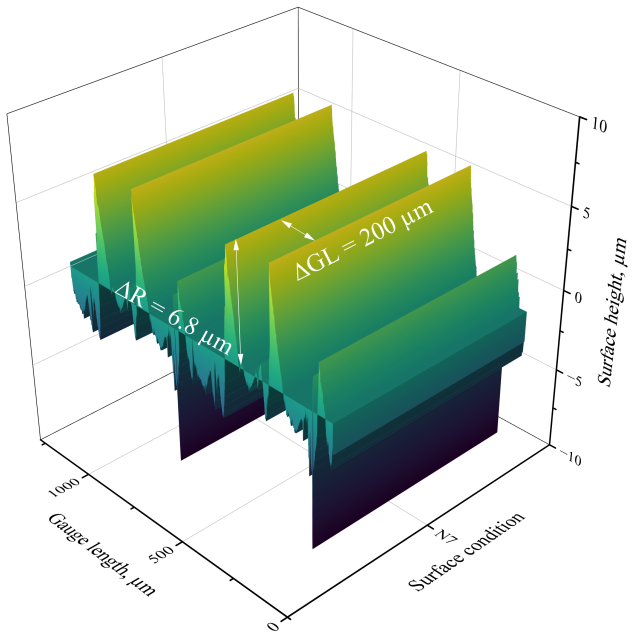

Figure 3.14: Investigation of the surface roughness based on the results of the laser-scanning-microscopy regarding the surface batch N7 of a 20MnMoNi5-5 steel

As it does not appear to be sufficient to consider only average surface values for a reliable assessment of surface roughness influence on fatigue behaviour, distribution functions are used within this research (figure 9.7 of journal contribution 4). As a result, conclusions can be drawn regarding the scattering of the surface roughness. In order to be able to generate distribution functions, sufficient data points must first be collected. Figure 3.15 shows graphically at which positions of the fatigue specimen surface roughness is measured. By determination of data points in the middle of the

gauge length, as well as at the transition to the radius, a total number of twelve data points per specimen is obtained.

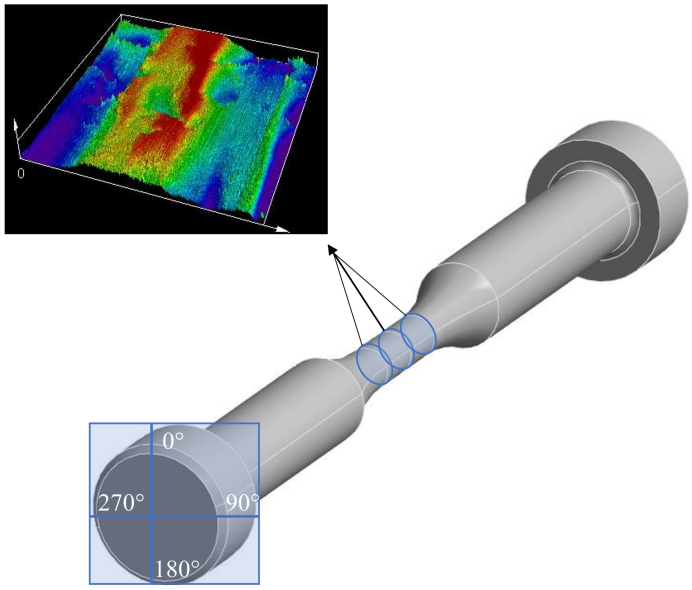

Figure 3.15: Schematic representation regarding the localisation of the measuring points for the roughness investigations of a 20MnMoNi5-5 steel

3.2 Methods

The main aspect of this research is the description and validation of the new LPM MiDAcLife, which is developed as part of this doctoral thesis. In addition to that, distinctive changes have been made regarding the already existing method StressLife. Therefore, it is also explained in more detail within this chapter. Both methods have in common that they are based on the combination of NDT-related measurement techniques with conventional fatigue testing and thus enable an accelerated provision of fatigue data, especially in the HCF regime. While StressLife requires a total of three to four fatigue specimen, resulting in a rather global assessment of fatigue properties, the experimental effort in case of MiDAcLife can be reduced to a minimum of only one fatigue specimen and one fatigue test. This allows fatigue data to be derived very locally. This chapter aims to explain the basics of both procedures. In the following chapter 4, the methods are compared and evaluated in terms of their applicability and accuracy with data from conventional fatigue analyses.

3.2.1 StressLife

The StressLife method is characterised by the accelerated provision of fatigue data under consideration of elastic, elastic-plastic and plastic portions of the material response as a result of dynamic loading. Even if the load amplitudes occurring during a fatigue process are mainly below the static yield strength, micro-plastic deformations still take place in favourably oriented grains. This emphasises the importance of taking multiple degradation portions into account, which is an advantage of StressLife compared to other lifetime prediction methods.

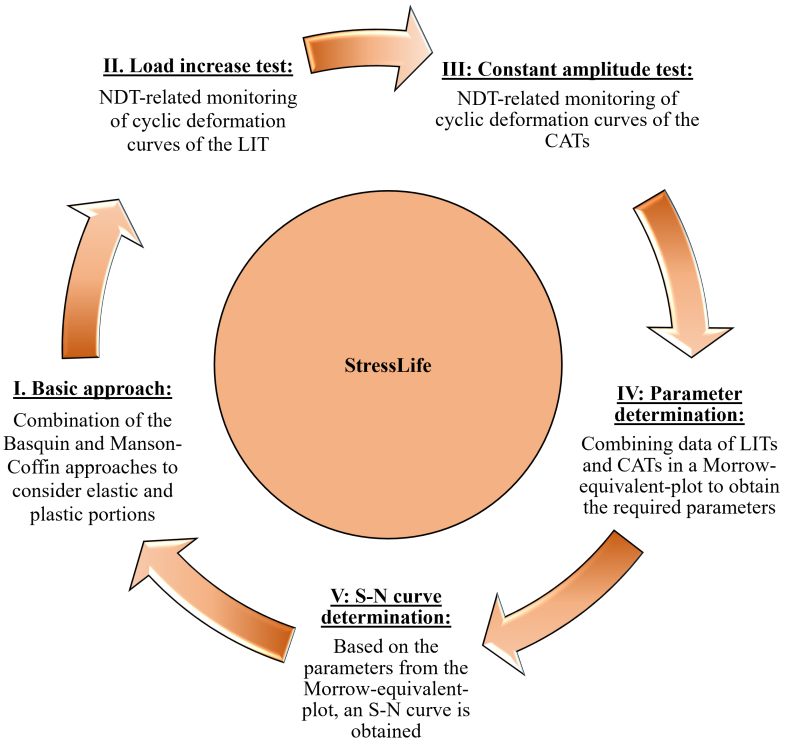

Figure 3.16: Schematic representation of the lifetime prediction method StressLife

The basis of StressLife is a LIT, which can be used to obtain several important information regarding fatigue properties. From the curve progression of the material response it can be deduced whether the material exhibits a merely cyclic softening or additional cyclic hardening processes. Depending on these cyclic deformation curves, it can be assessed if the material is characterised by a rather brittle or more ductile behaviour.
The second important information that can be derived from the LIT is the fatigue strength. By gradually increasing the stress amplitude and detecting the material response, the stress amplitude above which a non-linear increase in material response and therefore material degradation occurs can be determined. This value serves as an accelerated estimation of the fatigue strength of the material. Furthermore, the LIT is used to determine the values for the cyclic hardening exponent n', as well as the cyclic hardening coefficient K', which are essential for further calculations of StressLife parameters. Figure 3.16 provides a schematic overview of how an S-N curve is obtained according to StressLife.

Journal contribution 1 entitled "StressLife: A Short-Time Approach for the Determination of a Trend S-N Curve in and beyond the HCF Regime for the Steels 20MnMoNi5-5 and SAE 1045" in part II contains a detailed description of the relations used within StressLife. However, the most important insights are summarised at this point.
The averaged material response is determined for each load step of the LIT and plotted in a Morrow-equivalent-plot. This designation originates from the representation of the stress amplitude as a function of the plastic strain amplitude introduced by Morrow [243]. By using an allometric fit, given in equation 3.2, both an elastic n_e and a plastic portion of the cyclic hardening exponent n_p can be derived. The total cyclic hardening exponent n_{total} results from the summation of both

components.

$$\sigma_a = K \cdot (MR)^n \tag{3.2}$$

$$n_{total} = \frac{5}{\alpha_p + 5} \cdot n_e + \frac{\alpha_p}{\alpha_p + 5} \cdot n_p \tag{3.3}$$

The abbreviation MR of equation 3.2 represents the material response, whereas the parameter α_p describes the amount of data points localised in the plastic range of the Morrow-equivalent-plot. An increased value therefore indicates a more ductile material behaviour. In the elastic range, only five data points are considered, as otherwise the dependence on the starting stress amplitude would become too pronounced.
In case of StressLife, the stress amplitude is dependent on several parameters that are illustrated in equation 3.4.

$$\sigma_a = K' \cdot [B \cdot (2N_f)^b + C \cdot (2N_f)^c]^{n'} \tag{3.4}$$

In contrast to the LIT, K' and n' describe the cyclic hardening coefficient and exponent under consideration of constant amplitude loading. The parameters B and C indicate the Basquin coefficient accoring to Basquin [11] and the ductility coefficient proposed by Manson-Coffin [17, 19]. In order to estimate the Basquin exponent b and the ductility exponent c, the relations introduced by Morrow [243] are applied, which are shown in equation 3.5 and 3.6.

$$b = \frac{-n_{total}}{5 \cdot n_{total} + 1} \tag{3.5}$$

$$c = \frac{-1}{5 \cdot n_{total} + 1} \tag{3.6}$$

The determination of the remaining coefficients B and C requires two further equations that can be derived from the material response of two additional CATs. For this purpose, the material response is observed after half of the number of cycles to failure and transferred into the Morrow-equivalent plot. Using an allometric fit and recognising that the entire material response consists out of elastic and plastic components that can be described according to Basquin and Manson & Coffin, both parameters can be calculated. Based on the CAT data points, a third CAT can be calculated virtually. Fitting these CATs in the Morrow-equivalent plot results in the possibility to obtain the parameters K' and n' of equation 3.4

3.2.2 MiDAcLife

In contrast to StressLife, MiDAcLife (Miner Damage Accumulation Lifetime Prediction) is characterised by the fact that only one fatigue test (LIT) is required to provide an S-N curve in the HCF regime. Furthermore, both methods are based on different empirical approaches. While StressLife is based on relations according to Basquin and Manson & Coffin, MiDAcLife is based on the linear damage accumulation model, which was firstly introduced by Palmgren and Miner.

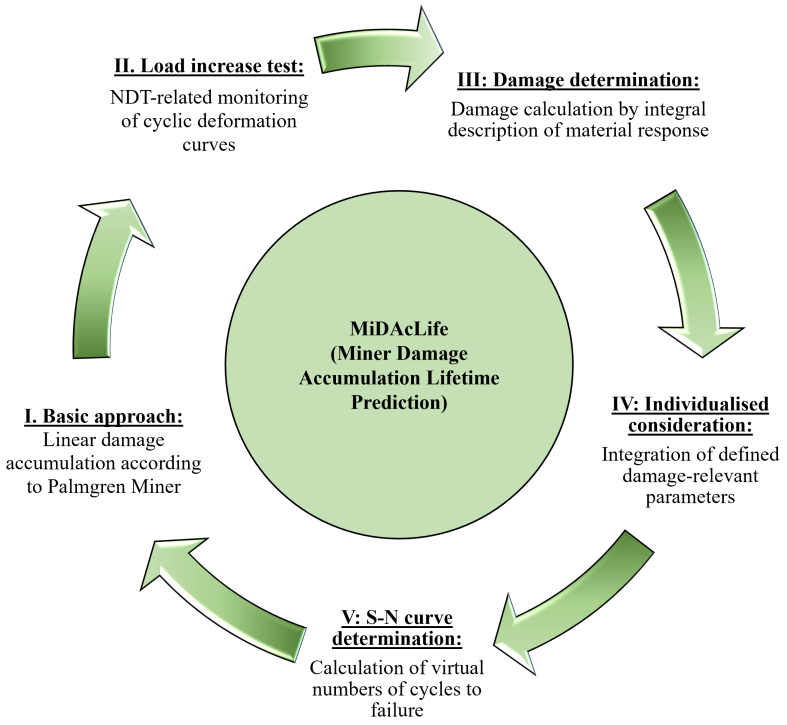

Figure 3.17: Schematic representation of the lifetime prediction method MiDAcLife

The LPM uses the material response to draw conclusions about the partial damage introduced during a load cycle. Knowing the number of applied cycles, a virtual number of cycles to failure can be estimated. An allometric fit according to conventional methods subsequently leads to the S-N curve. A schematic representation of the steps required for MiDAcLife is given in figure 3.17. As can be seen in figure 3.17, the basis of the LPM is the linear damage accumulation model according to Palmgren and Miner. This approach defines the induced partial damage D_i as the ratio of the applied number of load cylces n_i and the number of cycles to failure N_f.

$$D_i = \frac{n_i}{N_f} \tag{3.7}$$

In order to calculate the partial damage D_i, the correlation of the material response with the stress-strain-hysteresis is utilised as part of the process, as it can therefore be assumed that a change in material response is equivalent to an applied damage. Analogue to the evaluation according to StressLife, the averaged material response of each load step is determined and plotted as a function of the stress amplitude. The partial damage results from the integral consideration of the material response ϑ at a defined stress amplitude $\sigma_{a,i}$ and the subsequent normalisation to the entire area enclosed by the cyclic deformation curve.

$$D_i = \frac{\int_{\sigma_{a,i-1}}^{\sigma_{a,i+1}} \vartheta d\sigma_a}{\int_{\sigma_{a,start}}^{\sigma_{a,end}} \vartheta d\sigma_a} \tag{3.8}$$

In order to investigate the total area enclosed by the cyclic deformation curve, equation 3.8 integrates the curve with the limits $\sigma_{a,start}$, which represents the first step of the LIT and $\sigma_{a,end}$, indicating the last load level of the LIT. Similar to the previous chapter, a more detailed summary of the procedure is provided in the corresponding publications within part II of this thesis (Paper 2-4).
Figure 3.17 shows that there is a further key aspect called "Individualised consideration" between the determination of the partial damage and the provision of an S-N curve. This aspect results from the key objective of this research to integrate important damage-relevant parameters into the lifetime prediction. In future research this should enable an individualised S-N curve provision instead of a global consideration of fatigue properties. In addition to surface roughness, which is considered within this research, other influencing factors such as testing frequency, ambient temperature and corrosive influences must also be considered in future work.

4 Results and Discussion

The journal contributions attached in part II of this doctoral thesis mainly relate to the development and introduction of new LPMs and their applicability to various steels. The basis of this published research is the implementation of NDT-related measurement techniques, such as thermography and electrical resistance measurements, in destructive materials testing. Essentially, three main research aspects can be derived from the attached journal contributions. In addition to the modification of the StressLife method, which enables a global lifetime prediction based on three fatigue specimens, a particular focus is on the newly developed LPM MiDAcLife. Besides the evaluation of local fatigue properties, damage-relevant influencing factors can be integrated into the calculation method. This results in a significant reduction of the experimental testing effort. Since the individual subjects are considered separately within the respective publications, this chapter serves to link the individual aspects and to give a comprehensive overview regarding accelerated lifetime prediction.
A graphic illustration of the structure within this discussion section is provided in figure 4.1 and is intended to serve as guideline through the chapter. As part of a method development, focus is usually on an initial model material. However, validation tests on a single material appear to be insufficient in order to prove the applicability of an entire method. For this reason, both methods (StressLife, as well as MiDAcLife) were applied to different un- and low alloyed steels. Experimental data resulting from other research projects is taken for given validation purposes. These tests are labelled with a footnote at the relevant positions.

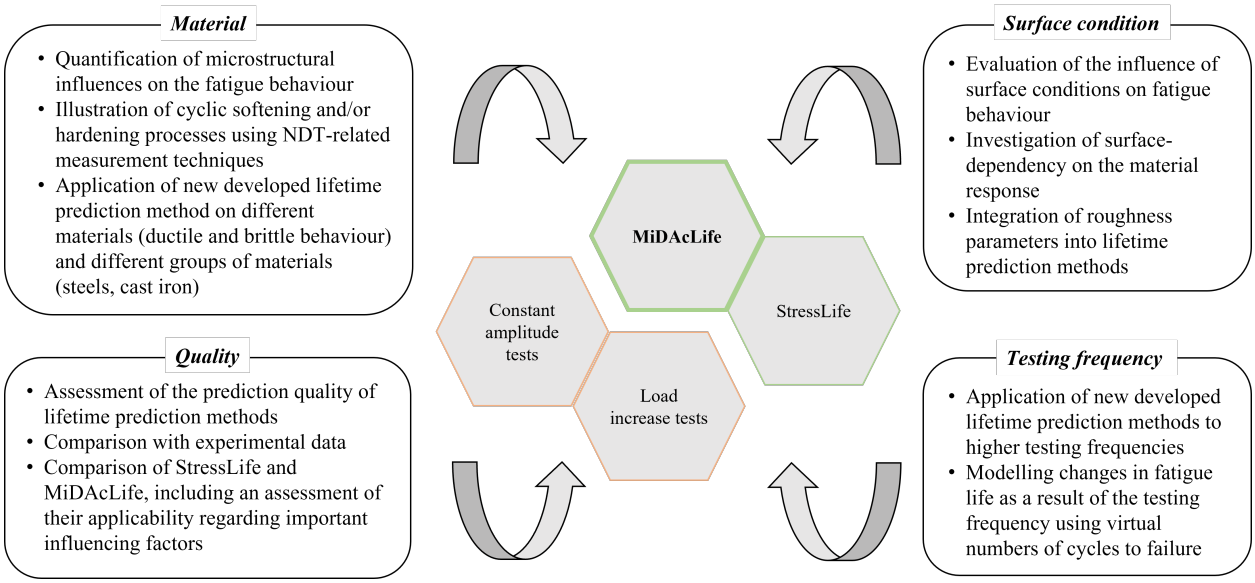

Figure 4.1: Schematic representation of the presented research results

From a materials science perspective, these materials most notably differ in their microstructural composition, which in turn depends on various factors. It is therefore essential to analyse parameters that mainly influence the microstructure. In the following, the impact of alloying elements, the influence of carbon content and the effect of heat treatment on cyclic deformation curves regarding CATs, as well as LITs is investigated. Apart from that, both LPMs, described in chapter 3.2, are examined with regard to their validity depending on material condition.

In addition to the consideration of influencing factors on a microscopic scale and their effect on test procedures and lifetime prediction, further mesoscopic and macroscopic factors as well as external conditions must be considered to ensure a reliable assessment of fatigue properties. Both LPMs are examined concerning their ability to incorporate parameters into lifetime calculations, such as increased surface roughness, which lead to a decreased lifetime, or increased testing frequency, that can result in higher numbers of cycles to failure.
The reduced testing effort in context of the accelerated provision of fatigue data naturally raises the question regarding the accuracy of the presented methods. In order to assess the quality of the lifetime estimation, a comparison with results of conventional models is sought within this research. However, it should be noted at this point that the accelerated LPMs do not claim to completely replace the conventional procedure of generating S-N curves, but should rather be regarded as a useful and highly informative extension of fatigue research. Consequently, a combination of conventional methods for validation and accelerated NDT-related methods for intial assessment and important indications of ongoing mechanisms appears to be the most sensible solution. Apart from the comparison with conventional determined S-N curves, both LPMs are compared with regard to their quality in order to identify possible limitations.
The ferritic-bainitc 20MnMoNi5-5 steel, which has already been described in chapter 3.1, serves as reference material for the presented results. In order to adequately illustrate different influencing factors, the results are supplemented by further materials at the respective sections.

4.1 Microstructural Influence on Fatigue Behaviour

4.1.1 Influence of Carbon Content

Depending on the application, certain requirements are placed on construction materials, particularly in terms of their mechanical properties. A change in properties of the material can be achieved by changing the chemical composition with alloying elements. To understand the influence of alloying elements on the cyclic behaviour of metallic materials, the effect of the most important and essential alloying element, carbon, must be considered first. As a result of elastic distortions caused by carbon atoms in the octahedral lattice gaps of the bcc α-Fe, the solubility of carbon atoms in α-Fe is severley limited. While a maximum of 0.001 wt.-% can be dissolved at room temperature, the solubility increases with rising temperature to a maximum value of 0.02 wt.-%. A further increase in carbon content leads to the formation of a second phase within the material, the so-called cementite. The microstructure therefore no longer consists only of ferritic components, but of ferrite and pearlite, which is characterised by a lamellar structure of cementite and ferrite lamellae. As a result of the orthorhombic lattice structure concerning cementite, a higher pearlite content leads to increased strength values but consequently to a more brittle behaviour of the material. Additionally, dislocation movement, which is responsible for plastic deformation, is severely restricted by the lamellar structure of pearlite, leading to an increased fatigue strength. In summary, it can be stated that plastic deformation processes take place in ferritic areas of the microstructure and that an increase in carbon content leads to embrittlement of the material. Apart from that, an increase in fatigue strength is expected as a result of the dislocation movement restriction.
To ensure the highest possible comparability with the reference material 20MnMoNi5-5, the influ-

ence of carbon content is investigated using an SAE 1020[1] steel, which is characterised by similar carbon content compared to the 20MnMoNi5-5 steel and an SAE 1045 steel[2]. Both steels are in a normalised condition, which is indicated by the suffix N in the material designation. Figure 4.2 shows the cyclic deformation curves of both steels considering LITs as well as CATs.

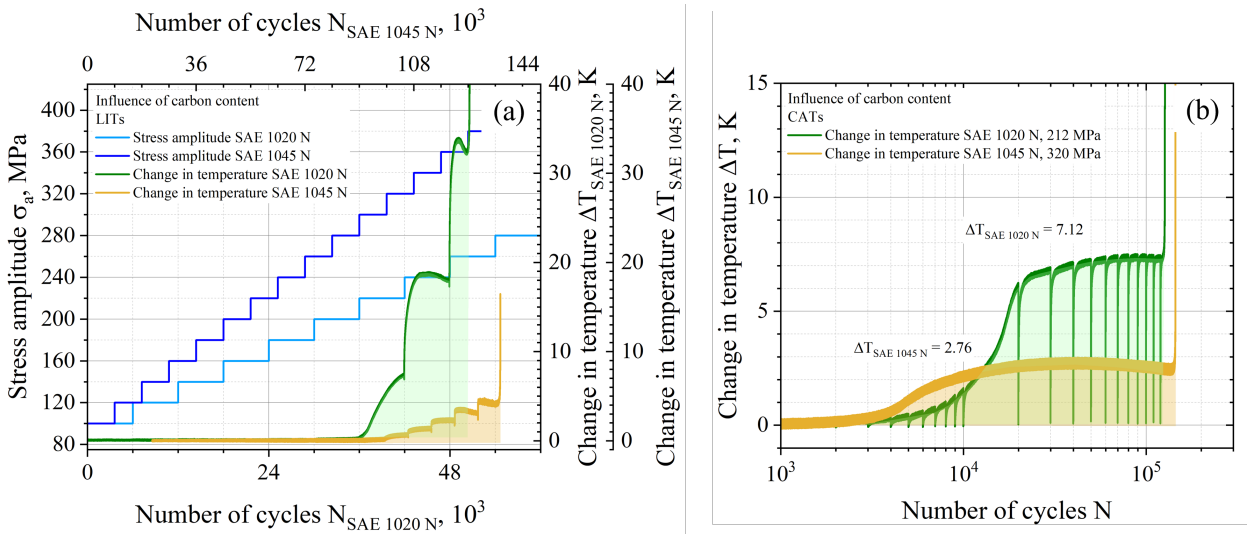

Figure 4.2: Investigations regarding the influence of carbon content on the fatigue behaviour based on cyclic deformation curves (a) Load increase test with $f = 5$ Hz, $\sigma_{a,start} = 100$ MPa, $\Delta\sigma_a = 20$ MPa and $\Delta N = 6000/9000$ (b) Constant amplitude tests with $f = 5$ Hz and $\sigma_a = 212/320$ MPa regarding the SAE 1020 N and SAE 1045 N steels

The LITs shown in figure 4.2(a) depict an indispensable part of the results presented within this thesis. It serves not only as input for both LPMs, but also enables a characterisation of the cyclic material behaviour regarding brittleness or ductility and an accelerated estimation of the value for the fatigue strength. Since both examined steels in figure 4.2 only imply carbon as alloying element, a rather ductile material behaviour is expected as a result of the high ferrit content. The pronounced material responses confirm this assumption. A common feature of both change in temperature curves is the occurrence of cyclic-softening and -hardening processes within the volume of the material as a result of dislocation formation, annihilation and rearrangements. Since the change in temperature directly correlates with the enclosed area of the stress-strain-hysteresis loop, an increase in material response indicates cyclic softening, whereas a decrease is linked to cyclic hardening. However, a comparison of the two curve progressions also reveals substantial differences. The first significant difference lies in the intensity of the material response, which is

[1]Experimental results
Project: STA 1133/10
University: University of Applied Sciences Kaiserslautern
Institude: Department of Materials Science & Materials Testing (WWHK)
Project manager: M. Sc. Haoran Wu

[2]Experimental results
Project: STA 1133/6
University: Saarland University
Institude: Chair for non-destructive testing and quality assurance (LZfPQ)
Project manager: M. Sc. Haoran Wu

evidently more pronounced in terms of the SAE 1020 steel. Considering half of the numbers of cycles to failure as reference points, the more ductile SAE 1020 steel already exhibits 4.4 % of the maximum change in temperature regarding the third last load level. A comparison with values of the last two load levels is not appropriate, since the values of the change in temperature are evidently dependent on the position of the measuring fields as a result of the continuous expansion of macro-cracks. The material response of the SAE 1045 steel is significantly lower, at 1.8 % of the reference temperature value.
Although comparing individual values provides important initial indications, it is prone to errors as a result of the measurement scattering. For this reason, the area enclosed by the cyclic deformation curves is considered as an additional evaluation parameter within this research. This integral approach is intended to reduce the influence of measurement inaccuracies on the evaluation. The ratio of both enclosed areas of figure 4.2(a) results in a scaling factor of 2.06, which confirms previous results and assumptions. Besides the intensity of the material response, it can also be stated, that a change in material response occurs at lower stress amplitudes in case of the SAE 1020 steel. While the specimen failure of the SAE 1020 steel appears at a stress amplitude of $\sigma_{a,end} = 260$ MPa, the first material response can be observed at the transition from 200 MPa to 220 MPa. Therefore, the fatigue strength can be estimated as 200 MPa. An analogue consideration in terms of the SAE 1045 steel leads to a failure level of 380 MPa and a fatigue strength of 280 MPa. The most important findings of the LIT evaluations displayed in figure 4.2(a) are summarised in table 4.1.

Table 4.1: Summary of the load increase test results to quantify the influence of different carbon content regarding the normalised SAE 1020 and SAE 1045 steels

Material	Stress amplitude failure [MPa]	Fatigue strength [MPa]	Scaling factor
SAE 1020 N	260	200	2.06
SAE 1045 N	380	280	

An additional type of experimental tests, which is mainly required for the StressLife evaluation, is the conventional CAT. It is characterised by a constant stress amplitude. Beside the inclusion of CAT data into the LPM StressLife, these tests are used to validate calculated S-N curves and serve as the basis for conventionally determined S-N curves.
Figure 4.2(b) displays the CAT results of both unalloyed steels. Each curve progression is divided into three characteristic regions. After an initial rapid increase of the material response in case of low cycle numbers, a plateau is reached, which is kept at a constant level over a large part of fatigue life. Briefly before failure of the specimen, a severe increase in material response is detectable. This change of the temperature curve can be attributed to frictional processes of fracture surfaces. An established method for assessing the material response of a CAT is the consideration of the change in temperature after half the numbers of cycles to failure. As already shown for the LITs in figure 4.2(a), the increased carbon content causes a greatly reduced change in temperature ($\Delta T_{SAE1020} = 7.12$ K; $\Delta T_{SAE1045} = 2.96$ K). An integral consideration, as in the terms of the LIT, provides a scaling factor of 2.2 that is in accordance with the scaling factor of table 4.1. A notable finding regarding the scaling factors is, that in both cases the scaling factor corresponds nearly exactly with the factor of the carbon content. This correlation could be investigated in further research. By correlating material response and carbon content, it might be possible to generate

virtual cyclic deformation curves.
Based on previous analyses, it can be concluded that an increased carbon content has a major influence on the test results of CATs and LITs. As a result of the increased pearlite content, the material response decreases and the fatigue strength is increased. In the following, these insights will be transferred to the lifetime prediction. Based on the NDT-related approaches according to MiDAcLife (green line) and StressLife (dashed orange line), the S-N curves of the SAE 1020 N and SAE 1045 N steels are given in figure 4.3. To assess the prediction quality, both LPMs are compared with results from conventional fatigue testing, which are represented by black lines. CATs used for validation purposes are illustrated as blue triangles. In order to gain an impression of the microstructure-related scatter of the respective material, figure 4.3 contains the S-N curves concerning failure probabilities of 10 %, as well as 90 % in addition to the 50 % S-N curve. To consider the material scatter within the fatigue strength estimation, fatigue strength is specified in terms of a stress amplitude range instead of an absolute value, which is indicated by a grey shaded area in figure 4.3. At this point, a significant advantage regarding performance of LITs becomes evident. A comparison of the fatigue strength values estimated in the LITs (figure 4.2(a)) matches the data determined conventionally and according to LPMs with a very high degree of accuracy. Assuming a limited cycle number of $2 \cdot 10^6$, conventional fatigue strength calculations result in a fatigue strength of 191.3 MPa for the SAE 1020 N steel, which corresponds to a deviation of 4.5 %. Besides that, the estimated fatigue strength values according to LPMs are also characterised by an extremely low deviation of 0.7 % in terms of the evaluation according to MiDAcLife and 1.3 % regarding StressLife.

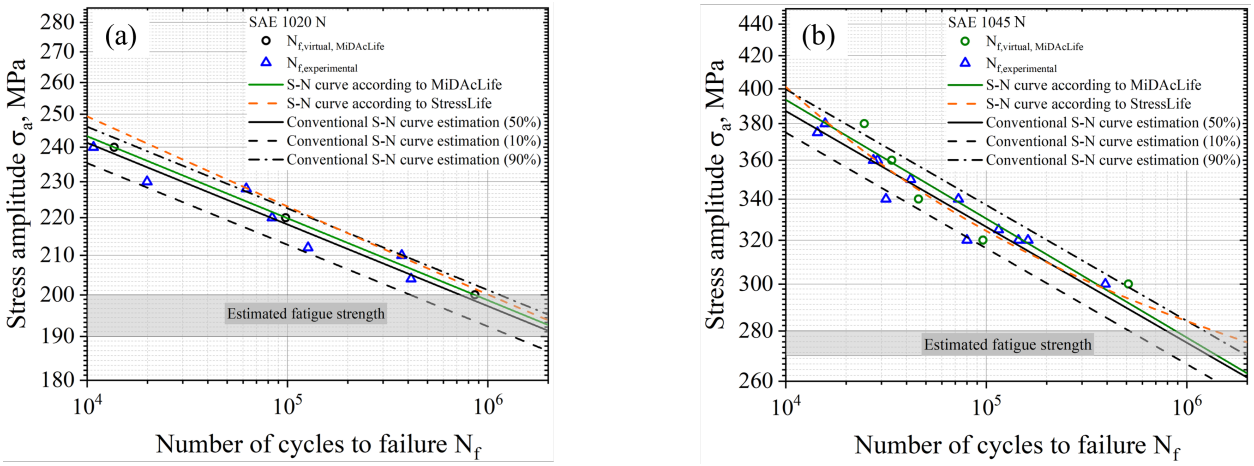

Figure 4.3: Investigations regarding the influence of carbon content on the fatigue behaviour based on accelerated determined S-N curves according to MiDAcLife and StressLife in comparison to conventionally determined S-N curves including different failure probabilities of 10, 50 and 90 % (a) SAE 1020 N steel (b) SAE 1045 N steel

While the global lifetime analysis according to StressLife in figure 4.3 is particularly adequate in estimating data points of the SAE 1045 N steel, MiDAcLife exhibits a very high level of agreement regarding the conventionally determined 50 % S-N curve. Applying the allometric approach to the conventional curve of the SAE 1020 N steel, results in a slope of b = 0.044, which exactly corresponds to the slope according to MiDAcLife. Although there is a slight difference in the slope

of the SAE 1045 N steel with b = 0.074 according to the conventional method and 0.076 according to MiDAcLife, the deviation becomes nearly negligible with 2.7 %.

Table 4.2: Summary of the parameters concerning the lifetime prediction methods MiDAcLife and StressLife in comparison to conventional methods regarding the normalised SAE 1020 and SAE 1045 steels

Method	Material	Parameters					
Conventional	SAE 1020 N	a [MPa]				k [-]	
		58.43				-22.84	
	SAE 1045 N	a [MPa]				k [-]	
		38.93				-13.49	
MiDAcLife	SAE 1020 N	σ_f' [MPa]				b [-]	
		364.75				-0.044	
	SAE 1045 N	σ_f' [MPa]				b [-]	
		793.02				-0.076	
StressLife	SAE 1020 N	K' [MPa · K^{-1}]	B [K]	C [K]	b [-]	c [-]	n' [-]
		176.7	1.115	5190	-0.099	-0.503	0.098
	SAE 1045 N	K' [MPa · K^{-1}]	B [K]	C [K]	b [-]	c [-]	n' [-]
		213.5	6.926	758.0	-0.086	-0.570	0.365

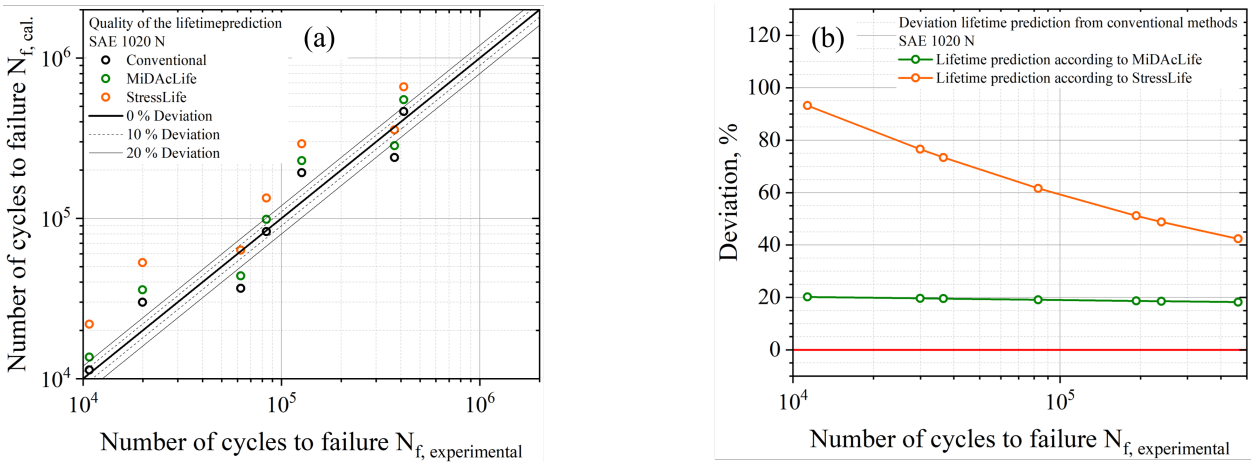

Figure 4.4: Investigations regarding the quality of the lifetime prediction methods MiDAcLife and StressLife considering the influence of carbon content on the fatigue behaviour in comparison to conventionally determined S-N curves including different failure probabilities of 10, 50 and 90 % (a) Comparison between the experimental numbers of cycles to failure and calculated numbers of cycles to failure (b) Deviation of MiDAcLife and StressLife from conventionally generated S-N curve of a SAE 1020 N steel

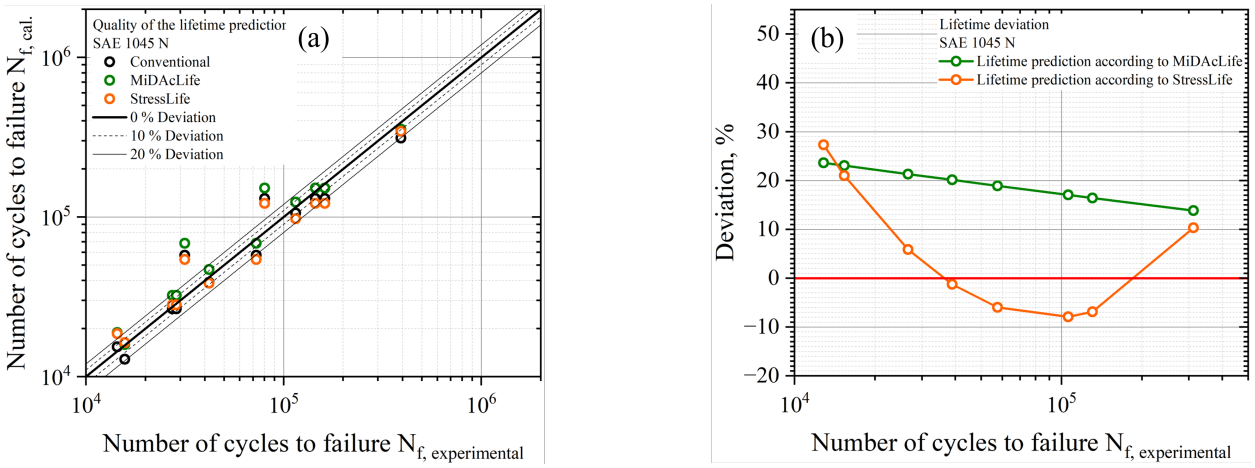

Figure 4.5: Investigations regarding the quality of the lifetime prediction methods MiDAcLife and StressLife considering the influence of carbon content on the fatigue behaviour in comparison to conventionally determined S-N curves including different failure probabilities of 10, 50 and 90 % (a) Comparison between the experimental numbers of cycles to failure and calculated numbers of cycles to failure (b) Deviation of MiDAcLife and StressLife from conventionally generated S-N curve of a SAE 1045 N steel

Based on previous analyses, it can be stated that MiDAcLife can be used regardless of carbon content. StressLife also enables a reasonable lifetime prediction, but with greater deviations in case of the two different materials. To determine the quality of the respective methods in a more efficient way, figures 4.4 and 4.5 contain a comparison of the experimental and the calculated numbers of cycles to failure. Apart from that, the results of the accelerated lifetime prediction are compared to conventionally generated S-N curves. By relating the calculated results to the experimental data points in figure 4.4(a), it can be concluded that both the virtual numbers of cycles according to MiDAcLife and the conventionally determined numbers of cycles to failure are arranged around the bisector and therefore precisely reflect fatigue behaviour of the SAE 1020 N. Additionally, figure 4.4(a) reveals that StressLife tends to an overestimation of fatigue lifetime, particularly in the region of lower cycle numbers. This increased deviation is illustrated in figure 4.4(b). While StressLife approaches conventional data points as the number of cycles increases, the deviation of MiDAcLife for the considered specimen remains almost constant at 20 %. This deviation can be interpreted as an offset, which results from the specimen reduction to only one specimen. Some values of the deviations, especially in terms of the StressLife evaluation, appear very high at first. However, the scattering of the material on respective load levels must urgently be taken into account at this point, as LPMs are only capable of calculating one data point on a load level. The so-called range of scatter T_N, which is determined using equation 4.1, is frequently used to characterise the scatter of the material [22].

$$T_N = \frac{N_{P90\%}}{N_{P10\%}} \tag{4.1}$$

According to equation 4.1, the range of scatter can be derived from the ratio of cycles regarding a failure probability of 90 % ($N_{P90\%}$) and 10 % ($N_{P10\%}$), respectively. This results in a range of scatter

of $T_N = 2.39$ in terms of the SAE 1045 N, corresponding to a deviation of approximately $\pm 69.5\,\%$ and $T_N = 2.79$ ($\pm 89.9\,\%$) for the SAE 1020 N. Taking these values into account, only the first data point of the StressLife evaluation is located outside the scatter of the material. Apart from that, the precision of the lifetime prediction according to MiDAcLife becomes more apparent considering a deviation of 20 % compared to conventional values despite a material scatter of $\pm 89.9\,\%$.

The quality assessment for fatigue evaluation concerning the SAE 1045 N is displayed in figure 4.5. The comparison of experimental and calculated data points from figure 4.5(a) suggests a more reduced deviation between the LPMs and the conventional S-N curve than in case of the SAE 1020 N. This assumption is confirmed by figure 4.5(b). The results of the MiDAcLife evaluation are characterised by a reliably low deviation from the conventional data regardless of the changed carbon content. Besides that, the prediction quality of StressLife is greatly improved compared to the results of the SAE 1020 N.
A final summary of important parameters and the accuracy of the LPMs is given in table 4.3. Within this table, the range of scatter is displayed by T_N and the fatigue strength by σ_e. The fatigue strength coefficient and exponent are indexed with σ'_f and b. As each value is assigned to a certain deviation in comparison to conventional calculations, the deviation is defined as the variable δ_i. From previous insights, it can be assumed that MiDAcLife particularly leads to comparable values in relation to conventional evaluations. Despite the increased deviations in terms of StressLife compared to MiDAcLife, mainly in the region of lower cycle numbers, the calculated numbers of cylces to failure are mostly within the range of scatter of the materials. The applicability of both NDT-related methods could therefore be demonstrated regarding different carbon contents.

Table 4.3: Comparison of the parameters concerning the lifetime prediction methods MiDAcLife and StressLife with conventional methods regarding the normalised SAE 1020 and SAE 1045 steels

SAE 1020 N							
Method	T_N [%]	σ_e [MPa]	δ_{σ_e} [%]	σ'_f [MPa]	$\delta_{\sigma'_f}$ [%]	b [-]	δ_b [%]
Conventional		191.3		361.1		-0.044	
MiDAcLife	±89.9	192.7	0.732	364.7	0.997	-0.044	0.457
StressLife		193.8	1.306	384.5	6.480	-0.047	6.818
SAE 1045 N							
Method	T_N [%]	σ_e [MPa]	δ_{σ_e} [%]	σ'_f [MPa]	$\delta_{\sigma'_f}$ [%]	b [-]	δ_b [%]
Conventional		261.4		765.9		-0.074	
MiDAcLife	±69.5	263.0	0.612	793.0	3.538	-0.076	2.703
StressLife		275.4	5.356	771.2	0.692	-0.072	2.703

4.1.2 Influence of Alloying Elements

For many applications, the properties of materials that can be adjusted by changing the carbon content are not sufficient. Especially with regard to improved mechanical properties or resistance to corrosion, other alloying elements are frequently used in addition to carbon. Apart from that, the use of defined alloying elements also has an influence on the machining process, since chip formation

is significantly affected by these elements. An increased proportion of alloying elements generally leads to increased strength values. One reason for this is the lattice distortion by differences in the atomic radii compared to iron atoms. These lattice distortions lead to a greater restriction of dislocation movement and therefore, higher stress amplitudes are required to induce damage into the material. Another reason for the increase in the material strength is the formation of precipitates, for example in terms of carbides, as it becomes apparent in the example of the reference material 20MnMoNi5-5 (described in chapter 3.1).
The materials 20MnMoNi5-5 and SAE 1020 QT[3] steel are used in the following section to analyse the influence of alloying elements on the testing methods CAT and LIT, as well as the LPMs MiDAcLife and StressLife. By choosing these steels, the previously evaluated influence of carbon content can be neglected, which means that the focus is on the remaining alloying elements. Since the heat treatment of the 20MnMoNi5-5 steel is strictly regulated by the KTA (Kerntechnischer Ausschuss), where the steel is subjected to a quenched and tempering-process, data from a quenched and tempered SAE 1020 steel is used. To ensure differentiation from the previously investigated SAE 1020 N steel, the quenched and tempered steel is labelled with the suffix "QT". As a result of the heat treatment of the material, increased strength values can be expected, which, however, also lead to a more brittle behaviour considering dynamic loading. A more detailed discussion on the influence of heat treatment will follow in a later section of this chapter. Analogue to figure 4.2, figure 4.6 displays the cyclic deformation curves of both testing materials regarding LITs, as well as CATs.

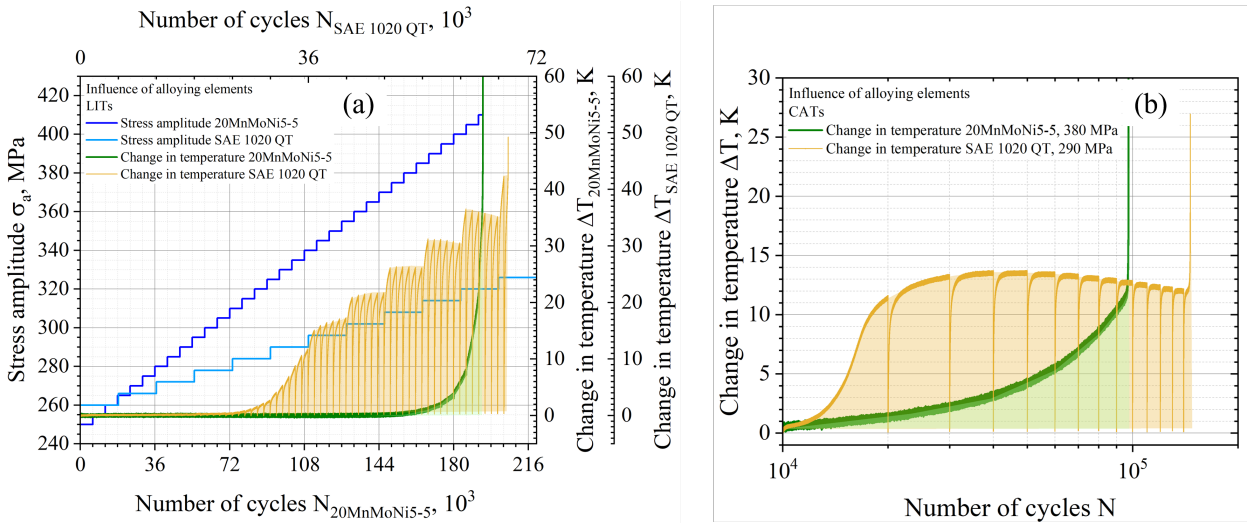

Figure 4.6: Investigations regarding the influence of alloying elements on the fatigue behaviour based on cyclic deformation curves (a) Load increase test with $f = 5$ Hz, $\sigma_{a,start} = 250/260$ MPa, $\Delta\sigma_a = 5/6$ MPa and Δ N = 6000 (b) Constant amplitude tests with $f = 5$ Hz and $\sigma_a = 380/290$ MPa regarding the 20MnMoNi5-5 and SAE 1020 QT steels

[3]Experimental results
Project: STA 1133/10
University: University of Applied Sciences Kaiserslautern
Institude: Department of Materials Science & Materials Testing (WWHK)
Project manager: M. Sc. Haoran Wu

A striking difference between figure 4.2(a) and 4.6(a) is the different curve progression of the stress amplitude. While an increase in the stress amplitude of 20 MPa is selected for both unalloyed steels in figure 4.2(a), figure 4.6(a) contains different values for the load increase. Furthermore, the LITs do not start at the same initial starting stress amplitude. Both can be attributed to the fact that a more brittle material behaviour with higher strength values can be expected as a result of alloying elements. A load increase of 20 MPa would lead to a demonstrably low number of data points within the plastic range considering a more brittle behaviour, as it is to be expected in case of the 20MnMoNi5-5 steel. As a result of this reduction of data points, an evaluation according to the LPMs becomes significantly more difficult or even impossible. However, a starting stress amplitude of 100 MPa with a decreased load step results in very high numbers of cycles. On the one hand, this leads to longer test durations, but also to an accumulation of damage, which is not representative for real material behaviour.
The increased strength and as a result the increased brittleness of the 20MnMoNi5-5 steel compared to the SAE 1020 QT steel can be inferred from the change in temperature curves of figure 4.6(a). The cyclic deformation curve of the 20MnMoNi5-5 steel, displayed as a green line, shows no significant material response over a large period of the specimens lifetime. A distinct increase of material response can only be observed shortly before specimen failure. Because of this, only cyclic softening processes within the material can be monitored, while the noticeably more ductile SAE 1020 QT steel exhibits slight hardening processes. Besides that, the intensity of the material response differs significantly. While the SAE 1020 QT steel shows a temperature difference of 8.37 K after half of the number of cycles to failure, the 20MnMoNi5-5 steel is characterised by an increase of 0.05 K, which is completely obscured by the measurement signal due to the thermoelastic effect. This results in a percentage value of 16.94 % for the unalloyed steel in relation to the total material response, whereas no reaction can be observed in terms of the low-alloyed 20MnMoNi5-5 steel. The scaling factor introduced in chapter 4.1.1 is even more distinctive with a value of 3.277. As a result of the microstructure and chemical composition, dislocation movement is already enabled at evidently lower stress amplitudes regarding the SAE 1020 QT steel. The first material response can be detected at a stress amplitude of approximately 278 MPa. In comparison, the fatigue strength of the 20MnMoNi5-5 steel is estimated to 370 MPa. The most important outcomes of the data given in figure 4.6(a) are summarised in table 4.4.

Table 4.4: Summary of the load increase test results to quantify the influence of alloying elements regarding the 20MnMoNi5-5 and SAE 1020 QT steels

Material	Stress amplitude failure [MPa]	Fatigue strength [MPa]	Scaling factor
SAE 1020 QT	326	278	3.277
20MnMoNi5-5	410	370	

A comparison of the material response progression considering dynamic loading with a constant stress amplitude in case of the CATs provides similar results. Figure 4.6(b) compares CATs with numbers of cycles to failure that are alike. A stress amplitude of 380 MPa is therefore selected for the 20MnMoNi5-5 steel, whereas the SAE 1020 QT steel is tested with a stress amplitude of 290 MPa. With an absolute value for the material response of 12.91 K after half of the number of cycles to failure, the change in temperature of the SAE 1020 QT steel is higher with a factor of

3.316 compared to the 20MnMoNi5-5 steel ($\Delta T_{20MnMoNi5-5} = 3.89$ K). An integral consideration as described in chapter 4.1.1, provides a scaling factor of 3.553, which is in close agreement with the data from the LIT of figure 4.6(a). The slight increase in this value of the scaling factor can be attributed to the difference in the number of cycles to failure of the individual CATs of approximately 50,000 cycles.
The theoretical approaches presented with regard to the influence of alloying elements, as well as the experimental test results illustrated in figure 4.6 are used in the following section to investigate fatigue properties with regard to lifetime prediction. Figure 4.7 provides conventionally determined S-N curves including different failure probabilities, as well as the S-N curves generated according to MiDAcLife and StressLife.

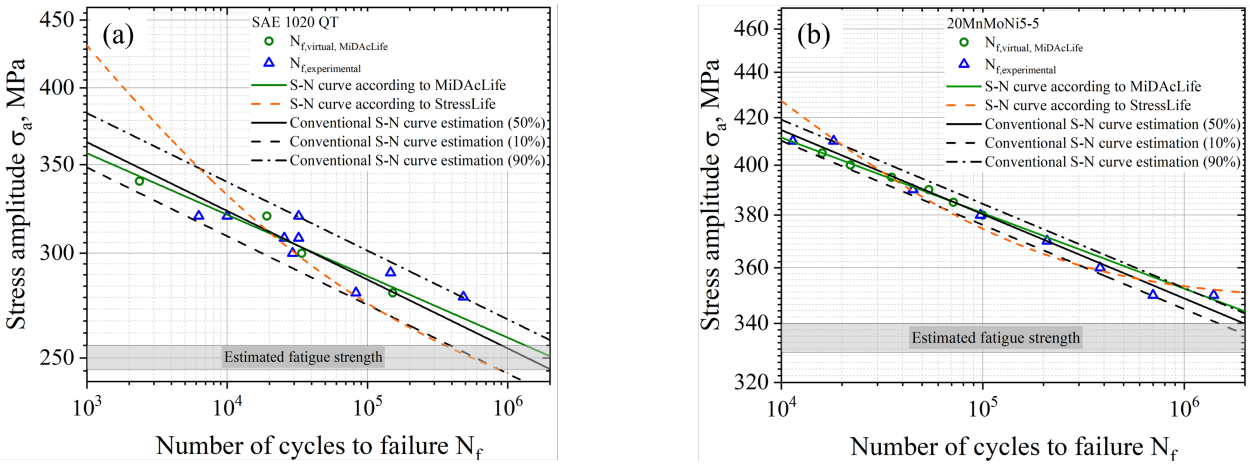

Figure 4.7: Investigations regarding the influence of alloying elements on the fatigue behaviour based on accelerated determined S-N curves according to MiDAcLife and StressLife in comparison to conventionally determined S-N curves including different failure probabilities of 10, 50 and 90 % (a) 20MnMoNi5-5 steel (b) SAE 1020 QT steel

Similar to the evaluation of the carbon content influence, figure 4.7 is characterised by a precise agreement between MiDAcLife and the conventional S-N curves. Analysing the SAE 1020 QT steel, an increased deviation is detectable for the StressLife evaluation, especially in the range of very low and high numbers of cycles to failure. This can be explained by the demonstrably higher scattering of the material compared to the normalised condition. As the global lifetime prediction according to StressLife consists of a combination of LITs and CATs, it is more error-prone than the local consideration according to MiDAcLife. The results of calculation presented in figure 4.7(a) and (b) indicate a fatigue strength of approximately 255 MPa in terms of the SAE 1020 QT steel, whereas the 20MnMoNi5-5 steel is characterised by an increased fatigue strength of approximately 340 MPa. A comparison with table 4.4 shows that the fatigue strength values for both materials are slightly overestimated within the LIT. This can be attributed to the progression of the material response. The more brittle material behaviour due to alloying elements (and heat treatment) leads to a reduced output of the material response as a result of dynamic loading. This makes early monitoring of the first response more difficult and can lead to minor deviations. However, with a deviation of approximately 9 % regarding the SAE 1020 QT steel and 8 % regarding the 20MnMoNi5-5 steel, these are moderate deviation values, which can nevertheless be used for an

accelerated estimation of the fatigue strength. All parameters of the LPMs shown in figure 4.7 are given in table 4.5.

Table 4.5: Summary of the parameters concerning the lifetime prediction methods MiDAcLife and StressLife in comparison to conventional methods regarding the 20MnMoNi5-5 and SAE 1020 QT steels

Method	Material	Parameters					
Conventional	SAE 1020 QT	a [MPa]				k [-]	
		52.32				-19.26	
	20MnMoNi5-5	a [MPa]				k [-]	
		73.75				-26.64	
MiDAcLife	SAE 1020 QT	σ'_f [MPa]				b [-]	
		491.9				-0.046	
	20MnMoNi5-5	σ'_f [MPa]				b [-]	
		561.2				-0.034	
StressLife	SAE 1020 QT	K' [MPa · K^{-1}]	B [K]	C [K]	b [-]	c [-]	n' [-]
		159.3	58.36	20,536	-0.146	-0.689	0.205
	20MnMoNi5-5	K' [MPa · K^{-1}]	B [K]	C [K]	b [-]	c [-]	n' [-]
		352.3	1.149	79,993	-0.018	-0.909	0.081

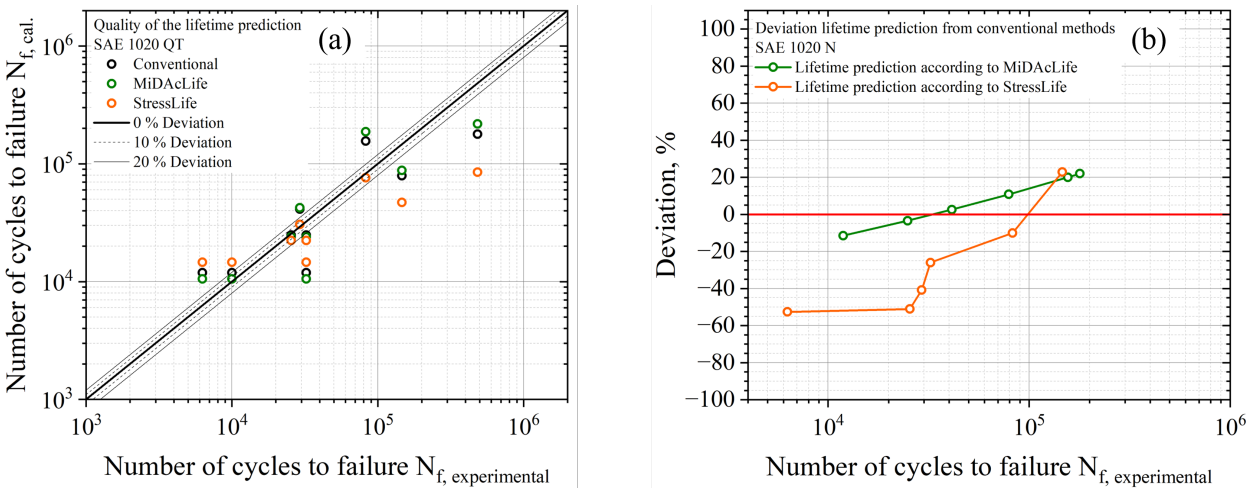

Figure 4.8: Investigations regarding the quality of the lifetime prediction methods MiDAcLife and StressLife considering the influence of alloying elements on the fatigue behaviour in comparison to conventionally determined S-N curves including different failure probabilities of 10, 50 and 90 % (a) Comparison between the experimental numbers of cycles to failure and calculated numbers of cycles to failure (b) Deviation of MiDAcLife and StressLife from conventionally generated S-N curve of an SAE 1020 QT steel

The increased strength of the 20MnMoNi5-5 steel compared to the unalloyed SAE 1020 QT carbon steel can be derived very well from the position parameters of the individual methods. The position of the S-N curve is defined by the parameter a concerning conventional evaluations, σ'_f in terms of the evaluation according to MiDAcLife and K' according to the StressLife method. All of these parameters exhibit greater values for the low alloyed steel than for the unalloyed steel. In order to be able to examine the influence of alloying elements on the accelerated lifetime prediction, the calculated numbers of cycles to failure are again compared with the experimental data in figures 4.8 and 4.9. The quality assessment of StressLife in terms of the SAE 1020 QT steel in figure 4.8 provides the insight that the experimental data points can be described with a high degree of precision in the range of $10^4 - 10^5$ cycles. In the transition area to the LCF regime and for cycle numbers greater than 10^5, the deviation increases rapidly. This is a consequence of an excessively high slope of the generated S-N curve, which can also be seen in figure 4.7(a). If the plastic portion is considered too intensely, the lifetime of the specimens at low stress amplitudes is underestimated, whereas at higher load amplitudes, it is overestimated. In contrast, the virtual numbers of cycles to failure according to MiDAcLife are characterised by very low deviation values in the range of 0 % - 20 % compared to the conventional S-N curve. At this point, it must be emphasised that an increase in the deviation of figure 4.8(b) is not equal to a poor quality of the lifetime prediction. While MiDAcLife shows an average deviation of 48.6 % regarding the experimental numbers of cycles to failure, the conventional method deviates from these data points by 48.4 %. Especially data points at lower stress amplitudes can be estimated with a higher prediction quality by MiDAcLife.

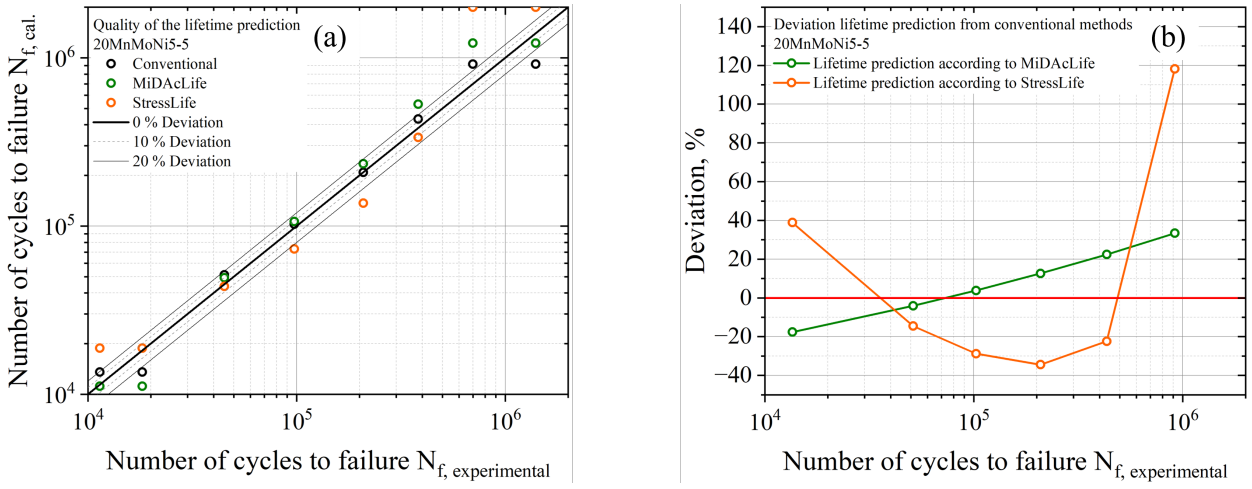

Figure 4.9: Investigations regarding the quality of the lifetime prediction methods MiDAcLife and StressLife considering the influence of alloying elements on the fatigue behaviour in comparison to conventionally determined S-N curves including different failure probabilities of 10, 50 and 90 % (a) Comparison between the experimental numbers of cycles to failure and calculated numbers of cycles to failure (b) Deviation of MiDAcLife and StressLife from conventionally generated S-N curve of a 20MnMoNi5-5 steel

An almost identical behaviour is given in figure 4.9 for the reference material 20MnMoNi5-5. Even if an increase in deviation compared to conventional data points can be detected as the number of cycles increases, the experimental data points in the range of high cycle numbers can be represented

in a more accurate way by MiDAcLife. Therefore, the high potential of this method can be derived from these results. Apart from that, figure 4.9(b) displays high deviation values for StressLife in the range of higher numbers of cycles to failure. Considering both elastic and plastic portions, a double-logarithmic plot for StressLife does not result in a linear relation. As a consequence, the curve runs into a plateau, which corresponds to the natural behaviour of the material. The fact that the S-N curve tails off in the direction of the fatigue strength, is one of the advantages of StressLife compared to purely elastic approaches.

In summary, the influence of alloying elements on fatigue behaviour of metallic materials can be demonstrated in various ways. By using NDT-related methods (in this case, thermography), the influence can already be shown in cyclic deformation curves of the materials SAE 1020 QT and 20MnMoNi5-5. A rather brittle material behaviour leads to pure cyclic softening processes within the volume of the material and reduces the material response. As a result of the reduced material response and thus the superimposition with the scattering of the measurement devices, the estimation of fatigue strength resulting from LITs is more challenging. However, deviations of less than 10 % are still acceptable for a first accelerated estimation. When it comes to lifetime prediction, the results of MiDAcLife agree with the results of conventional calculations regarding a low-alloyed steel. Particularly in the range of low stress amplitudes, experimental data points can be estimated with improved accuracy in some cases. Despite higher deviation of the results according to StressLife, the determined data points are within the range of scatter of the materials and the natural behaviour at the transition to the VHCF regime can be demonstrated in a representative way. All important findings are summarised in table 4.6.

Table 4.6: Comparison of the parameters concerning the lifetime prediction methods MiDAcLife and StressLife with conventional methods regarding the 20MnMoNi5-5 and SAE 1020 QT steels

SAE 1020 QT							
Method	T_N [%]	σ_e [MPa]	δ_{σ_e} [%]	σ'_f [MPa]	$\delta_{\sigma'_f}$ [%]	b [-]	δ_b [%]
Conventional		245.3		520.9		-0.052	
MiDAcLife	±264.7	250.8	2.242	450.0	13.61	-0.046	11.54
StressLife		236.7	3.506	569.3	9.291	-0.062	19.23
20MnMoNi5-5							
Method	T_N [%]	σ_e [MPa]	δ_{σ_e} [%]	σ'_f [MPa]	$\delta_{\sigma'_f}$ [%]	b [-]	δ_b [%]
Conventional		339.9		585.9		-0.037	
MiDAcLife	±39.61	344.2	1.265	561.2	4.216	-0.034	8.108
StressLife		350.9	3.236	535.8	8.551	-0.030	18.92

4.1.3 Influence of the Heat Treatment

Apart from chemical composition, the heat treatment of metallic materials is a distinctive factor in achieving desired properties. This process utilises a property of iron, known as allotropy. Depending on temperature, iron changes its lattice structure from body-centered cubic (bcc) to face-centered cubic (fcc) and vice versa. Therefore, the solubility of dissolved atoms changes due to the fact

that the octahedral gaps in bcc are smaller than in the fcc lattice. As a consequence of the lower solubility, the dissolved atoms precipitate in terms of an additional phase during cooling phase. However, this requires diffusion processes. Rapid quenching of the specimen from the austenite region prevents atoms from diffusing and therefore results in a forced solute state. The excess of dissolved atoms lead to a pronounced distortion of the lattice. Even if this state is characterised by extremely high hardness and strength values, the significantly reduced toughness is not sufficient for many applications. For this reason, the material is tempered at defined temperatures to enable a controlled diffusion movement and consequently ensure an optimum compromise between high strength and sufficient toughness of the material.
Since the heat treatment of the reference material 20MnMoNi5-5 is standardised by the KTA and therefore only one heat treatment condition is available within the scope of this research, the influence of heat treatment is investigated using an SAE 5120 steel[4]. As a result of the carbon content and alloying elements, both steels are comparable to a good approximation. The evaluation regarding CATs and LITs, as well as the assessment of the LPMs, is based on both previous chapters 4.1.1 and 4.1.2.

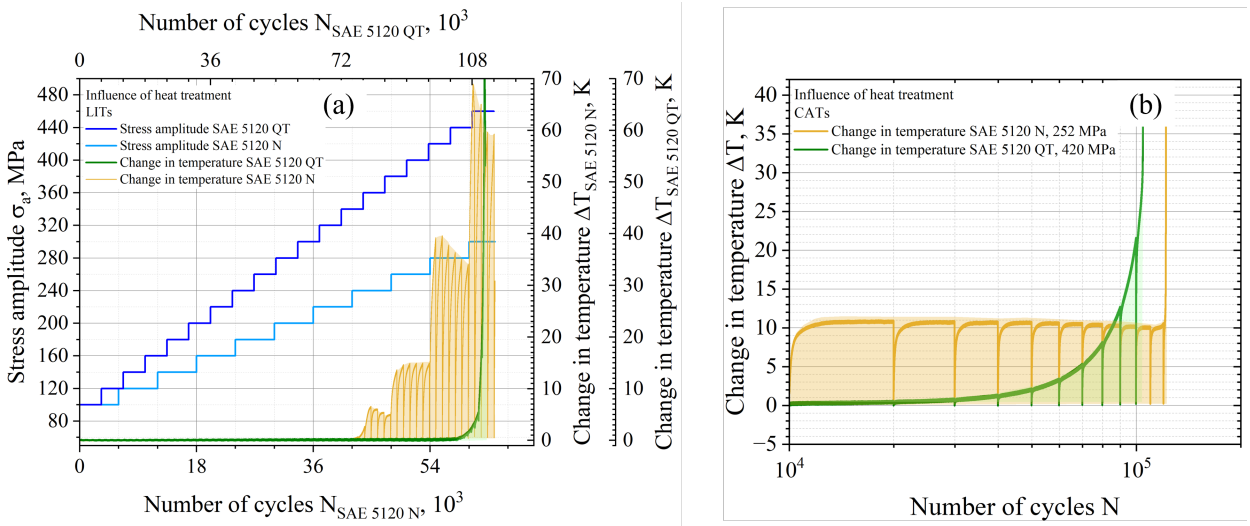

Figure 4.10: Investigations regarding the influence of heat treatment on the fatigue behaviour based on cyclic deformation curves (a) Load increase test with f = 5 Hz, $\sigma_{a,start}$ = 100 MPa, $\Delta\sigma_a$ = 20 MPa and Δ N = 9000/6000 (b) Constant amplitude tests with f = 5 Hz and σ_a = 252/420 MPa regarding the SAE 5120 N and SAE 5120 QT steels

Figure 4.10 illustrates the cyclic deformation curves of the SAE 5120 steel for LITs, as well as CATs. To investigate the influence of the heat treatment, a normalised and a quenched-tempered condition of the material is considered at this point. As a consequence of the quenching process, the dislocation movement within the SAE 5120 QT steel is significantly more limited than in case

[4]Experimental results
Project: STA 1133/10
University: University of Applied Sciences Kaiserslautern
Institude: Department of Materials Science & Materials Testing (WWHK)
Project manager: M. Sc. Haoran Wu

of the SAE 5120 N steel. Based on the progression of the change in temperature, a pure cyclic softening of the quenched and tempered steel can be inferred, whereas the normalised SAE 5120 steel tends to cyclic hardening and softening processes similar to the SAE 1020 steel from previous chapters. A scaling factor of 5.9 concerning the LITs presented in figure 4.10(a) and even 2.2 in terms of CATs shown in figure 4.10(b) confirms the higher intensity of the material response in the normalised condition. An overview of the estimated values for the fatigue strength and the scaling factors is given in table 4.7.

Table 4.7: Summary of the load increase test results to quantify the influence of heat treatment regarding the SAE 5120 N and SAE 5120 QT steels

Material	Stress amplitude failure [MPa]	Fatigue strength [MPa]	Scaling factor
SAE 5120 N	300	220	5.9
SAE 5120 QT	460	420	

Table 4.8: Summary of the parameters concerning the lifetime prediction methods MiDAcLife and StressLife in comparison to conventional methods regarding the SAE 5120 N and SAE 5120 QT steels

Method	Material	Parameters					
Conventional	SAE 5120 N	a [MPa]				k [-]	
		47.20				-17.56	
	SAE 5120 QT	a [MPa]				k [-]	
		80.41				-28.79	
MiDAcLife	SAE 5120 N	σ'_f [MPa]				b [-]	
		479.2				-0.055	
	SAE 5120 QT	σ'_f [MPa]				b [-]	
		635.8				-0.036	
StressLife	SAE 5120 N	K' [MPa · K^{-1}]	B [K]	C [K]	b [-]	c [-]	n' [-]
		208.0	7.194	31,548	-0.065	-0.673	0.082
	SAE 5120 QT	K' [MPa · K^{-1}]	B [K]	C [K]	b [-]	c [-]	n' [-]
		383.8	2.661	27,276	-0.030	-0.851	0.076

S-N curves for both material conditions are provided in figure 4.11. The significant increase in fatigue strength by a factor of approximately 1.8 from 220 MPa to 390 MPa in terms of the quenched and tempered condition is remarkable at this point. For the evaluation according to MiDAcLife, an almost identical progression of the S-N curve compared to the conventional curve can be confirmed. Only small differences within the slope of the S-N curves lead to the deviations shown in figure 4.12. Within these results, StressLife provides more precise values in the normalised condition than in the quenched-tempered condition. As in the previous chapter, the high deviation in the range of higher numbers of cycles to failure results from the progression of StressLife into a plateau. However, both figures 4.12 and 4.13 demonstrate the high prediction quality of MiDAcLife and

StressLife considering the influence of different heat treatment conditions. Table 4.9 summarises the parameters of each evaluation and their deviation from conventional data.

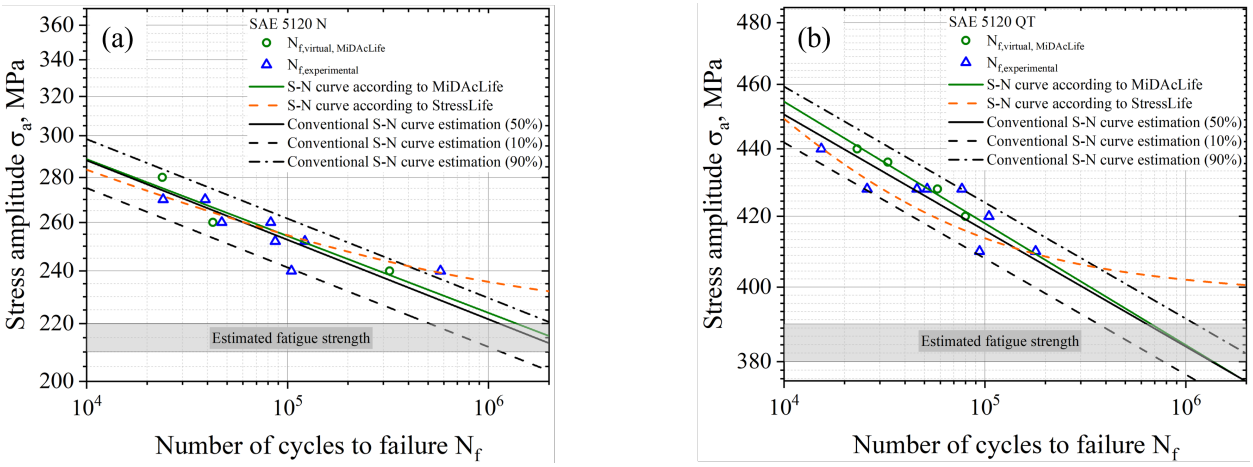

Figure 4.11: Investigations regarding the influence of heat treatment on the fatigue behaviour based on accelerated determined S-N curves according to MiDAcLife and StressLife in comparison to conventionally determined S-N curves including different failure probabilities of 10, 50 and 90 % (a) SAE 5120 N (b) SAE 5120 QT

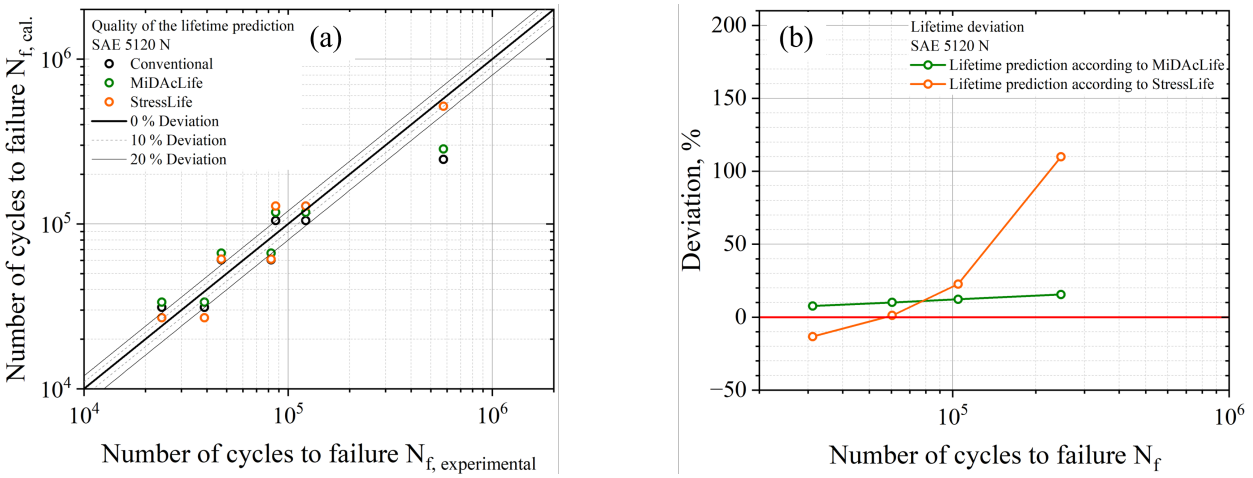

Figure 4.12: Investigations regarding the quality of the lifetime prediction methods MiDAcLife and StressLife considering the influence of heat treatment on the fatigue behaviour in comparison to conventionally determined S-N curves including different failure probabilities of 10, 50 and 90 % (a) Comparison between the experimental numbers of cycles to failure and calculated numbers of cycles to failure (b) Deviation of MiDAcLife and StressLife from conventionally generated S-N curve of a SAE 5120 N steel

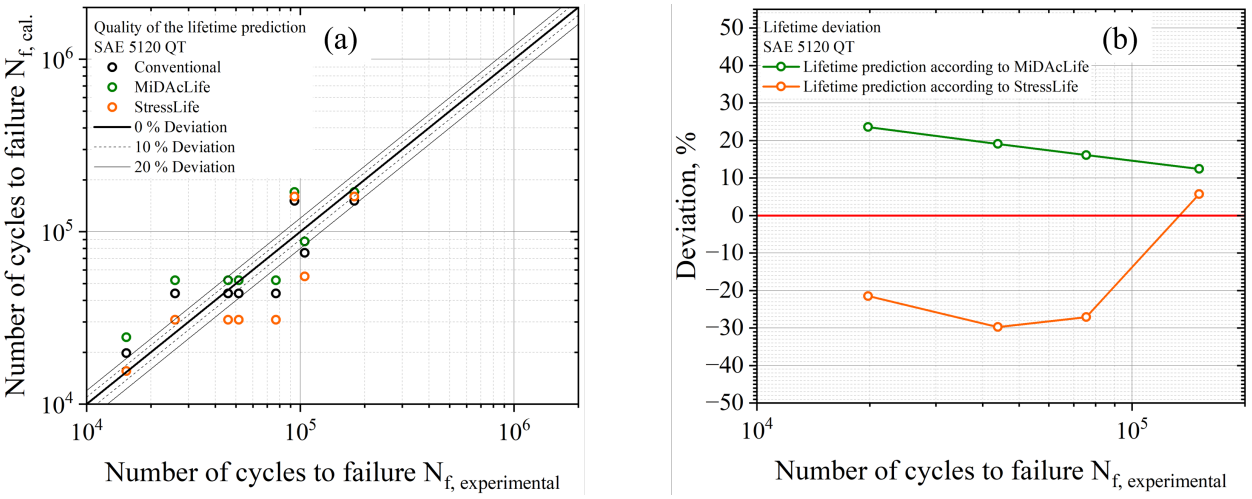

Figure 4.13: Investigations regarding the quality of the lifetime prediction methods MiDAcLife and StressLife considering the influence of heat treatment on the fatigue behaviour in comparison to conventionally determined S-N curves including different failure probabilities of 10, 50 and 90 % (a) Comparison between the experimental numbers of cycles to failure and calculated numbers of cycles to failure (b) Deviation of MiDAcLife and StressLife from conventionally generated S-N curve of a SAE 5120 QT steel

Table 4.9: Comparison of the parameters concerning the lifetime prediction methods MiDAcLife and StressLife with conventional methods regarding the SAE 5120 N and SAE 5120 QT steels

SAE 5120 N							
Method	T_N [%]	σ_e [MPa]	δ_{σ_e} [%]	σ'_f [MPa]	$\delta_{\sigma'_f}$ [%]	b [-]	δ_b [%]
Conventional		213.0		486.6		-0.057	
MiDAcLife	±151.7	215.6	1.221	479.2	1.521	-0.055	3.509
StressLife		232.1	8.268	381.8	21.54	-0.035	38.59
SAE 5120 QT							
Method	T_N [%]	σ_e [MPa]	δ_{σ_e} [%]	σ'_f [MPa]	$\delta_{\sigma'_f}$ [%]	b [-]	δ_b [%]
Conventional		374.8		620.4		-0.035	
MiDAcLife	±99.89	374.7	0.027	635.8	2.482	-0.037	5.714
StressLife		400.6	6.884	504.6	18.67	-0.016	54.29

Concluding the discussed derivations and insights of this chapter, the independence of the LPMs MiDAcLife and StressLife from microstructural influences can be confirmed. In particular, the local consideration of fatigue behaviour according to MiDAcLife provides results that almost completely correspond to the data of the conventional S-N curve determination. In certain cases, the experimental numbers of cycles to failure can be described even more precisely by MiDAcLife. Smaller deviations are not attributable to the method itself, but to the scattering of the material. These deviations might be remedied by a moderate increase of the number of experiments. Considering

the reduction of experimental effort by more than 90 % in certain cases, MiDAcLife is characterised by a high level of prediction quality. Due to the combination of NDT-signals from several tests and test methods, StressLife is significantly more error-prone than MiDAcLife. However, the global assessment of fatigue behaviour is also of great importance, as the progression of the S-N curve, especially in the transition to the VHCF regime, is closer to the expected material behaviour.

4.2 Influence of Surface Condition on Fatigue Behaviour

After the microstructural influence on fatigue behaviour and the effect on the LPMs MiDAcLife and StressLife have been investigated in detail in chapter 4.1, this chapter aims to explore the influence of increased surface roughness on fatigue behaviour of the 20MnMoNi5-5 steel. Journal Contribution 3 and 4, presented in part II of this thesis already provide an initial approach of how to integrate surface roughness parameters into the LPM MiDAcLife. A review of the applicability of StressLife regarding different surface conditions is still to be carried out. An additional objective of this chapter is to enable comparability with results of already existing, frequently used methods. The focus here is on a comparison with the FKM-guideline and the approach according to Murakami, which are both described in chapter 2.2.1. Analogue to the previous chapter, the lifetime prediction quality is evaluated in relation to the conventional S-N curve generation. At first, the respective CATs and LITs of different surface topographies are analysed, followed by a section that deals with the lifetime prediction under increased surface roughness.
In general, crack initiation and propagation starting from the specimen surface is the dominant failure mechanism in terms of cyclic loading within the HCF regime. At this point, it must be noted that this mainly applies for more homogeneous microstructures. If a material exhibits an inhomogeneous structure, as it is the case with for example cast materials, other damage mechanisms take place. Further information regarding cast materials are given in chapter 4.5.
Within the scope of this research, investigations are carried out on five different surface qualities, which are categorised into the groups N3, N5 and N7-N9. The reference surface is given by batch N3, which is characterised by the lowest surface roughness with $R_a = 0.1$ µm. The results of the cyclic deformation curves concerning CATs regarding batch N3 are given in figure 4.14.

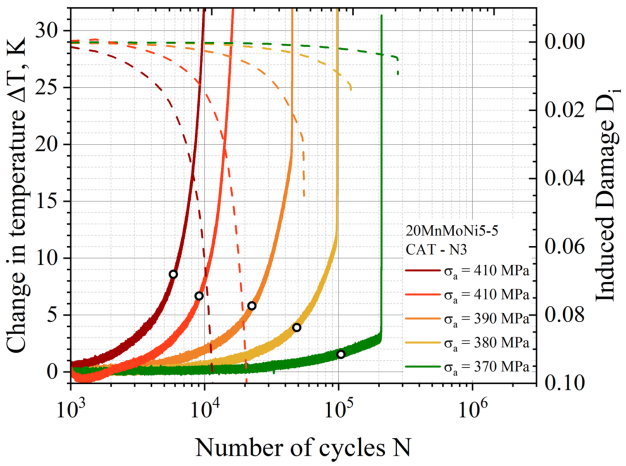

Figure 4.14: Investigations regarding the influence of surface condition on the fatigue behaviour based on cyclic deformation curves of constant amplitude tests concerning the surface batch N3 of a 20MnMoNi5-5 steel

In addition to the material response, the induced damage D_i is plotted as a function of the numbers of cycles in figure 4.14. For all CATs, the change in temperature purely rises with increasing numbers of cycles. Therefore, a cyclic softening behaviour of the material can be observed. Apart from that, it can be concluded that an increase in the load amplitude leads to an earlier and demonstrably more pronounced material response. While a stress amplitude of 410 MPa results in an increase of the material response starting from approximately 10^3 cycles, an increase regarding 370 MPa loading can only be detected from a number of approximately $2 \cdot 10^4$ cycles. Within figure 4.14, the values of the change in temperature after half of the number of cycles to failure are represented by unfilled circles. This illustrates the increase of the material response as a function of the stress amplitude.
Another way of confirming this relation is to compare the values of the applied partial damage. While the maximum value of the partial damage with regards to the 370 MPa CAT is given by $9 \cdot 10^{-3}$, the material is subjected to a damage of $1.7 \cdot 10^{-1}$ considering a 410 MPa loading. The reason for the given correlation can be found in the mobility of the dislocations. In order for dislocations to move, they must be displaced by an atomic distance. This requires a critical shear stress. As the dynamic loading is situated below the static yield strength, dislocation movement is only possible in favourably oriented grains. With an increased stress amplitude, dislocation movement and dislocation reactions can be initiated in more grains, whereas in terms of lower stress amplitudes, damage results from the accumulation of a high number of cycles.
The cyclic deformation curves of the remaining surface conditions are displayed in figure 4.15 and 4.16. The batches N5 and N7, presented in figure 4.15, are both characterised by a machining process with unworn cutting tools. The difference between the two batches results from a different feed rate and a mechanical polishing process in terms of N5. In contrast, figure 4.16 illustrates batches N8 and N9, which were machined with worn cutting tools and therefore exhibit higher roughness values. A more detailed description of each surface is included in chapter 3.1.3. In order to enable an assessment of the influence of surface roughness on the cyclic deformation curves regarding constant amplitude loading, CATs with identical stress amplitudes are compared with each other. The CAT of batch N3 with a stress amplitude of 380 MPa (shown as yellow curve

in figure 4.14) serves as a reference point. Analogue to previous evaluations, several factors are considered for the determination of roughness influence. Firstly, the material response after half of numbers of cycles to failure is compared for each surface condition. Secondly, the material behaviour is assessed on the basis of the area enclosed by cyclic deformation curves. In addition to that, the respective numbers of cycles to failure are analysed. As the lifetime of the specimens is significantly reduced as a result of the increased surface roughness in terms of N9 specimens, experiments were mostly carried out with lower stress amplitudes. Since there is no experimental result concerning a stress amplitude of 380 MPa, the results of a specimen loaded with 370 MPa are considered.

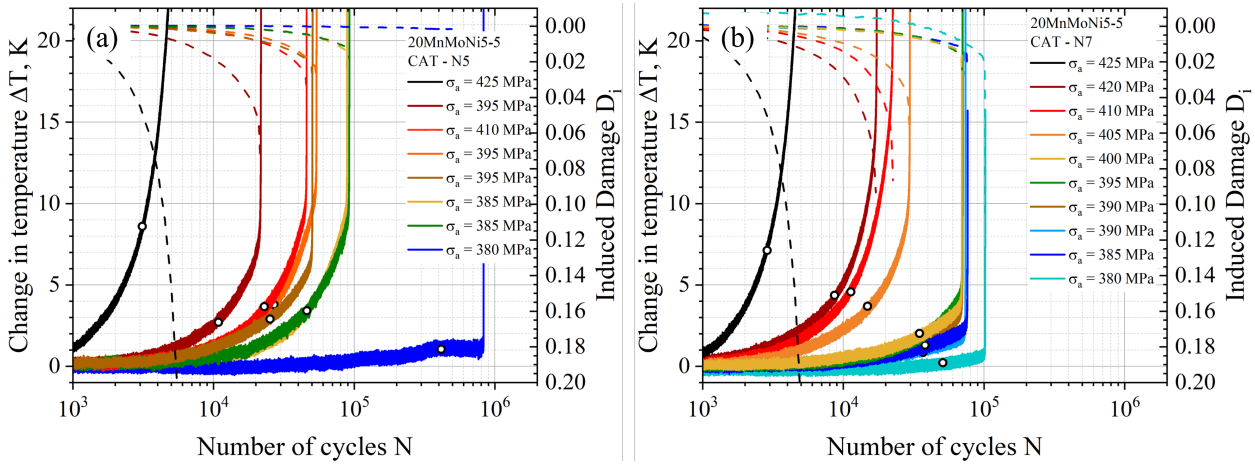

Figure 4.15: Investigations regarding the influence of surface condition on the fatigue behaviour based on cyclic deformation curves of constant amplitude tests concerning (a) surface batch N5 (b) surface batch N7 of a 20MnMoNi5-5 steel

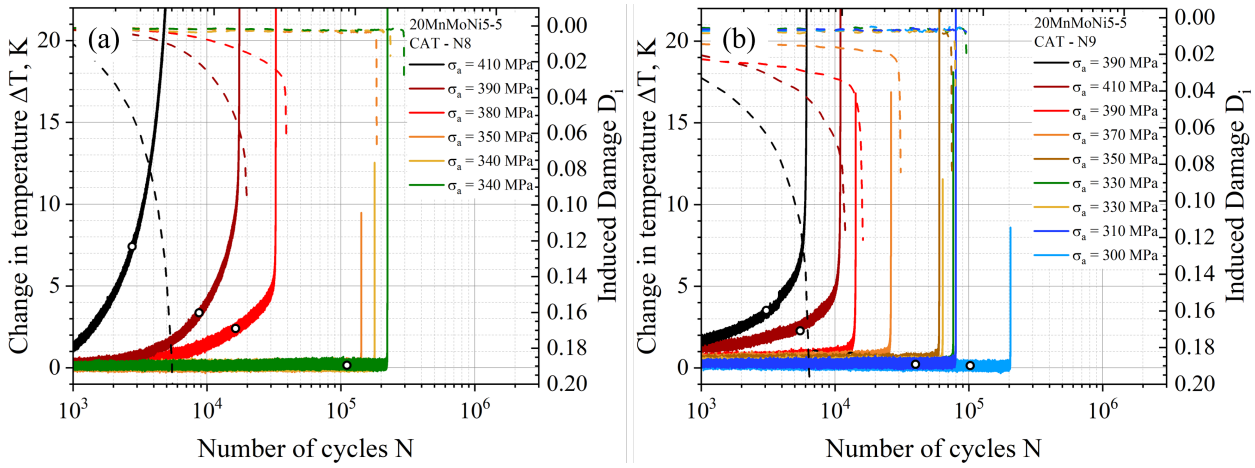

Figure 4.16: Investigations regarding the influence of surface condition on the fatigue behaviour based on cyclic deformation curves of constant amplitude tests concerning (a) surface batch N8 (b) surface batch N9 of a 20MnMoNi5-5 steel

Considering the N3 batch, a loading with 380 MPa leads to a lifetime of 97,356 cycles. The material

response can be characterised either by the absolute value of the change in temperature after half of the number of cycles to failure ($\Delta T = 3.96$ K), or the integral value τ, which represents the area enclosed by the cyclic deformation curve ($\tau = 4.70$). Since the enclosed area does not depend on the material response exclusively, but also on the number of cycles, it must be normalised to the number of cycles to failure. Although batches N3 and N5 exhibit identical turning parameters and have both undergone a polishing process, the CAT of N5 reaches an increased lifetime at 830,634 cycles. The material response is also significantly reduced with a change in temperature of $\Delta T = 1.045$ K and an integral value of $\tau = 0.829$. The difference between both batches can be explained by the manufacturing process of the specimens and the resulting residual stresses. While specimens of surface N3 are grinded before the mechanical polishing, this process step is omitted for specimens of N5. The resulting compressive residual stresses are therefore significantly reduced by a factor of two, which explains the reduced lifetime of N3. An overview of the parameters describing the influence of different surface conditions on CATs is given in table 4.10.

Table 4.10: Comparison of the cyclic deformation curves of the constant amplitude tests concerning different surface conditions with the reference surface batch N3 of a 20MnMoNi5-5 steel

20MnMoNi5-5						
Batch	N_f [-]	δ_{N_f} [%]	$\Delta T(N_f/2)$, [K]	$\delta_{\Delta T}$ [%]	τ [-]	δ_τ [%]
N3	97,356		3.955		4.702	
N5	830,634	753.2	1.045	73.58	0.829	82.37
N7	102,076	4.848	0.195	95.07	0.170	96.38
N8	32,667	66.44	2.395	39.44	2.489	47.06
N9	26,158	73.13	0.650	83.56	0.718	84.73

A consideration of the numbers of cycles to failure from table 4.10 leads to an important finding regarding the influence of surface roughness. Even though the roughness of batch N7 is noticeably increased compared to N3, there is no remarkable difference in the numbers of cycles to failure. As already mentioned, the lifetime extension of the N5 specimen can be explained by compressive residual stresses, since these are greater than the external stress amplitudes. As a result, the effect of surface roughness only seems to become meaningful above a certain threshold value. This observation is highly significant e.g. when it comes to manufacturing of components, as machining parameters can be adjusted to maximise production efficiency without risking a reduction in the fatigue lifetime of the specimen or component. However, the increased roughness regarding the surfaces N8 and N9 causes a serious deterioration in fatigue properties. While the specimen assigned to N8 is characterised by a lifetime reduction of nearly 67 %, even a reduced stress amplitude of 10 MPa in terms of the N9 specimen causes a lifetime reduction of 73.13 %. It can therefore be stated that the influence of surface condition is highly distinctive concerning the surface batches N8 and N9. It should be noted that roughness is assumed to be a static value within the context of this analyses. A dynamic change in surface topography as a result of slip bands is not taken into account. However, neglecting extrusions and intrusions appears to be a permissible simplification since the roughness resulting from machining process is extremely high compared to surface protrusion. A comparison of the temperature data of N8 and N9 reveals that the material response is more prominent in case of the N8 specimen. This is because of two possible circumstances. On the one

hand, the stress amplitude is increased by 10 MPa, which makes a comparability more difficult. The dependence of the material response on the stress amplitude has already been demonstrated in previous studies. Another explanation is the increased surface roughness of the specimen N9. This leads to a larger surface area of the specimen compared to N8. Consequently, a greater surface area is exposed to the lab air which leads to more effective cooling of the specimen and thus reduces the measured values. The specimens machined with unworn cutting tools support this approach. Resulting temperature data of the lowest surface roughness N3 is demonstrably higher compared to batches N5 and N7. Besides that, N7 exhibits lower values for the change in temperature at half of the number of cycles to failure and τ than N5.
Having shown the influence of surface roughness on the cyclic deformation curves of CATs, the influence on LITs is analysed analogue in the following section.

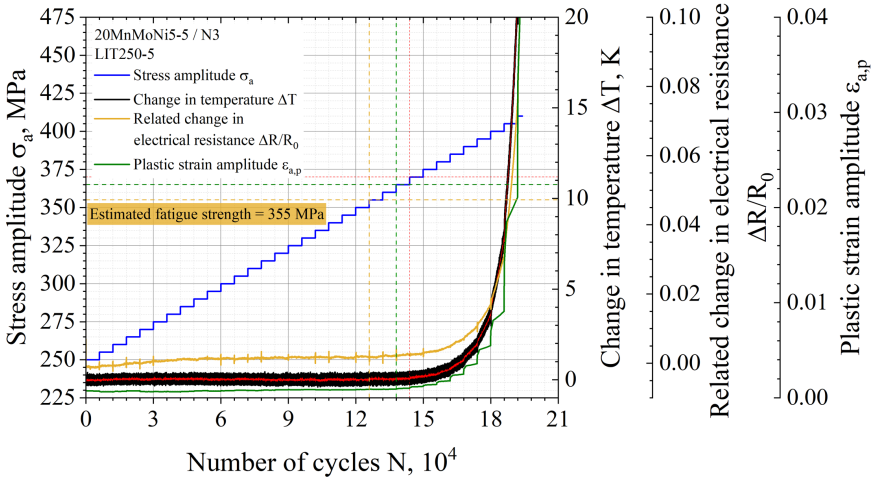

Figure 4.17: Investigations regarding the influence of surface condition on the fatigue behaviour based on cyclic deformation curves of load increase tests concerning the surface batch N3 of a 20MnMoNi5-5 steel

In addition to the assessment of fatigue behaviour under the influence of different surface conditions and the development of a new LPM, a further aim of this research is to integrate different NDT-related measurement devices into destructive fatigue testing. The advantage of varying the measurement technology is that different methods react sensitively to different damage mechanisms. As this aspect is already covered in the journal contributions of part II (especially within journal contribution 3), only a brief overview is provided at this point. Besides IR-thermography, two other methods are used to monitor the material response during cyclic loading. Especially electrical resistance measurements (4 point method) have the decisive advantage that defects in the volume of the material can be detected with high resolution. This would be particularly important in terms of VHCF loading of the material, where the initial damage is transferred into the volume of the material. Apart from that, fatigue tests are instrumented with a tactile extensometer to record the total strain amplitude. Even if this is not an NDT-related method, strain measurement represents the state of the art and is therefore suitable for validation purposes. The plastic strain amplitude shown in figure 4.17 is determined in a post-processing MATLAB calculation based on the stress-strain-hysteresis.
Because of the higher material strength and therefore rather brittle material behaviour and the re-

sulting lower values of the material response regarding the 20MnMoNi5-5 steel, it is more complex to estimate the fatigue strength in comparison to a more ductile behaviour. To ensure a reliable observation of the first material response, a moving average (red line) is used in addition to the original data of the temperature measurement (black line). This prevents an increase in material response from being superimposed by thermoelastic effects. An analysis of the respective measurement signals leads to an estimated fatigue strength range of 355 MPa - 370 MPa for the specimen of the N3 batch. Similar to the influence of microstructure discussed in the previous chapter, the cyclic deformation curve of N3 is used as a benchmark. The material response of the remaining LITs from batches N5-N9 is given in figure 4.18 and 4.19.

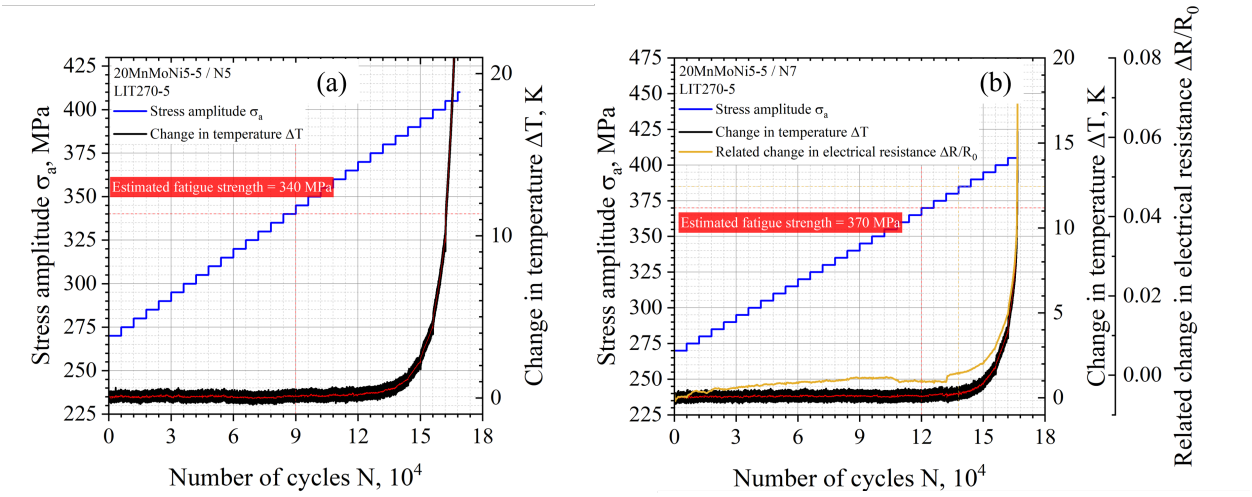

Figure 4.18: Investigations regarding the influence of surface condition on the fatigue behaviour based on cyclic deformation curves of load increase tests concerning (a) surface batch N5 (b) surface batch N7 of a 20MnMoNi5-5 steel

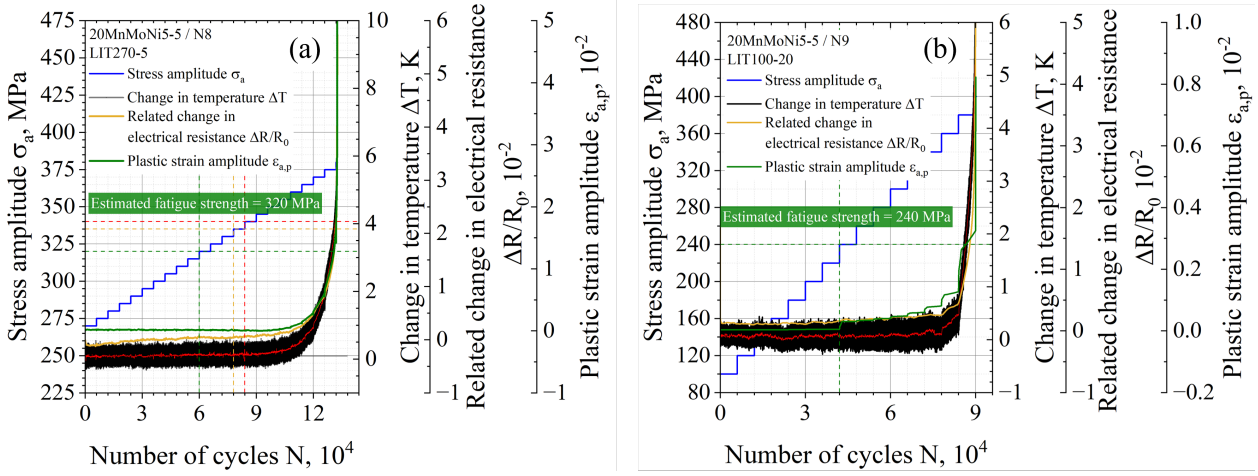

Figure 4.19: Investigations regarding the influence of surface condition on the fatigue behaviour based on cyclic deformation curves of load increase tests concerning (a) surface batch N8 (b) surface batch N9 of a 20MnMoNi5-5 steel

For reasons of comparability, important parameters of the curve progressions from figures 4.17, 4.18 and 4.19 are summarised in table 4.11. Within this table, the load level at which specimen failure occurs is labelled with $\sigma_{a,end}$. The data evidently depicts the difficulty of assessing the influence of surface roughness on fatigue behaviour based on the material response of a LIT. Even if the material response has a decreasing tendency, which is proven by τ, the estimation of fatigue strength is apparently subject to errors. Only in case of batch N9, a reduction in fatigue strength can be noticed, which is in contrast to previous expectations based on the evaluation regarding CATs. A comparison of the stress amplitude at which failure occurs does not provide any significant insights into the influence of surface roughness. However, it must be considered that the N9 LIT is performed with an increase in stress amplitude of 20 MPa and therefore the number of cycles to failure is decreased. To ensure an accurate assessment, identical test parameters would have to be chosen in further tests in comparison with N3.

Table 4.11: Comparison of the cyclic deformation curves of the load increase tests concerning different surface conditions with the reference surface batch N3 of a 20MnMoNi5-5 steel

20MnMoNi5-5						
Batch	$\sigma_{a,end}$ [MPa]	$\delta_{\sigma_{a,end}}$ [%]	τ [-]	δ_τ [%]	σ_e [MPa]	δ_{σ_e} [%]
N3	410.0		1.148		355.0	
N5	410.0	0.000	1.406	22.47	340.0	4.225
N7	405.0	1.219	0.470	59.06	370.0	4.225
N8	380.0	7.317	0.392	65.83	355.0	0.000
N9	400	2.439	0.286	75.09	240.0	32.39

In summary, the CAT data provide more accurate information regarding the influence of surface topography. Based on the CAT analyses, significantly reduced numbers of cycles to failure are expected for the lifetime prediction in terms of N8 and N9, whereas fatigue properties of N3, N5 and N7 should be similar. The assessment of the LPMs and their dependency on surface roughness is divided into two main parts. Firstly, the prediction quality is determined on the basis of a comparison with conventional data in accordance with chapter 4.1. The focus here is primarily on whether both methods, MiDAcLife and StressLife, are capable of modelling the influence of increased surface roughness. In the attached publication (journal contribution 4), the Fatigue Notch Factor has already demonstrated a possibility of integrating roughness values as a preliminary factor in the MiDAcLife evaluation. This enables a generation of virtual S-N curves for different surface conditions based on the reference surface N3. Common methods such as the FKM guideline or the approach according to Murakami only use static values to consider increased roughness. The second part of this section therefore compares the virtually calculated S-N curves with the FKM guideline and Murakami's approach, which emphasises the quality of the local, NDT-related MiDAcLife method.
The S-N curves that are generated with the different LPMs are given for the reference surface N3 in figure 4.20. Figure 4.20(a) displays the high level of agreement between the data points according to StressLife, MiDAcLife and the validation test results. Within the HCF regime, both curve progressions of MiDAcLife and the conventional method are similar to a good approximation. Only in transition regions to LCF and VHCF, a slight deviation regarding curve progression can be found.

StressLife equally enables a precise description of the fatigue behaviour of the polished N3 specimens. Figure 4.20(b) reflects the prediction quality by providing a relation between experimental test results and calculated numbers of cycles to failure. The majority of data points determined according to MiDAcLife are located within a deviation of 20 % compared to the validation CATs. Specific details concerning deviations of the LPMs from conventional S-N curves are given at the end of this chapter in table 4.12.

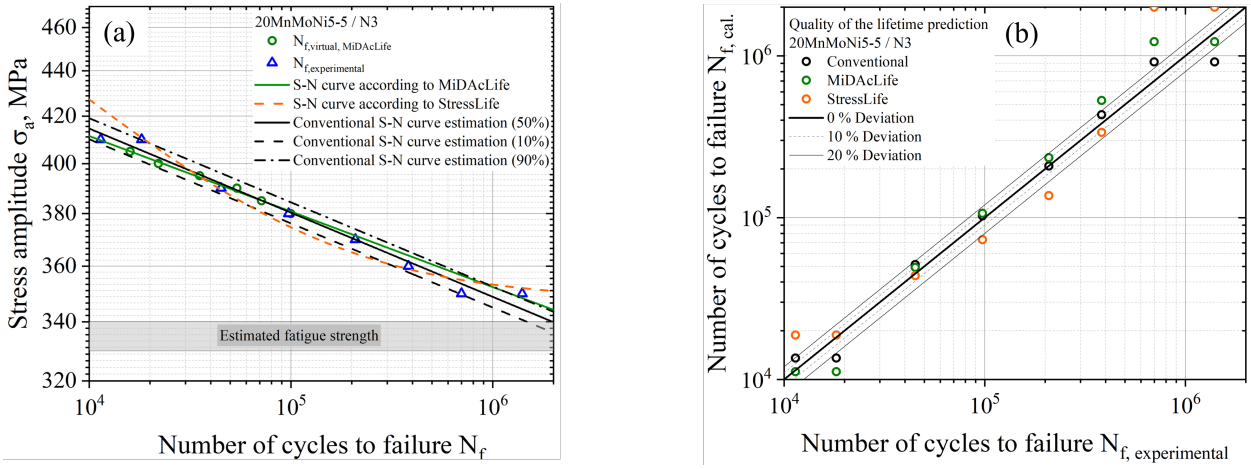

Figure 4.20: Investigations regarding the influence of surface roughness on the fatigue behaviour considering surface batch N3 (a) Accelerated determined S-N curves according to MiDAcLife and StressLife in comparison to conventionally determined S-N curves including different failure probabilities of 10, 50 and 90 % (b) Comparison between the experimental numbers of cycles to failure and calculated numbers of cycles to failure of a 20MnMoNi5-5 steel

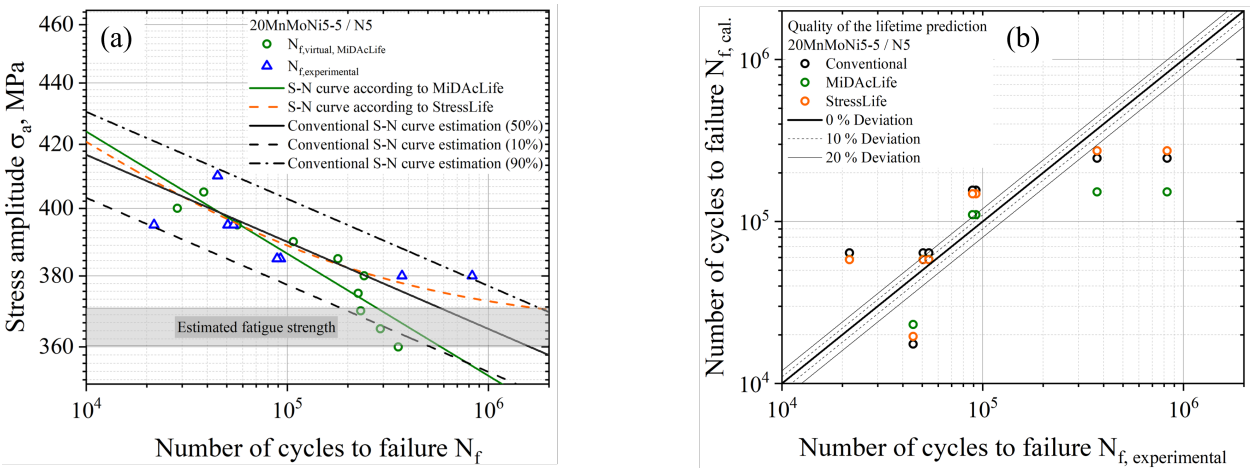

Figure 4.21: Investigations regarding the influence of surface roughness on the fatigue behaviour considering surface batch N5 (a) Accelerated determined S-N curves according to MiDAcLife and StressLife in comparison to conventionally determined S-N curves including different failure probabilities of 10, 50 and 90 % (b) Comparison between the experimental numbers of cycles to failure and calculated numbers of cycles to failure of a 20MnMoNi5-5 steel

The S-N curves of the polished batch N5 are presented in figure 4.21(a). As already mentioned, these specimens were not subject to a preliminary grinding process before polishing, what significantly increases compressive residual stresses. Especially in the region of lower stress amplitudes, this results in a demonstrably increased lifetime of the specimens compared to those of N3 in figure 4.20. Considering all experimental CATs, the slope of the conventional curve is vastly flattened compared to the MiDAcLife curve. Accordingly, MiDAcLife is characterised by a high deviation, despite the improved description of the validation points in the area of higher load amplitudes. Figure 4.21(a) reveals a decisive advantage of StressLife. While MiDAcLife cannot precisely depict the distinct increase in lifetime due to residual stresses in the range of high cycle numbers, the multi-parameter approach according to StressLife describes the data points with considerable accuracy and also significantly improved quality in contrast to conventional methods. In general, N5 is characterised by a substantially increased material scattering, which is illustrated in figure 4.21(b).

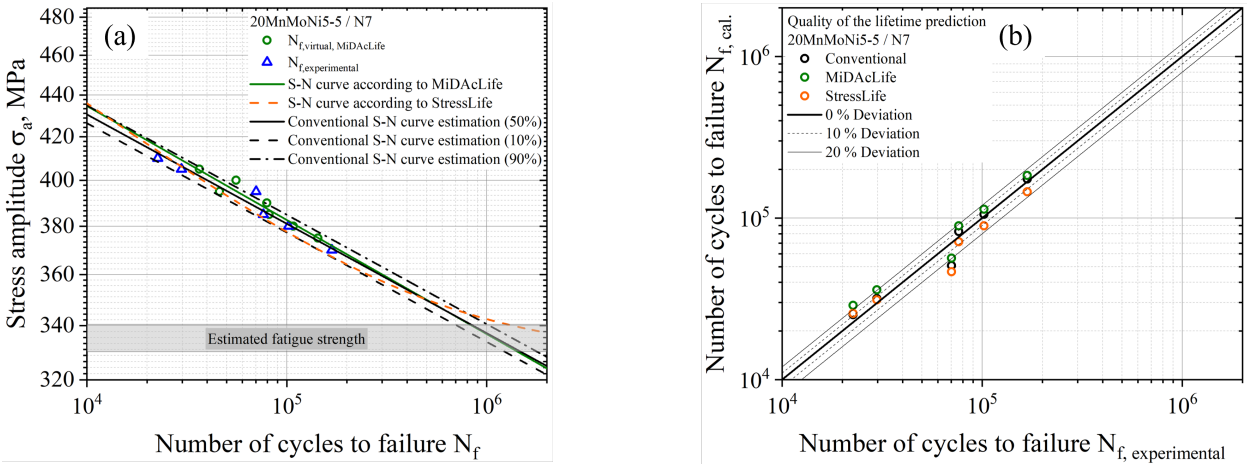

Figure 4.22: Investigations regarding the influence of surface roughness on the fatigue behaviour considering surface batch N7 (a) Accelerated determined S-N curves according to MiDAcLife and StressLife in comparison to conventionally determined S-N curves including different failure probabilities of 10, 50 and 90 % (b) Comparison between the experimental numbers of cycles to failure and calculated numbers of cycles to failure of a 20MnMoNi5-5 steel

Although specimens assigned to N7 exhibit slightly increased surface roughness due to the absence of the polishing process, the residual stresses are evidently lower and more homogeneous. Because of the homogeneity of the material properties as a result of the manufacturing process, a comparably limited scattering of the material under dynamic loading can be assumed, which is confirmed by figure 4.22. The experimental CATs depict a very low scatter and MiDAcLife as well as StressLife are characterised by an almost non-existent deviation from the conventional data. The decreased scatter is further illustrated by the lower width of the scatter bands of the 10 % S-N curve and the 90 % S-N curve. While the numbers of cycles calculated according to MiDAcLife are all within a deviation of less than 20 % in figure 4.22(b), only one data point occurs outside this scatter band in the conventional description and the description according to StressLife. An examination of fatigue strength values of batches N3-N7 confirms the hypothesis already established on the basis of the data received from the CATs and LITs, meaning that roughness does not have any significant influence on fatigue lifetime below a defined threshold value. While N3 and N7 are characterised by the same value regarding fatigue strength, an increased value can be observed in terms of N5 as a result of the increased compressive residual stresses.
The results of the roughness influence on the progression of the S-N curves of N8 and N9 are given in figures 4.23 and 4.24.

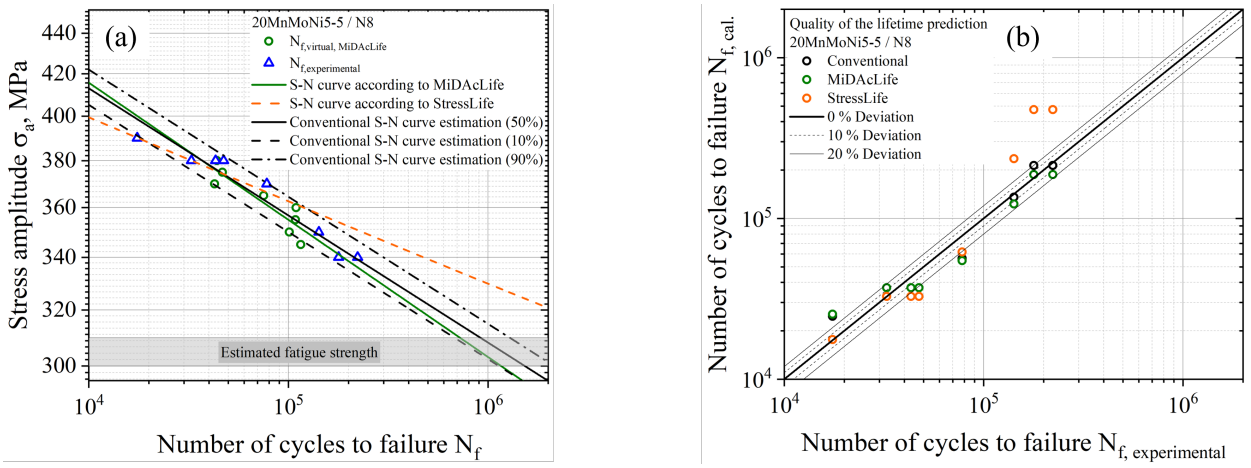

Figure 4.23: Investigations regarding the influence of surface roughness on the fatigue behaviour considering surface batch N8 (a) Accelerated determined S-N curves according to MiDAcLife and StressLife in comparison to conventionally determined S-N curves including different failure probabilities of 10, 50 and 90 % (b) Comparison between the experimental numbers of cycles to failure and calculated numbers of cycles to failure of a 20MnMoNi5-5 steel

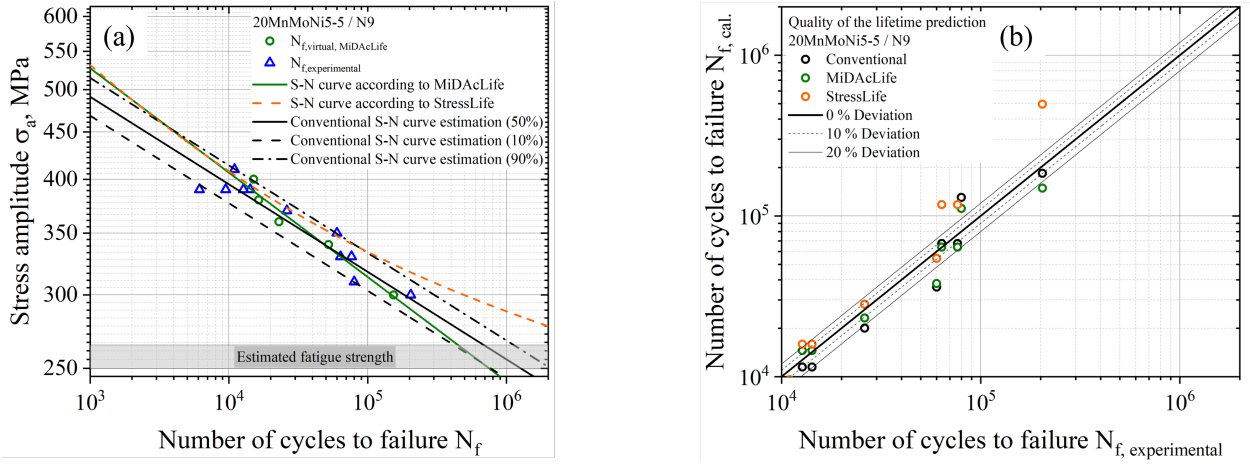

Figure 4.24: Investigations regarding the influence of surface roughness on the fatigue behaviour considering surface batch N9 (a) Accelerated determined S-N curves according to MiDAcLife and StressLife in comparison to conventionally determined S-N curves including different failure probabilities of 10, 50 and 90 % (b) Comparison between the experimental numbers of cycles to failure and calculated numbers of cycles to failure of a 20MnMoNi5-5 steel

A very important insight can be obtained from both illustrations. The S-N curves generated according to StressLife are proven to be too flat compared to the validation test results. This leads to an overestimation of the lifetime in the HCF regime and an underestimation in the LCF regime. The overestimation is more critical at this point. The reduced lifetime of the specimens as a result of increased stress concentration on the surface can therefore not be reliably modelled with the current version of StressLife. In comparison, calculations according to MiDAcLife appear to be independent of roughness influence. The estimated numbers of cycles to failure only differ slightly compared to the conventional S-N curve and are characterised by an accurate agreement with respect to experimental validation tests. As shown in figures 4.23(b) and 4.24(b), the deviation of StressLife is particularly severe in the range of high cycle numbers.

Table 4.12: Summary of the parameters concerning the lifetime prediction methods MiDAcLife and StressLife in comparison to conventional methods regarding different surface batches of the 20MnMoNi5-5 steel

Method	Batch	Parameters					
Conventional	N3	a [MPa]			k [-]		
		73.75			-26.65		
	N5	a [MPa]			k [-]		
		95.15			-34.79		
	N7	a [MPa]			k [-]		
		53.60			-18.83		
	N8	a [MPa]			k [-]		
		45.17			-15.74		
	N9	a [MPa]			k [-]		
		31.48			-10.58		
MiDAcLife	N3	σ'_f [MPa]			b [-]		
		561.2			-0.034		
	N5	σ'_f [MPa]			b [-]		
		614.8			-0.040		
	N7	σ'_f [MPa]			b [-]		
		724.1			-0.055		
	N8	σ'_f [MPa]			b [-]		
		781.7			-0.069		
	N9	σ'_f [MPa]			b [-]		
		1,148			-0.113		
StressLife	N3	K' [MPa · K^{-1}]	B, [K]	C, [K]	b [-]	c [-]	n' [-]
		352.3	1.149	79,993	-0.018	-0.909	0.081
	N5	K' [MPa · K^{-1}]	B [K]	C [K]	b [-]	c [-]	n' [-]
		372.6	1.577	14,174	-0.046	-0.771	0.059
	N7	K' [MPa · K^{-1}]	B [K]	C [K]	b [-]	c [-]	n' [-]
		376.0	0.248	48,203	-0.021	-0.895	0.076
	N8	K' [MPa · K^{-1}]	B [K]	C [K]	b [-]	c [-]	n' [-]
		355.0	0.078	979.5	-0.091	-0.543	0.078
	N9	K' [MPa · K^{-1}]	B [K]	C [K]	b [-]	c [-]	n' [-]
		420.4	1.289	53.20	-0.104	-0.480	0.346

In addition to that, both figures display the striking advantage of MiDAcLife in generating reliable values within the range of a 20 % deviation even under the influence of an increased surface roughness. The most important parameters deriving from previously obtained findings are compiled in table 4.12. A comparison of the previously provided parameters of table 4.12 is concisely concluded within table 4.13. It should be mentioned that the deviation compared to conventional S-N curves is consequently evaluated when it comes to the assessment of the quality concerning LPMs. A comparison with individual validation points is challenging, since it is highly influenced by the scatter of the material. However, as the scatter is considered within the conventional S-N curve, a comparison with the function of the conventional method appears to be most representative. In order to investigate deviations in terms of StressLife, it must be considered that the multi-parametric approach is simplified to a two-parametric approach.

Table 4.13: Comparison of the parameters concerning the LPMs MiDAcLife and StressLife with conventional methods regarding different surface batches of the 20MnMoNi5-5 steel

N3							
Method	T_N [%]	σ_e [MPa]	δ_{σ_e} [%]	σ'_f [MPa]	$\delta_{\sigma'_f}$ [%]	b [-]	δ_b [%]
Conventional		339.9		585.9		-0.037	
MiDAcLife	±39.13	384.3	13.06	561.2	4.216	-0.034	8.108
StressLife		350.9	3.236	535.8	8.551	-0.030	18.92
N5							
Method	T_N [%]	σ_e [MPa]	δ_{σ_e} [%]	σ'_f [MPa]	$\delta_{\sigma'_f}$ [%]	b [-]	δ_b [%]
Conventional		357.8		542.9		-0.029	
MiDAcLife	±446.9	342.5	4.276	614.8	13.24	-0.040	37.93
StressLife		370.3	3.494	493.1	9.173	-0.020	31.03
N7							
Method	T_N [%]	σ_e [MPa]	δ_{σ_e} [%]	σ'_f [MPa]	$\delta_{\sigma'_f}$ [%]	b [-]	δ_b [%]
Conventional		325.0		702.3		-0.053	
MiDAcLife	±23.25	324.1	0.277	724.1	3.104	-0.055	3.774
StressLife		337.3	3.785	631.2	10.12	-0.044	16.98
N8							
Method	T_N [%]	σ_e [MPa]	δ_{σ_e} [%]	σ'_f [MPa]	$\delta_{\sigma'_f}$ [%]	b [-]	δ_b [%]
Conventional		295.0		741.5		-0.064	
MiDAcLife	±44.99	289.1	2.000	781.7	5.421	-0.068	6.250
StressLife		320.8	8.746	583.0	21.38	-0.041	35.94
N9							
Method	T_N [%]	σ_e [MPa]	δ_{σ_e} [%]	σ'_f [MPa]	$\delta_{\sigma'_f}$ [%]	b [-]	δ_b [%]
Conventional		239.5		943.5		-0.095	
MiDAcLife	±87.55	223.9	6.514	1,148	21.67	-0.112	17.89
StressLife		277.6	15.91	785.4	16.76	-0.073	23.16

In conclusion, the influence of surface roughness on the accelerated lifetime prediction can be analysed from the presented research. As the results of the CATs have shown before, the S-N curve can also be used to demonstrate that roughness only seems to have an influence on the lifetime above a certain limit value. The process-oriented local evaluation of fatigue behaviour according to MiDAcLife enables a generation of S-N curves independent of the corresponding surface roughness. StressLife, on the other hand, is characterised by a precise agreement in the area of low surface roughness values, but loses accuracy with increasing roughness influence.
Another advantage of MiDAcLife that should be emphasised is the possibility of calculating virtual S-N curves for different surface conditions based on just one reference surface. For this purpose, roughness is included in the calculation as a Fatigue Notch Factor. A detailed description of the method can be found in journal contribution 4 of part II within this thesis. Using the approaches according to the FKM guideline and the proposed $\sqrt{area}$-method by Murakami, roughness influence can be estimated in a simple approximation. The use of static values leads to considerable deviations compared to the NDT-related method MiDAcLife. A comparison of the results of all three methods is shown in the following section. Within figures 4.25, 4.26, 4.27 and 4.28, the virtual S-N curves based on the surface N3 are displayed by a green line. The methods of the FKM guideline and Murakami are illustrated as grey and yellow lines, respectively.

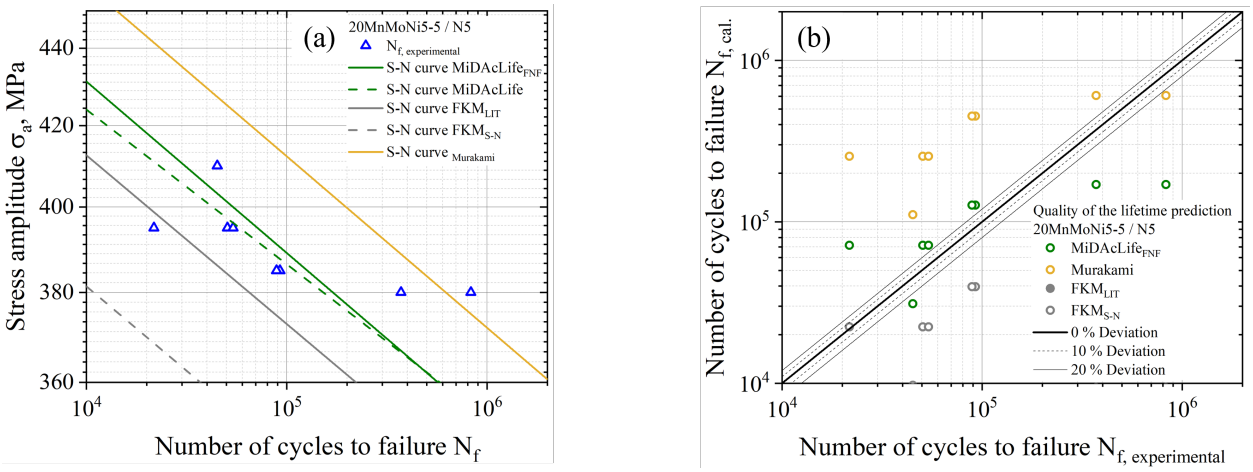

Figure 4.25: Investigations regarding the influence of surface roughness on the fatigue behaviour based on the reference surface batch N3 considering surface batch N5 (a) Comparison of the virtual estimated S-N curve using the Fatigue Notch Factor in MiDAcLife with approaches according to the FKM-guideline and Murakami. (b) Comparison between the experimental numbers of cycles to failure and calculated numbers of cycles to failure of a 20MnMoNi5-5 steel

The relation of the fatigue strength of N3 and the stress concentration factor according to the FKM guideline results in the fatigue strength value of the new surface. As the fatigue strength can be derived from the S-N curve as well as from the LIT, both variants are considered within the figures above. For reasons of comparability, S-N curves according to MiDAcLife are given additionally as dashed green lines. This allows the virtual S-N curve to be compared to the original MiDAcLife curve. A comparison with conventional data is omitted because of the detailed analyses in previous sections, as a precise correspondence between MiDAcLife and conventional S-N curves has already

been proven.

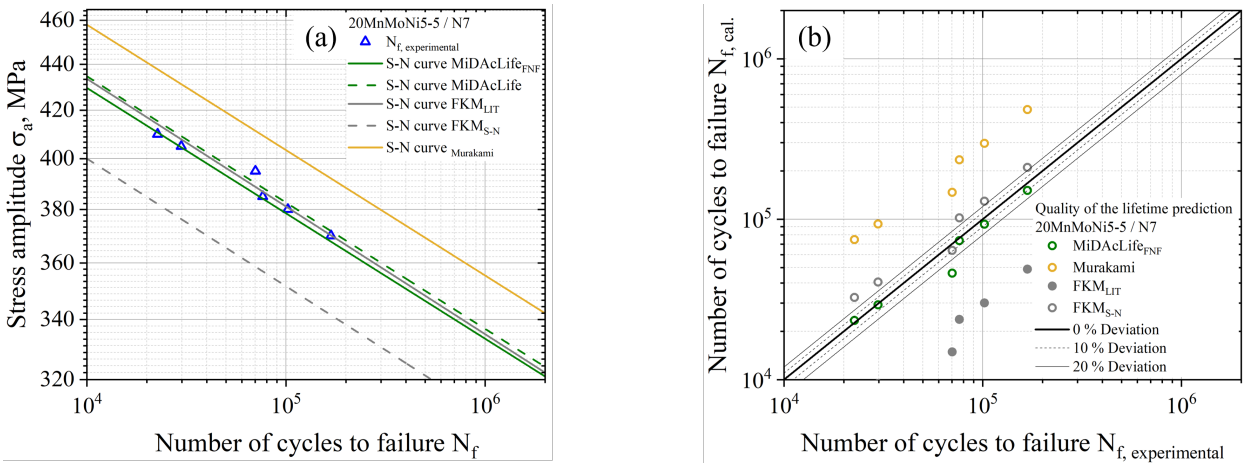

Figure 4.26: Investigations regarding the influence of surface roughness on the fatigue behaviour based on the reference surface batch N3 considering surface batch N7 (a) Comparison of the virtual estimated S-N curve using the Fatigue Notch Factor in MiDAcLife with approaches according to the FKM-guideline and Murakami. (b) Comparison between the experimental numbers of cycles to failure and calculated numbers of cycles to failure of a 20MnMoNi5-5 steel

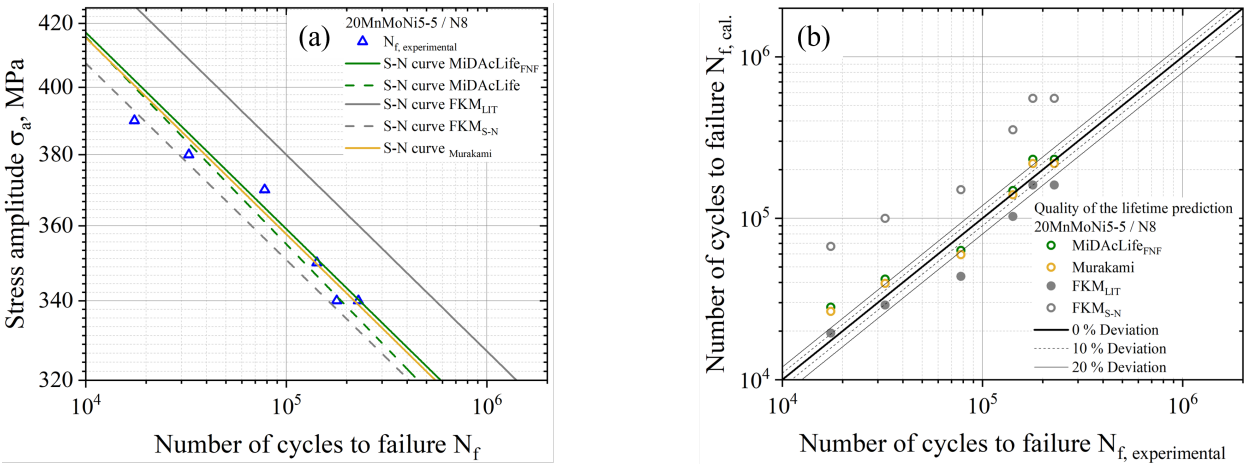

Figure 4.27: Investigations regarding the influence of surface roughness on the fatigue behaviour based on the reference surface batch N3 considering surface batch N8 (a) Comparison of the virtual estimated S-N curve using the Fatigue Notch Factor in MiDAcLife with approaches according to the FKM-guideline and Murakami. (b) Comparison between the experimental numbers of cycles to failure and calculated numbers of cycles to failure of a 20MnMoNi5-5 steel

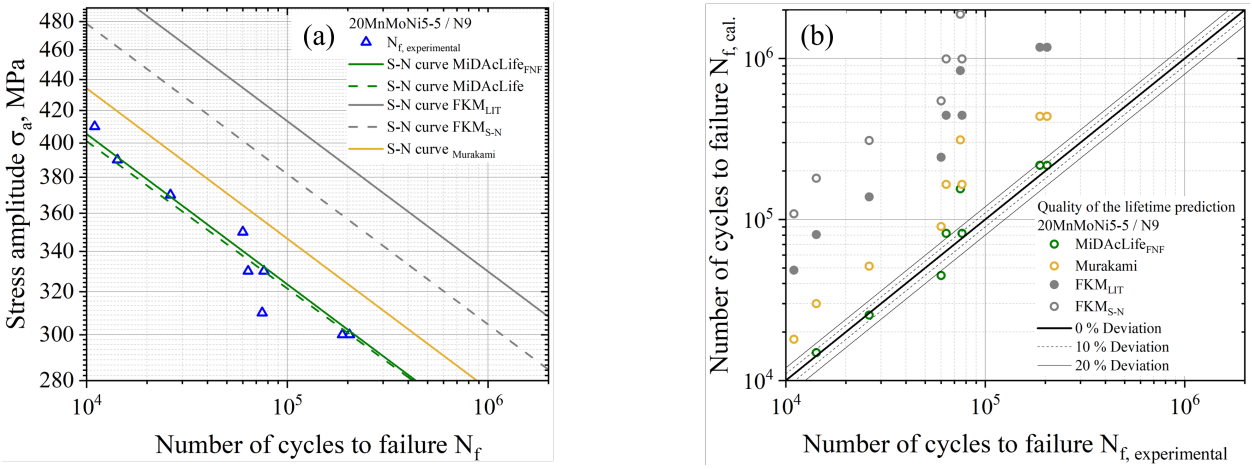

Figure 4.28: Investigations regarding the influence of surface roughness on the fatigue behaviour based on the reference surface batch N3 considering surface batch N9 (a) Comparison of the virtual estimated S-N curve using the Fatigue Notch Factor in MiDAcLife with approaches according to the FKM-guideline and Murakami. (b) Comparison between the experimental numbers of cycles to failure and calculated numbers of cycles to failure of a 20MnMoNi5-5 steel

Except for the evaluation regarding N8, Murakami's approach leads to an overestimation of the lifetime concerning the 20MnMoNi5-5 steel. The reason for this could be the consideration of surface roughness as a periodic structure in which the ratio of the distance between two grooves and their height is regarded as constant. However, real surface conditions are characterised by a surface roughness that deviates greatly from periodic structures. More pronounced roughness peaks, that result in a significant lifetime reduction, can therefore not be taken into account within the calculations. Another obstacle is the determination of the values required for this approach. The aperiodic topography of the surfaces inevitably results in a subjective assessment of the data, leading to inaccurate results.
A consideration of the approach according to the FKM guideline reveals a distinct tendency with increasing surface roughness. While the lifetime of the 20MnMoNi5-5 steel is underestimated in case of lower roughness values, an increased surface roughness results in an overestimation of the fatigue data, which is evidently more critical. The deviation in the evaluation regarding batches N3 to N7 can be attributed to the fact, that the FKM guideline is characterised by the implementation of safety factors. Although this can prevent premature component failure, excessive safety factors lead to over-dimensioning of components, which runs counter to the potential for lightweight construction. A great potential of the NDT-related methods can be derived from this finding, as safety factors can be reduced depending on the material response through a process-orientated fatigue consideration. In order to explain the overestimation of the lifetime prediction at very high surface roughness, it is firstly necessary to consider which parameters are included within the calculation. According to equation 2.8, the stress concentration factor is essentially influenced by the tensile strength R_m in addition to the roughness height R_z. Because of high shear stresses compared to fatigue testing, surface condition only is assigned to have a minor effect and therefore cannot be reliably integrated into lifetime prediction of N8 and N9.
In contrast, the virtual lifetime prediction according to MiDAcLife enables demonstrably precise

results for the fatigue assessment regarding all surface conditions. All of the presented S-N curves in figure 4.25, 4.26, 4.27 and 4.28 are based on the data of just one LIT of surface N3, as well as the estimation of the fatigue strength using the specific hardness. A more detailed explanation of the procedure can be found in the corresponding journal contributions from part II (journal contribution 4). In addition to virtually generated S-N curves, the presented figures contain the original S-N curve according to MiDAcLife based on the respective LIT of each surface condition. To assess the quality of the virtual curves, table 4.14 provides a comparison with original parameters of the MiDAcLife evaluation.

Table 4.14: Summary of the parameters concerning the lifetime prediction method $\text{MiDAcLife}_{\text{FNF}}$ regarding different surface conditions of the 20MnMoNi5-5 steel

20MnMoNi5-5				
Batch	σ'_f [MPa]	$\delta_{\sigma'_f}$ [%]	b [-]	δ_b [%]
N5	651.0	5.888	-0.044	10.00
N7	713.0	1.537	-0,055	0.722
N8	759.0	2.900	-0.065	4.412
N9	1,000	2.891	-0.098	2.083

4.3 Integration of Statistical Approaches into the Accelerated Lifetime Prediction

Local changes in the microstructure of materials as well as different local stress concentrations, for example in case of increased surface roughness, lead to an influence on fatigue properties, as shown in chapter 4.1 and 4.2. The fact that the mentioned differences are usually very localised, results in a material-dependent scattering of the data, which must urgently be considered within lifetime prediction. Statistical distribution functions are used to illustrate the scatter, which enable an estimation of S-N curves regarding different failure probabilities. According to conventional methods, either the scatter of each load level is evaluated or the results of the CATs are transferred to a virtual load level and analysed via Log-Normal or Weibull distribution. However, in both cases, a very high number of fatigue tests is necessary, which again increases the costs and experimental time effort enormously.
The aim of future research must therefore be to integrate statistical approaches into the accelerated lifetime prediction. Based on conventionally determined scatter bands, some kind of lifetime prediction bands are to be presented, considering the material-dependent scatter of defined load levels. As a first approach, the following section shows how a combination of several MiDAcLife evaluations can be used to enable a statistical assessment of fatigue behaviour in terms of the 20MnMoNi5-5 on the basis of just six fatigue specimens and six fatigue tests. Since it has already been demonstrated in chapter 4.2 that the surface condition for N3 to N7 has no significant influence on the lifetime, the results of the respective CATs are summarised in order to enlarge the database of the statistical investigation. The result of this analysis is given in figure 4.29.

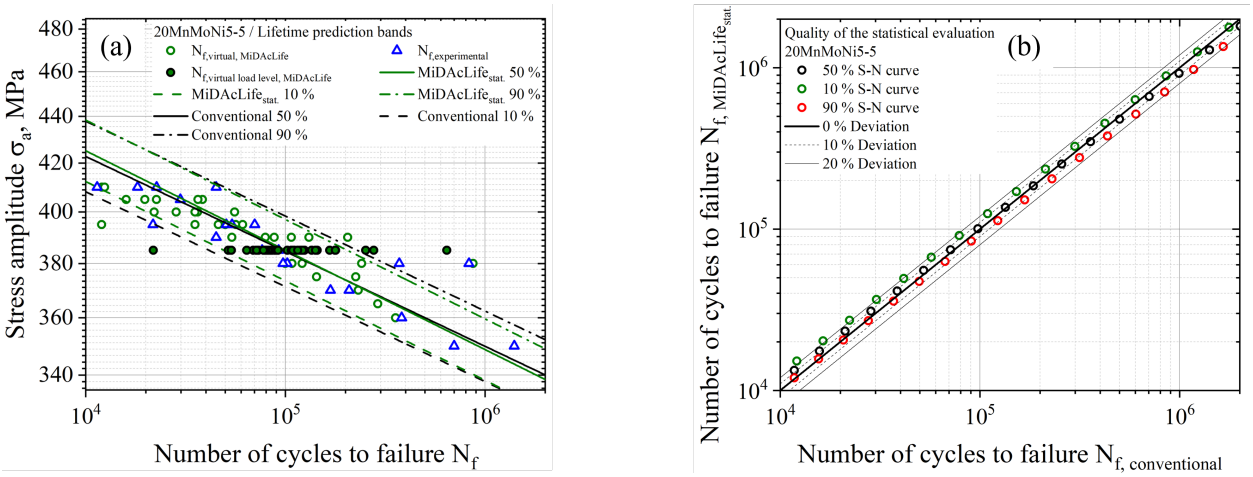

Figure 4.29: Investigations regarding the integration of statistical approaches into the accelerated lifetime prediction method MiDAcLife based on the results of four load increase tests (a) Accelerated determined S-N curves according to MiDAcLife in comparison to conventionally determined S-N curves including different failure probabilities of 10, 50 and 90 % (b) Comparison between the experimental numbers of cycles to failure and calculated numbers of cycles to failure of a 20MnMoNi5-5 steel

Within figure 4.29, data points virtually calculated using MiDAcLife are illustrated as unfilled green circles, while experimental CATs are displayed by blue triangles. The green filled circles represent data points shifted to an average virtual load level, which are used for a statistical evaluation of MiDAcLife. While the black lines display conventional statistical evaluations, the lifetime prediction bands are shown as green lines. By combining the data of six LITs, a database of 40 numbers of cycles to failure can be generated. This corresponds to an increase of approximately 48 % compared to conventional experimental data (27). At the same time, the experimental effort is reduced by nearly 78 %.

Two key aspects can be derived from figure 4.29. Firstly, both the conventional S-N curve including determined scatter bands and the MiDAcLife curve including lifetime prediction bands describe the experimental validation points with a very high degree of accuracy. With exception concerning two of the 27 data points, all validation tests can be found within the predicted scatter range for both evaluation methods. In addition to that, the positions, as well as the slopes of the MiDAcLife approach are almost identical to those of the conventional method. The marginally increased slope of the accelerated method can be seen primarily in figure 4.29(b), as there is a slight deviation from the bisector in the range of the transition to the LCF regime and at high numbers of cycles to failure. The parameters of the S-N curves, as well as the respective deviations are given in table 4.15. The extremely small deviations of less than 5 % of the parameters presented in table 4.15 indicate the potential regarding the integration of statistical approaches into the accelerated lifetime prediction. In particular, the fatigue strength hardly differs from conventional data with values of less than 1 %. An important next approach in future research will be the investigation of further statistical methods. Apart from conventional distribution functions, distributions that are optimised for small amounts of specimens or even non-parametric functions could also be used to generate lifetime prediction bands and thus provide a major advance in the safety of lifetime prediction methods.

Table 4.15: Comparison of the parameters concerning the lifetime prediction method MiDAcLife including statistical approaches with conventional methods regarding different failure probabilities of the 20MnMoNi5-5 steel

10 % S-N curve						
Method	σ_e [MPa]	δ_{σ_e} [%]	σ'_f [MPa]	$\delta_{\sigma'_f}$ [%]	b [-]	δ_b [%]
Conventional	328.4		595.9		-0.041	
MiDAcLife	328.3	0.030	612.7	2.819	-0.043	4.878
50 % S-N curve						
Method	σ_e [MPa]	δ_{σ_e} [%]	σ'_f [MPa]	$\delta_{\sigma'_f}$ [%]	b [-]	δ_b [%]
Conventional	340.1		617.2		-0.041	
MiDAcLife	338.5	0.470	631.8	2.366	-0.043	4.878
90 % S-N curve						
Method	σ_e [MPa]	δ_{σ_e} [%]	σ'_f [MPa]	$\delta_{\sigma'_f}$ [%]	b [-]	δ_b [%]
Conventional	352.3		639.2		-0.041	
MiDAcLife	349.1	0.908	651.4	1.909	-0.043	4.878

4.4 Applicability of MiDAcLife Under Consideration of Increased Testing Frequencies

In addition to material-related factors, fatigue behaviour of metallic materials can be influenced by external conditions. The results shown up to this chapter refer to a testing frequency of 5 Hz. Since dislocation movement and therefore plastic deformation of the material is a highly time-dependent process, the fatigue lifetime can be strongly influenced by a change in testing frequency. An increased frequency leads to a reduction within reaction time of dislocations, resulting in an increased lifetime of the specimen. Additional effects, such as self-heating phenomena due to insufficient heat dissipation, are not considered, but must be investigated in more detail in future research. This research focuses primarily on the newly developed method MiDAcLife. As the comparability with conventional data has already been demonstrated in previous chapters and a comparison to the LPM StressLife has also been drawn, the following results only relate to the evaluation according to MiDAcLife. Figures 4.30 and 4.31 display the results of the MiDAcLife evaluation for testing frequencies of 80 Hz and 260 Hz. The experimental data of an SAE 1045 steel in a normalised condition, that was used for these investigations, originates from a DFG (Deutsche Forschungsgemeinschaft) funded project with the grant number STA 1133/22-1[5].
Similar to previously provided results, the MiDAcLife curve is illustrated with a green line, whereas the conventional S-N curve is shown as a black line. The experimental validation tests are still marked as blue triangles.

[5]CAT data points for validation
Project: STA 1133/22-1
University: University of Applied Sciences Kaiserslautern
Institude: Department of Materials Science & Materials Testing (WWHK)
Project manager: M. Sc. Jonas Anton Ziman

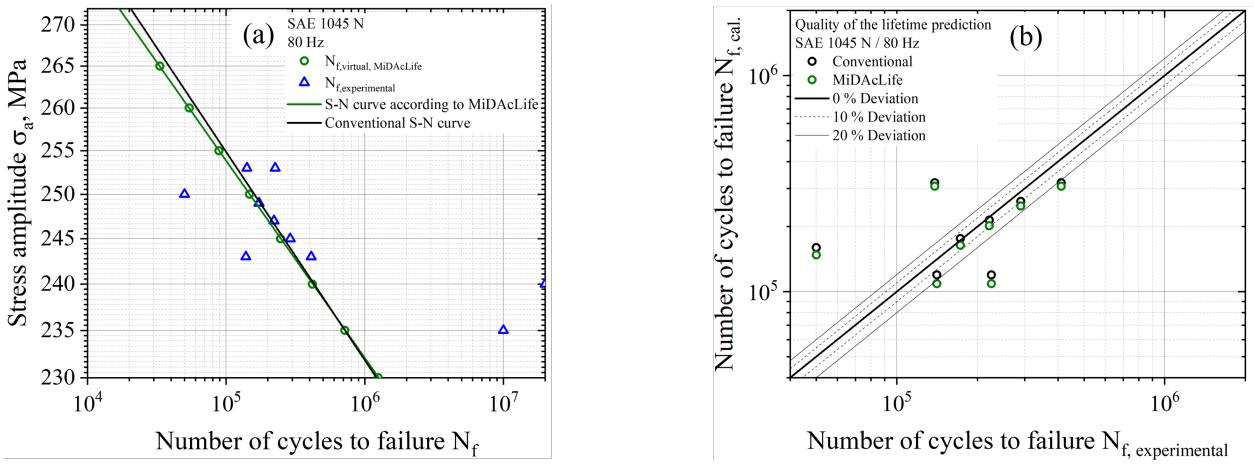

Figure 4.30: Investigations regarding the influence of increased testing frequency on the fatigue behaviour considering a frequency of 80 Hz (a) Accelerated determined S-N curve according to MiDAcLife in comparison to the conventionally determined S-N curve (b) Comparison between the experimental numbers of cycles to failure and calculated numbers of cycles to failure of a 20MnMoNi5-5 steel

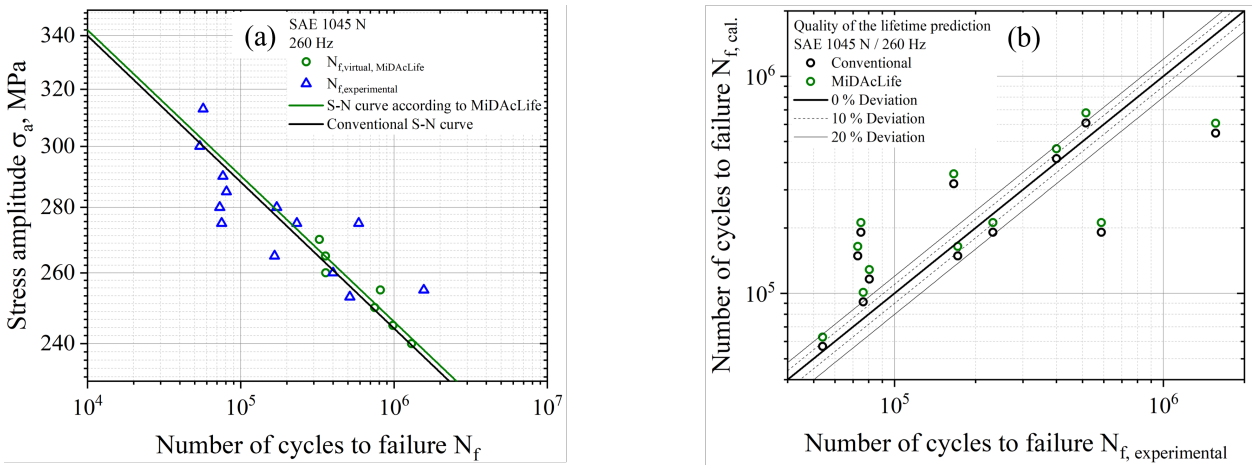

Figure 4.31: Investigations regarding the influence of increased testing frequency on the fatigue behaviour considering a frequency of 260 Hz (a) Accelerated determined S-N curve according to MiDAcLife in comparison to the conventionally determined S-N curve (b) Comparison between the experimental numbers of cycles to failure and calculated numbers of cycles to failure of a 20MnMoNi5-5 steel

In both figures 4.30 and 4.31, the influence of the testing frequency on the LPM is characterised by an demonstrably comparable relation of MiDAcLife and the conventional S-N curves regarding previously presented results of other influencing factors. Despite the increased scatter concerning the conventionally performed CATs, the calculations according to MiDAcLife provide S-N curves that are in precise agreement with the conventional curves in terms of slope and position for both frequencies. Deviations regarding the slope and the location of the curve progressions are

summarised in table 4.16, whereas a comparison regarding the calculated numbers of cycles to failure according to both methods is given in table 4.17.

Table 4.16: Comparison of the parameters concerning the lifetime prediction method MiDAcLife with conventional methods regarding different testing frequencies of a 20MnMoNi5-5 steel

20MnMoNi5-5					
Frequency, [Hz]	Method	σ'_f [MPa]	$\delta_{\sigma'_f}$ [%]	b [-]	δ_b [%]
80	Conventional	409.0		-0.041	
	MiDAcLife	397.3	2.860	-0.039	4.878
260	Conventional	659.2		-0.072	
	MiDAcLife	662.0	0.424	-0.072	0.278

Table 4.17: Summary of the numbers of cycles to failure according to the lifetime prediction method MiDAcLife regarding different testing frequencies of a 20MnMoNi5-5 steel

SAE 1045 N, 80 Hz					
σ_a [MPa]	$N_{f,experimental}$ [-]	$N_{f,Conventional}$ [-]	δ_{N_f} [%]	$N_{f,MiDAcLife}$ [-]	δ_{N_f} [%]
245	290,102	261,268	9.939	248,739	14.26
243	411,000	318,954	22.39	307,084	25.28
249	172,621	176,158	2.049	164,037	4.973
247	221,340	214,362	3.152	201,826	8.816
253	141,114	119,522	15.30	108,897	22.83
253	225,675	119,522	47.04	108,897	51.75
243	138,735	318,954	129.9	307,084	121.3
250	50,007	159,785	219.5	147,977	195.9
SAE 1045 N, 260 Hz					
σ_a [MPa]	$N_{f,experimental}$ [-]	$N_{f,Conventional}$ [-]	δ_{N_f} [%]	$N_{f,MiDAcLife}$ [-]	δ_{N_f} [%]
275	232,186	190,997	17.74	211,636	8.849
275	588,000	190,997	67.52	211,636	64.01
300	54,000	56,924	5.415	62,822	16.34
280	171,768	148,647	13.46	164,573	4.189
290	76,505	91,229	19.25	100,839	31.81
313	56,839	31,549	44.49	34,749	38.86
280	72,894	148,647	103.9	164,573	125.8
285	80,623	116,202	44.13	128,546	59.44
275	75,000	190,997	154.66	211,636	182.2
265	166,027	319,767	92.59	354,928	113.8
260	400,000	416,797	4.199	463,036	15.76
253	515,260	609,292	18.25	677,742	31.53
253	1565,745	546,072	65.12	607,198	61.22

An increase in testing frequency by a factor of 16 to 80 Hz results in a deviation of the fatigue strength coefficient of approximately 3 % compared to conventional calculations. Additionally, the slope of the MiDAcLife curve only differs insignificantly from the conventional determined results by 4.9 %. The explicit correlation concerning the calculated parameters is even more pronounced considering a testing frequency of 260 Hz. Within these results, deviations of less than 0.5 % for the slope as well as the fatigue strength coefficient can be determined, which is negligible in view of the material-dependent scatter. An average calculation regarding the deviation of all experimental obtained data points leads to a value of 56 % in case of a testing frequency of 80 Hz and 51 % for 260 Hz considering the conventional fatigue life determination. In contrast to this, MiDAcLife provides a deviation of 56 % and 58 %, respectively, which again demonstrate the high level of agreement between the accelerated lifetime prediction and the conventional method. Based on the presented results, the applicability of the LPM MiDAcLife regarding increased testing frequencies can be verified.

4.5 Expansion of MiDAcLife to Cast Materials

The results presented so far have focused primarily on the lifetime prediction of un- and low alloyed steels. These materials are characterised by a more homogenious microstructure. Especially within the HCF regime, fatigue damage essentially originates from the specimens surface. The sum of the partially induced damage can be assumed to be equal to 1. The activation of further damage mechanism leads to a more complicated evaluation of fatigue properties, since the scattering increases enormously. For this reason, the applicability for cast materials is tested within this chapter. For these investigations, an EN-GJS-1050-6[6] is used, which is characterised by an ausferritic matrix. Furthermore, spheroidal graphite precipitates are embedded within this matrix. Since the morphology and the size of the graphite precipitates are subjected to statistical deviations, the increased scatter of the material can be explained. The S-N curves of the material are given in figure 4.32. As in previous chapters, the quality of the LPM is assessed on the basis of a comparison with conventional data. Figure 4.32(a) illustrates the lifetime evaluation according to MiDAcLife under the assumption of $D = 1$ (green unfilled circles), which corresponds to a total damage of 100 %. In particular, the comparison with the conventional S-N curve for a failure probability of 90 % provides an insight into the challenge that is associated with cast materials. In terms of such inhomogeneous microstructures, specimen failure does not occur exclusively from the surface. Besides graphite-matrix detachment processes, pores and shrinkage resulting from manufacturing processes are also of crucial importance. Since these factors lead to a great reduction of the lifetime, the assumption of a specimen failure at 100 % damage is idealised and therefore results in an overestimation of the lifetime compared with real data. This overestimation becomes highly critical, particularly with regard to safe component design.

[6]CAT data points for Validation
Project: LeKoGuss WEA (0324279A)
University: RWTH Aachen University
Institude: Chair and Institute for Materials Applications in Mechanical Engineering (IWM)
Project manager: M. Sc. Felix Weber

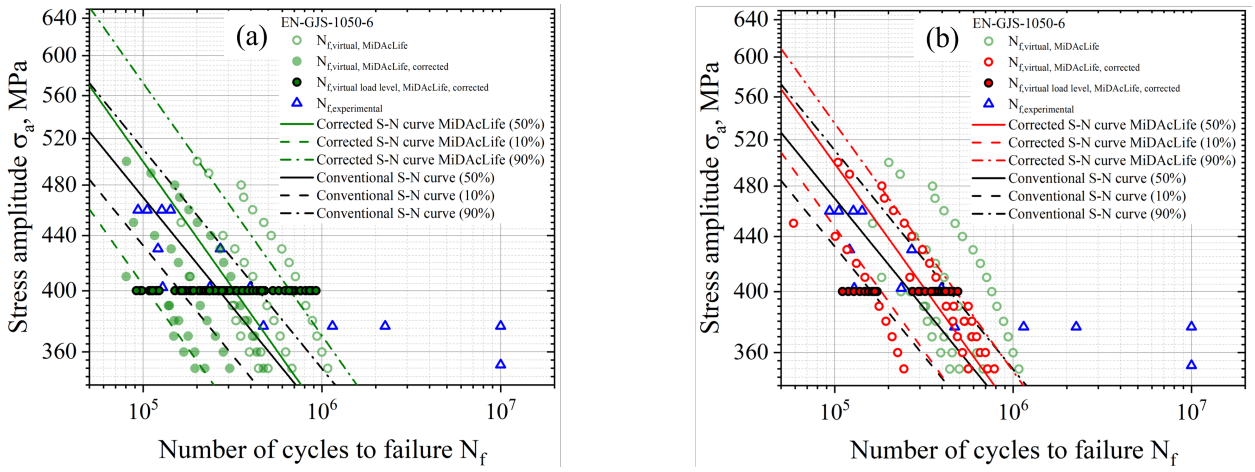

Figure 4.32: Investigations regarding the influence of different damage mechanisms on the fatigue behaviour considering cast materials (a) Accelerated determined S-N curve according to MiDAcLife in comparison to conventionally determined S-N curves concerning a damage sum of 1 and 0.4 (b) S-N curve generation according to MiDAcLife using the distribution of the material response in order to assess the damage factor process-orientated of an EN-GJS-1050-6 cast iron

To account for cast material specific microstructural artefacts, Schoenborn et al. [244] examined the values of the real applied damage sum in comparison to a total damage that is equal to 1. Depending on the material, significantly reduced values of the total damage can be estimated at which premature specimen failure already occurs. In addition to the virtual data points calculated under the assumption of 100 % damage, figure 4.32(a) contains the results of MiDAcLife (filled circles) with a defined total damage of $D = 0.4$. The data points indicate the strong influence of the total damage on the lifetime. The solid green-coloured S-N curve in figure 4.32(a) represents the average curve progression resulting from the outcomes of a damage of $D = 0.4$ as well as $D = 1$. From the illustration, it can be stated that the consideration of a smaller value for the total damage enables a more accurate approximation to the real data. Additionally, the numbers of cycles to failure are no longer overestimated. The parameters of the conventional S-N curve determination as well as the accelerated method according to MiDAcLife, taking into account different types of total damage, are given in table 4.18.

Table 4.18: Comparison of the parameters concerning the lifetime prediction method MiDAcLife with conventional methods regarding different damage mechanisms in terms of cast materials

EN-GJS-1050-6					
Damage	Method	σ'_f [MPa]	$\delta_{\sigma'_f}$ [%]	b [-]	δ_b [%]
1	Conventional	3114		-0.164	
	MiDAcLife	4653	49.42	-0.189	14.02
0.4	Conventional	3114		-0.164	
	MiDAcLife	3462	11.18	-0.166	1.219

The parameters in table 4.18 demonstrably emphasise the improved quality of the lifetime prediction, considering the reduced values for the total damage. While the results of MiDAcLife exhibit a deviation of nearly 50 % for σ'_f in case of $D = 1$, the deviation can be reduced to a value of 11.18 % by considering $D = 0.4$. Even the slope of the S-N curve, which is already an acceptable approximation of the conventional data in the original evaluation, with a deviation of 14 % , can be reduced to 1.219 %.
However, using the factor 0.4 leads to an expansion of the scatter bands, which deviate significantly from the conventional data. The reason for this is that a simplification is made by only considering the limit values of the damage. Accordingly, a possibility must be introduced, by which the factor for the respective LIT can be calculated in a specific way. Based on this finding, the area enclosed by the cyclic deformation curve is determined for each LIT and normalised to the respective number of cycles to failure. This enables the generation of a distribution function for the results, which can be used to define the factor considering the deviation from the maximum value of the distribution function. The recalculated data points, including the scatter bands, are shown in figure 4.32(b), whereas the density function according to Weibull is given in figure 4.33.

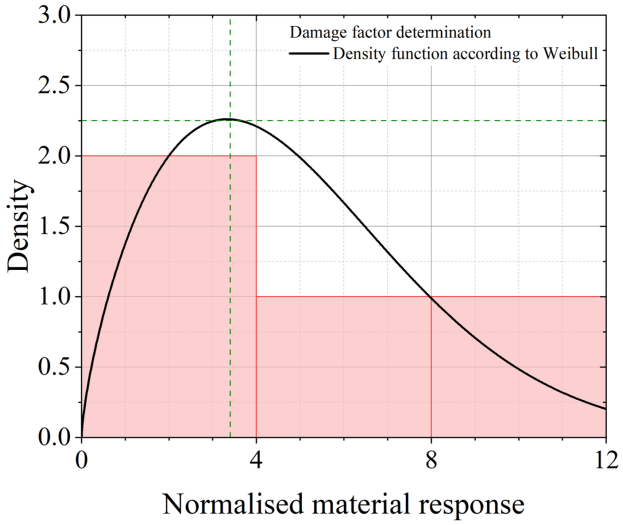

Figure 4.33: Investigations regarding the influence of different damage mechanisms based on the damage factor determination using the normalised material response and statistical approaches concerning an EN-GJS-1050-6 cast iron

Due to the integration of the material response, the scatter bands can be estimated in demonstrably precise approximation to the conventional scatter bands. All parameters regarding the distribution function and the resulting factors are displayed in table 4.19.
Based on the results and analyses of figure 4.32 and table 4.18 as well as table 4.19, it can be concluded that the accelerated lifetime prediction method MiDAcLife can also be extended to more inhomogeneous materials such as cast materials. However, more complex damage mechanisms must be taken into account in the calculations in order to prevent an under-dimensioning of components as a result of an overestimated lifetime. A simplified assumption of $D = 1$ is not permissible at this point, which means that the investigation of the appropriate damage parameter is of great

importance for the quality of the lifetime prediction. Considering the illustration according to figure 4.32, the examination of the material response in order to determine the damage factor can be inferred as a promising approach.

Table 4.19: Summary of the parameters regarding the damage factor determination based on an integral consideration of the material response of an EN-GJS-1050-6

EN-GJS-1050-6			
Specimen number	Norm. material response	Max. value distribution	Damage factor
1	2.357	3.402	1.443
2	1.910		1.781
3	6.607		0.515
4	9.370		0.363

5 Summary and Outlook

5.1 Summary

The presented doctoral thesis deals intensively with the possibilities of an accelerated provision of fatigue data. Combining non-destructive and destructive materials testing can therefore significantly reduce the amount of specimens and consequently achieve remarkable cost savings. A large proportion of the presented research is carried out on un- and low alloyed steels with particular focus on the 20MnMoNi5-5 steel. This ferritic-bainitic steel was mainly used in spraylines of German nuclear power plants. In order to reliably evaluate fatigue properties of a material, a precise knowledge of its microstructural composition is required. For this purpose, both light- as well as scanning electron microscopic investigations were applied, which are described in chapter 3.1. Apart from that, an important and central aspect of this research is the consideration of damage-relevant factors such as surface integrity. For this reason, a total of five batches regarding different surface conditions were machined and also characterised in chapter 3.1. In addition to that, the development of a new lifetime prediction method that enables the provision of virtual S-N curves based on a demonstrably reduced amount of specimens is an overarching objective of this research. Based on the journal contributions of part II and the preceding discussion section, a variety of research hypotheses can be formulated, which were examined and validated within the scope of the presented thesis. A selection of central key research aspects is listed below.

- The information content regarding fatigue testing of metallic materials can demonstrably be increased by the application of NDT-related measuring techniques as an extension to conventional destructive methods.
- The acquired process-orientated data can be used as an input for newly developed lifetime prediction methods and therefore lead to a significant improvement concerning the prediction quality.
- The newly developed lifetime prediction method MiDAcLife, which is based on the linear damage accumulation model according to Palmgren and Miner, enables an accelerated provision of fatigue data based on only one fatigue test.
- By integrating the material response into the approach according to Palmgren and Miner instead of the control variable, virtual numbers of cycles to failure can be calculated in addition to the more localised consideration of fatigue properties.
- Despite various influencing factors such as roughness, carbon content, alloying elements or heat treatment, the lifetime prediction methods MiDAcLife and StressLife are characterised by an enhanced prediction quality, which makes them comparable to conventionally determined S-N curves.
- The influence of the surface roughness on the fatigue behaviour of a 20MnMoNi5-5 steel can evidently be shown.
- By calculating a Fatigue Notch Factor and the newly introduced specific hardness of a material, surface roughness parameters can be integrated into the lifetime prediction method MiDAcLife and therefore enable a generation of virtual S-N curves based on only one reference condition.

- The proposed lifetime prediction methods are capable of the extension to additional damage mechanisms concerning further material classes such as cast materials.
- Despite the reduced amount of required specimens in case of a lifetime prediction according to MiDAcLife, statistical approaches can be integrated and therefore lead to the possibility of generating lifetime prediction bands.

Especially journal contribution 1 and journal contribution 3 provide a noteworthy input to the integration of non-destructively determined measurement signals into the lifetime prediction. While the discussion section is mainly based on thermographic data, the sensitivity of electrical resistance methods could be demonstrated within these publications. Furthermore, journal contribution 3 proved that NDT-related methods are able to provide additional information compared to conventional strain-based methods, especially in terms of low plastic deformations. Monitoring the material response as a result of dynamic loading also enables the estimation of important characteristic values as well as the assessment of the material behaviour. Especially the reliability of the accelerated estimation of fatigue strength could be shown in context of this thesis. Besides that, the integrated material response was used as an assessment parameter to evaluate the influence of different damage-relevant factors.
A primary focus of this research is the development of a new lifetime prediction method called MiDAcLife (chapter 3.2.2 and journal contributions 2-4), based on the approach according to Palmgren and Miner. Because of the assumption of linearity, the approach proposed by Palmgren and Miner leads to significant deviations in the predicted results. However, the integration of the material response within the framework of MiDAcLife leads to a non-linear consideration of the damage progression, enabling a high level of accuracy in the lifetime prediction. In addition to that, the method is characterised by the fact that a process-orientated parameter is included in the calculation instead of the control variable. This allows very local and individualised conclusions to be drawn regarding the fatigue behaviour. The number of required specimens can also be reduced significantly using the new method MiDAcLife, which results in time and cost savings. Besides the development of MiDAcLife, the prediction method StressLife was modified within this thesis (journal contribution 1). It provides another example of using the material response as an input parameter of the lifetime prediction. Besides the data resulting from load increase tests, the material response after half of the number of cycles to failure from different constant amplitude tests was used.
To assess the prediction quality of the lifetime prediction methods MiDAcLife and StressLife, the calculated date points were examined within the journal contributions and the discussion section using conventionally conducted experimental constant amplitude tests. Therefore, the high degree of correlation between experimental and virtual data points could be demonstrated. Apart from that, the discussion section includes a comparison of conventionally determined S-N curves and the S-N curves according to the proposed accelerated methods. Especially regarding MiDAcLife, a precise agreement was observed. The increased deviation of the data points according to StressLife could be explained by the multi-parametric approach, which differs from the purely elastic approach of MiDAcLife and the conventional method. In order to further validate the newly developed method MiDAcLife, various factors such as different carbon content, the influence of alloying elements and heat treatments were considered within this research. The validity of the method was demonstrated independently of the previously mentioned influencing factors.
The surface roughness of a specimen is an important factor that can significantly influence fatigue behaviour of steels, particularly in the high cycle fatigue regime. The investigations presented in

chapter 4.2 led to the conclusion that the surface roughness must exceed a defined threshold value in order to have a significant effect on the lifetime of the specimen. While the S-N curves of batches N3-N7 were characterised by a similar curve progression, a highly notable lifetime reduction could be observed regarding N8 and N9. The findings are particularly important from a manufacturing point of view, as they allow manufacturing parameters to be adjusted accordingly, and therefore ensuring a more effective manufacturing process. In order to be able to include the lifetime reduction into the evaluation according to MiDAcLife, roughness was modelled mathematically using a Fourier-transformation (journal contribution 4). This allowed roughness to be included as Fatigue Notch Factor in the calculation of the slope concerning the virtual S-N curve based on the reference surface N3. To determine the location parameter of the S-N curve, a new variable, the specific hardness, was introduced, which allows an estimation of the fatigue strength of a material. In particular, the comparison of the virtual generated data with conventional data in chapter 4.2 highlighted the advantages of this process-orientated approach.
Within the journal contributions of part II, lifetime prediction methods could only be validated on different un- and low alloyed steels. These materials are characterised by similar failure mechanisms, especially in the high cycle fatigue regime. Considering other materials, such as cast iron, however, additional aspects must be taken into account because of the inhomogeneity of the microstructure (e.g. graphite matrix delamination). For this reason, MiDAcLife was examined regarding its applicability to cast materials in chapter 4.5. Especially, the significantly increased scattering of the material compared to steels is challenging. Comparable to chapter 4.3, a methodology was developed that enables a consideration of the scattering within the lifetime by introducing lifetime prediction bands, despite the significantly reduced amount of specimens.

5.2 Outlook

On the basis of the presented results, four central research aspects for future research projects can be derived. Even though the applicability to casting materials already provides a first step towards the expansion of MiDAcLife to additional material groups, the method is to be applied to further materials in future research. In this context, an expansion with regard to additively manufactured specimens, as well as austenitic materials and welded components, would be a promising approach, particularly in view of the nuclear energy origins of the research projects EKusaP. In this case, additional factors such as a highly increased material response in terms of austenitic specimens or unmelted powder nests of additively manufactured specimens would have to be considered in the lifetime prediction. From a manufacturing point of view, the influence of manufacturing parameters of an SLM process is also of great importance.
Apart from that, this thesis is intended to provide the basis for the provision of individualised S-N curves. In order to ensure a cost-effective but reliable lifetime prediction, different influencing factors are to be investigated in future research and included as parameters into the virtual calculations. This has already been demonstrated for the influence of surface roughness considering the Fatigue Notch Factor. In future, further variables such as the ambient temperature, the testing frequency or the presence of a corrosive medium should be integrated into MiDAcLife as factors or functions.
As a result of the drastically reduced number of specimens, the proposed method needs to be further developed regarding statistical validation. By improving the integration of statistical approaches, the lifetime prediction can be significantly optimised with regard to the assessment of

the scattering. Therefore, a compromise must be found between the number of specimens required to obtain reasonable results and the specimen reduction in order to minimise time- and cost-effort. The last aspect to be mentioned is the load sequence of the fatigue tests. As part of the investigations regarding StressLife and MiDAcLife, load increase tests with a step wise increase of the load amplitude were selected. Due to the pure increase of the stress amplitudes, sequence effects cannot be taken into account sufficiently within the calculations. In future research, the load sequence should be selected in a progressively more complex manner, building on a simple load sequence, in order to ensure a step towards a reliable component design with regard to operationally relevant loading conditions.

PART II

Journal Contribution I

StressLife: A Short-Time Approach for the Determination of a Trend S-N curve in and beyond the HCF Regime for the Steels 20MnMoNi5-5 and SAE 1045

Materials

F. Weber[1,2], J. Koziol[1], P. Starke[1,2]

[1] Department of Material Sciences and Materials Testing (WWHK), Institute QM[3] University of Applied Sciences Kaiserslautern, Schoenstr.11, Kaiserslautern, 67659, Germany

[2] Faculty of Natural Sciences and Technology, Saarland University, Campus, Saarbrücken, 66123, Germany

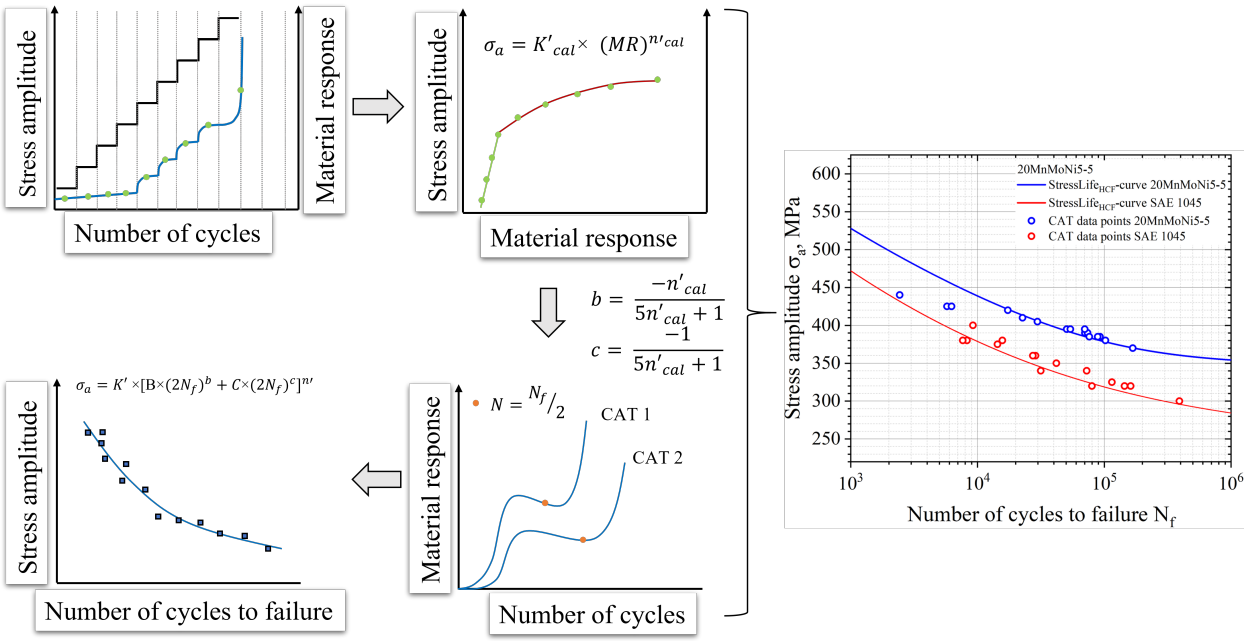

StressLife: A Short-Time Approach for the Determination of a Trend S-N curve in and beyond the HCF Regime for the Steels 20MnMoNi5-5 and SAE 1045

Abstract

Within the scope of this research, a new short-time procedure designated as $\text{StressLife}_{\text{HCF}}$ was developed. Through a combination of classic fatigue testing and non-destructive monitoring of the material response due to cyclic loading, a process-oriented fatigue life determination can be carried out. A total of two load increase and two constant amplitude tests are required for this procedure. By using data from non-destructive measurements, the parameters of the elastic approach according to Basquin and the plastic approach according to Manson-Coffin are determined and combined within the $\text{StressLife}_{\text{HCF}}$ calculation. Furthermore, two additional variations of the $\text{StressLife}_{\text{HCF}}$ method were developed in order to be able to accurately describe the S-N curve over a wider range. The main focus of this research is on a 20MnMoNi5-5 steel, which is a ferritic-bainitic steel (1.6310). This steel is widely used for spraylines in German nuclear power plants. In order to validate the findings, tests were also performed on an SAE 1045 steel (1.1191).

6.1 Introduction

For components, structures and specimens subjected to dynamic loads, the understanding of fatigue behavior is of great importance to avoid unexpected material failure. The well-known S-N curve, also called Wöhler curve, is typically used to determine the lifetime of materials, which is necessary for industrial design or material selection for specific applications. It shows the relation between the applied load and the fatigue life of a material [21,245]. The S-N curve is typically separated into different ranges, which differ mainly in their fatigue damage process. Conventionally, experiments in the Low Cycle Fatigue regime (LCF) are strain-controlled. The mathematical description is based on the approach of Manson and Coffin, which is given in equation 6.1 [17–19]. The equation is composed of the following parameters: the plastic strain amplitude $\varepsilon_{a,p}$, the fatigue ductility coefficient ε'_f and the fatigue ductility exponent c.

$$\varepsilon_{a,p} = \varepsilon'_f \cdot (2 \cdot N_f)^c \tag{6.1}$$

In contrast to the LCF regime, experiments in the Very High Cycle Fatigue (VHCF) regime are mainly carried out stress-controlled. Due to the low stress amplitudes, a purely elastic description of the fatigue behavior according to Basquin is assumed [11]. With the stress amplitude σ_a, the Basquin coefficient B and the fatigue strength exponent b, equation 6.2 can be obtained.

$$\sigma_a = B \cdot (2 \cdot N_f)^b \tag{6.2}$$

The High Cycles Fatigue (HCF) regime of an S-N curve is characterised by an elastic-plastic material behavior. Therefore, a superimposition of the approaches according to Basquin (equation 6.2) and Manson-Coffin (equation 6.1) is used in order to describe the S-N curve. The resulting Manson-Coffin-Basquin approach is given in equation 6.3 [246].

$$\varepsilon_{a,t} = \varepsilon_{a,e} + \varepsilon_{a,p} = \frac{\sigma'_f}{E} \cdot (2 \cdot N_f)^b + \varepsilon'_f \cdot (2 \cdot N_f)^c \tag{6.3}$$

In equation 6.3, $\varepsilon_{a,t}$ designates the total strain amplitude, whereas $\varepsilon_{a,e}$ is the elastic strain amplitude. A variety of approaches already exists for the determination of the required parameters of equation 6.3. In 1965, Manson developed the four-point correlation method. It uses four different points on the elastic and plastic curves of the strain-number of cycles plot. Each point is determined from tensile test data [247, 248]. Based on this approach, a variety of other calculation methods have developed which determine the parameters from equation 6.3 [247, 249–252]. Furthermore, there are calculation models that take the hardness of the materials instead of the tensile strength into account. As an example, the method according to Roessle [253] can be considered here. Moreover, energy-based models are used to describe the fatigue behavior of a material. In contrast to a correlation of the fatigue life with the stress or strain, these approaches have the aim to correlate the fatigue life with the plastic work done per cycle. In order to describe the damage during the fatigue process, Ellyin and co-workers introduced a special form of the cyclic strain density as a suitable parameter. The total strain energy density ΔW_t results from the sum of the plastic portion of the strain energy density ΔW_p and the elastic portion ΔW_e [254–257].

$$\Delta W_t = \Delta W_e + \Delta W_p \tag{6.4}$$

The advantage of these methods is that the fatigue behaviour can be described in the LCF as well as in the HCF regime. For the reasons mentioned above, certain parallels can be drawn between the energy-based approaches and the approaches presented in this paper. Due to the thermal conductivity of metallic materials and the fact that nearly all the energy introduced is dissipated in terms of heat (approximately 90-95 %), strain and temperature measurements correlate with each other. Similar to the energy-based approaches, the modifications of the StressLife method also attempt to obtain a accurate description of the S-N curve in the different regimes.

The goal of the newly developed short-time procedure $\text{StressLife}_{\text{HCF}}$ (HCF = High Cycle Fatigue) is, to enable a stress-controlled elastic-plastic description of an S-N curve in the HCF-regime with as few specimens as possible. Conventional methods use a large number of specimens, which makes the generation of an S-N curve a very time- and cost-consuming procedure. In comparison, the developed method $\text{StressLife}_{\text{HCF}}$ requires only four fatigue tests to calculate all parameters of the S-N curve. The experiments consist of two load increase tests (LIT) and two constant amplitude tests (CAT). An advantage of the new method compared to the previously mentioned methods is that nondestructive measurement techniques (NDT) are used to detect the material response to dynamic loading. The values determined from this are directly included in the lifetime evaluation. This process-oriented view of the fatigue process instead of a lifetime-oriented view can increase the information content significantly. The $\text{StressLife}_{\text{HCF}}$ method evolved from the existing short-time method $\text{StressLife}_{\text{tc}}$ (tc = trend curve) whose explanation can be found in [258]. In addition to the procedure $\text{StressLife}_{\text{HCF}}$, the two variations $\text{StressLife}_{\text{LHC}}$ (LHC = Low and High Cycles) and $\text{StressLife}_{\text{HVC}}$ (HVC = High and Very High Cycles) were developed within the framework of the current research. The aim of these methods is to improve the representation of the transition areas of the S-N curve. The department of materials science and materials testing at the University of Applied Sciences Kaiserslautern has already developed a number of short-time

procedures over recent years such as SteBLife, StrainLife and MiDAc-Life which can be found in [236,238,259,260]. The StressLife method described in this paper differs from the other methods because the fatigue properties are described by an elastic-plastic approach, whereas SteBLife and MiDAc-Life are only based on an elastic and linear approach, respectively. The difference to StrainLife is that the experiments are performed under stress-controlled condition instead of strain-controlled. Furthermore, the StressLife method is clearly distinguished from previous methods by the calculation of the S-N curve in the transition regions.

6.2 Materials and Methods

6.2.1 Materials

The main focus within this research is on the 20MnMoNi5-5 steel (1.6310), which is widely used for spraylines in German nuclear power plants. The steel is mostly comparable to the SAE 5120 considering the chemical composition. To demonstrate the validity of the $\text{StressLife}_{\text{HCF}}$ procedure, tests were additionally performed on the steel SAE 1045 (1.1191). The chemical composition of both materials can be seen in Table 6.1.

Table 6.1: Chemical composition in wt. – % of the 20MnMoNi5-5 and SAE 1045 steels according to own analysis and in comparison with ASTM A533B and DIN EN 10083-1

Material		C	Si	Mn	Cr	Ni	Mo	S
1.6310	Certificate:	0.218	0.246	1.385	0.076	0.762	0.487	0.003
	ASTM:	0.190	0.200	1.290	0.120	0.800	0.530	0.008
1.1191	Certificate:	0.470	0.230	0.720	0.670	0.070	0.014	0.013
	DIN:	0.500	0.400	0.800	0.400	0.400	0.100	0.035

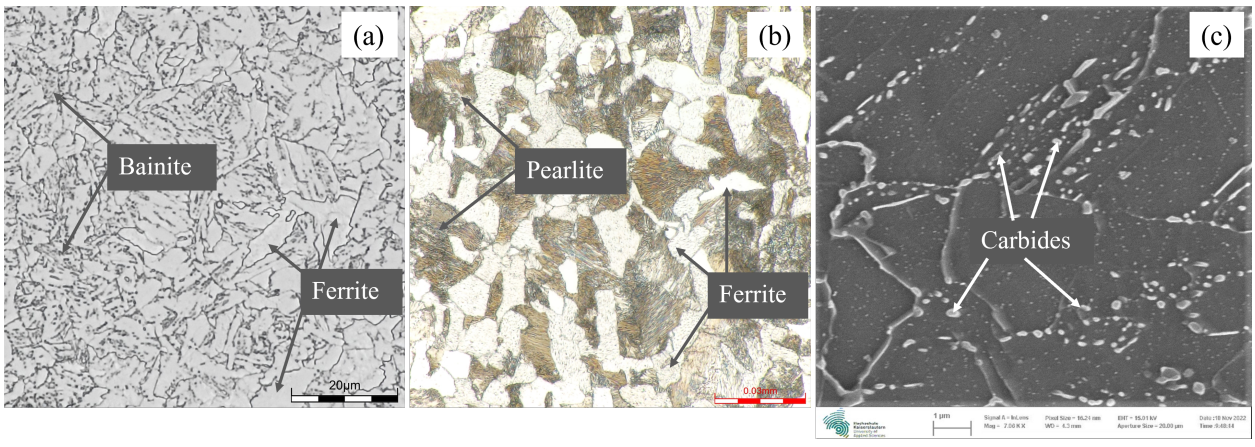

Figure 6.1: Micrographs of (a): quenched and tempered steel 20MnMoNi5-5; (b): normalised SAE 1045; (c): SEM-micrograph 20MnMoNi5-5 including carbides.

The applied 20MnMoNi5-5 steel has a ferritic-bainitic microstructure, whereas the SAE 1045 has a ferritic-pearlitic structure. Micrographs of both materials, which were taken by a digital microscope type DSX1000 by the company EVIDENT (EVIDENT Europe, Hamburg, Germany), are given in Figure 6.1. The ferritic-bainitic structure of the 20MnMoNi5-5 steel can be identified in Figure 6.1(a). It results from a water-spray quenching of the pipes from which the specimens of the 20MnMoNi5-5 were taken. The microstructure consists of lighter areas, which represents the ferritic portion, and darker areas, which show the bainitic portion. The difference between the bainitic and the pearlitic structure can be derived very nicely from the two Figures 6.1(a) and 6.1(b). While the bainitic structure is irregular and rather needle-shaped, the pearlite has a clear structure arranged in lamellae. The lighter areas in Figure 6.1(b) represent the ferrite analogue to Figure 6.1(a). According to [261, 262], carbides usually form as an additional phase in steels with a bainitic structure. Taking the limited diffusion possibilities of substitutional soluted atoms into account, it is assumed that most of the carbides are present as cementite Fe_3C. Due to the alloy composition of the material, additional Mn and Mo carbides are assumed. For an improved resolution of the carbides, a SEM image was taken using a GEMINI by ZEISS (Carl Zeiss, Oberkochen, Germany). The microstructure including the carbides can be seen in Figure 6.1(c).

6.2.2 Methods

All fatigue tests (LIT as well as CAT) were performed at a testing frequency of 5 Hz at ambient temperature. The testing rigs are servo-hydraulic testing systems type EHF-L and EHF-U, with a maximum load capacity of 20 kN and 50 kN by the company Shimadzu (Shimadzu Europe, Duisburg, Germany). Both LIT and CAT were carried out stress controlled at a load ratio of R=-1, using a sinusoidal load-time-function. For the measurement of the cyclic deformation curves of the materials, different NDT-methods were used. The main focus is on the thermographic evaluations which operate with an IR-camera of the type TIM450 by Micro-Epsilon (Micro-Epsilon Messtechnik GmbH & Co. KG, Ortenburg, Germany) within the experiment. Furthermore, the strain was determined by means of a tactile extensometer and on selected tests by the use of a DIC-system by LIMESS (LIMESS Messtechnik und Software GmbH, Krefeld, Germany). The whole setup is given in Figure 6.2.
To record information in terms of the change in temperature, the specimens surface temperature is measured in three sections. T_1 is the temperature in the middle of the gauge length, whereas T_2 and T_3 transmit the temperature information at each shaft of the specimen. Because of the fact that the deformation in the shafts are purely elastic due to the significantly larger diameter, equation 6.5 can be used to describe the material response to cyclic loading based on the change in temperature ΔT.

$$\Delta T = T_1 - 0.5 \cdot (T_2 + T_3) \tag{6.5}$$

The information from the change in temperature is from great importance because it is closely linked to microstructural changes due to cyclically induced deformations. The theoretical background of the temperature measurement can be deduced from the consideration of the stress-strain hysteresis loop. The area of the hysteresis loop describes the cyclic plastic deformation energy, which is transformed into internal energy U and heat energy Q. The internal energy enables microstructural changes in dislocation structure and density, voids and pores, and micro- up to macro-cracks [178]. The temperature measurement is ideally suitable for the characterisation of the material response

to cyclic loading because of the good heat conduction properties of metallic materials. The predominant portion of 90 % to 95 % [166] of the plastic deformation work dissipates as heat and thus leads to an increase in specimen temperature. The remaining part is converted as internal energy, which is the cause of microstructural changes (e.g. dislocation reactions, micro- and macro-crack formation and propagation).

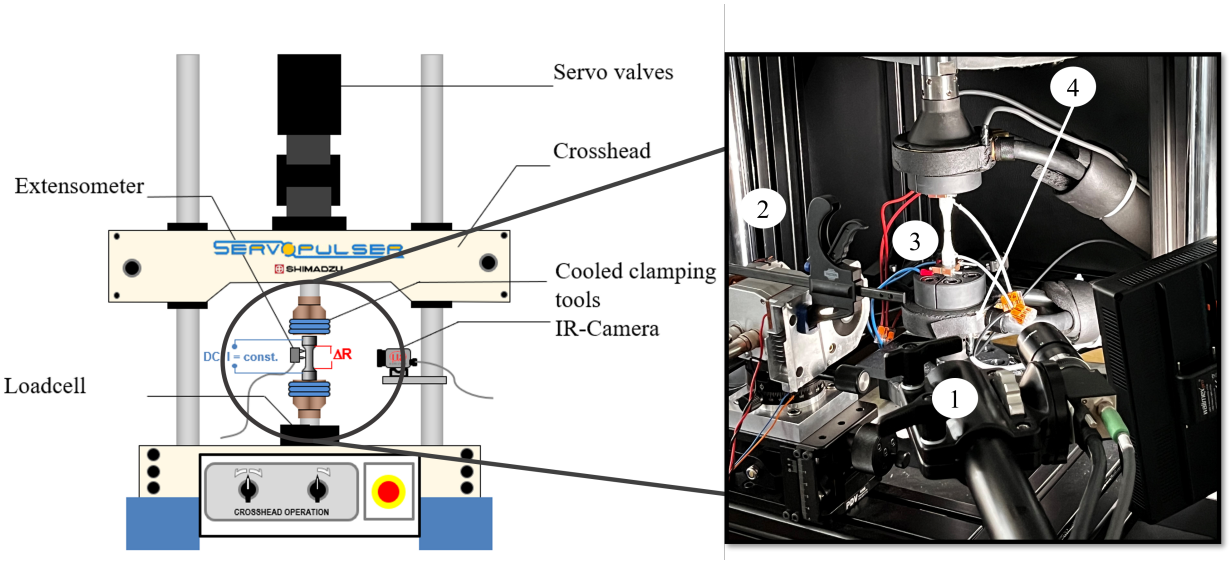

Figure 6.2: Experimental setup servohydraulic testing rig (EHF-L 20kN). (1) DIC system and illumination; (2) IR-camera thermoIMAGER TIM 450; (3) Electrical Resistance measurement; (4) Watercooled clamps

6.2.3 Fatigue life calculation method StressLife$_{\mathrm{HCF}}$

StressLife$_{\mathrm{HCF}}$ provides the basis for the complete evaluation process of the S-N curve, whereby the procedure is basically a modification of the original StressLife$_{\mathrm{tc}}$-method. In order to generate a trend S-N curve with this method, only four specimens were required. As a first step, a LIT needs to be performed.The starting stress amplitude of the LIT must be well below the fatigue strength of the material. In general, the parameters for load increase tests can be estimated along the following criteria. The empirical relationship applicable here was developed on the basis of numerous results from completed investigations at the Department of Material Science and Materials Testing and validated on various unalloyed and low-alloyed steels (steels without phase transformation processes). Here, both the yield strength ratio and the ratio between the fatigue strength and yield strength (both are strongly dependent on the respective material condition) are included and correlated via the hardness (Vickers) with a correlation factor Z. For ductile materials, Z is 1.56 MPa $\cdot$ HV30^{-1}, for medium strength materials 1.44 MPa $\cdot$ HV30^{-1} and for high-strength materials MPa $\cdot$ HV30^{-1}.

$$\sigma_{a,start,max} = HV \cdot Z - 150\,MPa \tag{6.6}$$

The resulting starting stress amplitude $\sigma_{a,start,max}$ indicates the respective maximum value (but may also be lower). In order to ensure a good comparability, most LITs are carried out with

$\sigma_{a,start} = 100\,MPa$, in the case that the materials fulfil the criteria mentioned above. With regard to the step length in the LIT (at 5 Hz), 6000 load cycles for pure and predominantly softening materials, 9000 load cycles for alternating cyclic softening and hardening (predominantly ductile material states) have proven to be appropriate, since energetically stable states (especially with regard to the dissipated energy) occur within these cycle ranges. During this experiment, the material response on the cyclic loading as well as the step-wise load increase is measured in terms of the applied measurement techniques (thermography, resistometry, DIC). The original StressLife$_{\mathrm{tc}}$-method only uses one LIT. Here, the problem arises in particular with brittle material behaviour, as the generated data points in the plastic range are evidently too low and therefore an evaluation can only be carried out inadequately. For this reason, two LITs were used in the StressLife$_{\mathrm{HCF}}$ method. The following boundary conditions for the two LITs must be taken into account: $\sigma_{a,start,2} > \sigma_{a,start,1}$ and $\Delta\sigma_1 > \Delta\sigma_2$. This adjustment ensures an improvement in the quality of the final evaluation, especially in the elastic-plastic range. The measured cyclic deformation curve from the two LITs can be used as a first estimation of the fatigue strength of the examined material and to assess the appropriate stress amplitudes for the CATs [172, 263]. The procedure for the determination of a trend S-N curve in the HCF regime according to the StressLife$_{\mathrm{HCF}}$ method is given in Figure 6.3.

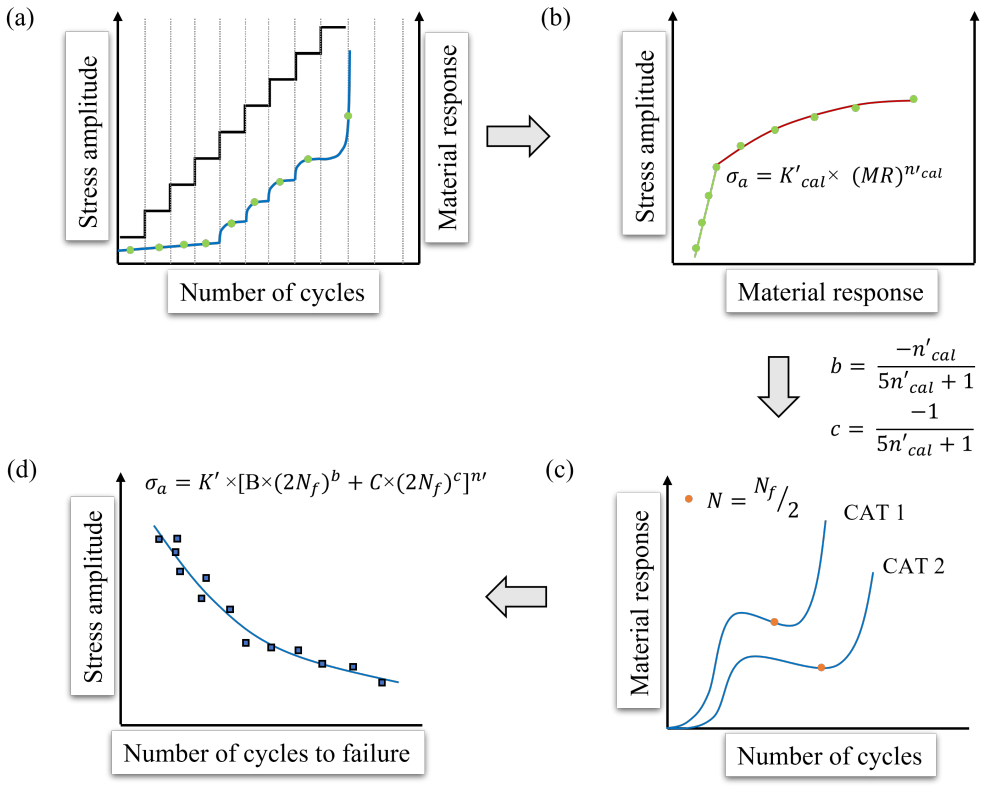

Figure 6.3: Schematic representation of the StressLife$_{\mathrm{HCF}}$ method for calculating a trend S-N curve in the HCF regime with four specimens. (a) Slope of the stress amplitude and the material response of a LIT; (b) Stress amplitude of each load step plotted against the average value of the material response; (c) Cyclic deformation curve of both required CAT including the materials response at half of the cycles to failure; (d) S-N curve according to StressLife$_{\mathrm{HCF}}$ including CAT data points for validation.

A distinction was made between the cyclic hardening exponent n'_{cal} and the cyclic hardening coefficient K'_{cal}, which are only used for the calculation of the parameters b and c, and the parameters n' and K', which are used in order to describe the S-N curve.
Figure 6.3(a) shows that the material response increases in the elastic-plastic range above a certain stress amplitude. Therefore, the fatigue strength can be estimated as the stress amplitude at which no material response occurs at last. In order to calculate the fatigue strength exponent b and the ductility exponent c, the average values of the material response of each load step is plotted against the corresponding stress amplitude, which can be seen in Figure 6.3(b). It should be noted here that the use of the mean value is only permissible since there is no extensive cyclic hardening within the load steps. However, this relation is strongly influenced by the materials' condition. The more brittle the material behavior is, the less pronounced is the plastic range. Being different from StressLife$_{\mathrm{tc}}$, only the elastic-plastic behavior within the generalized Morrow plot is considered for the HCF regime. In order to take the material condition into account in the calculation of the fitting parameter n'_{cal}, a weighting of the values for the elastic and the plastic portions is made. For this purpose, the elastic range, which according to the authors is defined as the last five elastic data points, is fitted using an allometric fit. The plastic range is fitted in an analogue way. At this point, the value α_{pl} is introduced for the quantitative assessment of the plastic range. It shows the amount of data points in the plastic region of a LIT. With the slope of the elastic (n_{el}) and the plastic range (n_{pl}), the hardening exponent n_{total} for the HCF regime can be determined according to equation 6.7.

$$n_{total} = \frac{5}{\alpha_{pl} + 5} \cdot n_{el} + \frac{\alpha_{pl}}{\alpha_{pl} + 5} \cdot n_{pl} \tag{6.7}$$

According to Morrow [243], the weighted hardening exponent n_{total} from equation 6.7 can be used to calculate the required parameters from equation 6.8 and 6.9.

$$b = \frac{-n_{total}}{5 \cdot n_{total} + 1} \tag{6.8}$$

$$c = \frac{-1}{5 \cdot n_{total} + 1} \tag{6.9}$$

In the case of equation 6.8 and 6.9, it must be noted that these are empirical relations and are therefore subject to error. However, due to the good agreement of the data of previous research, this influence is neglected. The specification on only five data points in the elastic range is necessary, as the evaluation would otherwise be dependent on the start amplitude of the LIT. Figure 6.3(c) shows an example of what cyclic deformation curves of CATs can look like (in the case of normalized ferritic-pearlitic steels). The slope starts with an increase of the material response, corresponding to a cyclic softening of the material due to dislocation reactions. A distinction can be made between dislocation movement, formation of dislocation walls and cells, as well as changes in the dislocation density. The cyclic softening process is followed by a cyclic hardening process which is caused by the mutual obstruction of the dislocations, until the material finally shows secondary cyclic softening in consequence of macroscopic crack formation and propagation. An advantage of calculating the S-N curve on the basis of the CATs is that transient cyclic effects in the plastic regime of the LIT can be compensated, thus ensuring high accuracy of the results. Due to the proven correlation

between the plastic strain amplitude and the change in temperature, the material response can be separated into two portions in analogy to the strain-life approach [64]. The total response M_t is given by the summation of the elastic (M_{el}) and the plastic portion (M_{pl}) [264].

$$M_t = M_{el} + M_{pl} \tag{6.10a}$$

$$M_t = \frac{\sigma'_f}{E} \cdot (2N_f)^b + \varepsilon'_f \cdot (2N_f)^c \tag{6.10b}$$

$$M_t = B \cdot (2N_f)^b + C \cdot (2N_f)^c \tag{6.10c}$$

The elastic content of equation 6.10a can be described by the generalised Basquin equation, whereas the plastic content is described by the Manson-Coffin equation. To determine the two coefficients B and C, equation 6.10c must be applied to both CATs. The material reaction needs to be tapped at a defined stage. Within this research, the definition is $N = 0.5 \cdot N_f$. By rearranging equation 6.10c, equation 6.11 and 6.12 can be obtained in order to calculate the missing parameters.

$$C = \frac{(2N_{f,1})^b \cdot \Delta T_2 - (2N_{f,2})^b \cdot \Delta T_1}{(2N_{f,2})^c \cdot (2N_{f,1})^b - (2N_{f,1})^c \cdot (2N_{f,2})^b} \tag{6.11}$$

$$B = \frac{\Delta T_1 - C \cdot (2N_{f,1})^c}{(2N_{f,1})^b} \tag{6.12}$$

Based on this method, all parameters for the generation of a trend S-N curve (Figure 6.3(d)) in the HCF regime can be determined. The final expression used to describe the S-N curve is given by equation 6.13.

$$\sigma_a = K' \cdot [B \cdot (2N_f)^b + C \cdot (2N_f)^c]^{n'} \tag{6.13}$$

6.2.4 Fatigue life calculation method StressLife$_{\mathrm{LHC}}$

Based on the StressLife$_{\mathrm{HCF}}$ method, further methods can be derived, which extend the description of the S-N curve beyond the HCF regime. In order to describe the S-N curve in the transition area to the LCF regime, StressLife$_{\mathrm{LHC}}$ (LHC = Low and High Cycles) was developed. The schematic explanation of this method is given in Figure 6.4. It is assumed that the slope of the S-N curve must be different in the LCF and HCF regime due to different damage processes.

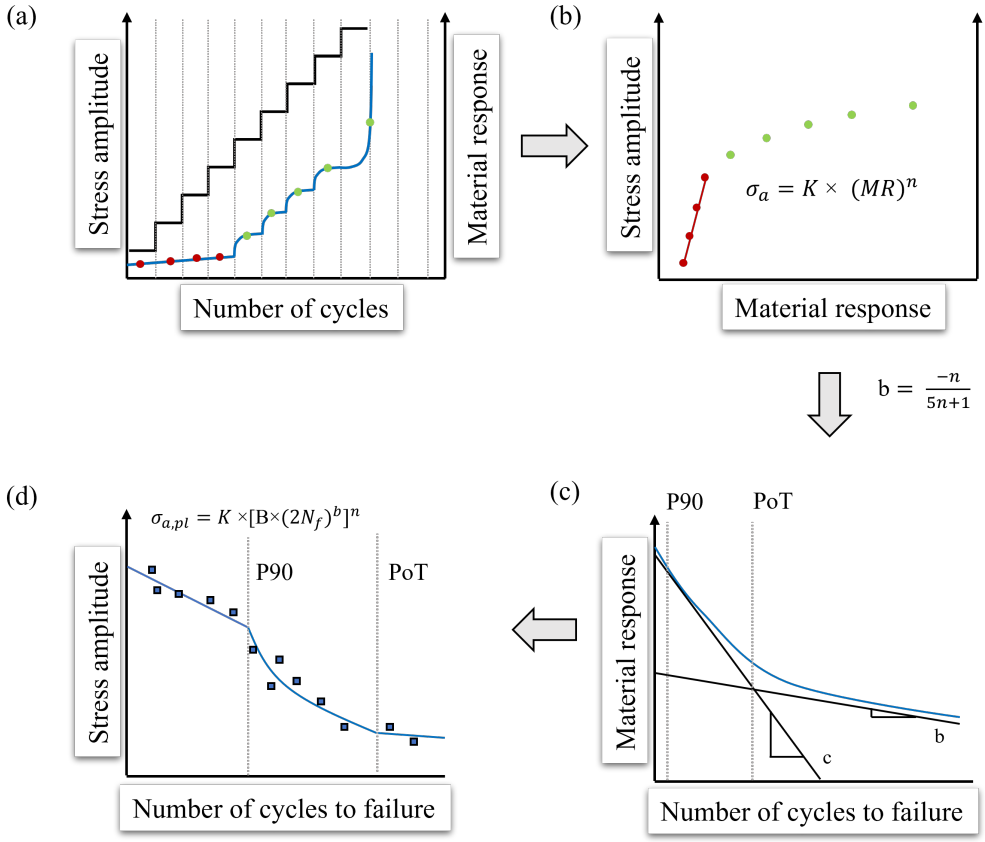

Figure 6.4: Schematic representation of the StressLife$_{\mathrm{LHC}}$ method for calculating a trend S-N curve in the transition range to the LCF regime with four specimens. (a) Slope of the stress amplitude and the material response of a LIT; (b) Stress amplitude of each load step plotted against the average value of the material response; (c) Elastic, plastic and total material response plotted against the number of cycles to failure including the PoT and P90; (d) S-N curve according to StressLife$_{\mathrm{LHC}}$ including CAT data points for validation in the transition range.

In this method, a LIT is carried out in an analogue procedure to StressLife$_{\mathrm{HCF}}$ (Figure 6.4(a)). However, only data points from the plastic region are used in order to obtain the fitting data for the calculation of c, which is shown in Figure 6.4(b). Because of the fact that in the transition to the LCF regime plastic deformation dominates, the elastic portion is neglected and therefore the fatigue strength exponent does not need to be calculated. Figure 6.4(c) shows the elastic, plastic and total material response plotted against the number of cycles to failure. At this point, two definitions might be introduced. The point of transition (PoT) is defined as the number of cycles at which the elastic and the plastic portion of the material response are equal. In order to be able to define the point of the S-N curve at which the slope changes in the transition area, P90 is introduced. It is defined as the point at which the plastic portion accounts for 90 % of the total material response. With the help of the anchor point from StressLife$_{\mathrm{HCF}}$ at the P90 point and the known slope c, which is calculated by the fitting parameter from Figure 6.4(b), the S-N curve in the transition area to the LCF regime can be identified. Equation 6.14 describes the S-N curve and

takes only plastic parameters into account.

$$\sigma_a = K' \cdot [C \cdot (N_f)^c]^{n'} \tag{6.14}$$

6.2.5 Fatigue life calculation method StressLife$_{\mathrm{HVC}}$

Contrary to the natural behavior of ferritic steels, the determined S-N curves according to StressLife$_{\mathrm{HCF}}$ do not form a plateau at the transition to the VHCF regime. Because of this outcome, it is assumed that there must be another change of the slope when the elastic portion of the material response starts to dominate in comparison to the plastic portion. The approach of the StressLife$_{\mathrm{HVC}}$ method (HVC = High and Very High Cycles) is to adopt a purely elastic description of the S-N curve, as the number of cycles of failure increases. A schematic overview of this method is given in Figure 6.5.

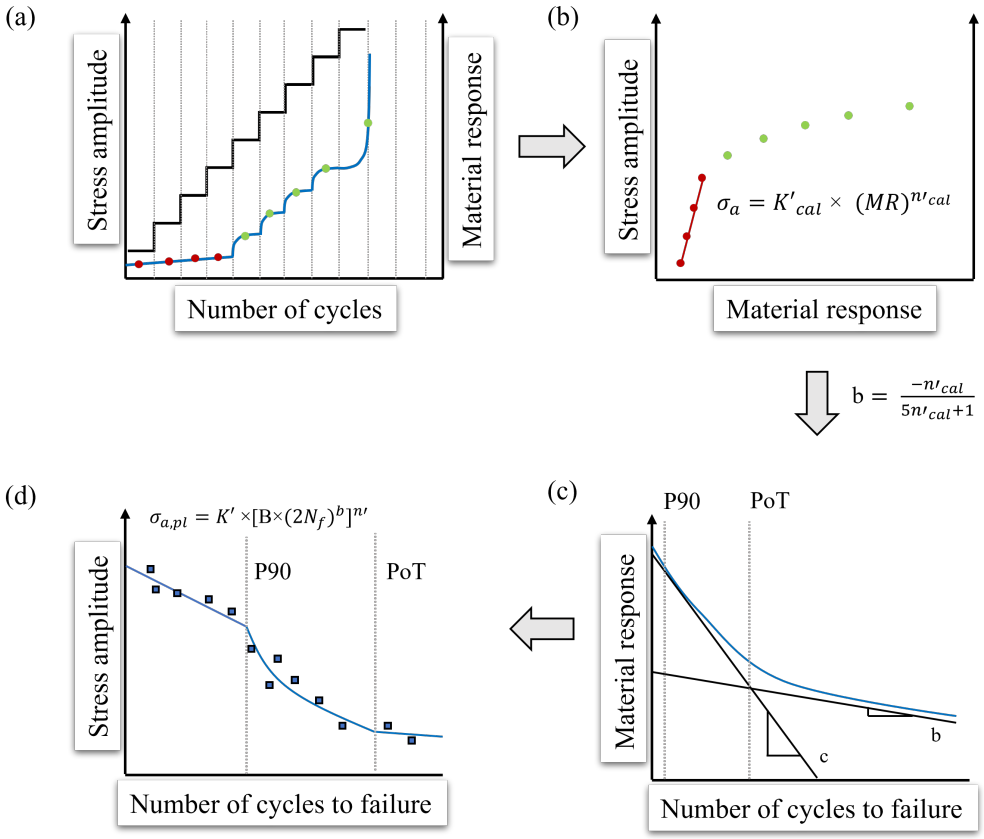

Figure 6.5: Schematic representation of the StressLife$_{\mathrm{HVC}}$ method for calculating an trend S-N curve in the transition range to the VHCF regime with four specimens. (a) Slope of the stress amplitude and the material response of a LIT; (b) Stress amplitude of each load step plotted against the average value of the material response; (c) Elastic, plastic and total material response plotted against the number of cycles to failure including the PoT and P90; (d) S-N curve according to StressLife$_{\mathrm{HVC}}$ including CAT data points for validation in the transition range.

In contrast to the previously described methods, only the elastic data points from the LIT from Figure 6.5(a) are included in the calculation for the transition to the VHCF range. It is assumed that in the VHCF regime, only damage processes with moreover elastic portions take place. For this reason, only the fatigue strength exponent b is required from the fitting parameters of Figure 6.5(b). According to Wagener and Melz [265], the PoT should be indicated as a knee-point in the order of 10^4 cycles. Below the PoT, the hysteresis loop shows a measurable plastic portion of the material response. Above this point, the plastic portion is assumed to be negligible. The elastic description of the S-N curve is given in equation 6.15.

$$\sigma_a = K' \cdot [B \cdot (N_f)^b]^{n'} \tag{6.15}$$

6.3 Results and Discussion

6.3.1 Load increase test

The basic requirement for the lifetime evaluation method according to $\text{StressLife}_{\text{HCF}}$ is always the performance of a LIT, which is given in Figure 6.6 for the two materials 20MnMoNi5-5 and SAE 1045. For simplification, the focus is on the presentation of thermographically measured data of the second of the two LIT. It should be noted that other measurement techniques, such as electrical resistance or optical strain measurements, can also be used.

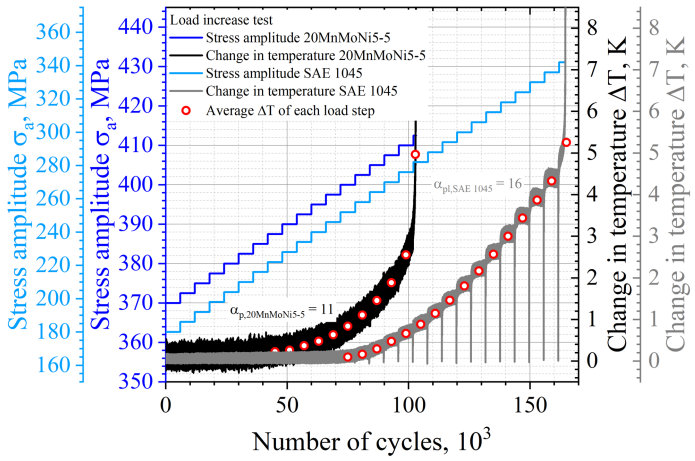

Figure 6.6: Cyclic deformation curve of a load increase test of the 20MnMoNi5-5 steel with $\sigma_{\text{a,start}} = 370\,\text{MPa}, \Delta\sigma = 2.5\,\text{MPa}$ and $\Delta\text{N} = 6 \cdot 10^3$; Cyclic deformation curve of a load increase test of the SAE 1045 steel with $\sigma_{\text{a,start}} = 180\,\text{MPa}, \Delta\sigma = 6\,\text{MPa}$ and $\Delta\text{N} = 6 \cdot 10^3$.

Figure 6.6 evidently reflects the different conditions of the two materials. The rather brittle behavior of the 20MnMoNi5-5 steel (black curve) leads to the result that only a small number of data points lie in the plastic range of the LIT, whereas the normalised SAE 1045 steel has a significantly higher portion of data points in the plastic range. The fact that the SAE 1045 steel exhibits a more pronounced material response than the 20MnMoNi5-5 steel can be explained at the microstructural

level. Although the 20MnMoNi5-5 steel has a lower carbon content than the SAE 1045 steel, it has a higher amount of alloying elements which lead to a lattice distortion and therefore less plastic deformation. Furthermore, the treatment condition of the material has a major influence on the cyclic deformation curve. The quenched-tempered condition of the 20MnMoNi5-5 leads to a higher dislocation density compared to the normalised condition of the SAE 1045. Materials with a higher dislocation density usually exhibit a pure cyclic softening. This softening process is expressed in the increase of the change in temperature in Figure 6.6. From the discussed reasons, it becomes evident that the evaluation according to StressLife depends on the material condition. In order to take this into account, the value α_{pl} is introduced. It is a tool for the quantitative evaluation of the material behaviour.

6.3.2 StressLife$_{\mathrm{HCF}}$

The basic module of the presented new StressLife methods is StressLife$_{\mathrm{HCF}}$. It is used to determine the S-N curve in the HCF regime. According to Figure 6.3, the relation of the stress amplitude and the material response can be derived from the LIT, which is shown in Figure 6.7.

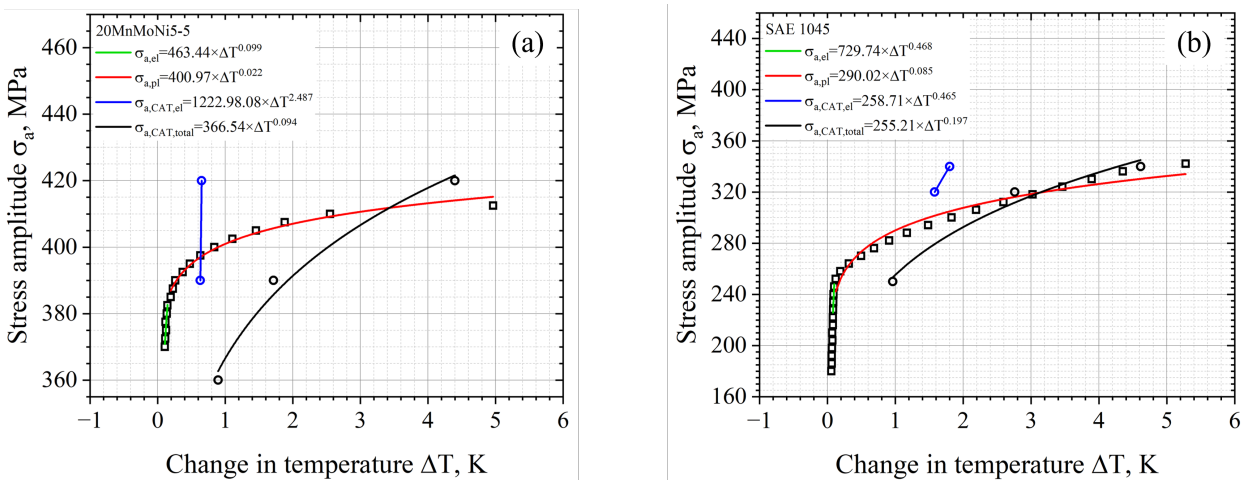

Figure 6.7: Relation between stress amplitude and change in temperature including the elastic change in temperature of the CATs and the calculated CAT for StressLife$_{\mathrm{HCF}}$ of **(a)** the 20MnMoNi5-5 steel and **(b)** the SAE 1045 steel.

Using the fit parameters from the allometric fit in the elastic and plastic range (Figure 6.7), the parameters n, b and c can be obtained according to equations 6.7, 6.8 and 6.9. The missing parameters B and C can be calculated from equation 6.11 and 6.12. The calculated parameters are summarised in Table 6.2.

According to equation 6.10c, the material response is composed of an elastic portion, described by Basquin and a plastic portion described by Manson-Coffin. Both, as well as the slope of the total material response are given in Figure 6.8(a) and (b).

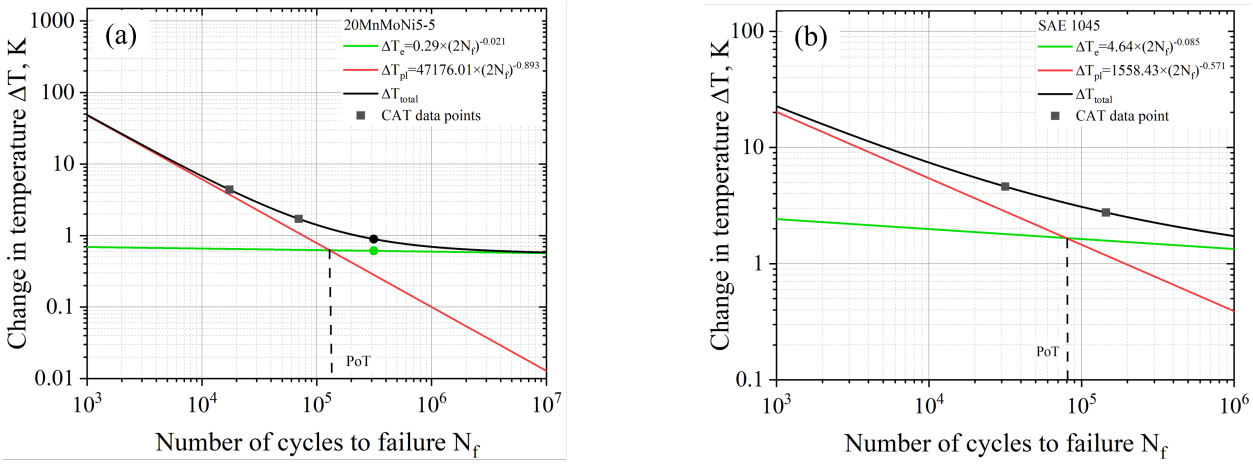

Figure 6.8: (a) Calculated elastic, plastic and total material response of the 20MnMoNi5-5 steel to an applied load as a function of N_f according to equation 6.10 with the experimental data derived from the CATs; (b) Calculated elastic, plastic and total material response of the SAE 1045 to an applied load as a function of N_f according to equation 6.10 with the experimental data derived from the CATs.

The point marked as PoT (Point of Transition) in Figure 6.8 indicates the number of cycles at which the elastic and the plastic components of the material response have the same value. Above the PoT, the elastic portion of the material response is the predominant process, whereas below the PoT the plastic portion is the main process. From the Figures 6.8(a) and (b), it can be deduced that the position of the PoT is highly material-dependent. Compared to the 20MnMoNi5-5 steel, the SAE 1045 shows a significantly higher material response and the intercept of the elastic function with the ordinate is about one order of magnitude higher than the one of the 20MnMoNi5-5 steel. Consequently, the PoT shifts towards lower number of cycles to failure.

To determine the S-N curve according to the StressLife$_{HCF}$ method, an additional CAT must be calculated. By using the data of this calculated CAT, the missing parameters of the StressLife curve can finally be determined. The determination of the missing parameters is the same as for StressLife$_{tc}$ and can be found in [258, 266]. The final results for the calculation according to StressLife$_{HCF}$, including several CAT data points as a validation, is given in Figure 6.9.

Both curves are characterised by a high accuracy in the description of the CAT data points in the HCF regime. However, the SAE 1045 steel has a lower fatigue strength than the 20MnMoNi5-5 steel. This can be explained by the higher content of alloying elements in the 20MnMoNi5-5 steel. At this point it must be taken into account that the slopes are based on the results of just one LIT. In order to be able to take the natural scatter of the materials into account, statistical evaluations need to be performed. Therefore, several LIT have to be carried out. By including the elastic and the plastic material response in the StressLife$_{HCF}$ equation, the HCF regime can be described very well, but the transition to the adjacent regimes are not sufficient due to different damage processes. For this reason, two additional modules of the method were developed.

Table 6.2: Parameters from the $\text{StressLife}_{\text{HCF}}$ calculation.

Material	n'_{cal} [-]	b [-]	c [-]	B [K]	C [K]	n' [-]	K' [MPa · K^{-1}]
20MnMoNi5-5	0.024	-0.021	-0.893	0.814	42414.79	0.094	366.54
SAE 1045	0.15	-0.086	-0.571	4.642	1558.43	0.197	255.21

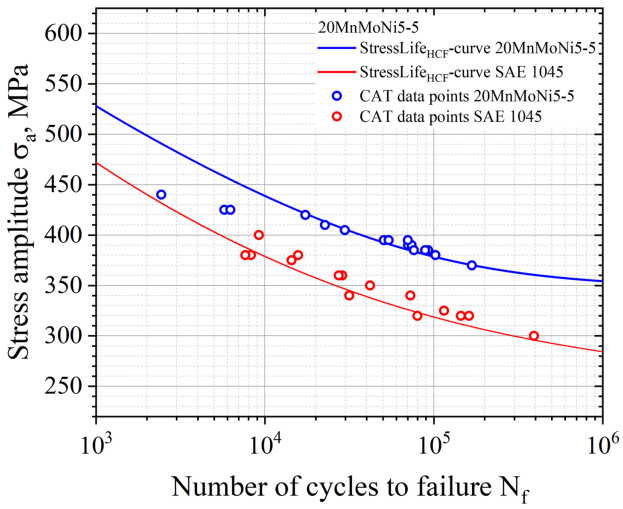

Figure 6.9: S-N curve according to $\text{StressLife}_{\text{HCF}}$ for a 20MnMoNi5-5 steel and a SAE 1045 steel, including CAT data points for validation.

6.3.3 $\text{StressLife}_{\text{LHC}}$

In the range of lower number of cycles to failure, there must be a change in the slope of the S-N curve due to changed damage processes. For example, the surface finish has a decisive influence in the HCF regime, while the surface loses influence in the range of lower cycle numbers. The CAT data points from Figure 6.9 of the 20MnMoNi5-5 steel, which lie below 10^4 cycles, confirm this assumption. As described in chapter 6.2.4, only the plastic data points of the Morrow equivalent plot were used, which can be seen in Figure 6.10(a). Compared to Figure 6.7, it is evident that the slope of the fit function is highly dependent on the selected data points. A consideration of only the plastic range leads to lower values of the slope than an elastic-plastic consideration. This leads to the consequence that parameters of the S-N curve change enormously. Using the equations 6.9 and 6.14, the $\text{StressLife}_{\text{LHC}}$ curve can be determined. The result is given in Figure 6.10(b). Above the P90, the two curves of the $\text{StressLife}_{\text{LHC}}$ and $\text{StressLife}_{\text{HCF}}$ calculations are identical and describe the CAT data points with a high accuracy. Below the P90, the CAT data points are better described by the $\text{StressLife}_{\text{LHC}}$ curve, with one exception of a CAT at 420 MPa. A possible reason for the better accuracy of the $\text{StressLife}_{\text{LHC}}$ calculation is that the deformation in this fatigue range is mainly characterised through moreover plastic processes and thus the elastic-plastic description of the $\text{StressLife}_{\text{HCF}}$ can not represent the realistic slope of the S-N curve. Table 6.3 summarises all parameters of the $\text{StressLife}_{\text{LHC}}$ calculation.

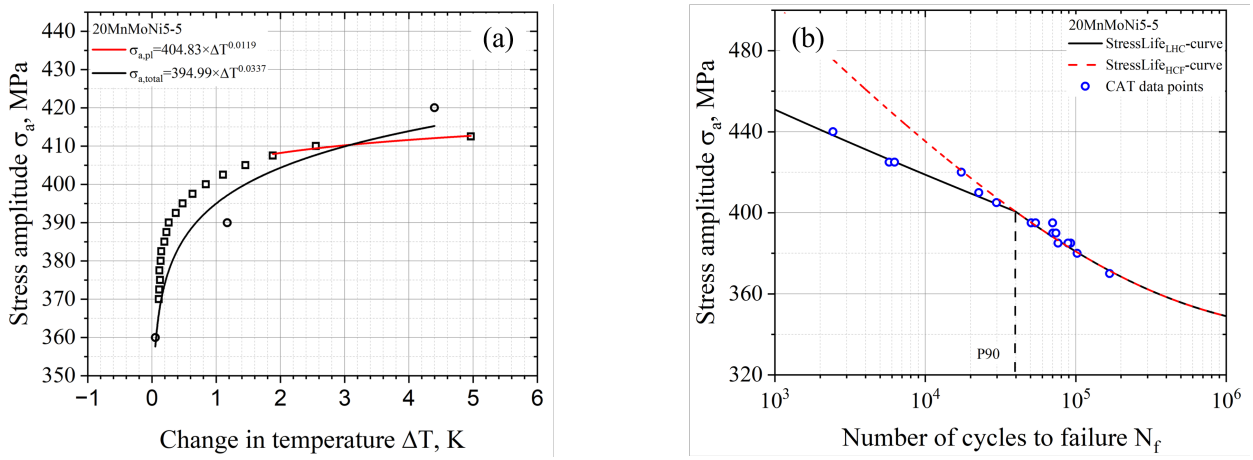

Figure 6.10: (a) Relation between the stress amplitude and the change in temperature including the plastic change in temperature of the CATs and the calculated CAT for the $\text{StressLife}_{\text{LHC}}$ calculation; (b) S-N curve according to $\text{StressLife}_{\text{LHC}}$ (black) and $\text{StressLife}_{\text{HCF}}$ (red) for a 20MnMoNi5-5 steel, including CAT data points for validation.

Table 6.3: Results $\text{StressLife}_{\text{LHC}}$ calculation.

Material	n'_{cal} [-]	b [-]	c [-]	B [K]	C [K]	n' [-]	K' [MPa · K^{-1}]
20MnMoNi5-5	0.012		-0.944		67047	0.034	394.40

Considering a transition point such as the one displayed in Figure 6.10(b), physical evidence also appears in these results, since without a change in the slope of the S-N curve, an extremely high intercept with the ordinate would be achieved.

6.3.4 $\text{StressLife}_{\text{HVC}}$

In the case of decreasing load amplitudes and therefore an increasing number of cycles, the elastic portion of the material response increases in comparison to the plastic portion. At the PoT, both parts of the material response have the same value. The position of the PoT is strongly material- and manufacturing dependent and can already occur in the HCF regime or at a higher number of cycles to failure in the transition to the VHCF regime. The approach of the $\text{StressLife}_{\text{HVC}}$ calculation is based on the assumption that only elastic data points of the Morrow-equivalent plot, which is given in Figure 6.11(a), are included in the calculation.
A comparison of Figure 6.7(b) and Figure 6.11(a) provides the information that the slope used for the calculation is significantly larger in the case of the $\text{StressLife}_{\text{HVC}}$. This strongly influences the results of all other parameters. The evaluation is carried out in the same way as the evaluations of $\text{StressLife}_{\text{HCF}}$ and $\text{StressLife}_{\text{LHC}}$ with the exception that only the elastic parameters B and b are taken into account. The results of the lifetime evaluation according to $\text{StressLife}_{\text{HVC}}$ are given in Figure 6.11(b) and the parameters are summarised in Table 6.4. Figure 6.11(b) shows that the $\text{StressLife}_{\text{HCF}}$ curve underestimates the CAT data points of the SAE 1045 in the area above

the PoT. Compared to this, the StressLife$_{\mathrm{HVC}}$ curve, which only takes the elastic slope of the Morrow-equivalent plot into account, describes the data points with a higher accuracy.

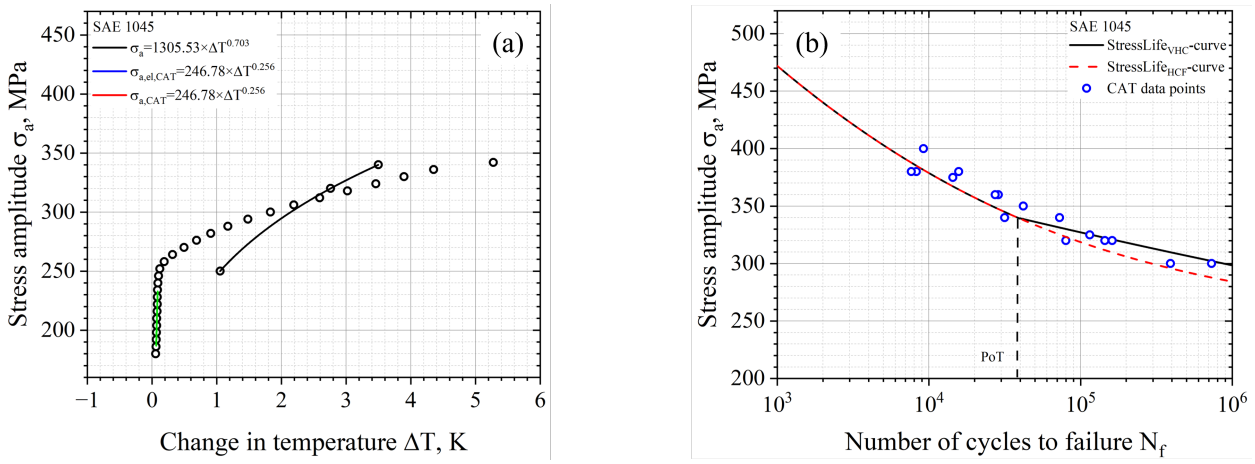

Figure 6.11: (a) Relation between the stress amplitude and the change in temperature of a SAE 1045 including the elastic change in temperature of the CATs and the calculated CAT for the StressLife$_{\mathrm{HVC}}$ calculation; (b) S-N curve according to StressLife$_{\mathrm{HVC}}$ (black) and StressLife$_{\mathrm{HCF}}$ (red) for an SAE 1045 steel, including CAT data points for validation.

Table 6.4: Results StressLife$_{\mathrm{HVC}}$ calculation.

Material	n'_{cal} [-]	b [-]	c [-]	B [K]	C [K]	n' [-]	K' [MPa · K^{-1}]
SAE 1045	0.703	-0.1557	-	20.13	-	0.256	246.78

6.4 Conclusion

Within the scope of this research, the authors developed a new short time procedure designated as StressLife$_{\mathrm{HCF}}$. The aim of this calculation method is to determine the lifetime of metallic materials with a small number of only four specimens. The method is based on the approaches according to Manson-Coffin for describing the plastic portion of the fatigue damage and Basquin in order to describe the process elastically. In addition, two modifications to the method have been developed, which are to be considered as an expansion of the method. These methods can be summarised as follows:

6.4.1 StressLife$_{\mathrm{HCF}}$

- The method enables a generation of an S-N curve with a small specimens effort of a maximum of four specimens.
- By the combination of conventional fatigue testing methods and non-destructive measurements techniques, the information regarding ongoing fatigue processes is highly increased.

- The $\text{StressLife}_{\text{HCF}}$ - equation consists of the approaches according to Manson-Coffin and Basquin.
- Through the extension to two load increase tests, the accuracy of the evaluation can be significantly increased.
- By weighting the elastic and plastic portions of the load increase test, the determination of the slope can be optimised.
- The generated S-N curve describes the constant amplitude test data points with a high accuracy.

6.4.2 $\text{StressLife}_{\text{LHC}}$ and $\text{StressLife}_{\text{HVC}}$

- Both methods are modifications of the $\text{StressLife}_{\text{HCF}}$ method, based on the same approaches and calculations.
- These modifications are developed in order to enable a description of an S-N curve beyond the high cycle fatigue regime.
- The relation of the material response and the number of cycles is used in order to calculate the anchor points PoT (Point of Transition) and P90 (90 % plastic part of the material response).
- The S-N curve is divided into three different ranges. At lower number of cycles, only the plastic part of the material response is considered in the calculation, whereas in the case of higher numbers of cycles only the elastic part is used.

The $\text{StressLife}_{\text{HCF}}$ process is to be further validated and expanded in additional tests, also with other materials such as pure metals, cast iron and additive manufactured specimens. Furthermore, important influencing factors such as residual stresses and surface qualities are to be included in the method. The modifications $\text{StressLife}_{\text{LHC}}$ and $\text{StressLife}_{\text{HVC}}$, on the other hand, still need to be backed up with further tests in the respective areas. Another important aspect is the statistical validation via additional load increase tests and constant amplitude tests. Up til now, only stress-controlled tests have been used for the developed procedure. In further research, strain-controlled tests should also follow.

Acknowledgements

The authors from the Department of Material Science and Materials Testing (WWHK) of the University of Applied Sciences Kaiserslautern would like to thank the Federal Ministry for the Environment, Nature Conservation, Nuclear Safety and Consumer Protection (Bundesministerium für Umwelt, Naturschutz, Nukleare Sicherheit und Verbraucherschutz, BMUV) for the financial support. Furthermore, the authors would like to thank the GRS (Gesellschaft für Anlagen-, und Reaktorsicherheit) as the project management agency, Shimadzu Europe and EVIDENT (former Olympus) for their support in technical equipment provision. Selected experimental data for validation were taken from a DFG project with the grant number STA1133/6-1. For this reason, additional thanks to the German Research Foundation (Deutsche Forschungsgemeinschaft, DFG) as the project management agency and to Haoran Wu as the project manager.

Journal Contribution II

A new short-time procedure for fatigue life evaluation based on the linear damage accumulation by Palmgren-Miner

International Journal of Fatigue

F. Weber[1,2], H. Wu[1,2], P. Starke[1,2]

[1] Department of Material Sciences and Materials Testing (WWHK), Institute QM[3] University of Applied Sciences Kaiserslautern, Schoenstr.11, Kaiserslautern, 67659, Germany

[2] Faculty of Natural Sciences and Technology, Saarland University, Campus, Saarbrücken, 66123, Germany

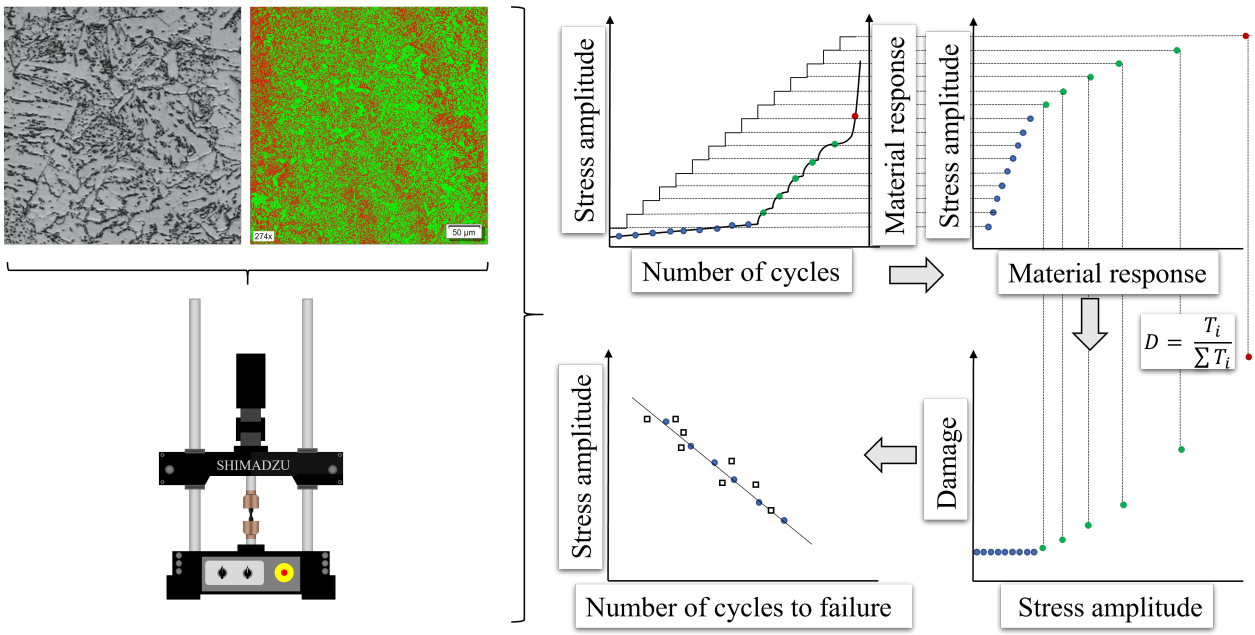

A new short-time procedure for fatigue life evaluation based on the linear damage accumulation by Palmgren-Miner

Abstract

The aim of the presented research is to develop a new short-time-procedure based on the linear damage accumulation according to Palmgren-Miner, which can provide an S-N curve in the HCF regime based on results of only one fatigue test. Load increase tests were carried out to determine the partial damage per load level from the material response by using NDT-methods. By converting the calculated partial damage of each load step into the corresponding number of cycles to failure, an S-N curve can be generated. This research focuses on a quenched-tempered 20MnMoNi5-5 steel. The validation was performed on three further steels.

7.1 Introduction

To avoid sudden material failure due to dynamic loading, the fatigue properties of materials must be analysed in detail. The conventional way for assessing and providing fatigue data is the use of S-N curves, also known as Woehler curves, established and introduced by August Woehler, which shows the relation between the applied load amplitude and the respected number of cycles to failure [3,21]. The generation and provision of S-N curves require a high amount of specimens and is therefore a very cost- and time-consuming process. For this reason, the need for the development of short-time procedures arises. The aim of these methods is to assess the fatigue properties of metallic materials with a reduced number of specimens by combining conventional destructive testing with non-destructive testing methods (NDT). Several short-time procedures were developed and used over recent years. Existing methods as StressLife, StrainLife and SteBLife are applicated on different un-, low- and high-alloyed steels and show an overall good accordance between the predicted and experimental determined lifetime [236, 237, 258]. All of these methods are designed to predict the fatigue life of specimens subjected to constant amplitude loading, while components or structures in service are often exposed to dynamic loads of varying amplitude and frequency. Moreover, still three specimens are needed in order to calculate an S-N curve. Therefore, a new short-time procedure called MiDAcLife (Miner Damage Accumulation Lifetime prediction) is developed, which takes these variable parameters into account. This method uses the linear damage accumulation according to Palmgren Miner [12, 13] to generate an S-N curve in the HCF regime by using one load increase test (LIT). A LIT starts at a very low stress amplitude below the fatigue strength. Within the experiment, the specimen undergoes a step-wise increase of the stress amplitude until failure. Compared to previously mentioned methods, this procedure enables a determination of the S-N curve based on only one specimen and fatigue test. The advantage here is that not only the number of cycles could be reduced, but also a process-oriented determination of the S-N curve is guaranteed due to the NDT-measurements which are sensitiv to micro-plastic deformation in the early state of the fatigue process.

7.2 Materials and Methods

7.2.1 Materials

The material that is mainly used in the context of these investigations is the ferritic-bainitic steel 20MnMoNi5-5 (1.6310). This steel is mainly used in German nuclear power plants for coolant pipes (spraylines) and pressure vessels and is most comparable to SAE 5120 steel in terms of its chemical composition. The specimens were separated from pipes with an inside diameter of 706 mm and a thickness of 47 mm. The heat-treatment of the pipes is in accordance with the KTA (Kerntechnischer Ausschuss, nuclear committee) guidelines and can be described as follows. The normalisation was carried out at a temperature of 910 °C, followed by water quenching and tempering at a temperature of 680 °C for 40 min. Two micrographs of 20MnMoNi5-5 captured with a DSX 1000 digital microscope from EVIDENT (EVIDENT Europe GmbH, Hamburg, DE) are shown in figure 7.1. Figure 7.1(a) shows an overview, whereas figure 7.1(b) gives a more detailed view on the structure of the material.

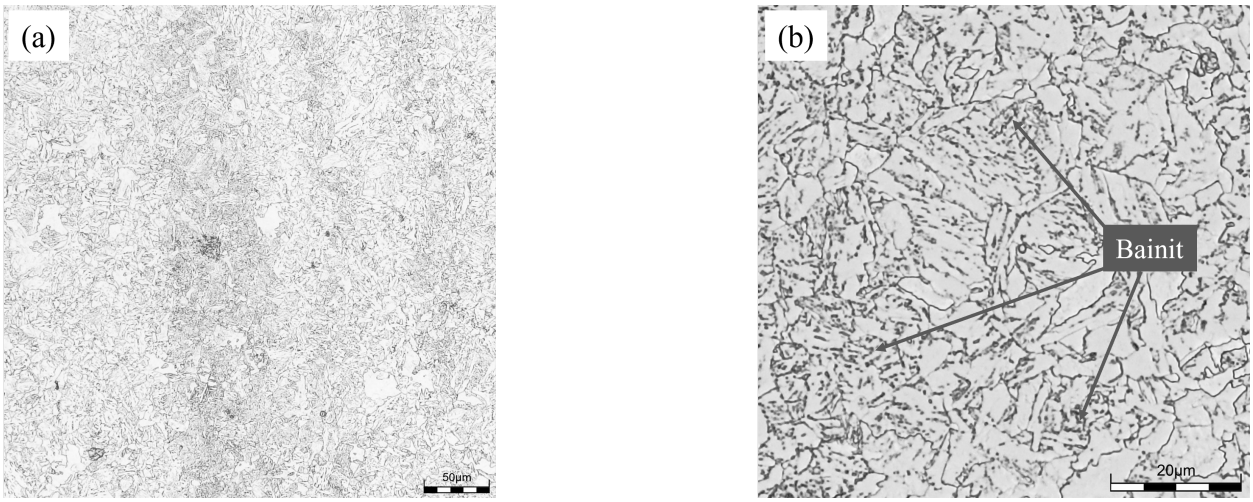

Figure 7.1: Micrographs of 20MnMoNi5-5 steel. (a) Overview micrograph; (b) Detailed consideration micrograph.

Within figure 7.1, lighter and darker regions can be identified. The lighter areas evidently represent the ferritic grains with a very low carbon content. The pearlite is characterised by a clearly recognisable lamellar structure of Fe and Fe_3C, which can be not seen in the darker areas. For this reason, it is assumed to be a bainitic structure. Bainite forms in a temperature range between the pearlite and martensite stage. Therefore, only the carbon atoms are able to diffuse and bainite consists of ferrite with small embedded carbides [267]. In general, a distinction can be made between lath-like and granular bainitic structure [268]. Based on the irregular arrangements of the bainitic structure in figure 7.1, the presence of granular bainite can be inferred.

The formation of carbides and their type depends, among other things, on the alloying composition. Mn and Mo are both carbide former, whereby Mo has a stronger tendency here. A scanning electron microscope (SEM) type GEMINI by ZEISS (Carl Zeiss, Oberkochen, DE) and a laser scanning microscope type LEXT by EVIDENT are used to visualise the carbide structure. The results are given in figure 7.2.

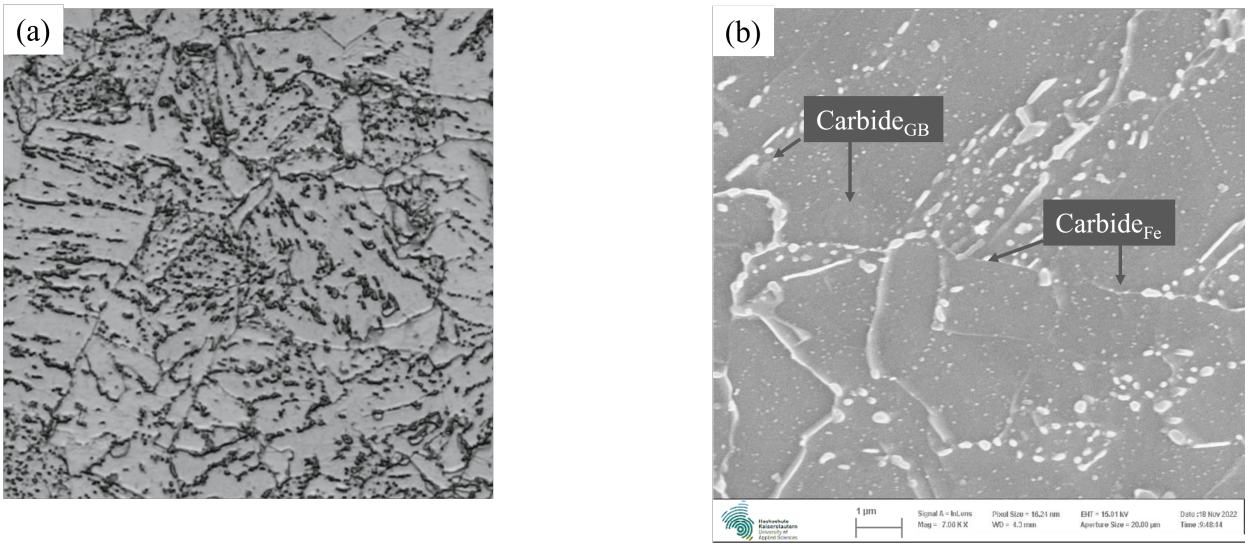

Figure 7.2: Micrographs of 20MnMoNi5-5 steel: Examination of the carbides. (a) Visualization of the carbides with a SEM type GEMINI; (b) Visualization of the carbides with a laser scanning microscope type LEXT.

A more detailed analysis of the distribution and the size of the carbides in figure 7.2 shows that there are probably two types of carbides in the material. Large carbides can be detected along the grain boundaries, which are referred to as Carbide$_{GB}$ (GB = Grain Boundaries). Beside the large carbides along the grain boundaries, a large number of smaller carbides can be found within the grains (Carbide$_{FE}$). Previous research of Cho et al. shows that Mo segregate at the grain boundaries and form carbides [269, 270]. For this reason, it is assumed that the Carbide$_{GB}$ are mostly Mo-carbides leading to the further assumption that the smaller carbides within the ferritic grains are mostly Mn-carbides. This assumption fits with the work of Ahmadabadi, in which Mn formed intercellular carbides [271]. A comparison of figure 7.2(a) and 7.2(b) leads to the finding that the Mo-carbides can already be clearly detected with the laser scanning microscope and therefore no SEM analysis is required, which in turn is needed for the much smaller Mn-carbides for visualisation.

To analyse the microstructure more precisely, a phase analysis (figure 7.3(a)) and a grain size determination (figure 7.3(b)) of the specimen were carried out by using the digital microscope. The microstructure analysis from figure 7.3 leads to the result that 62 % of the microstructure consists of ferritic and thus 38 % of bainitic grains, whereby these also include the carbides in each case. The average grain size is estimated as 7.28 µm^2.

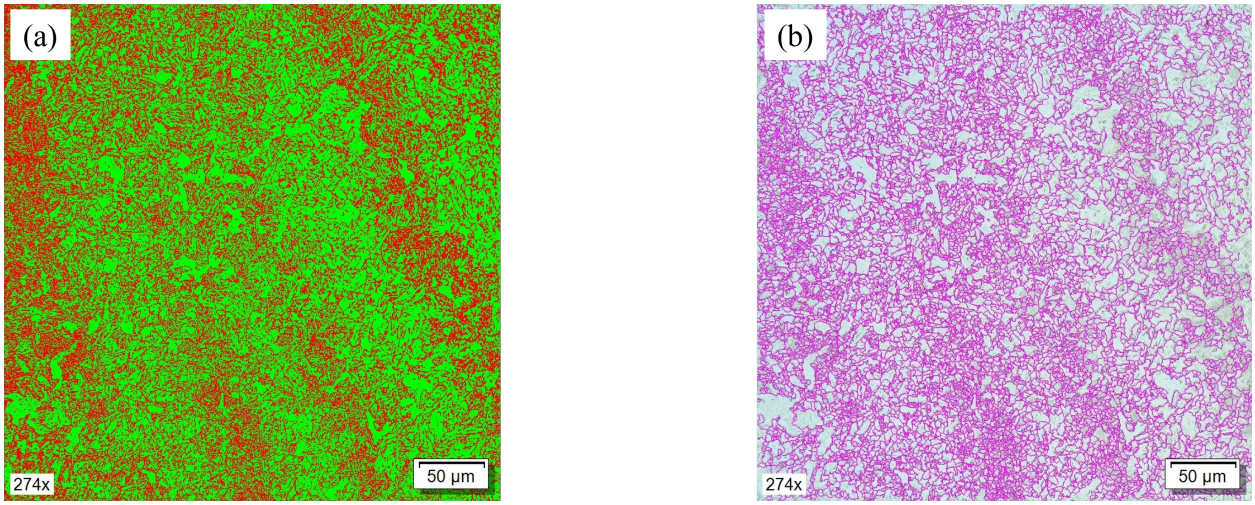

Figure 7.3: Microstructural analysis of the 20MnMoNi5-5 steel. (a) Phase fraction 20MnMoNi5-5; (b) Grain size 20MnMoNi5-5.

The chemical composition of the material was determined by spectral analysis, while the mechanical properties were determined by means of tensile test. The results are given in table 7.1 and 7.2.

Table 7.1: Chemical composition in wt.% of the 20MnMoNi5-5 steel: values according to own analysis (SEW 028).

Element	C	Si	Mn	Cr	Ni	Mo	S	P
wt.%	0.218	0.246	1.385	0.076	0.762	0.487	0.003	0.010

Table 7.2: Mechanical properties of the 20MnMoNi5-5 steel: values according to own analysis.

E [GPa]	$R_{p\,0.2}$ [MPa]	$R_{p\,0.2}/R_m$ [%]	R_{eH} [MPa]	R_{eL} [MPa]
231	523	79	561	521

R_m [MPa]	d_0 [mm]	F_{max} [kN]	A_5 [%]	S_0 [mm^2]
664	10	52	24	78

In order to validate the new short-time procedure MiDAcLife, it was also applied on three other steels, whose more detailed analysis can be found in [176, 183]. The geometry of the specimens used for the fatigue tests is given in figure 7.4.

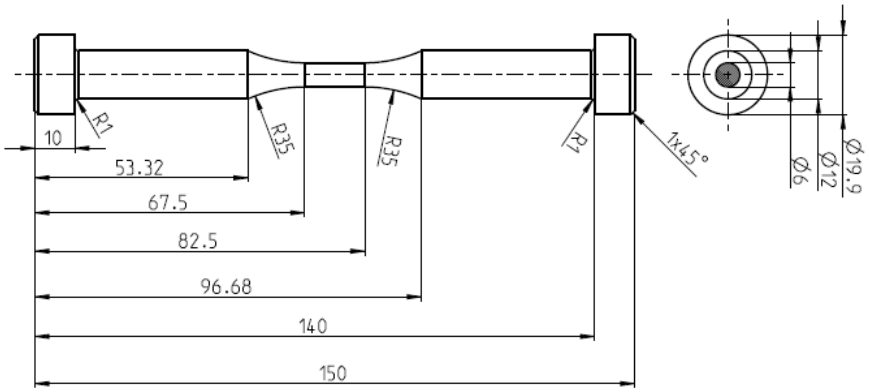

Figure 7.4: Specimen geometry of the applied fatigue specimen.

7.2.2 Methods

The fatigue tests on the 20MnMoNi5-5 steel were carried out on a 20 kN servo-hydraulic testing rig type EHF-L by Shimadzu (Shimadzu Europe, Duisburg, DE), while the fatigue tests on the other steels used for validation were carried out on a 50 kN test rig of the type EHF-U. All tests were performed under stress-controlled condition at ambient temperature with a load ratio of R = -1 using a sinusoidal load-time function. The load frequency was set to 5 Hz. The complete experimental setup of the 20 kN testing rig is shown in figure 7.5.

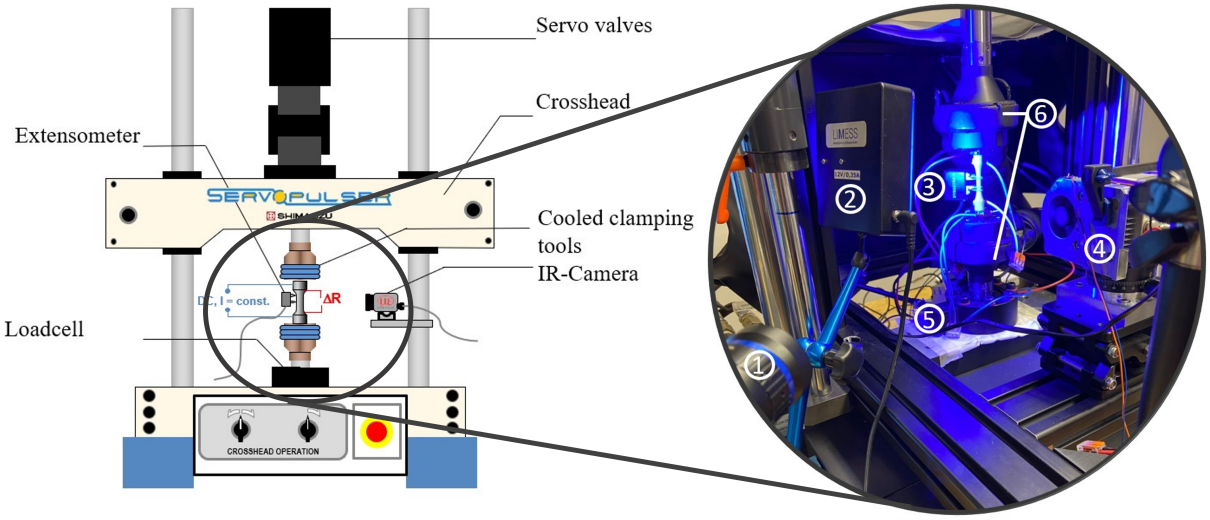

Figure 7.5: Experimental setup of the servo-hydraulic testing rig (20 kN) including the measurement techniques; 1. DIC camera; 2. Illumination DIC; 3. Tactile extensometer; 4. IR-camera; 5. Electrode and sensing wires of the 4-point DC resistance measurement device; 6: water-cooled clamps.

To maximise the amount of information regarding the fatigue processes taking place in the different stages of the lifespan of the specimen, different measurement techniques were used. The measurement setup includes thermographic, electrical, optical and tactile methods for data acquisition. As a first step, only the thermometric data, provided through an IR-camera type thermoIMAGER TIM450 (Micro-Epsilon Messtechik, Ortenburg, DE) as well as electrical resistance data are used to calculate S-N curves according to the new method MiDAcLife. The benefit of this method is that the MiDAcLife procedure only requires one LIT and no further results from CATs which is an advantage against methods as StressLife and PhyBal. The load increase test is started at a stress amplitude significantly below the fatigue strength of a material. After a defined number of cycles (in this case after $6 \cdot 10^3$ cycles), the stress amplitude is increased step wise by $\Delta\sigma_\mathrm{a}$ varying between 4 MPa and 20 MPa depending on the material as well as the material condition. If the material shows a more brittle behaviour, the amount of data points in the plastic range of the LIT is severely limited and thus the value of $\Delta\sigma_\mathrm{a}$ needs to be rather small. To verify the obtained S-N curve, multiple CATs were performed at different load levels. More detailed descriptions and explanations regarding the application of LITs and CATs as well as technical data of the test rig and IR-camera are given in [235, 272].

7.3 Theory

The generation of S-N curves is a very cost- and time-consuming procedure which is why there is an urgent need for an estimation of the fatigue life of a specimen or component with less effort. The estimation is mostly carried out by so-called damage hypothesises. In the linear damage accumulation according to Palmgren-Miner, each load level is assigned to a partial damage $\mathrm{D_i}$ which represents the relation between the load cylces $\mathrm{n_i}$ applied to the specimen at a defined load amplitude and the number of cycles to failure at the same load amplitude $\mathrm{N_f}$ which is shown in equation (7.1) [12, 13].

$$D_i = \frac{n_i}{N_f} \tag{7.1}$$

The failure of the specimen or component occurs when the sum of the partial damages equals 1 [273]:

$$\Sigma D_i = \Sigma \frac{n_i}{N_f} = 1 \tag{7.2}$$

There are different approaches for the application of the damage accumulation model. The first one is the elementary Palmgren-Miner rule according to [12, 13]. It is assumed that no fatigue strength σ_FL (FL = Fatigue Limit) exists or only stress amplitudes greater than the fatigue strength σ_a contribute to the damage. According to Haibach [2], a neglect of the fatigue strength leads to a an overestimation of the contribution of stress amplitudes below the fatigue strength. As a result, the calculated value for the damage is too high and thus the number of cycles to failure $\mathrm{N_f}$ too low. The reliable way to consider the fatigue strength is to use the original Miner rule which is given in equation (7.3) and (7.4):

$$\sigma_a \geq \sigma_{FL} : N = N_{FL} \cdot (\frac{\sigma_a}{\sigma_{FL}})^{-k} \tag{7.3}$$

$$\sigma_a \leq \sigma_{FL} : N = N \rightarrow \infty \tag{7.4}$$

N_{FL} from quation (7.3) is the number of cycles at which the fatigue strength point is located. The parameter k indicates the slope of the S-N curve.

The modified Miner rule considers a fatigue strength decrease as a function of progressive damage. Due to the flattening of the slope, damage is also attributed to the lower load levels, but in a weakened manner [2, 274].

$$\sigma_a \leq \sigma_{FL} : N = N_{FL} \cdot (\frac{\sigma_a}{\sigma_{FL}})^{-(2k-1)} \tag{7.5}$$

In addition to the Palmgren-Miner approach, there is a large number of other, more complex approaches, that take additional parameters into account. Examples can be found in the literature [266, 275–277].

In previous research, it has already been shown that the temperature measurement is a sensitive tool to detect cyclic softening and/or hardening processes [258, 278]. These processes are directly related to the area enclosed by the mechanical stress-strain hysteresis. If the material response shows an increase in the change in temperature, this corresponds to the cyclic softening processes taking place in the material. This confirms that the change in temperature is also related to the partial damage of each load step. By rearranging equation (7.1), the number of cycles to failure for each load step can be calculated.

$$N_{f,i} = \frac{n_i}{D_i} \tag{7.6}$$

While the number of applied load cycles n is known, the partial damage of each load step needs to be determined. Here the assumption is considered, that the total damage of the fatigue test consists of the sum of the change in temperature of each step. Because of the fact that in the last load step, the applied cycles do not reach the value of $6 \cdot 10^3$, which is the defined step length of each load step, this step needs to be considered separately with an own value for the applied cycles n_i with $n_i < 6 \cdot 10^3$. The chosen step length of $6 \cdot 10^3$ cycles has been shown to be suitable from previous research, as the duration is sufficient to reach a saturation state of the measurement but not too high to cause into much damage. An additional boundary condition in the elementary Miner rule is, that the linear damage accumulation is limited to stress amplitudes above the fatigue strength of the material. Due to this outcome, only the load steps in the elastic-plastic range of the LIT are taken into account. As a first step, the change in temperature ΔT_i is calculated by subtracting the first value T(1) of the temperature data from the following data points T_i according to equation (7.7).

$$\Delta T_i = T_i - T(1) \tag{7.7}$$

Afterwards, the average of each load step $\Delta T_{i,average}$ is determined by equation (7.8). The dependency of ΔT_i on the interval f has to be taken into account in order to consider each load level in the calculation.

$$\Delta T_{i,average} = \frac{1}{n_{sl}} \cdot \sum_{i=1}^{x} \Delta T_i(f) \tag{7.8}$$

$$f \in [(i-1) \cdot n_{sl} \cdot 20 + 1 : n_{sl} \cdot 20 \cdot i]_{i=1}^{x} \tag{7.9}$$

The parameter n_{sl} describes the number of cycles of the load steps, whereas x is defined as the number of load steps. The factor 20 from equation (7.9) must be included due to the measuring frequencies of the IR-camera of 100 Hz and the servo-hydraulic testing rig of 5 Hz.

If the LIT consists of x load steps, the following equation (7.10) shows the relation of the change in temperature and the partial damage:

$$D_i = \frac{\Delta T_{i,average}}{\Sigma_i^{x-1} \Delta T_{i,average}} \tag{7.10}$$

With the known values for D_i and n_i, the number of cycles to failure can be calculated for different stress amplitudes according to equation (7.6). As a result, the stress amplitude can be plotted as a function of the number of cycles to failure. To describe the obtained data points, the empirical approach of Basquin is used showing the relation of σ_a and N_f [11].

$$\sigma_a = \sigma_{f'} \cdot (2 \cdot N_f)^b \tag{7.11}$$

Where $\sigma_{f'}$ is the fatigue strength coefficient and b is the Basquin exponent. By using an allometric fit function in terms of

$$y = a \cdot x^d \tag{7.12}$$

the material parameters can be obtained. Figure 7.6 gives an overview of how the S-N curve according to the MiDAcLife method is generated. The filled circles represent the calculated CAT from the LIT, whereas the black bordered squares represent the experimentally performed CAT. At this point it should be noted, that the calculated and provided S-N curve indicates the relation between the applied stress amplitude and the number of cycles to failure for this specific specimen and its specific defect distribution. In order to take the materials inhomogeneities into account, further LIT must be carried out and based on this data via probabilistic features the scatter of the lifetime at different load levels can be calculated.

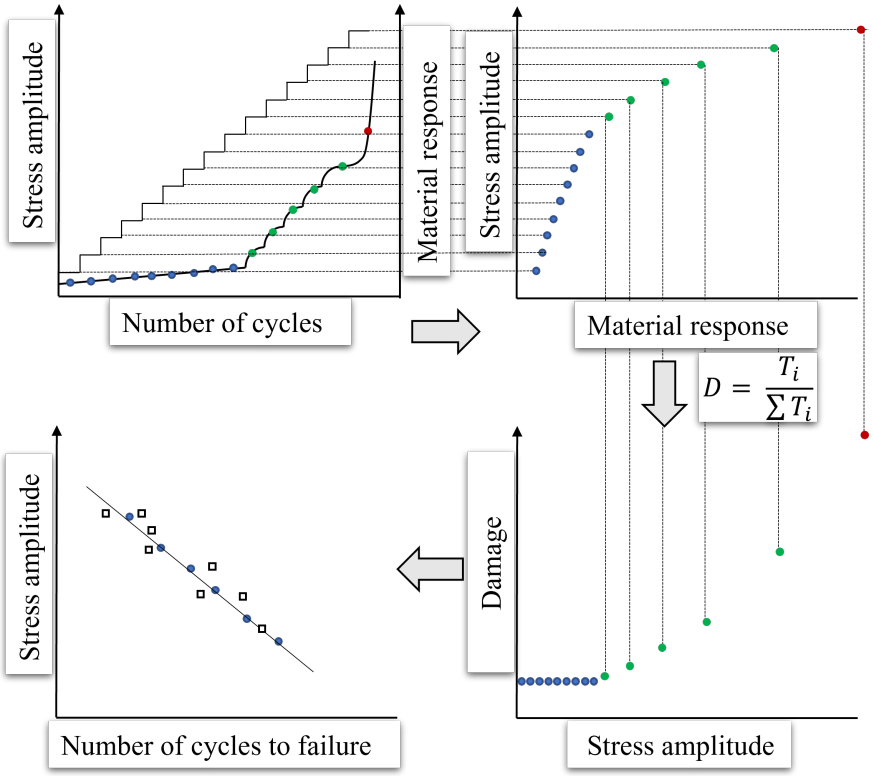

Figure 7.6: Schematic representation of the MiDAcLife method for calculating an S-N curve from one load increase test.

7.4 Results and Discussion

7.4.1 Load increase test

A LIT is a very useful tool not only to calculate an S-N curve but also to estimate the fatigue strength of a material [171, 172]. The slope of the material's response, e.g. the change in temperature, can be used to determine the stress amplitude at which failure would still occur, allowing conclusions to be drawn about the fatigue strength. The results of the LIT for 20MnMoNi5-5 steel are given in figure 7.7(a) together with the calculated values for the average change in temperature for each load step.
Figure 7.7(a) shows cyclic deformation curves for the quenched and tempered 20MnMoNi5-5 steel based on two different measurement techniques. The red line represents the thermograhic data from the IR-camera, whereas the black line is derived from electrical resistance measurements. As mentioned before, the specimens were manufactured from a pipe assembled by a drawing process. Due to the processing history, a high dislocation density already exists and therefore the steel tends to be rather brittle, which leads to cyclic softening with regard to its cyclic deformation behaviour. Both curve progressions from figure 7.7(a) confirm this assumption. To estimate the material's fatigue strength, it is necessary to assess the stress amplitude at which only an uncritical material response occurs at last. Based on this consideration, the fatigue strength can be estimated to the range 370 MPa - 380 MPa. Due to the brittle material behaviour, very small $\Delta\sigma$ values were set for

the LITs as previously defined. To show that the calculation according to MiDAcLife is not only valid for materials with brittle behaviour, but also for more ductile materials, the results of LITs for normalised SAE 1020 (+N, C22R), normalised SAE 1045 (+N, C45E) and quenched-tempered 20MnCrS5 +QT are given in figure 7.7(b).

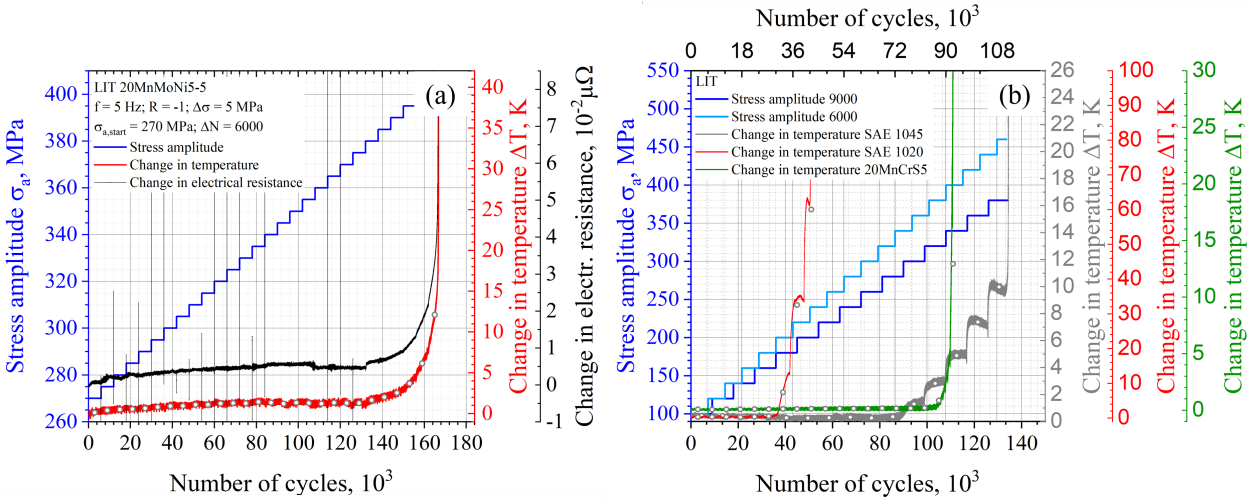

Figure 7.7: (a) Cyclic deformation curves of a load increase test for the 20MnMoNi5-5 steel with $\sigma_{a,start} = 270\text{MPa}, \Delta\sigma = 5\text{MPa}$ and $\Delta N = 6 \cdot 10^3$; (b)Cyclic deformation curves of a load increase test of the SAE 1020 +N and 20MnCrS5 +QT steels with $\sigma_{a,start} = 100\text{MPa}, \Delta\sigma = 20\text{MPa}$ and $\Delta N = 6 \cdot 10^3$; Cyclic deformation curves of a LIT SAE 1045 +N with $\sigma_{a,start} = 100\text{MPa}, \Delta\sigma = 20\text{MPa}$ and $\Delta N = 9 \cdot 10^3$

In analogy to the approach for the 20MnMoNi5-5 steel, the fatigue strengths of each material can be estimated by considering the change in the slopes for the respective material responses. The fatigue strength of the SAE 1020 +N is in the range of 180 MPa - 200 MPa, whereas the value for the 20MnCrS5 can be estimated with 420 MPa. It should be noted that for the SAE 1045 +N steel the step length of the LIT was chosen to be longer ($9 \cdot 10^3$ cycles) compared to the other materials, which is indicated by the dark blue chart. The determination of the fatigue strength of this material results in a value of 280 MPa. By comparing the results of the cyclic deformation curves in figure 7.7(a) and figure 7.7(b), it is evident that the slope depends on the material itself and is also affected by its manufacturing history as well as heat treatment. The 20MnMoNi5-5 and 20MnCrS5 steel have a similar chemical composition and were both in quenched-tempered conditions (but with different heat treatment parameters). Due to the alloy composition and the material condition, the defect density is relatively high compared to the other materials/material conditions, which leads to a reduced dislocation mobility, which in turn is reflected in the continuously softening deformation behaviour in the fatigue tests expressed through steadily increasing change in temperature values. The steels in normalised condition, on the other hand, show a completely different behaviour. Due to their heat treatment, significantly more dislocation reactions take place and after a first cyclic softening process, both materials tend to cyclic hardening during the load steps of the LITs. It is noticeable that the material response of SAE 1045 occurs at a significantly higher number of cycles compared to SAE 1020, which can be attributed to a higher pearlite ratio due to the higher carbon content.

7.4.2 MiDAcLife

As described in previous chapters, the damage of each loading step is calculated with the change in temperature. Alternatively, other measurement techniques can be used, which will also be implemented in future investigations. In figure 7.8, the evolution of the material damage is given for the 20MnMoNi5-5 steel in terms of black data points. The first material response occurred at a stress amplitude of 380 MPa, so the load steps from this stress amplitude onward are considered in the MiDAcLife evaluation. As an additional information, the damage of any stress amplitude can be calculated by an allometric fit as it is shown with the black line in figure 7.8. With the known values of the partial damage per load step, the corresponding number of cycles to failure can be calculated according to equation (7.6). The results of the partial damage calculation and the corresponding number of cycles to failure are summarised in table 7.3.

Table 7.3: Results of partial damage per load step and corresponding number of cycles to failure.

ΔT [K]	σ_a [MPa]	Sum(ΔT) [-]	D_i [-]	N_f [-]
0.896	380	0.896	0.113	53060
1.125	385	2.021	0.142	42277
1.348	390	3.369	0.170	35282
1.827	395	5.197	0.230	26037
2.731	400	7.928	0.345	17416
4.677	405	12.605	0.590	10169

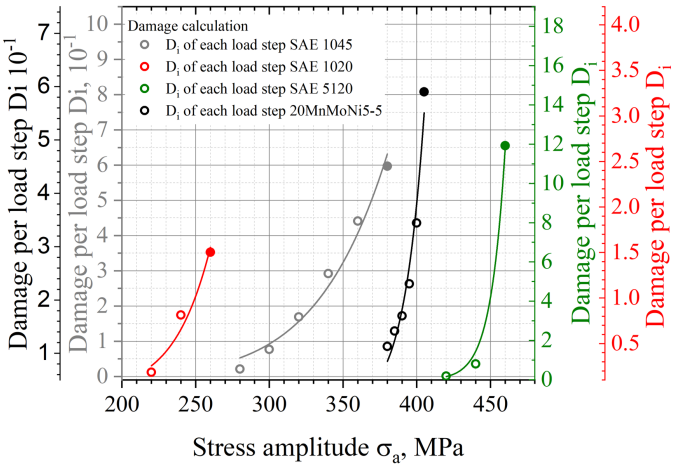

Figure 7.8: Partial damage per load step as a function of the stress amplitude for the SAE 1020, SAE 1045, SAE 5120 and 20MnMoNi5-5 steels.

Figure 7.8 also shows the course of the partial damage per loading step for the SAE 1020 (red), SAE 1045 (grey) and the SAE 5120 (green). As stated before, the last loading step must be considered separately as the test did not reach 6,000 cycles at this stress amplitude; it is therefore highlighted as a filled circle. The normalisation of the values is therefore based on the temperature information of the penultimate load step, which results in the fact that the damage value in the last

load step becoming greater than 1, which is physically insignificant. The black squares in figure 7.9(a) represent the calculated data points from the LIT of the 20MnMoNi5-5 steel and are further summarised in table 7.3. To obtain the missing parameters b and $\sigma_{f'}$ of the S-N curve according to Basquin, an allometric fit is used. Here too, all data points except the last one at 405 MPa are taken into account because of the previously discussed reason. The fit is characterised by a very high degree of accuracy. The parameters of the generated S-N curve for all tested materials are summarised in table 7.4. In order to validate the S-N curve, several CATs were performed. The result of the MiDAcLife calculation as well as the ones of the CATs for validation are given in figure 7.9(a). Considering the experimentally determined fatigue lives of the CATs (blue circles), the remarkably good agreement with the CAT values calculated by the information from the LIT (black squares) becomes clear. In the high-cycle fatigue (HCF) regime, the generated S-N curve describes the CAT data points very well. A noticeable deviation occurs in the transition range to the LCF regime (low cycle fatigue), which is in this case defined for cycles below 10^4. However, this is to be expected due to the different fatigue damage processes in the different regions LCF and HCF. The linear approach according to Basquin is only valid for the HCF regime and therefore, deviations at cycles smaller then 10^4 can be neglected.
In figure 7.7(a), the fatigue strength of the material was estimated to the range 370 MPa - 380 MPa. The data displayed in figure 7.9(a) confirm this assumption, since one CAT reaches nearly one million cycles at a stress amplitude of 380 MPa. Based on this, it can be concluded that the fatigue strength must be just below 380 MPa. Furthermore, the S-N curve depicts the comparatively brittle material behaviour of the 20MnMoNi5-5 steel, which was already suspected in the cyclic deformation curves in figure 7.7(a), as the failure of the specimen only occurs in a very small range of stress amplitudes from 380 MPa - 425 MPa.

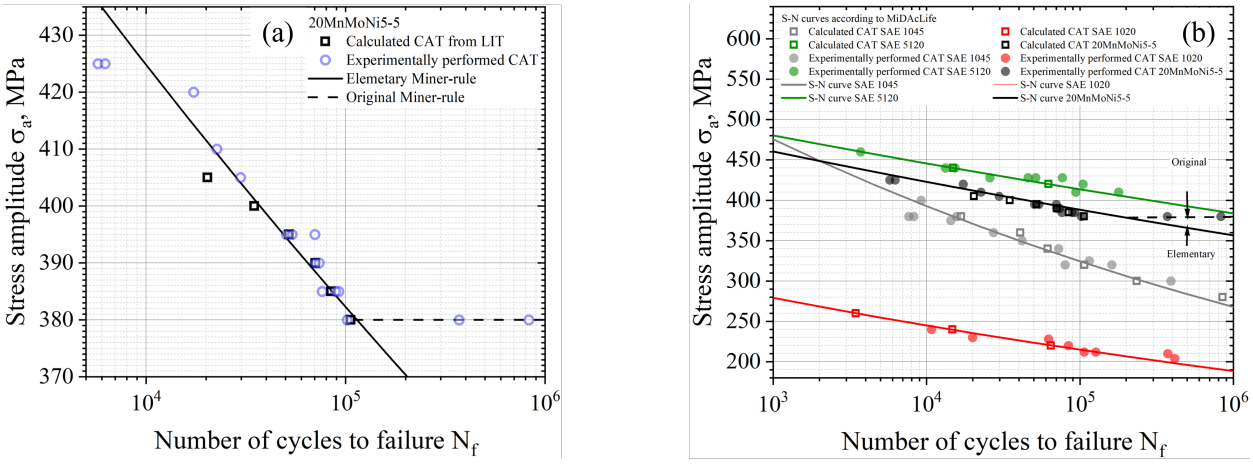

Figure 7.9: (a) S-N curve calculated according to MiDAcLife, including constant amplitude tests as a validation for the 20MnMoNi5-5 steel; (b) S-N curve calculated according to MiDAcLife, including constant amplitude tests as a validation for the SAE 1045, SAE 1020 and SAE 5120 steels

The dashed line here describes an approach based on the original Palmgren-Miner damage accumulation, while the solid line shows a variant adapted from the elementary approach. Figure 7.9(b) presents the results of other steels to validate the approach developed for the 20MnMoNi5-5

steel. As it was already shown for the 20MnMoNi5-5 steel in figure 7.9(a), a very good agreement between experimental and calculated fatigue data can also be given for the three other materials. Moreover, the assumption is confirmed that the two curves of the materials SAE 1045 and SAE 1020 in normalised material conditions are below those of the SAE 5120 steel, which is due to its quenched-tempered condition. When considering the stress amplitude at a value of $N_f = 10^6$ cycles, it can also be seen that the fatigue strength estimation from figure 7.7(b) was very accurate. Table 7.4 summarises the parameters for all tested materials.

Table 7.4: Results MiDAcLife S-N curve generation.

Material	$\sigma_{f'}$ [MPa]	b [-]
20MnMoNi5-5	647.92	-0.046
SAE 5120	600.83	-0.032
SAE1045	845.07	-0.083
SAE 1020	413.53	-0.057

As a final result, it should be pointed out that this evaluation is not only independent of the materials/material states examined, but that other measurement techniques can also be used in addition to thermography. Table 7.5 shows the MiDAcLife results when calculated on the basis of the results of the electrical resistance measurement ΔR, which can be seen in figure 7.7(b).

Table 7.5: Results MiDAcLife with electrical resistance.

ΔR [10^3 µΩ]	σ_a [MPa]	Sum [10^3]	D_i [-]	N_f [-]
6.16	380	6.16	0.123	97655
6.92	385	13.09	0.138	86892
8.35	390	16.65	0.166	72091
11.16	395	22.26	0.223	53913
17.55	400	34.99	0.349	34287
33.38	405	66.57	0.666	18024

With the data from table 7.3, the parameters for the S-N curve can be determined to $\sigma_{f'} = 651.67$ and b $= -0.046$. The deviation to the thermographic evaluation is rather small.

7.5 Conclusion

Within the scope of the present research, a new short-time method was developed based on the material response of a load-increase test (LIT). The material response can be measured by different methods. In the present research, the temperature data of an IR camera and the electrical resistance were considered. The basis of the new method is the linear damage accumulation according to Palmgren Miner. It can be summarised as follows:

- The partial damage of each loading step of a LIT can be calculated by normalising the values of the change in temperature to the last step at which the specified number of cycles was reached.
- By rearranging Palmgren Miner's equation, the number of cycles to failure for a notional CAT of each stress amplitude of the LIT can be calculated based on the partial damage.
- The parameters of the S-N curve according to Basquin can be received by using an allometric fit.
- It only requires one LIT to generate an S-N curve for the lifetime prediction in the HCF-regime.
- The method is independent of the material and its heat treatment condition and different measurement techniques can be used.

The authors goal is to validate the methods on more materials. It could be interesting to test the new method not only on steels, but also on other material groups such as cast irons. Furthermore, important factors such as alloying composition, roughness, residual stresses and hardness as well as notch geometries might be taken into account. So far, the method is only based on a linear approach, which will be extended in future research.

Acknowledgements

The authors would like to thank the Federal Ministry for the Environment, Nature Conservation, Nuclear Safety and Consumer Protection (Bundesministerium für Umwelt, Naturschutz, nukleare Sicherheit und Verbraucherschutz, BMUV, funding reference number: 1501623) for the financial support of this project. The authors would like to thank the GRS (Gesellschaft für Anlagen- und Reaktorsicherheit) as the project management agency as well as the University of Applied Sciences Kaiserslautern for further financial support for the procurement of lab infrastructure. Additional thanks to Shimadzu Europe and EVIDENT (former OLYMPUS) for their support in technical equipment provision.

Journal Contribution III

A nonlinear lifetime prediction method for un- and low alloyed steels by damage determination based on non-destructive measurement techniques

Fatigue & Fracture of Engineering Materials & Structures

F. Weber[1,2], Moritz Maul[1], Florian Juner[1] P. Starke[1,2]

[1] Department of Material Sciences and Materials Testing (WWHK), Institute QM[3] University of Applied Sciences Kaiserslautern, Schoenstr.11, Kaiserslautern, 67659, Germany

[2] Faculty of Natural Sciences and Technology, Saarland University, Campus, Saarbrücken, 66123, Germany

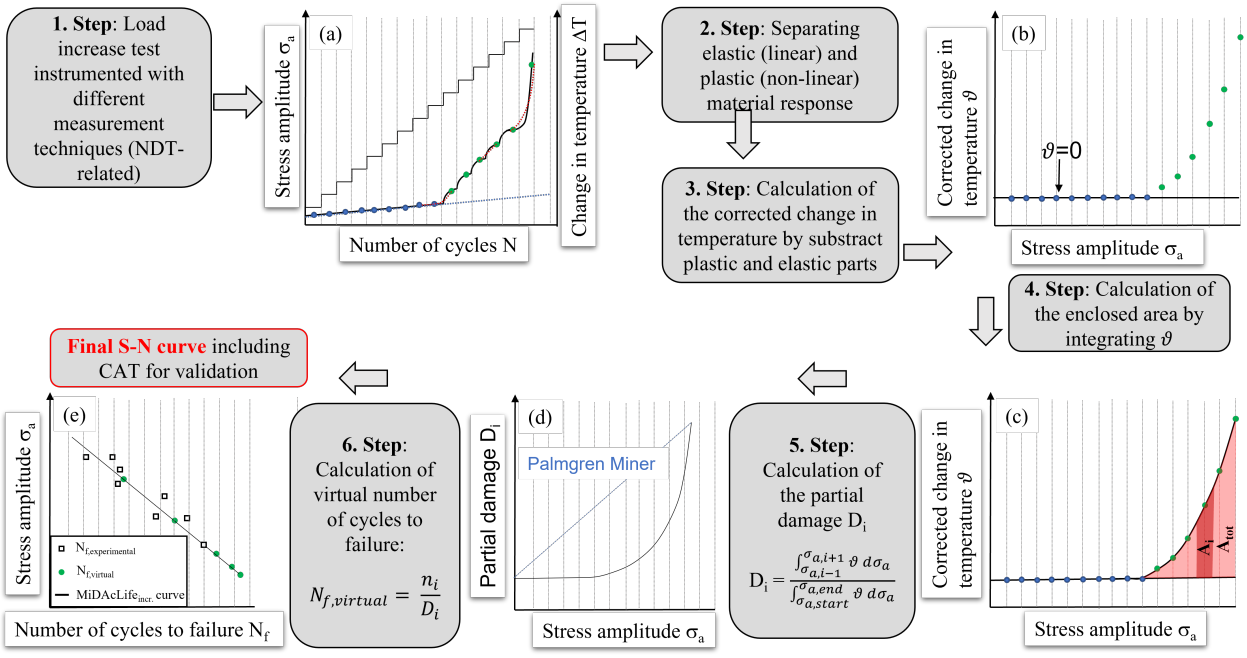

A nonlinear lifetime prediction method for un- and low alloyed steels by damage determination based on nondestructive measurement techniques

Abstract

Materials used in nuclear power plants are exposed to cyclic loading, which is why the understanding of fatigue behaviour is of great importance. Due to high time investments and resulting increased costs, Lifetime Prediction Methods, which significantly reduce the amount of specimens, have already been developed. Within this paper, the Lifetime Prediction Method MiDAcLifeincr is presented, which enables a determination of a trend S-N curve in the High-Cycle-Fatigue-regime based on only one fatigue test and the combination of conventional fatigue testing with NDT-related measurement techniques. The process-orientated monitoring of the cyclic deformation behaviour provides the basis for the time- and cost-effective provision of fatigue data. Compared to previous methods, the consideration of variable loading is an essential aspect of the research application. The test material is a 20MnMoNi5-5 steel, the results of which are extended to include other steels for validation reasons.

8.1 Introduction

To minimize the possibility of sudden failure of dynamically loaded components, it is essential to precisely characterise the fatigue behaviour of the construction materials used to avoid serious damage. The design of cyclically loaded components is usually based on S-N curves representing the relation between the applied load and the number of cycles to failure [3]. Since constant stress amplitudes are rarely found in real applications, specific type of methods has to be developed. These types of methods enable to calculate the materials‘ lifetime in case of variable amplitude loading. A very simple and common used approach is the linear damage accumulation according to Palmgren Miner [12, 13]. The approach is based on the assumption that a dynamic load is related to a partial damage D_i within the material. This partial damage accumulates with an increasing number of load cycles until the failure of the specimen or a component occurs. In the case of steels, the critical value of the total damage D is equal to one.

$$D = \sum D_i = \sum \frac{n_i}{D_i} \tag{8.1}$$

The partial damage D_i of a defined load amplitude is therefore defined by equation 8.1 as the ratio of the number of applied cycles n_i and the number of cycles to failure N_i. The simplest variants of the Miner rule are the elementary and the original Miner rule. In the elementary Miner rule, the existence of the fatigue strength is not taken into account. In contrast, the original form includes the fatigue strength in a rudimentary way, with the simplification that the number of cycles tends towards infinity for load amplitudes below the fatigue strength. In recent years, it has been shown that the Palmgren Miner approach is a simple and fast method for estimating the fatigue life under variable dynamic loading, but the assumption of linearity that is made leads to significant deviation in the results caused by the non-linearity of the material mechanism and the resulting damage. For that reason, a large number of further developments have already been

published, which include the non-linear fatigue behaviour. In 1967, Manson recognized, that the linear damage rule does not consider the order of applied loading and therefore developed the double linear damage rule [133, 279]. The idea was to separate the linear damage rule into two phases consisting of the linear damage rule for crack initiation and the linear damage rule for crack propagation. Due to Manson's adaptations by separating the fatigue processes, the original approach was improved while maintaining simplicity. However, the determination of the knee-point is, among other aspects, a weak point of the method [127]. The knee-point is defined as the cycle ratio at the first load level which is sufficient to initiate an effective macro-crack [279]. In later research, Subramanyan was able to develop a non-linear damage model, which uses iso-damage lines for fatigue life prediction [129]. It is assumed that the iso-damage lines converge at the knee point of an S-N curve. For a dynamic load with two steps, the cyclic ratio of the applied cycles and the number of cycles to failure is given by equation 8.2:

$$C_3 = 1 - (C_2 + C_1^{\alpha_1})^{\alpha 2} \tag{8.2}$$

Due to the definition of the exponents α_i in equation 8.2, the fatigue strength σ_e was included in these calculations.

$$\alpha_i = \frac{\sigma_{i+1} - \sigma_e}{\sigma_i - \sigma_e} \tag{8.3}$$

Despite the numerous already existing methods and modifications, non-linear damage accumulation is also of great importance in current research work, which can be shown by a number of references [124, 153, 280–282]. According to Bjørheim et. al. [151], damage can be expressed in terms of a differential equation given in equation 8.4:

$$\frac{dD}{D} = q(\sigma, m) \cdot \frac{dn}{n} \tag{8.4}$$

where the damage D is a function of the parameter q and the applied cycles n. The parameter q is in turn a function of the stress amplitude σ_a and the material properties m. In order to solve equation 8.4, the following approach is used:

$$Log(D) = q(\sigma, m) \cdot Log(n) + C \tag{8.5}$$

Via mathematical relationships represented in [151], damage can be expressed by using equation 8.6.

$$D = \left(\frac{n}{N_f}\right)^{q(\sigma,m)} \tag{8.6}$$

In comparison to the linear approach of Palmgren Miner, damage is a function of the stress amplitude σ_a, the material properties m and consequently dependent on the number of applied load cycles n and the number of cycles to failure $\mathrm{N_f}$. The main focus within this research is to integrate NDT-related measurement techniques into the conventional fatigue testing in order to increase the

information content as an outcome of the fatigue process. This research deals with temperature-, electrical resistance- and strain measurements. There are already some previous research results from other research groups, focusing on these topics. Especially temperature measurements using IR-camera technique are of great interest in previous and present research. La Rosa [170] introduced a method which uses thermographic data to obtain information with regard to the dynamic properties. This proposed method enables an estimation of the fatigue strength with an extremely reduced number of specimens and tests, respectively. It is based on a pixel-by-pixel determination of the specimen surface, which shows the relation of the change in temperature with the number of cycles. The authors could show that a notable temperature increase is only visible for stress amplitudes above the fatigue strength. Furthermore, the change in temperature is a function of the stress amplitude. Higher stress amplitudes lead to a higher increase in the change in temperature. To estimate the fatigue strength, the change in temperature is plotted against the corresponding stress amplitude and the load step at which a first increase can be monitored is detected. Fargione et al. [231] extended the Risitano method to determine not only the fatigue strength but also to generate S-N curves. By using the equilibrium between the energy induced in the specimen and the sum of the internal energy and dissipated heat, the authors stated that the plastic deformation energy is proportional to the dissipated heat. With the determination of the parameter Φ which describes the integral of the change in temperature as a function of N, an S-N curve can be determined by calculate different number of cycles to failure. Cappello et val. [283] also used thermographic measurements to establish a correlation between the harmonic content of the temperature and the material dissipation on a SAE 1045 steel. The aim of this research was to analyse the phase difference between the first and the second harmonic components of the temperature signal. An accuracy improvement of the dissipated energy measurement for fatigue life estimation was carried out by Shiozawa et al. [284] using the phase 2f lock-in method, which is also based on the phase information as an extension of conventional lock-in methods. Rigon et al. [285] proposed a model which enables an analysis of the specific heat loss at the tip of notched specimens. Furthermore, some previous research, e.g. [176, 286], used the entropy as a parameter describing the material behaviour under dynamic loading. Due to the large number of methods that use thermography to assess fatigue properties, only a selection of further literature is referred to here [173, 287–291]. In addition to thermographic evaluations, the consideration of the electrical resistance as an indicator of microstructural changes is a useful tool. Wu et al. [292] used a combination of tensile and fatigue tests equipped with electrical and magnetic methods to generate trend S-N curves in the HCF-regime. The determination of the strain in carbon fibers, using electrical resistance measurements is given by Todoroki et al. [293]. Another method, dealing with the damage accumulation during a fatigue process in the HCF-regime is proposed by Sun et al. [206]. Further studies on the relation between the electrical resistance and mechanical properties can be found in [208, 209, 212, 294–298]. Most of the mentioned methods above require either an already existing S-N curve, or a large number of fatigue tests leading to increased time effort and costs. As a result, the need arises to extend the existing approaches with a process-orientated lifetime prediction. This process-oriented monitoring of the fatigue life is guaranteed by using non-destructive measurement (NDT) techniques as infrared (IR) camera systems, digital image correlation (DIC), electrical resistance measurements or magnetic (field strength) measurements. The goal of the so-called lifetime prediction methods (LPM) is to enable a better design of dynamically loaded components or structures by the investigation of the response of the material to the applied loads. With a better understanding of the ongoing microstructural changes during a fatigue test, safety factors in S-N curves might be reduced, which leads to better dimensioning of components. This

is a decisive factor from an ecological and economic point of view. A number of LPM have already been developed at the Department of Materials Science and Materials Testing at the University of Applied Sciences Kaiserslautern. These enable the generation of a trend S-N curve in the High Cycle Fatigue (HCF) regime [238,299]. These methods allow a reliable prediction of the fatigue life, based on one load increase test (LIT) / strain increase test (SIT) and two constant amplitude tests (CAT). By using a stepped specimen geometry, the method SteBLife enables the determination of a trend S-N curve with only one specimen [235]. Even though the above-mentioned methods have provided an increase in information about ongoing fatigue mechanism and a considerable saving in time and costs, it is not possible to calculate the fatigue life in combination with the induced damage per load cycle. For this reason, the method MiDAcLife (Miner Damage Accumulation Lifetime Prediction) was developed, which is based on only one LIT [259] and represents a first step towards a lifetime prediction of randomly loaded structures or components. Within the framework of this research, the MiDAcLife method is further improved as MiDAcLife$_{\mathrm{incr}}$. For each load amplitude (in this case stress amplitude), the material response is considered separately, and the calculation is based on an integrated corrected temperature curve. The incremental consideration of the material response as a result of the dynamic loading enables the potential that different damage mechanisms and microstructural changes, e.g. dislocation structures, can be taken into account in a more efficient way. It permits a lifetime prediction of virtual CATs for different materials with a very small deviation compared to conventional conducted CATs.

8.2 Materials and Methods

8.2.1 Material

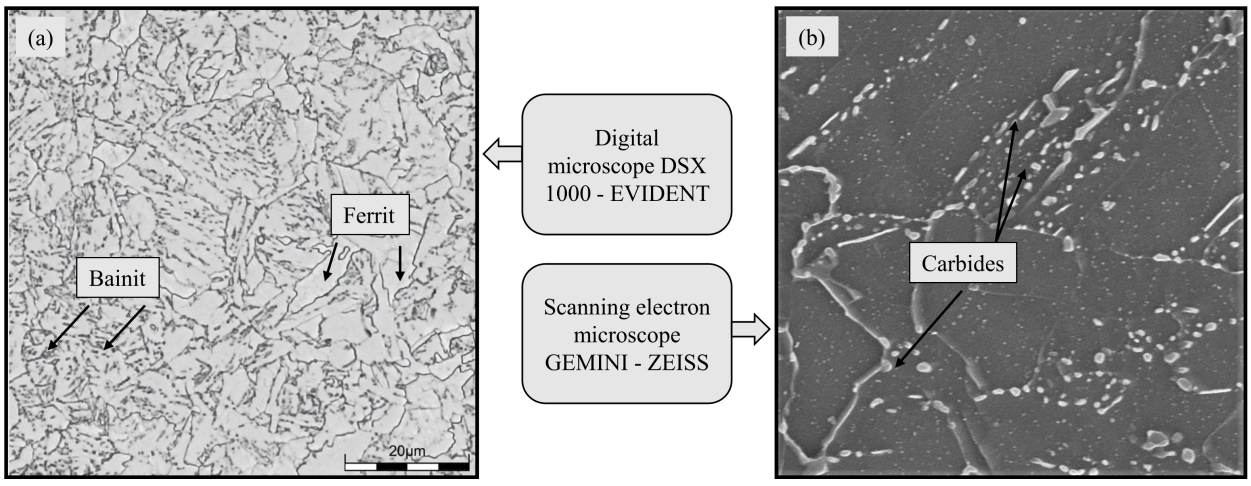

Figure 8.1: Micrographs of the 20MnMoNi5-5 steel using digital (a) and scanning electron microscopy (b).

The material used in this research is a 20MnMoNi5-5 steel (1.6310), which is mainly used as a material for spray lines in German nuclear power plants. The for this application typical ferritic-bainitic microstructure of the steel is illustrated in figure 8.1. Due to its chemical composition, the 20MnMoNi5-5 steel is mostly comparable to a SAE 5120. The microstructure of the 20MnMoNi5-

5, which is a low-alloyed steel, is mainly ferritic with irregular orientated needle-shaped bainitic portions. The specimens were taken out of a pipe subjected to a water-spray quenching heat treatment. In figure 8.1(b) it is also noticeable that there are carbides within the material, forming some kind of clusters especially along the grain boundaries

Even if the Lifetime Prediction Method is being developed on a 20MnMoNi5-5 steel, the validation on other materials is urgently needed in order to evaluate the results. For this reason, the $\text{MiDAcLife}_{\text{incr}}$ method was also applied to the steels SAE 1045 (1.1191), SAE 1020 (1.1149), SAE 5120 (1.7149) and SAE 4140 (1.7225). The chemical compositions of all materials investigated in this work are given in table 8.1 A detailed analysis of the above mentioned steels can be found in literature [183, 235, 259, 299].

Table 8.1: Chemical composition of the investigated materials according to own analysis

Material	C	Si	Mn	Cr	Ni	Mo	S
1.6310	0.218	0.246	1.385	0.076	0.762	0.487	0.003
1.1191	0.470	0.230	0.720	0.670	0.070	0.014	0.013
1.7149	0.195	0.273	1.314	1.060	0.093	0.024	0.024
1.1149	0.236	0.287	0.480	0.118	0.114	0.014	0.018
1.7225	0.400	0.260	0.740	1.070	0.090	0.180	0.020

Due to the differing microstructural compositions and the material conditions, the independency of cyclic hardening or cyclic softening behaviour can be demonstrated as part of the method development. Within this research, round specimens with a cylindrical gauge length, which allows the application of the before-mentioned measurement techniques, were used. The geometry of the specimens is given in figure 8.2.

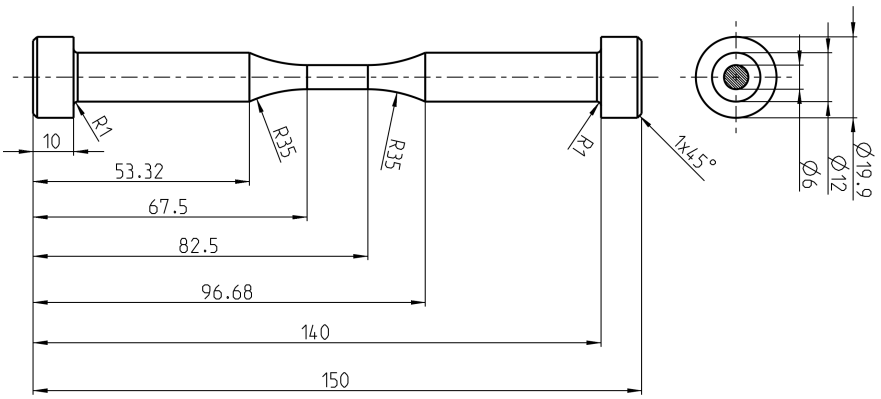

Figure 8.2: Dimension of the round specimen for load increase tests.

The specimens were machined using a turning process with a rotational speed of 600 rpm and a feed rate of 0.05 mm/min. A drawing of the specimen geometry is given in figure 8.2. To ensure a good and, above all, reproducible surface quality, the specimens were mechanically polished after turning, resulting in a surface roughness value of R_a =0.1 µm.

8.2.2 Methods

8.2.3 Experimental setup

The fatigue experiments of this research were performed stress-controlled on two servo-hydraulic testing rigs by the company Shimadzu Europe GmbH (Duisburg, Germany), type EHF-U and EHF-L with a maximum dynamic load of 50 kN and 20 kN, using sinusoidal load-time-functions. The load ratio was chosen to R = -1, whereas the loading frequency was set to 5 Hz. All tests were performed at ambient temperature. The experimental setup is given in figure 8.3. The basic idea of the proposed method is to gain a maximum of information during a fatigue process by integrating different measurement techniques into the setup. The main results within the framework of this research originates from the temperature measurement using an IR-camera type thermoIMAGER TIM 450 by the company Micro-Epsilon Messtechnik GmbH & Co. KG (Ortenburg, Germany), which enables the detection of the mean dissipated heat. The spectral range of the camera is 7.5 - 13 µm and the optical resolution amounts 382 x 288 pixels, resulting in a thermal sensitivity of 0.04 K. In Addition to the temperature measurement, the change in electrical resistance and the plastic strain amplitude is determined. For electrical resistance measurements, a four-point method configuration with a high accurate power supply by the company TOELLNER Electronic Instrumente GmbH (Herdecke, Germany) is used and the change in electrical resistance can be monitored with a measuring device NI 9238 by the company National Instruments (Austin, USA) (input voltage range: ± 500 mV). It enables a sensitive detection of the microstructural defect evolution (e.g. increase/decrease of dislocation density, microcracks) during the fatigue process. By using a tactile extensometer type DYNASTRAIN by the company Shimadzu Europe GmbH (Duisburg, Germany) with a gauge length of 12.5 mm, the total strain amplitude can be recorded. By postprocessing the total strain amplitude in a MATLAB program, the plastic strain amplitude can be derived from the mechanical stress-strain hysteresis loop.

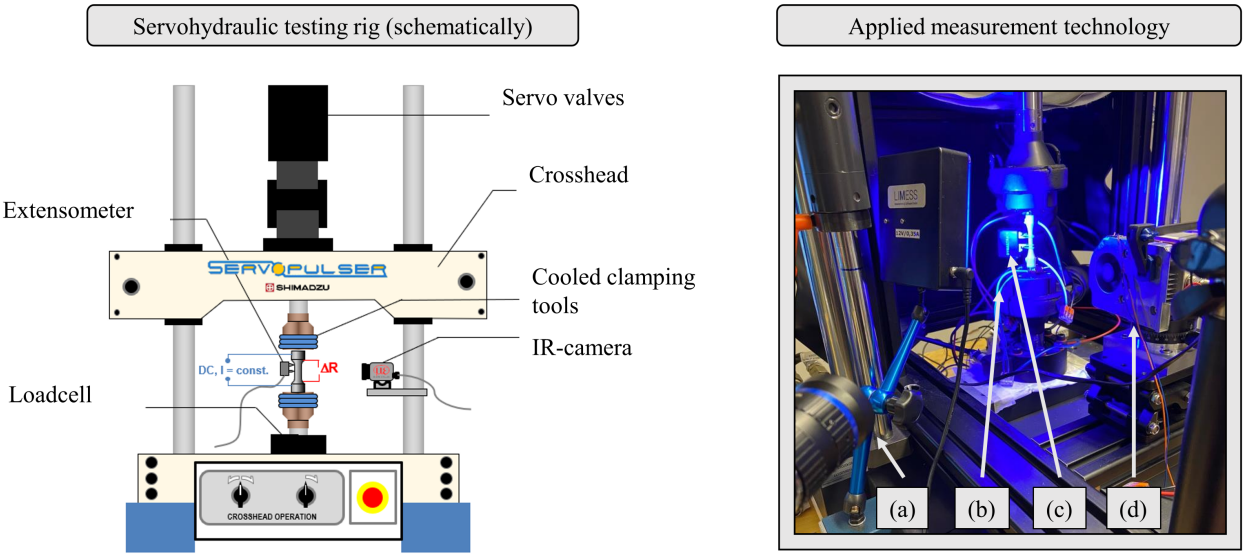

Figure 8.3: Schematic illustration of the servo hydraulic testing rig (left) and applied measurement technology (right): (a) DIC (Digital Image Correlation); (b) Electrical resistance measurement; (c) Tactile Extensometer; (d) IR-camera.

A more detailed description of the experimental setup is given in [259, 299]. Within this research the main focus is on load increase tests (LIT). Constant amplitude tests are only carried out to validate the quality (slope and position) of the generated S-N curve. Table 8.2 summarises the experiments carried out with the 20 MnMoNi5-5 steel.

Table 8.2: Test plan 20MnMoNi5-5 for the evaluation according to MiDAcLife$_{\text{incr}}$

Specimen	Experiment	Parameters
20MnMoNi5-5-LIT	LIT (for calculation)	$\sigma_{\text{a,start}} = 250$ MPa $\Delta\sigma_{\text{a}} = 5$MPa
20MnMoNi5-5-CAT1	CAT (for validation)	$\sigma_{\text{a}} = 390$MPa
20MnMoNi5-5-CAT2	CAT (for validation)	$\sigma_{\text{a}} = 380$MPa
20MnMoNi5-5-CAT3	CAT (for validation)	$\sigma_{\text{a}} = 410$MPa
20MnMoNi5-5-CAT4	CAT (for validation)	$\sigma_{\text{a}} = 370$MPa
20MnMoNi5-5-CAT5	CAT (for validation)	$\sigma_{\text{a}} = 350$MPa
20MnMoNi5-5-CAT6	CAT (for validation)	$\sigma_{\text{a}} = 410$MPa
20MnMoNi5-5-CAT7	CAT (for validation)	$\sigma_{\text{a}} = 345$MPa

8.2.4 MiDAcLife$_{\text{incr}}$

To expand the already existing LPMs like StressLife, StrainLife and SteBLife, only one LIT forms the basis of the procedure according to MiDAcLife$_{\text{incr}}$. The basic approach of MiDAcLife$_{\text{incr}}$ is schematically given in figure 8.4.
As a first step of the evaluation according to MiDAcLife$_{\text{incr}}$, a LIT needs to be conducted stress-controlled with a starting stress amplitude $\sigma_{\text{a,start}}$ evidently below the fatigue strength of the material. After a defined number of cycles, the stress amplitude is increased by $\Delta\sigma_{\text{a}}$. This process needs to be repeated until specimen failure occurs. From previous investigations, a suitable step length of the LIT for materials with a predominantly cyclic softening behaviour was estimated to 6,000 cycles. In comparison, a step length of 9,000 cycles is selected for materials that exhibit cyclic hardening behaviour after initial softening. These values seem to be suitable, as an energetically stable state is reached with regard to the dissipated energy. A more detailed description of how the parameters of a LIT must be chosen, can be found in literature [299,300]. The main idea of the method is that the damage induced into the specimen directly correlates with the material response (8.4). Equation 8.6 also indicates the dependency of the accumulated damage from the material properties. In order to be able to evaluate these properties, the material response due to the fatigue loading is measured by using different NDT-related techniques. For instance IR-thermography or electrical resistance measurements, are very sensitive tools to measure and evaluate changes in microstructure during the fatigue process [173,184,301–310], whereby the focus in this article is on the use of temperature data. Additionally, values from related change in electrical resistance and plastic strain amplitude are included into the consideration.

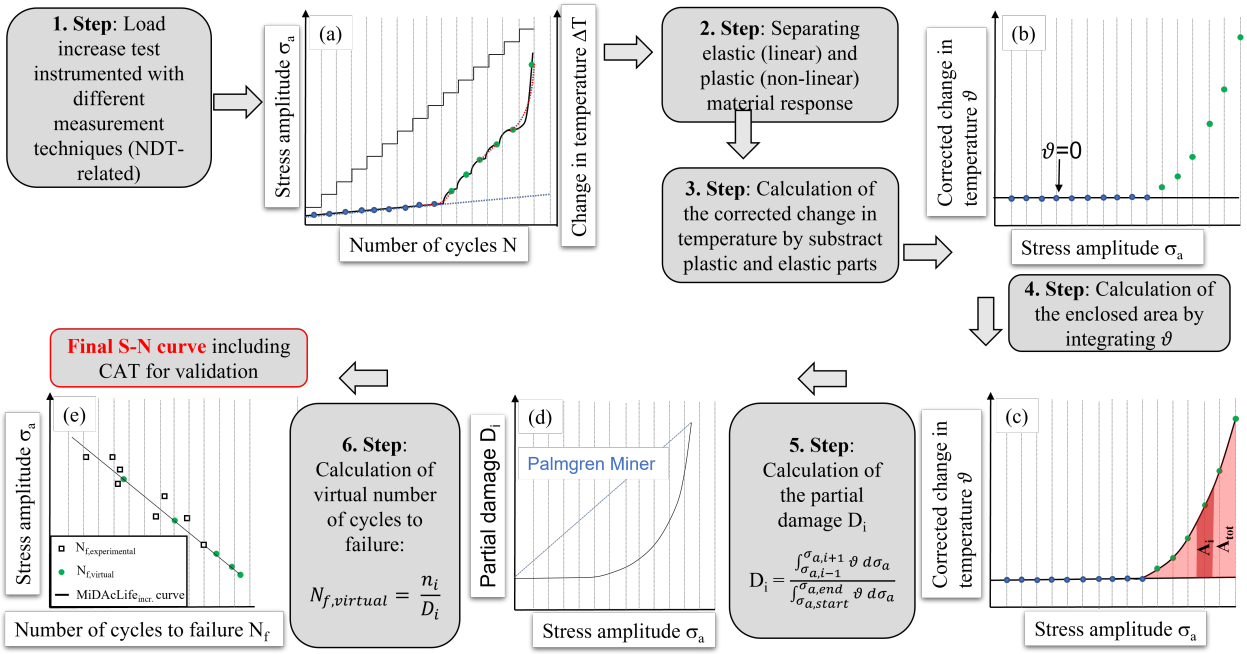

Figure 8.4: Schematic illustration of the lifetime prediction method MiDAcLifeincr. (a) Load increase test and the corresponding material response; (b) Corrected change in temperature as a function of the stress amplitudes from the load increase test; (c) Integration of the corrected change in temperature to calculate the partial damage Di; (d) Comparison of the course of partial damage according to Palmgren Miner (linear) and MiDAcLifeincr (non-linear); (e) Final S-N curve according to MiDAcLifeincr including experimental CAT as validation points.

Thermoelastic portions of the temperature signal are symmetrical under tension and compression and therefore do not contribute to a temperature increase. Therefore, assuming that only the plastic portions of the material response need to be considered for the damage calculation, a reliable separation of these two portions is essential, which is step 2 of the calculation process. The damage introduced into the material as a result of the fatigue loads, causes a release of energy. The main portion of the energy dissipates as heat [166], whereas the remaining part is stored strain energy. Boulanger [169] summarized the temperature development during a fatigue test with equation 8.7:

$$\rho c_p \left(\frac{\partial \theta}{\partial \tau} + \frac{\theta}{\tau_{eq}} \right) = s_{the} + d_1 \tag{8.7}$$

where ρ describes the density of the specimen, c_p the heat capacity and $\dot{\varepsilon}$ the temperature variation with respect to the initial equilibrium temperature. The factor τ_{eq} stands for the heat loss to the environment and s_{the} for a heat source due to thermoelasticity, whereas d_1 is a heat source due to dissipation. This leads to the conclusion that the temperature development is made up of dissipation and thermoelasticity. The energy and therefore the heat induced into the specimen can be formulated as:

$$w = \int_{N'} s_{the}(\dot{\varepsilon}) + d_1 dN \tag{8.8}$$

The heat source from equation 8.8 is a function of the strain rate $\dot{\varepsilon}$. In a simplified consideration, the strain rate is only influenced by the stress amplitude. Due to the fact that the load levels of the LIT are below the yield strength, for most part even below the fatigue strength, a linear material behaviour can be assumed. This linear behaviour results in a linearity of the first term of the integral. Based on the above assumptions, the induced energy can be expressed as a linear function combined with an integral of the dissipated heat.

$$w_h = \sum_{i=1}^{m} g(\sigma_{a,i}) \cdot n_i + \int_{N'} d_1 dN \tag{8.9}$$

In equation 8.9, g is a linear function which is only influenced by the stress amplitude $\sigma_{\mathrm{a,i}}$ (stress amplitude of the individual load steps of the LIT). In order to exclude the linear portion in the calculation, a temperature correction needs to be performed, which indicates step 3 of the evaluation. The corrected change in temperature results from the subtraction of the plastic and the elastic material response and is given in figure 8.4(b). Due to the incremental consideration of the allometric description of the plastic range of the LIT, various microstructural changes and different damage mechanism, e.g., differing dislocation structures, can be considered as a function of the applied stress amplitude in each calculation step. $\mathrm{MiDAcLife_{incr}}$ utilises that the partial damage of each load step correlates with the enclosed area by the corrected change in temperature curve, which is why each partial damage can be mathematically described with a quotient of the two integrals. This relation is given in equation 8.10.

$$D_i = \frac{\int_{\sigma_{a,i-1}}^{\sigma_{a,i+1}} \vartheta d\sigma_a}{\int_{\sigma_{a,start}}^{\sigma_{a,end}} \vartheta d\sigma_a} \tag{8.10}$$

where $\sigma_{\mathrm{a,start}}$ is the starting stress amplitude of the LIT and $\sigma_{\mathrm{a,end}}$ describes the stress amplitude of the last load step. The integral consideration of the corrected change in temperature data marks step 4 in $\mathrm{MiDAcLife_{incr}}$ and can be seen in figure 8.4(c), whereas (d) shows the comparison of the linear damage curve according to Palmgren Miner and the non-linear curve according to $\mathrm{MiDAcLife_{incr}}$ (step 5). With the assumption of equation 8.1, it is possible to calculate virtual number of cycles to failure $\mathrm{N_f}$,virtual for each stress amplitude of the LIT (step 6). These data points can be converted into an S-N curve according to Basquin using an allometric fit (figure 8.4(e)). The validation of the S-N curve is carried out with the implementation of experimental CAT, performed in a conventional manner.

8.3 Results and Discussion

8.3.1 Results of load increase tests

A LIT can be compared to the image of a "fingerprint" of the respective material. It enables a first estimation of the fatigue endurance limit and an evaluation of the material behaviour. In case of the 20MnMoNi5-5 steel, the starting stress amplitude is set to 250 MPa, which results from

previous investigations. The step length is chosen to 6,000 cycles and for the load increase 5 MPa was used. All parameters for the LITs are given in Table 8.3, whereby $\sigma_{a,f}$ is defined as the load step at which the failure of the specimen occurs.

Table 8.3: Parameters of the LIT for the 20MnMoNi5-5 steel

$\sigma_{a,start}$ [MPa]	$\Delta\sigma_a$ [MPa]	ΔN [-]	$\sigma_{a,f}$ [MPa]
250	5	6,000	410

Figure 8.5 shows the result of the LIT (given parameters) for the 20MnMoNi5-5 steel with the slopes of the stepwise increased load amplitude and the material responses for different measurement techniques. The red line represents the change in temperature, the blue line the related change in electrical resistance (quotient of change in electrical resistance and the initial electrical resistance in the unloaded state) and the grey line the plastic strain amplitude. All three quantities indicate a pure cyclic softening behaviour expressed through increasing values of the various material responses. The increase in plastic strain amplitude indicates an extension of the width of the stress-strain hysteresis loop and is associated with cyclic softening behaviour. The increase and decrease in the plastic strain amplitude allows conclusions to be drawn about the material behaviour. More ductile materials tend to undergo cyclic hardening processes after an initial cyclic softening, while high-strength (more brittle) materials usually only exhibit pure softening behaviour. For this reason, the steel 20MnMoNi5-5 seems to show a more brittle behaviour. This insight can also be confirmed by the fact that the change in the material response during the fatigue test is very small and significant increases only occur in the last load steps.

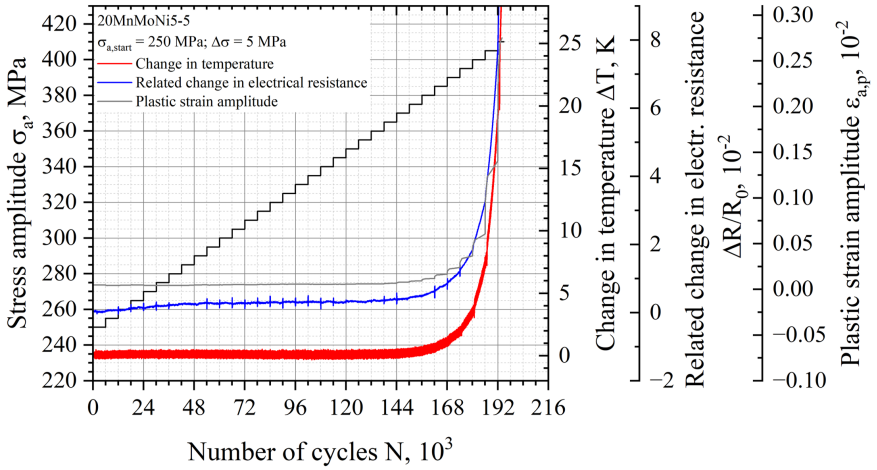

Figure 8.5: LIT for the 20MnMoNi5-5 steel with the slopes for the stress amplitude and the material responses on the basis of the change in temperature, related change in electrical resistance and the plastic strain amplitude.

In order to make a first estimate of the fatigue strength, the material response must be analysed in more detail, which is shown in figure 8.6(a).
The dashed lines from figure 8.6(a) corresponds to the elastic portion of the material response. To determine the fatigue strength of the material, the stress amplitude at which a first change in the material response can be detected must be considered. It should be noted at this respect that the change in temperature does not exhibit a greater scatter than the other two measuring methods. The deviation of the temperature data and thus the formation of some kind of scatter bands results from the thermoelastic effect. This effect is based on the principle that the change in temperature of a specimen can be affected by a changing volume as a result of an applied load. While elastic tensile loads result in cooling, elastic compressive loads cause the specimen to heat up [311–313]. Since the evaluation of the fatigue strength is made more difficult by the thermoelastic effect, the smoothed signal of the change in temperature is also shown in figure 8.6(a), which makes it easier to recognise the first increase in the material response.

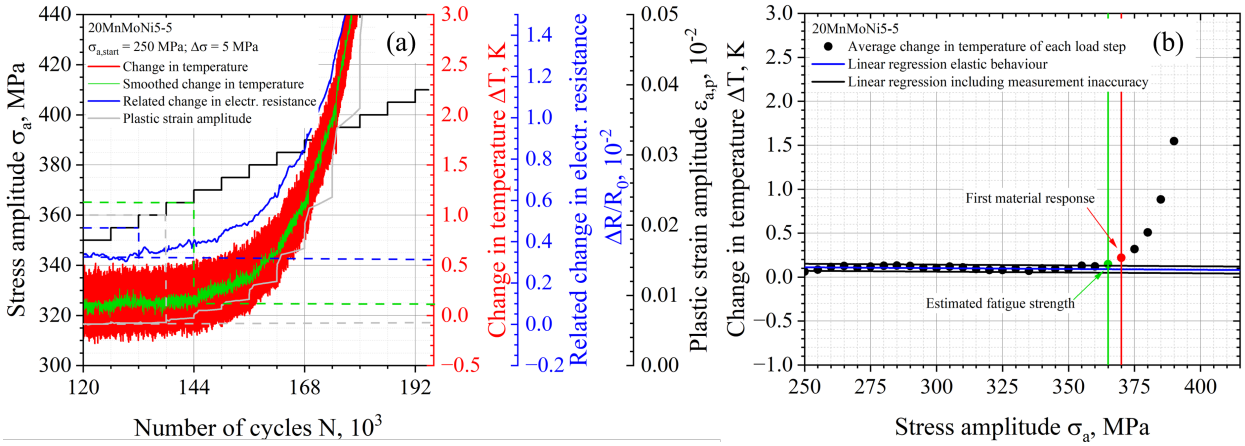

Figure 8.6: (a) Detailed determination of the fatigue strength of the 20MnMoNi5-5 steel based on the LIT using the change in temperature, the related change electrical resistance, and the plastic strain amplitude; (b) Exemplary determination of the fatigue strength of the 20MnMoNi5-5 steel considering the thermal sensitivity of the IR-camera.

Every measurement technique is superimposed by certain measurement uncertainties and/or the measurement sensitivity, which must be taken into account. The exact determination of the fatigue strength, taking the thermal sensitivity of the IR-camera into account, is shown as an example in figure 8.6(b).
The blue line in figure 8.6(b) represents the linear regression of the elastic portion of the material response. Both black lines indicate the scatter band due to the thermal sensitivity. To examine the fatigue strength, the stress amplitude needs to be considered at which the first material response greater than the scattering occurs. In this case the first increase can be detected at a stress amplitude of 370 MPa. Therefore, the last load level at which no damage can be determined is 365 MPa which is consequently defined as the fatigue strength of the material. While the change in temperature and the plastic strain amplitude led to an estimation of the fatigue strength of 365 MPa and 360 MPa, the related change in electrical resistance indicates the first material responses at a lower load level, resulting in an estimated fatigue strength of 355 MPa. The deviation of the fatigue strength can be explained by the different sensitivities to the respective material mechanisms

of the measurement techniques used.

8.3.2 MiDAcLife$_{incr}$

As a first step in the MiDAcLife$_{incr}$ evaluation, the average data points of the material response for each load level must be extracted and plotted as a function of the corresponding stress amplitude. To enable a comparison of different measurement techniques, the data points of the temperature measurement are extended in figure 8.7(a) by those of the strain- and electrical resistance measurements.

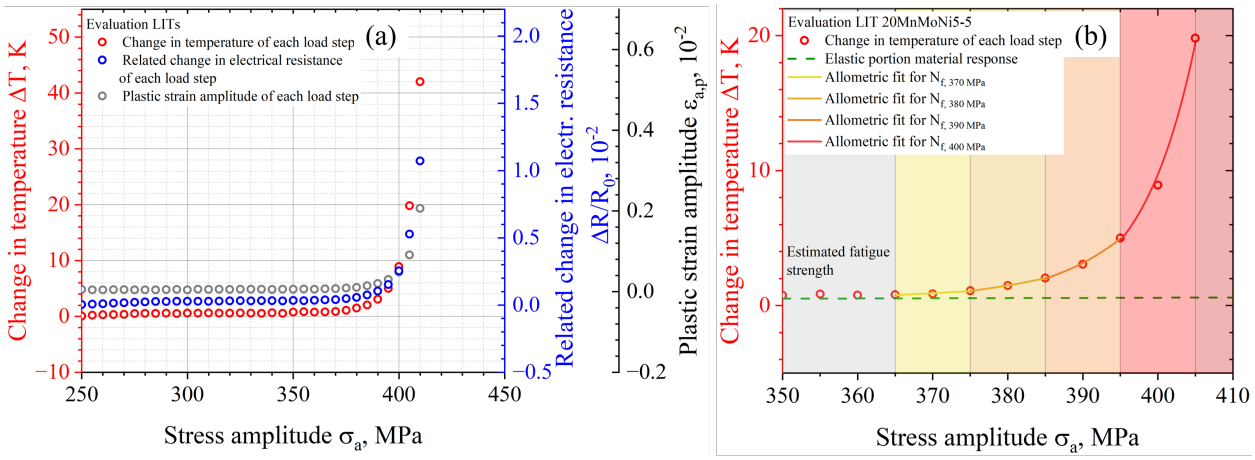

Figure 8.7: (a) Average values of the change in temperature, related change in electrical resistance and plastic strain amplitude for each load step of the LIT for the 20MnMoNi5-5 steel; (b) Analysis of the LIT data with the elastic fit function (green dashed line) and the different allometric fit functions (yellow to red) for the incremental consideration of the plastic range for the 20MnMoNi5-5 steel.

The figure above illustrates that all three measurement methods show a similar curve progression. It also indicates that the curves initially display a linear relationship until the material response increases from a certain stress amplitude and therefore changes to a non-linear behaviour. Following this assumption, particularly in the HCF regime, only the plastic portions of the material response contribute to the damage, the curves need to be corrected for the elastic portion. The following evaluation is based on change in temperature data, but can also be carried out equivalently using data sets from other measurement techniques. In figure 8.7(b), the elastic portion of the LIT is fitted linear (green dashed line), whereas the plastic region is fitted incrementally with different allometric fits (yellow, orange and red). The reason for the incremental approach is that different stress amplitudes cause different damage mechanism and therefore, the slope of the function must be considered separately. In order to calculate the number of cycles to failure of a virtual CAT at a stress amplitude of $\sigma_{a,i}$, the allometric fit is applied to the data points of $\sigma_{a,i-1}$ to $\sigma_{a,i+1}$.

Furthermore, the fatigue strength of the 20MnMoNi5-5 steel can be estimated to be approx. 365 MPa, which agrees well with the results of the LIT from figure 8.6(a). The corrected material response curve (here corrected change in temperature curve ϑ) results from the difference between

the allometric and the linear fit and is given in figure 8.8(a). The partial damage Di of each load level is calculated by integrating the function at the considered stress amplitude and then normalising to the value of the total area enclosed by the curve, which is given in equation 8.10. As an example, the integration for a stress amplitude of 390 MPa (orange) and the entire material response (grey) can be seen in figure 8.8(a).

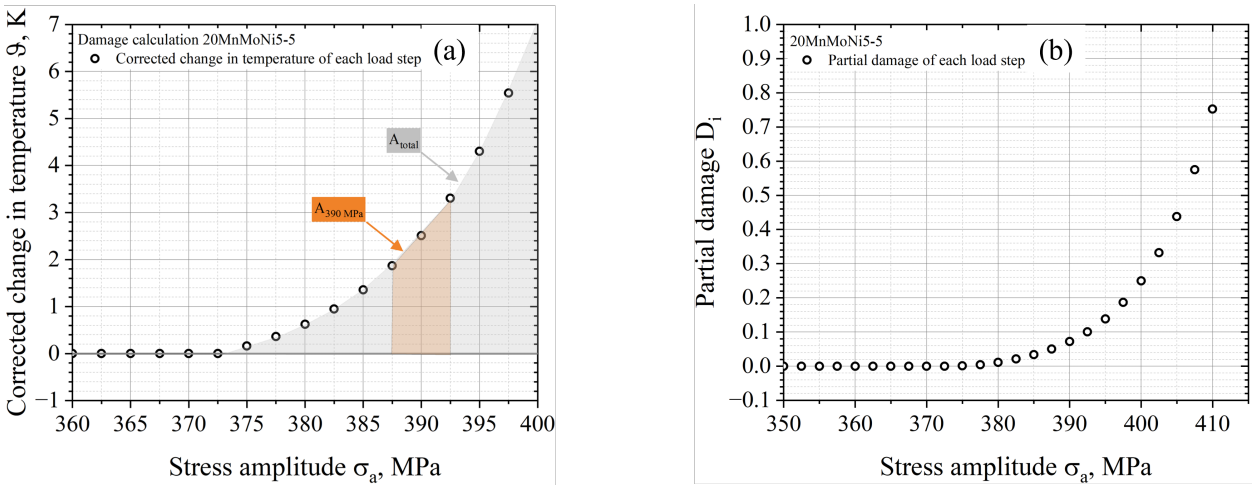

Figure 8.8: (a) Corrected change in temperature slope as a function of the stress amplitude for the 20MnMoNi5-5 steel. Additional schematic indication of the damage calculation via the respective areas enclosed by the curve; (b) Partial Damage Di of each load level of the 20MnMoNi5-5 steel based on the change in temperature evaluation.

From the above figures and equation 8.10(a), the values of the partial damage can be calculated and plotted against the stress amplitude, which is given in figure 8.8(b). Based on the partial damage of each load level, the number of cycles to failure for virtual CATs can be determined by using the values for the applied load cycles n and the partial damage Di into equation 8.1. An allometric fit of the data points can be used to obtain an S-N curve according to Basquin's approach. The result for the steel 20MnMoNi5-5 is given in figure 8.9. As stated in figure 8.9, red data points represent the virtual CATs of the MiDAcLifeincr calculation based on change in temperature data. The figure also contains calculated data derived from the values of the change in electrical resistance (blue) and the plastic strain amplitude (grey). In order to validate the calculated S-N curve, further experimental CATs were carried out. The results are shown as black data points in the same diagram. In addition, two CATs were carried out in the higher cycle range on a resonance testing rig. Due to the different frequencies (5 and 260 Hz), these tests were marked by triangles. These data points can only be regarded as an initial estimate, as the influence of the testing frequency was not further investigated in this study. According to the literature, an increase in fatigue life can be assumed in case of increased testing frequency. The calculated S-N curve has the following form:

$$\sigma_a = \sigma_f \cdot (N_f)^b \tag{8.11}$$

The good agreement between the calculated and the experimental data points can already be recognised from the presented results. It is noticeable that the evaluation based on the plastic

strain amplitude does not describe the experimental results as well as the change in temperature or the electrical resistance, especially at lower stress amplitudes. From this insight, the great potential of NDT related methods compared to conventional strain measurements can be deduced, as the tactile extensometer appears to have reached its resolution limit. A comparison of the coefficients σ_f and exponents b related to equation 8.11 of the applied measurement techniques is given in Table 8.4.

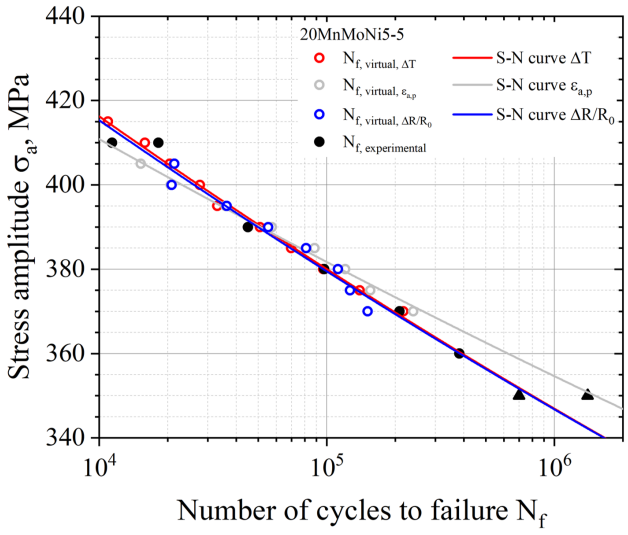

Figure 8.9: S-N curve calculated according to MiDAcLifeincr as well as experimental determined lifetimes for validation for 20MnMoNi5-5 steel.

Table 8.4: Overview of coefficients σ_f and exponents b of S-N curves calculated according to MiDAcLifeincr for 20MnMoNi5-5 steel.

Material response	σ_f [MPa]	b [-]
Change in temperature	599.2	-0.040
Related change in electrical resistance	595.8	-0.039
Plastic strain amplitude	551.4	-0.032

In order to validate the method, the LPM is also applied to four other steels. The cyclic deformation curves of the respective LIT are illustrated in figure 8.10(a) and figure 8.10(b). The subdivision into rather brittle and ductile material behaviour only serves to provide a better structure in the diagrams. In general, two different material behaviours can be seen in figure 8.10(a) and figure 8.10(b). The temperature-based cyclic deformation curves of SAE 4140, SAE 5120 and 20MnMoNi5-5 steels (shown in blue shades) indicate a continuous more or less steady increase in the material response, which represents the pure cyclic softening behaviour typical for higher-strength (more brittle) material states. In particular, the fact that the cyclic deformation curves of 20MnMoNi5-5 and SAE 5120 steels show a high degree of similarity, can be attributed to their chemical composition. Due to the quenched and tempered microstructure of the SAE 4140 steel, cyclic softening behaviour is also to be expected here. The group of more ductile materials, shown

in figure 8.10(b) as orange-coloured temperature curves, is represented by the steels SAE 1045 and SAE 1020. Both steels are unalloyed carbon steels, whereby the SAE 1045 steel has a significantly higher carbon content. Due to the fact that plastic deformation is mainly limited to the ferrite grains, the higher values in material response in the case of the SAE 1020 steel (higher ferrite content compared to SAE 1045 steel) can be explained. In both cases, especially in the last load steps, a decrease of the change in temperature can be detected. This leads to the insight, that both steels tend to a cyclic hardening behaviour after initial cyclic softening (after load increase) as soon as the amount of plastic deformation is high enough. The final results of the S-N curve generation according to MiDAcLife$_{incr}$ are given in figure 8.11, whereas the parameters of the evaluation are listed in Table 8.5.

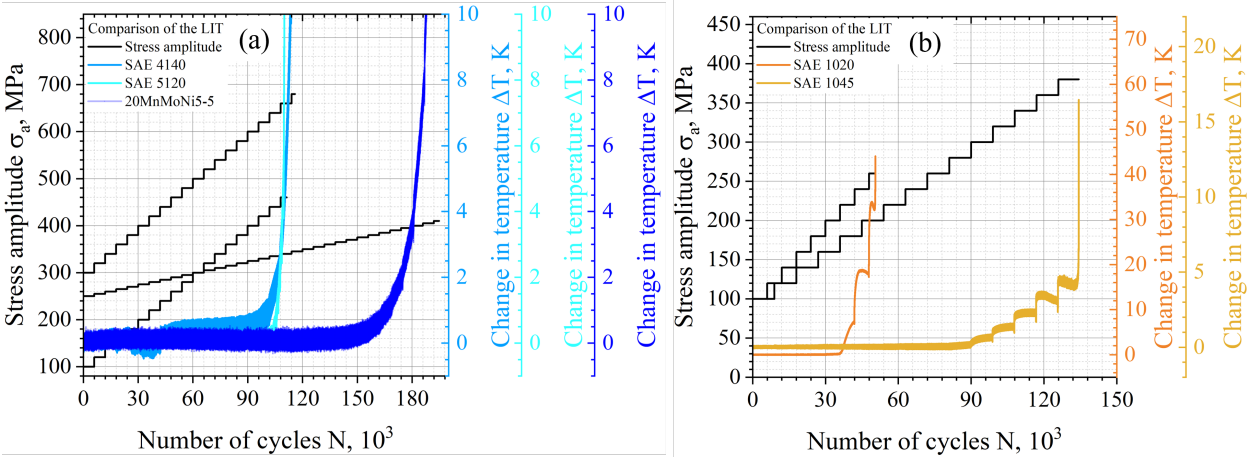

Figure 8.10: (a) Cyclic deformation curves of the LITs based on the temperature of the steels SAE 4140, SAE 5120 and 20MnMoNi5-5; (b) Cyclic deformation curves of the LITs based on the temperature of the steels SAE 1020 and SAE 1045.

Table 8.5: Overview of coefficients σ_f and exponents b of S-N curves calculated according to MiDAcLife$_{incr}$ on the basis of change in temperature data for SAE 4140, SAE 5120, SAE 1045 and SAE 1020 steels.

Material	σ_f [MPa]	b [-]
1.7225	2514	-0.132
1.7149	619.2	-0.034
1.1191	780.9	-0.075
1.1149	367.7	-0.046

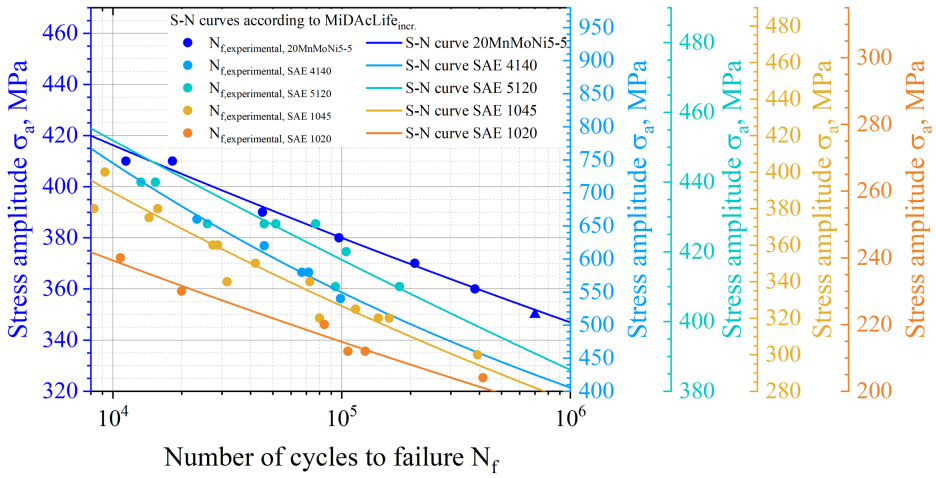

Figure 8.11: S-N curves calculated according to MiDAcLifeincr as well as experimental determined lifetimes for validation for 20MnMoNi5-5, SAE 4140, SAE 5120, SAE 1045 and SAE 1020 steels.

To assess the quality of the LPM MiDAcLife$_{\text{incr}}$, the calculated lifetimes are compared with the experimental determined data points, which is shown in figure 8.12.

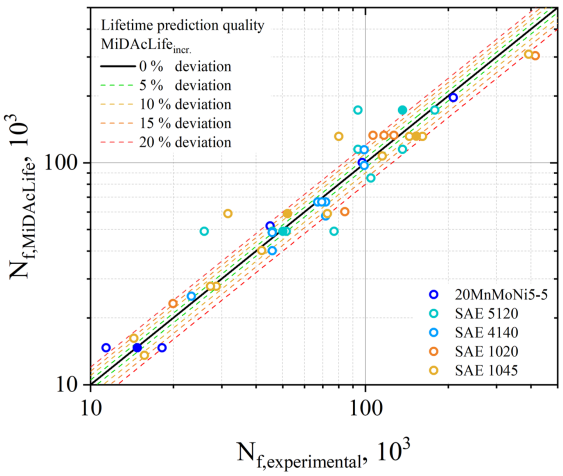

Figure 8.12: Evaluation of the fatigue life prediction based on a comparison of the virtual (calculated) and experimentally determined lifetimes with the labelling of 5% – 20% scatter bands.

In figure 8.12, virtual (calculated) and experimental determined data points are plotted against each other. The solid black line indicates a deviation of 0 %, whereas the dashed green lines represent the +/- 5 % deviation. Furthermore, deviations of +/- 10 % (yellow), +/- 15 % (orange) and +/-20 % (red) are also given in terms of dashed lines in the same diagram. In general, it can be stated that the calculation provides very accurate results compared to the experimental data. Only nine (from 46) test results show a deviation of more than 20 %, which corresponds to a share of 19.5 %. Conversely, this means that 80.5 % of the data points are within the 20 % deviation

range, of which almost 40 % show a deviation of less than 5 %. It should be noted that deviations can be caused not only by the calculation but also, for example, by the natural scattering of the material due to a statistical distribution of defects on the surface and volume of the specimen under consideration. One possible approach to consider this material scatter is to perform several LITs and nominate their results using statistical approaches. Based on these findings, the method for predicting the fatigue life of steels can be further validated.

8.4 Conclusion

The Lifetime Prediction Method $\text{MiDAcLife}_{\text{incr}}$ was developed and introduced as part of this research. Load increase tests were carried out on the steel 20MnMoNi5-5, which is used in spray lines of nuclear power plants. The material response during fatigue loading was detected using different measurement techniques such as IR thermography, electrical resistance and conventional stress-strain measurement. By using the determined correlation among the measured material response and the damage induced into the material, virtual lifetime values can be determined for result-orientated set stress amplitudes. The most important aspects with regard to the research work carried out and an outlook are summarized as follows.

- The lifetime prediction method $\text{MiDAcLife}_{\text{incr}}$ enables to calculate an S-N curve in the High Cycle Fatigue regime on the basis only one load increase test.
- There is a correlation between the in-situ measured material response due to fatigue loading and the damage induced into the material per load cycle.
- The applicability of the lifetime prediction method is independently of the applied measurement technique, whereby the change in temperature and the change in electrical resistance have a significantly higher resolution than tactile extensometers.
- Due to the temperature correction and the incremental consideration of the material response, the potential to consider different damage mechanisms is provided.
- The estimated virtual lifetimes of constant amplitude tests show a very small deviation from the experimental determined lifetimes.
- In further research, the method is being extended to other materials and material groups, such as additively manufactured or cast-iron materials.
- Different influencing parameters such as the surface roughness or residual stresses are going to be included into lifetime prediction methods. The aim here is to enable a conversion of the respective S-N curves depending on the influencing factors.
- Statistical approaches are integrated in perspective by carrying out several load increase tests and using variation calculation approaches to cover the scatter of the materials as well.

Acknowledgements

This research is supported by the Federal Ministry for the Environment, Nature Conservation, Nuclear Safety and Consumer Protection (Bundesministerium für Umwelt, Naturschutz, Nukleare Sicherheit und Verbraucherschutz, BMUV, grant number: 1501623). Furthermore, the authors would like to thank the project management agency GRS (Gesellschaft für Anlagen-, und Reaktorsicherheit), the University of Applied Sciences Kaiserslautern for financial support in the procurement of test infrastructure, Shimadzu Europe and EVIDENT (former Olympus) for their support in technical equipment provision. To validate the developed method, data sets from further completed research projects were additionally used. For this reason, the authors would also like to thank the German Research Foundation (Deutsche Forschungsgemeinschaft, DFG) for the financial support in the projects with the grant numbers STA1133/6-1, STA 1133/10, STA 1133/20-1.

Journal Contribution IV

Implementation of modelled surface roughness in the accelerated lifetime prediction of a 20MnMoNi5-5 steel

International Journal of Fatigue

F. Weber[1,2], P. Starke[1,2]

[1] Department of Material Sciences and Materials Testing (WWHK), Institute QM[3] University of Applied Sciences Kaiserslautern, Schoenstr.11, Kaiserslautern, 67659, Germany

[2] Faculty of Natural Sciences and Technology, Saarland University, Campus, Saarbrücken, 66123, Germany

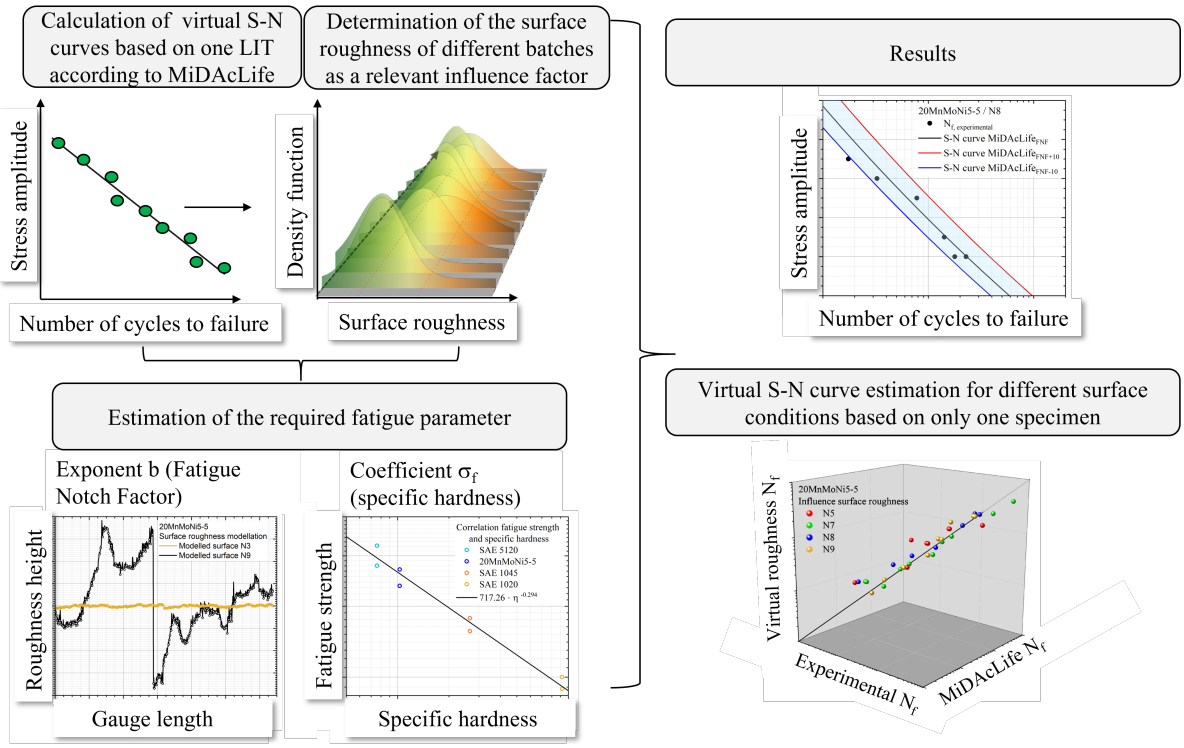

Implementation of modelled surface roughness in the accelerated lifetime prediction of a 20MnMoNi5-5 steel

Abstract

Fatigue of metals is a complex, multi-parametric phenomenon with a high amount of influencing factors. In order to ensure a reasonable lifetime prediction of specimens, structures or components, the impact of these factors need to be understood in detail. Since fatigue cracks mostly initiate at the surface, especially in the high cycle fatigue regime, the surface condition is a very important factor, which has to be taken into account. The presented research proposes a method to model the surface roughness using a Fourier transformation to calculate a fatigue notch factor, which can be included in the accelerated lifetime prediction method MiDAcLife. Therefore, it is possible to generate virtual S-N curves for different surface conditions based on only one fatigue test. The investigated material is a ferritic-bainitic 20MnMoNi5-5 steel, which is mainly used in spray-lines of German nuclear power plants. In addition, a method for calculating the fatigue strength of various materials is presented in which a newly defined parameter, the specific hardness, is introduced.

9.1 Introduction

The aging of components in nuclear power plants leads to an increasing need to develop new methods, which enable an evaluation of the integrity of structures and/or components in the field of nuclear engineering. To assess the integrity, simulations need to be improved on the basis of experimental data. A very important influencing factor of the fatigue process is surface roughness. Therefore, the goal of this research is to consider roughness parameters in the lifetime prediction of a 20MnMoNi5-5 steel, which is mainly used in spray-lines of German nuclear power plants. Assuming cyclic loading in the high cycle fatigue (HCF) regime, crack initiation takes over the most prominent portion of the fatigue life. In previous research, it has been shown that in most cases, fatigue cracks initiate at the surface of a specimen, especially at locations with an increased stress concentration. This observation leads to the conclusion that the surface roughness needs to be considered in the fatigue life calculation.

To describe the stress concentration, Neuber [47] proposed an semi-empirical equation of the stress concentration factor K_t, including standard parameters of the surface roughness.

$$K_t = 1 + n \cdot \sqrt{\lambda \frac{R_z}{\rho}} \tag{9.1}$$

The stress state is given by the factor n, whereas R_z can be defined as the surface height and ρ as the notch radius. A geometric estimation of the surface irregularities is given by λ, representing the ratio of the spacing and the height. This model was further extended by Arola et al. [49, 50], calculating an effective stress concentration factor $\overline{K_t}$. This approach includes the arithmetical average roughness R_a, the peak-to-valley height R_y, the effective valley radius $\overline{\rho}$ and R_z into the calculation and is given in equation 9.2.

$$\overline{K_t} = 1 + n \left(\frac{R_a}{\overline{\rho}} \right) \left(\frac{R_y}{R_z} \right) \tag{9.2}$$

Another approach is given by the FKM-guideline [54] in equation 9.3, which uses the static tensile strength R_m in addition to the surface parameter R_z.

$$K_{R,\sigma} = 1 - a \cdot log \left(\frac{R_z}{\mu m} \right) \cdot log \left(\frac{2R_m}{R_{m,N,min}} \right) \tag{9.3}$$

Kleemann et al. [314] utilised, among others, the approach of equation 9.3 in order to calculate the fatigue strength of different materials as a function of the surface finish, given by a factor F_S, a factor including the residual stresses F_{RS} and the hardness of the material, described by F_{HV}.

$$\sigma_w = \sigma_{w,0} \cdot F_S \cdot F_{RS} \cdot F_{HV} \tag{9.4}$$

At this point it should be noted that $\sigma_{w,0}$ designates the fatigue strength of an unnotched specimen.

Using geometrical parameters to evaluate the influence of the surface roughness on the fatigue strength, Murakami [56, 58] proposed the $\sqrt{area}$-method. It enables an estimation of the fatigue strength as a function of the material's hardness and the $\sqrt{area}$-parameter. The relation is given by equation 9.5.

$$\sigma_w = 1.43(HV + 120)/(\sqrt{area})^{1/6} \tag{9.5}$$

The fatigue strength is expressed by σ_w, whereas $\sqrt{area}$ is a function of the geometrical parameters of the surface roughness. This approach is for example used by Itoga et al. [59], presenting a study which includes rotary bending tests in order to determine the surface roughness effect on step-wise S-N characteristics of a Ni-Cr-Mo steel.
Singh et al. [83] introduced a new method to describe the effect of the surface roughness on the fatigue behaviour of materials (in this case of an AISI 4130 steel), modelling the microstructure and a rough surface of a specimen. To characterise the material degradation due to fatigue loading, the model uses damage parameters from S-N curves of smooth specimen. An additional approach of Xu et al. provided an FE method in order to analyse the stress concentration factor and the relative stress gradient of notches with surface topography [87]. In 2023, Kethamukkala et al. [77] developed an extension of a previously developed time-based sub-cycle fatigue crack growth model for additive manufactured materials, which also uses the approach according to Arola (equation 9.2), to take the effect of an increased surface roughness into account. An analytic approach of calculating the fatigue notch factor (FNF) for different surface finishes was given by Zhu et al. [90], introducing this parameter into the fatigue life calculation of an SAE 4140.
Because of the large number of publications addressing the influence of roughness on the fatigue behaviour of metals, only a selection of further literature references will be referred to at this point [52, 63, 65, 72, 73, 78, 85, 88, 315–317].

The need of an accelerated estimation of fatigue properties arises because of the large amount of specimen that is required to generate an S-N curve. Therefore, different lifetime prediction

methods (LPM) have been developed at the Department of Material Sciences and Materials Testing (WWHK) at the University of Applied Sciences Kaiserslautern in recent years [52, 236, 258–260, 299]. Based on the linear damage accumulation model according to the approach proposed by Palmgren and Miner, MiDAcLife in one of these LPM. It enables a calculation of virtual number of cycles to failure by the combination of conventional fatigue testing and NDT-related measurement techniques, such as thermography or electrical resistance measurements. Based on a load increase test (LIT), the material response is monitored and correlated with the damage induced into the specimen. The aim of this current research is to extend the LPM by integrating the surface roughness into the calculation, resulting in a possibility of an S-N curve estimation only based on roughness information. In addition, conventional constant amplitude tests (CAT) are carried out on a 20MnMoNi5-5 to verify and validate the calculation results.

9.2 Material and methods

9.2.1 Material

The material used within this research is a 20MnMoNi5-5 steel with a ferritic-bainitic microstructure (mostly comparable to an SAE 5120), which is prevalent in German nuclear power plants as a material for spray-lines. A detailed analysis of the material is given in previous research results published in [259, 299]. The influence of the surface roughness on the fatigue properties of the 20MnMoNi5-5 is determined on five different surface finishes within the framework of this research. In order to ensure a standardised and practical classification of the specimens, the surfaces are machined in accordance to DIN EN ISO 1302 [242], dividing surfaces into roughness indicators N1 to N12 (0.025 µm - 50 µm) according to their average roughness value R_a. Table 9.1 provides an overview of the roughness classification according to DIN EN ISO 1302.

Table 9.1: Roughness classification according to DIN EN ISO 1302

Roughness R_a [µm]	Roughness indicator	Roughness R_a [µm]	Roughness indicator
0.025	N1	1.600	N7
0.050	N2	3.200	N8
0.100	N3	6.300	N9
0.200	N4	12.50	N10
0.400	N5	25.00	N11
0.800	N6	50.00	N12

Table 9.2 provides an outline of the machining parameters that were varied and modified for each batch, resulting in the test batches N3-4, N5-6, N7, N8 and N9. Due to the scattering of the machining process and the small differences of the mean surface value in the groups of lower surface roughness, a combination of the classification N3 and N4 (in the following referred to as N3), as well as N5 and N6 (in the following referred to as N5) is proposed.

Table 9.2: Machining parameters N3-N9 batches 20MnMoNi5-5

Batch	Feed Rate [mm/min]	Rotational Speed [rpm]	Cooling
N3	0.05	600	✓
N5	0.05	600	✓
N7	0.20	600	✓
N8	0.20	600	✓
N9	0.20	600	✓
Batch	Pre-Grinding	Polishing	Mod. tools
N3	✓	✓	x
N5	x	✓	x
N7	x	x	x
N8	x	x	✓
N9	x	x	✓

All tests are performed using round specimen, taken out of a pipe with a diameter in the specimens' cross section of 6 mm and a gauge length of 15 mm. A detailed information regarding the geometry of the specimens is given by figure 9.1. Table 9.3 provides average information regarding damage-relevant parameters such as surface roughness and residual stresses, where the increased values of the compressive residual stresses for the batches N3 and N5 originate from the polishing process.

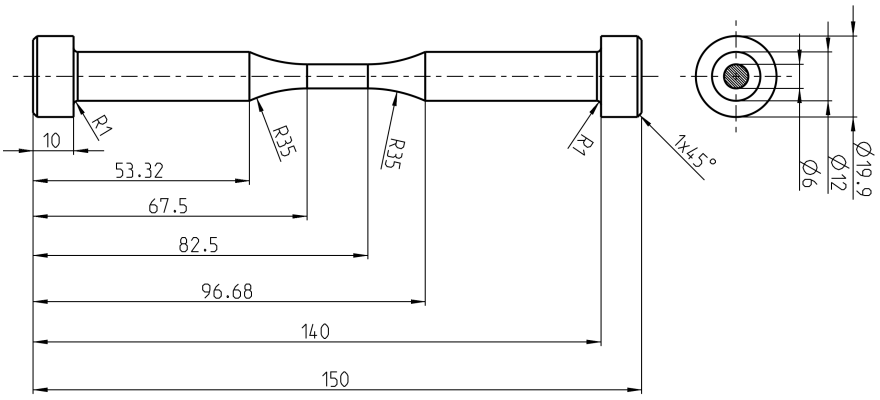

Figure 9.1: Dimensions of the round specimens used.

Table 9.3: Average values of roughness and residual stresses of each surface condition

Batch	Roughness R_a [µm]	Residual stresses [MPa]
N3	0.129	-244.2
N5	0.985	-494.5
N7	1.944	128.5
N8	4.595	159.2
N9	9.713	-20.33

9.2.2 Methods

Within this research, all fatigue tests were performed stress-controlled on a servo-hydraulic testing rig type EHF-L by the company Shimadzu (Shimadzu Deutschland GmbH, Duisburg, Germany). To enable a fatigue life estimation according to the method MiDAcLife, several load increase tests were performed with a sinusoidal load-time function and a stress ratio of R = -1. Figure 9.2 illustrates the experimental setup schematically, including the applied measurement techniques. To perform an accurate LIT, it must start at a stress amplitude that is below both the yield strength and the fatigue strength and increases the stress amplitude after a defined number of cycles. Within this research, the step length is defined as 6,000 cycles. A more detailed guideline of how the parameters of a LIT have to be chosen is given in [259, 299]. The current results are based of the signals of an IR-camera type thermoIMAGER TIM 450 (Micro-Epsilon Messtechnik GmbH & Co. KG, Ortenburg, Germany), electrical resistance measurements, using a four-point method configuration with a high accurate power supply (TOELLNER Electronic Instrumente GmbH, Herdecke, Germany) and a tactile extensometer type DYNASTRAIN (Shimadzu Deutschland GmbH, Duisburg, Deutschland).

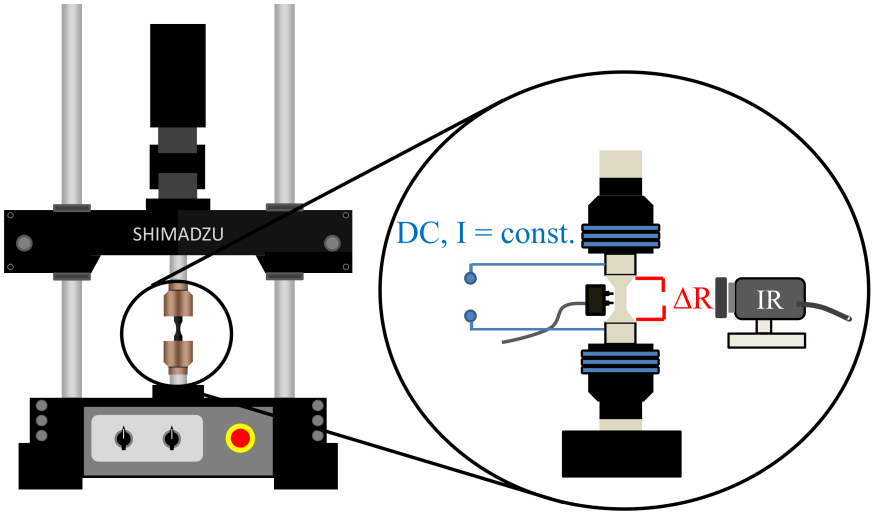

Figure 9.2: Schematic illustration of the servo-hydraulic testing rig EHF-L 20 kN, including the applied measurement techniques IR-camera, electrical resistance measurement and tactile extensometer.

MiDAcLife

MiDAcLife (Miner Damage Accumulation Lifetime Prediction) is a recently developed lifetime prediction method, based on the linear damage accumulation according to the approach of Palmgren Miner. It enables an estimation of virtual number of cycles to failure and therefore a generation of virtual S-N curves. Figure 9.3 provides a short overview of the proposed method. The main focus is on a LIT, instrumented with different NDT-related measurement techniques such as IR-camera or electrical resistance measurements (four point method). The process-orientated monitoring of the

material response allows the partial damage to be estimated on the basis of an integral calculation. With the determined partial damage of each load step and the defined parameters of the LIT, a virtual number of cycles to failure can be calculated. The S-N curve is given as a result of an allometric fit of the virtual data points. A more detailed description of the lifetime prediction according to MiDAcLife is given in [259, 318]. Beside, figure 9.3 contains information about the integration of the surface roughness as an influence factor, which is presented in the following chapters.

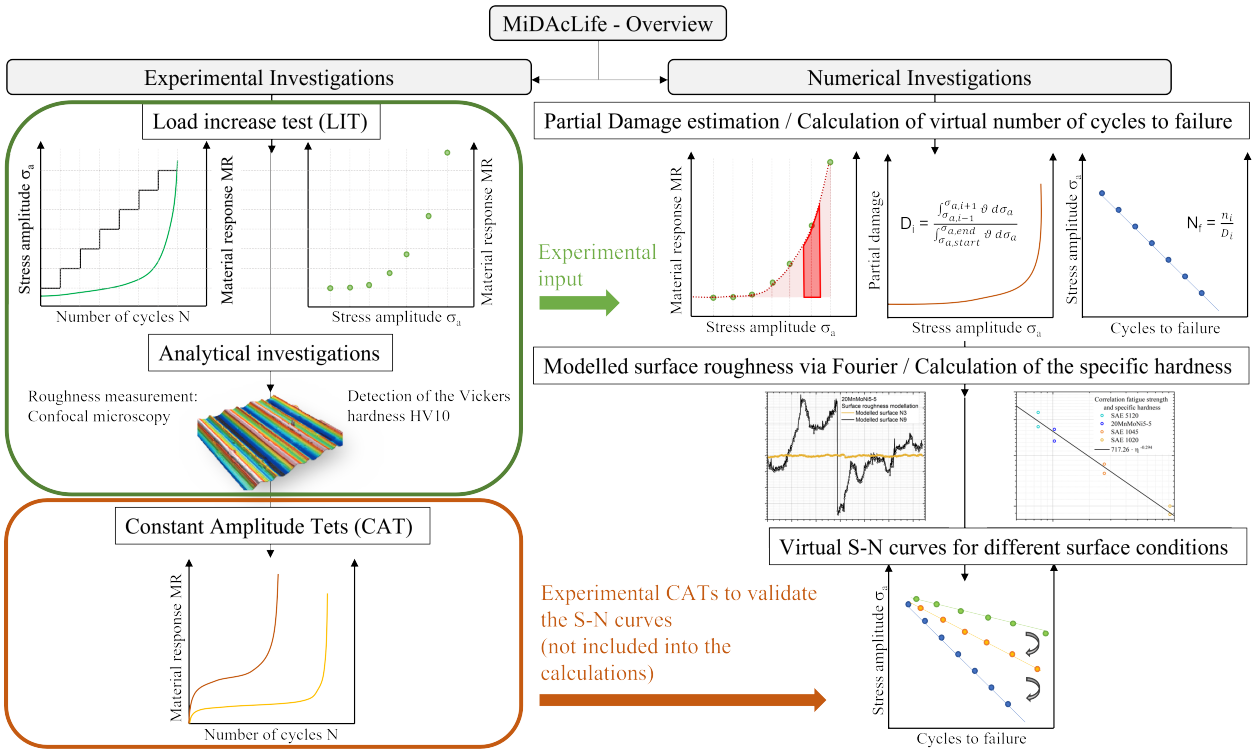

Figure 9.3: Schematic illustration of the MiDAcLife method based on a load increase test and the modelled surface roughness

9.2.3 Fatigue Notch Factor determination

Different surface roughness parameters such as R_a and R_z are measured using a confocal microscope type Smartproof 5 by the company ZEISS (Carl Zeiss Microscopy Deutschland GmbH, Oberkochen, Germany) and a laser-scanning-microscope type LEXT OLS5100 by the company EVIDENT (EVIDENT Europe GmbH, Hamburg, Germany). To ensure a statistically reliable assessment of the specimens roughness, each specimen is measured at a total of 12 measuring points. A schematic illustration of where the roughness parameters are determined is given in figure 9.4.

Using a normal function, a distribution of the R_a values of each batch can be obtained. The advantage of considering a distribution instead of an absolute value is that scattering of fatigue results can be assessed in a better way by the shape of the distribution. If the distribution have clear defined peaks, there is a homogeneous roughness within the batch, resulting in a lower scattering of the fatigue life.

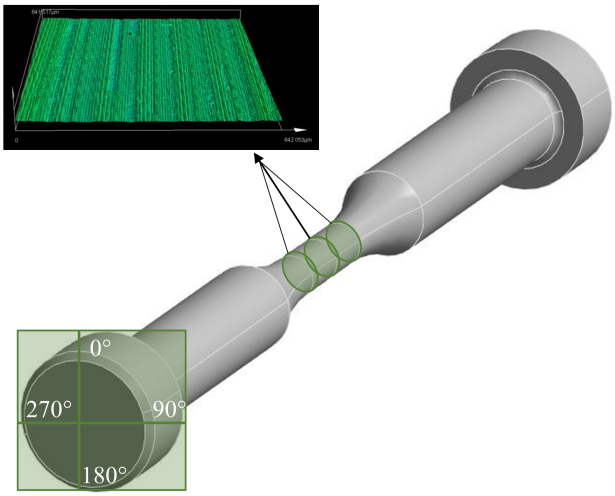

Figure 9.4: Experimental determination of the surface roughness parameters in order to generate a roughness distribution.

To calculate the FNF according to [3, 90, 319], the experimental measured surface data needs to be described mathematically. Therefore the topography is considered as a superposition of cosine functions, which is given in equation 9.6 [90, 92, 93].

$$Z(x) = -\sum_{i=1}^{n} A_i \cdot cos(\frac{2\pi x}{\lambda_i} + \varphi_i) \tag{9.6}$$

In equation 9.6, A_i represents the amplitude, λ_i the wavelength and φ_i the phase of the wave number i. According to the approach of Cheng et al. [93, 319], the FNF is defined by the following equation in which a_0 is the material characteristic length.

$$K_f = 1 + 4\pi \cdot \sum_{i=1}^{n} \frac{A_i}{\lambda_i} \cdot \left(1 - \frac{\pi a_0}{2\lambda_i}\right) \cdot e^{\frac{-\pi a_0}{\lambda_i}} \cdot cos\left(\frac{2\pi x}{\lambda_i} + \varphi_i\right) \tag{9.7}$$

The material characteristic length is a function of the fatigue crack growth threshold ΔK_{th} and the fatigue strength σ_e:

$$a_0 = \left(\frac{\Delta K_{th}}{\sigma_e}\right) \tag{9.8}$$

All required parameters from equation 9.7 can be obtained by a Fourier-transformation. The resulting FNF is further used in the lifetime prediction according to MiDAcLife.
At this point it should be noted that the surface roughness within this research is considered as a static value. However, the surface roughness changes during a fatigue process because of microstructural mechanisms, which can be described by different models [34]. One of these, is the well-known EGM model according to Essmann et al. [320], dividing the surface profile formation at emerging persistent slip bands (PSB) in two main parts: the rapid formation of static extrusions and the slow development of surface roughness due to irreversible slip. Nevertheless, since the

roughness values within this research are very high compared to surface profiles build by extrusions and intrusions, a static consideration is permissible.

9.2.4 Virtual S-N curve determination

As a first step of the S-N curve determination, an S-N curve for one surface condition (in this case N3) needs to be calculated using the experimental data of a LIT. The evaluation is conducted in accordance with the MiDAcLife method, which has been developed and validated on different steels in previous research [259, 318]. The induced damage per load cycle correlates with the material response caused by dynamic loading. The aim of the present research is to generate different virtual S-N curves on the basis of one experimentally determined S-N curve. Therefore, two general parameters need to be derived from the FNF. Because of the influencing effect of the surface roughness on fatigue behaviour, the slope of the S-N curve will change with increasing surface roughness. Based on that, the slope has to be re-calculated. Zhu et al. [90] uses the FNF K_f and the slope of the experimentally determined S-N curve b_0 in order to estimate the fatigue strength exponent b.

$$b = b_0 - \frac{1}{7} \cdot log(K_f) \tag{9.9}$$

However, knowledge regarding the slope of the S-N curve from equation 9.9 is not sufficient, as the position of the curve is still unclear. To estimate the position of the S-N curve, a new method is proposed within this paper.

Since the analysis of fatigue strength of a material requires a high amount of specimens, Görzen et al. [321] developed a method called "Cyclic Indentation Testing", based on the approach of Murakami [56, 322]. The proposed method quantifies the cyclic deformation behaviour obtained in cyclic indentation tests and uses a combination with the Vickers hardness of the material to calculate the fatigue strength.
Due to the present test execution with a load ratio of R = -1 it is not possible to use this approach directly, which is why a modification is necessary. While [321] uses the cyclic hardening exponent from an indentation test, the present research calculates the fatigue strength by correlating the fatigue strength with the product of the Vickers hardness and the cyclic hardening exponent derived from the LIT (specific hardness). To ensure a high fit quality, several data points, originating from a data base of the WWHK, are included into the fit. Furthermore, each material is represented by two data points displaying the fatigue strength derived from the S-N curve at a total cycle number of $2 \cdot 10^6$ and the estimated fatigue strength from the corresponding LIT.
Using equation 9.9 and the definition of the cyclic hardening exponent according to Morrow [243] (equation 9.10), the decrease of the fatigue strength due to the increased surface roughness can evidently be shown and the corresponding S-N curve can be calculated.

$$n = \frac{-b}{1 + 5 \cdot b} \tag{9.10}$$

9.3 Results and Discussion

9.3.1 Influence of the surface roughness on fatigue behaviour

To ensure a reasonable estimation of virtual fatigue data based on roughness measurements, the lifetime reduction caused by an increased surface roughness needs to be quantified experimentally. MiDAcLife, which is described in more detail in [259, 318], is applied on all surface conditions to generate the corresponding S-N curves. The method is based on only one fatigue test (load increase test), given as an example of N3 in figure 9.5 and uses NDT-related measurement techniques to monitor the material response, resulting from a dynamic loading.

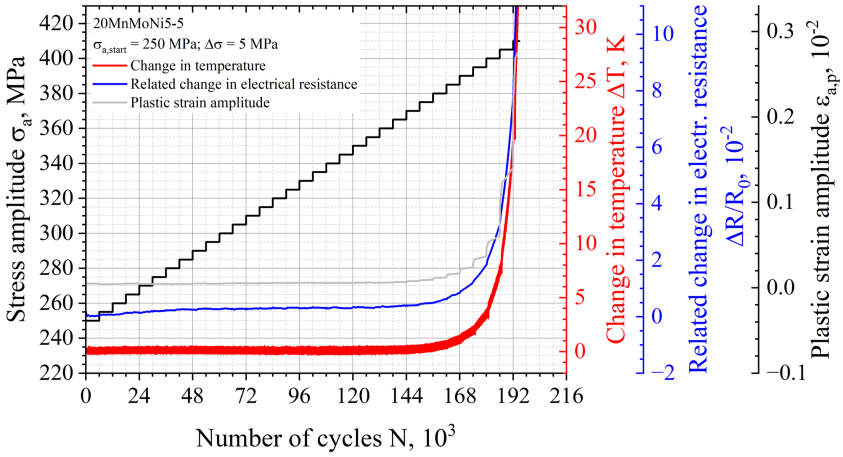

Figure 9.5: N3: Cyclic deformation curve of the LIT of a 20MnMoNi5-5 with the material response measured via thermography, resistometry and extensometer.

The obtained cyclic deformation curves are correlated with the induced damage, which enables an estimation of a virtual number of cycles to failure according to the Palmgren Miner approach. In order to examine the material response during the LIT, different measurement techniques are used. Within this research, a tactile extensometer, an IR camera and electrical resistance measurements are used. Because of the steadily increasing course of the measured signals, a cyclic softening material behaviour can be stated. Figure 9.6 summarises the S-N curves generated according to MiDAcLife for each surface condition, based on the evaluation of the change in temperature. The unfilled circles represent the virtual number of cycles to failure, whereas the filled circles display number of cycles to failure from conventional CATs for validation. It can evidently be stated, that there is a reasonable agreement of the calculated and the experimental determined number of cycles to failure. Only the specimens of the N5 charge show an increased scattering, especially in the range of higher cycle numbers. Because of the machining process, the N5 specimens exhibit high compressive residual stresses compared to the load amplitudes, leading to an increased lifetime, because the residual stresses cannot be degraded rapidly.
While the influence of the surface roughness can evidently be shown for the N8 and N9 batches in form of a decreasing lifetime, there is no significant impairment notable for the batches N3-N7. Therefore, batches N3-N7 are highlighted with a grey band, enclosing the CAT data points. Considering a stress amplitude of σ_a= 360 MPa, the number of cycles to failure of the N8 batch is reduced by approximately 80 % compared to the surface conditions N3-N7. Even more severe is the

lifetime-decrease caused by the surface condition N9 with a reduction of approximately 90 %. The influence of the surface roughness decreases with decreasing load cycles, resulting in different slopes of the S-N curve. The reason for this influence-reduction is given by different damage mechanisms in case of higher load amplitudes in the transition to the LCF regime, where the surface condition is not of great importance anymore. According to the insights of figure 9.6, it can be summarised that the fatigue behaviour is significantly influenced by the surface roughness if a certain threshold is reached.
Since the S-N curves of figure 9.6 are based on one LIT for each surface batch, the aim of the following presented research is to calculate the S-N curves of the batches N5-N9 without any additional experimental effort.

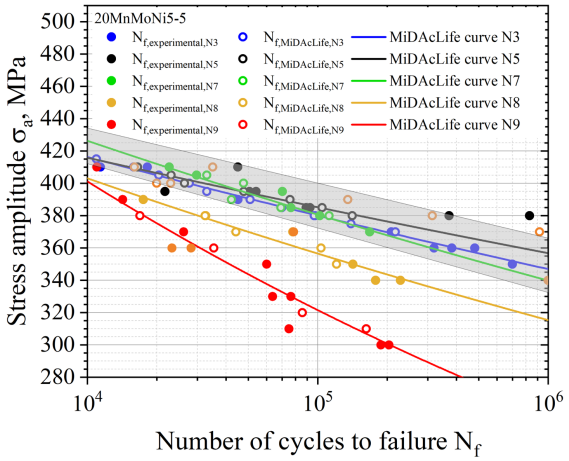

Figure 9.6: S-N curves calculated according to MiDAcLife including data points from conventional constant amplitude tests for validation.

9.3.2 Fatigue notch factor determination

The evaluation of the surface roughness is shown as an example on the two batches N3 and N9. It should be noted, that the remaining batches are analysed in an analogous way. To record the surface topography statistically, a normal distribution according to equation 9.11 is applied.

$$f(x, \mu, \sigma) = \frac{1}{\sigma\sqrt{2\pi}} \cdot e^{-\frac{1}{2}\left(\frac{x-\mu}{\sigma}\right)^2} \tag{9.11}$$

Equation 9.11 is a function of the expectancy value µ and the standard deviation σ. All required parameters are summarised in table 9.4 for N3-1, N5-3, N7-2, N8-1 and N9-2, since these specimens are loaded as a LIT and therefore are directly included into the lifetime prediction according to the MiDAcLife approach.

The results of the distributions for N3 and N9 are given in figure 9.7(a) and 9.7(b).

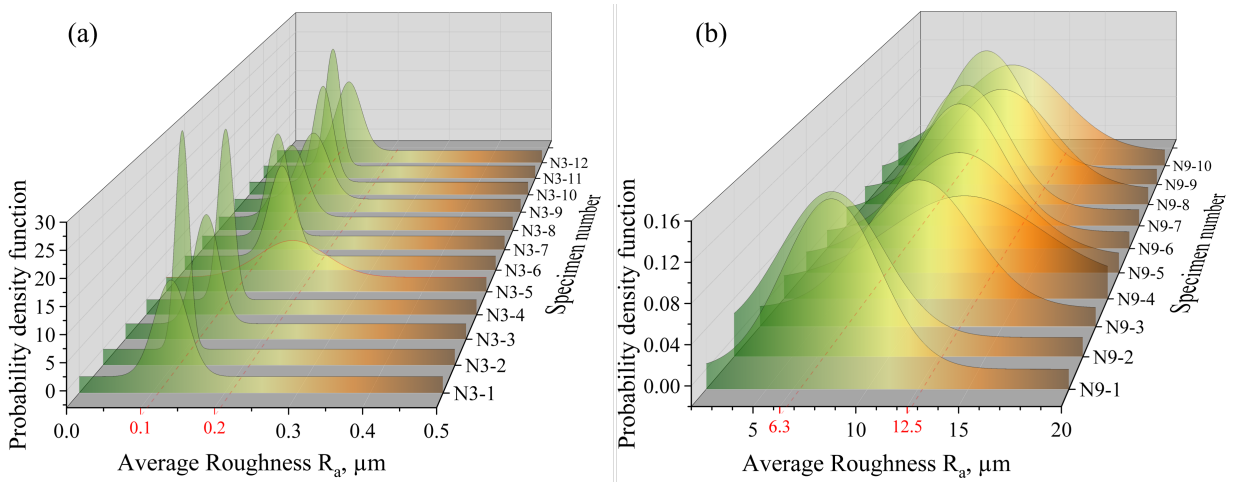

Figure 9.7: (a) Surface distributions of the batch N3; (b) Surface distributions of the batch N9

Table 9.4: Parameters of the normal distribution function for the specimens loaded as a LIT

Specimen	Expectancy value μ	Standard deviation σ
N3-1	0.126	0.023
N5-3	0.872	0.205
N7-2	1.961	0.309
N8-1	4.954	1.154
N9-2	7.045	2.655

The highlighted values illustrate the roughness ranges according to the norm DIN EN ISO 1302. Based on the shape of the roughness peaks, the difference between both batches can be recognised. While N3 specimens are characterised by defined peaks with a narrow width and high intensities, specimens of the N9 batch are represented by peaks with a larger width in the range of 20 µm and lower values for the probability density function. Because of the expansion of the roughness peaks to higher roughness values, a larger scatter in the fatigue behaviour can be expected. The advantage of the distribution-based description of the surface roughness becomes apparent considering figure 9.7(b). The mean value for the surface roughness of specimens N9-3 and N9-4 is in accordance with the mentioned DIN EN ISO 1302. However, even though both specimens are tested at the same stress amplitude of 390 MPa, the number of cycles to failure of specimen N9-4 is about 50 % lower compared to N9-3 (N9-3: 14.240, N9-4: 6.139). While comparing both distributions, it can be stated that there is an evidently higher probability of greater roughness values in case of the N9-4 specimen, leading to a lifetime-reduction. A comparison of the five different batches is given in figure 9.8. To ensure a comprehensive overview within the figure, the amount of illustrated specimens is limited to the LIT of each batch. Because of the differing values for the probability density function for each batch, resulting in a great scaling range of the axis, a meaningful comparison of the roughness distributions is challenging. Therefore, each peak is normalised to its maximum. The previously proposed correlation between the peak-shape and the roughness classification is being confirmed by figure 9.8.

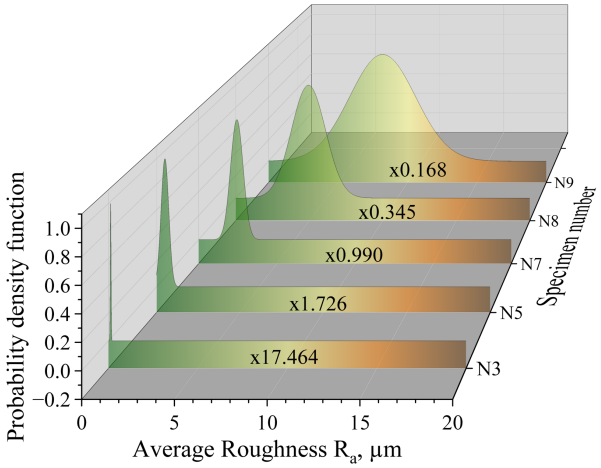

Figure 9.8: Comparison of the distribution functions of all tested surface conditions N3-N9.

After the evaluation of the experimental measured topography data, the surface roughness needs to be described mathematically in order to calculate the FNF. For this reason a MATLAB-script is developed, which uses cosine-functions to illustrate the modelled surface. Once again, the shown evaluation of the MATLAB-script is reduced to batches N3 and N9 and is given in figure 9.9. Considering a multi-notch approach, each peak of the surface roughness is considered as a micro-notch and is therefore marked with circles in figure 9.9 and included in the FNF calculation according to equation 9.7. Table 9.5 shows the result of the FNF estimation for all surface conditions. In addition, the fatigue strength exponent is calculated according to equation 9.9.

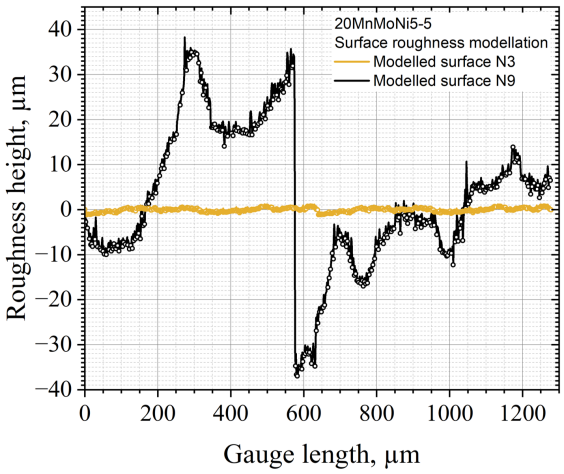

Figure 9.9: Modelled surface topography of the batches N3 and N9 to calculate the fatigue notch factor

Table 9.5: Results of the FNF calculation

Batch	Fatigue notch factor	Fatigue strength exponent
N3	1.150	-0.039
N5	1.250	-0.044
N7	1.500	-0.056
N8	1.720	-0.065
N9	2.980	-0.098

9.3.3 Fatigue Strength Determination

To provide a virtual S-N curve based on the surface roughness as an influencing factor, it is not sufficient to only calculate the slope as described in chapter 9.3.2. To estimate the position of the curve, an anchor-point (in this case the fatigue strength) needs to be determined. Within this research, the fatigue strength is defined as the stress amplitude at which a total of $2 \cdot 10^6$ cycles is reached. The fatigue strength estimation is therefore, according to chapter 9.2.4, based on the correlation of the fatigue strength and the specific hardness of different materials. Figure 9.10 displays the given relation.

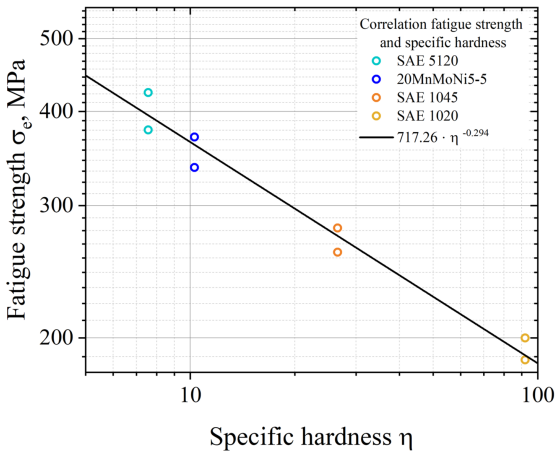

Figure 9.10: Correlation of the fatigue strength and the specific hardness of the materials SAE 5120, 20MnMoNi5-5, SAE 1045 and SAE 1020.

To receive the relation from figure 9.10, a database consisting of four different steels (SAE 5120, 20MnMoNi5-5, SAE 1045 and SAE 1020) is applied. For each material, the fatigue strength, obtained from the load increase test data, as well as the stress amplitude of the generated S-N curve at a total of $2 \cdot 10^6$ cycles is considered, resulting in equation 9.12.

$$\sigma_e = 717.26 \cdot \eta^{-0.294} \tag{9.12}$$

Assuming a homogeneous hardness distribution and using equation 9.10, the values of the specific hardness for all surface conditions can be obtained using the fatigue strength exponents of table 9.4. Furthermore, the corresponding fatigue strength for each surface roughness can be estimated based on the previously proposed relation. All required parameters are given in table 9.6.

Table 9.6: Results of the fatigue strength calculation

Batch	b [-]	n [-]	η [HV]	σ_e [MPa]	σ'_f [MPa]
N5	-0.044	0.056	11.90	346	651
N7	-0.056	0.077	16.41	315	713
N8	-0.065	0.096	20.31	296	759
N9	-0.098	0.192	40.54	241	1000

According to Basquin, an S-N curve in the HCF regime can be described by an allometric fit.

$$\sigma_a = \sigma'_f \cdot (2N_f)^b \tag{9.13}$$

All required variables of equation 9.13 are known from previously presented approaches, which enables a calculation of the missing parameter σ'_f.

9.3.4 Integration of the modelled surface roughness into the lifetime prediction method MiDAcLife

Using the results obtained in chapter 9.3.2 and 9.3.3, it is possible to generate virtual S-N curve for each surface condition based on only one LIT of the N3 batch. Since the fatigue strength calculation according to figure 9.10 is a function of specific hardness, which originates from the value of the Vickers hardness, the results show a certain amount of scattering depending on the Vickers hardness. A deviation of about 10 % is assumed at this point. To consider these deviations, not only the mean value for the Vickers hardness (211 HV) is included in the evaluation, but also the deviations of ±10 %, resulting in scatter bands of the S-N curves. Figure 9.11a shows the result for the virtual S-N curve generation of the N5 batch based on the fatigue and roughness data of the N3 specimen. The black curve of figure 9.11a represents the virtual S-N curve based on the average value of the Vickers hardness. To cover the scattering within the hardness of the material, the blue curve represents the S-N curve calculated with -10 % of the average hardness, whereas the red line originates from +10 % of the average hardness. To assess the quality of the given virtual S-N curve, a comparison with the experimental CAT data points of figure 9.6, displayed as black circle, is drawn. Since FKM is an important guideline that is frequently used in practical applications, the evaluation is extended to include the roughness factor from [54].

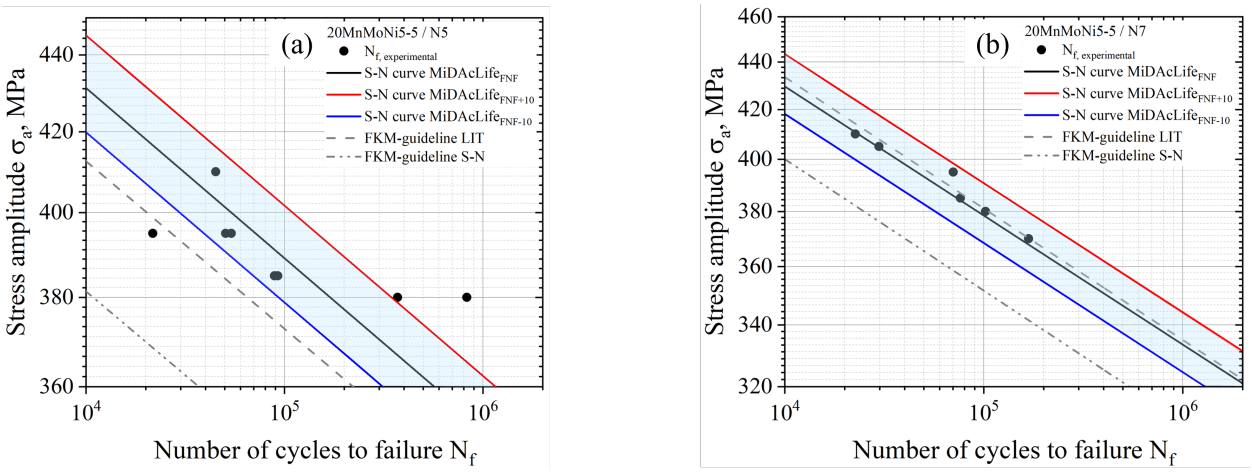

Figure 9.11: (a) Virtual generated S-N curve of the N5 batch, calculated from the fatigue data of the N3 specimen and the surface roughness evaluation, including data points from experimental CATs for validation; (b) Virtual generated S-N curve of the N7 batch, calculated from the fatigue data of the N3 specimen and the surface roughness evaluation, including data points from experimental CATs for validation

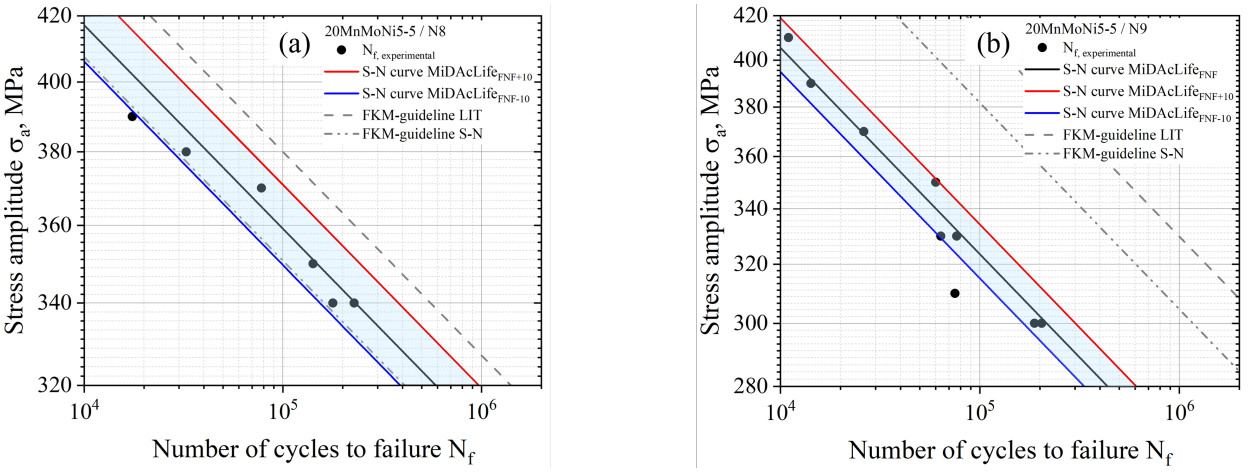

Figure 9.12: (a) Virtual generated S-N curve of the N8 batch, calculated from the fatigue data of the N3 specimen and the surface roughness evaluation, including data points from experimental CATs for validation; (b) Virtual generated S-N curve of the N9 batch, calculated from the fatigue data of the N3 specimen and the surface roughness evaluation, including data points from experimental CATs for validation

This evaluation method is given as a grey S-N curve, based on the data of the LIT as well as the S-N curve of the surface N3. To prove the proposed method, virtual S-N curves of the remaining batches are estimated in an analogue way. The results are given in figures 9.11b, 9.12a and 9.12b.

A general conclusion after these results is that the agreement between the virtual S-N curves and

the conventional determined number of cycles to failure for each batch is proven to be at a very good level. Furthermore, it is possible to consider deviations in the fatigue life, using different values for the materials hardness. For the batches N7-N9, all data points can be well described by the blue area enclosing the three calculated S-N curves. The only exception at this point is the N5 batch, which, however, generally shows a significantly larger scatter even in the experimental test results. As already discussed in chapter 9.3.1, this can be attributed to the increased compressive residual stresses compared to the other batches resulting from the machining process. A comparison of the current evaluation with the results of the FKM guideline leads to the conclusion that the FKM shows greater deviations, particularly in cases N5 and N9, whereas the data from N7 and N8 can also be described well by the FKM. This can be attributed to the high residual compressive stresses in the specimens of the N5 batch, which are not integrated in the approach according to [54]. In the case of the extremely high roughness values, the pronounced scattering of the roughness values leads to the deviations

In previously shown figures, the quality of the proposed method could only be quantified optically. In order to compare the test results, it is necessary to establish a correlation between the experimental data points, the virtual data points according to MiDAcLife and the virtual data points based on only one fatigue test for all five surface conditions. This relation is illustrated in figure 9.13.

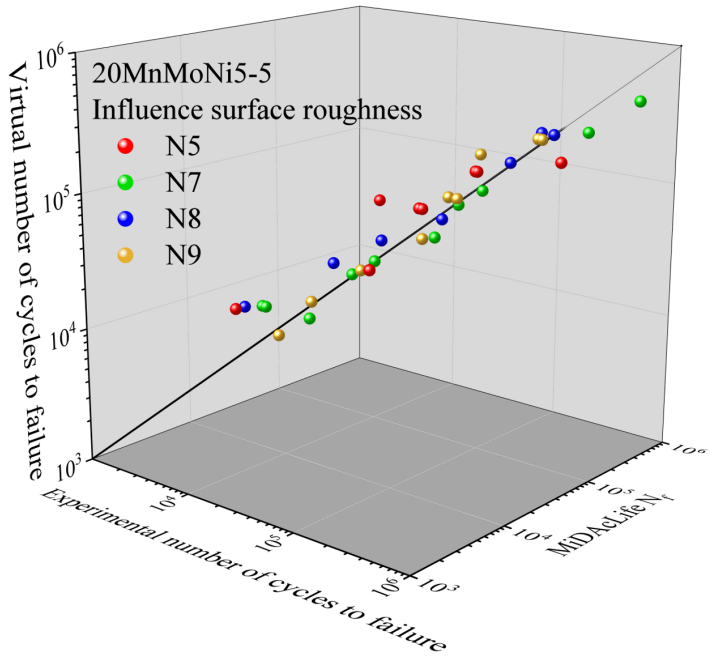

Figure 9.13: Correlation between the experimentally obtained CAT data points, the virtual calculated data points according to MiDAcLife and the virtual CAT data points resulting from the roughness measurements

All data points accumulate around the spatial diagonal, which corresponds to a very good compliance. This illustration confirms the good agreement of the previously discussed methods with the

experimental numbers of cycles to failure. It is noticeable that there is a higher deviation at lower number of cycles because of the transition to the LCF-regime, where different damage mechanism compared to the HCF regime are dominant. The same deployment applies for higher number of cycles to failure in the transition to the VHCF regime. In this case, defects in the volume of the specimens become more important than defects on the surface of a specimen.

9.4 Conclusion

To evaluate the influence of the surface roughness on the fatigue behaviour of a 20MnMoNi5-5 steel used in spray-lines of German nuclear power plants, the lifetime prediction method MiDAcLife is applied to five different surface conditions. Furthermore, the presented research focuses on converting S-N curves by integrating the surface roughness as a fatigue notch factor. Therefore, the measured surface topography needs to be modelled using a Fourier transformation. The most important aspects of the presented research are summarised as follows.

- The lifetime prediction method MiDAcLife enables an estimation of S-N curves based on only one fatigue test (load increase test).
- Considering the surface roughness, a lifetime-reduction effect only occurs from a defined threshold value. If the roughness is lower than the threshold value, no significant influence can be determined.
- Using a Fourier transformation to describe the surface topography mathematically, a fatigue notch factor can be obtained. This factor can be used in different relations to calculate fatigue parameters like the fatigue strength exponent or the fatigue strength coefficient.
- By introducing the specific hardness, which represents the product of the hardness and the cyclic hardening exponent of a material, the fatigue strength of a material can be estimated.
- The proposed method enables a generation of five different virtual S-N curves, using only one load increase test with a smooth specimen.

Based on the results of this research, there are numerous interesting research aspects for future investigations. In the following, some examples are given to extend the present work.

- The data base for the correlation between the fatigue strength and the specific hardness needs to be extended.
- Since the MiDAcLife method considers only one fatigue test in the fatigue life estimation, there is a lack of statistical validation. Therefore, some statistic aspects must be taken into account.
- Because of microstructural mechanisms leading to the formation of extrusions and/or intrusions during fatigue, the surface roughness is not a static value, which is why the change in surface properties (roughness and residual stress) should also be considered in future work.
- To validate the proposed methods, the influence of the surface roughness has to be investigated on further materials and different groups of materials, for example casting or additive manufactured materials.

- Since the 20MnMoNi5-5 steel is used for nuclear power applications, it is also exposed to different temperatures due to the operating conditions. Because of this, the temperature influence needs to be taken into account in further research.

Acknowledgements

The authors would like to thank the Federal Ministry for the Environment, Nature Conservation, Nuclear Safety and Consumer Protection (Bundesministerium für Umwelt, Naturschutz, Nukleare Sicherheit und Verbraucherschutz, BMUV) for supporting this research. Furthermore, the authors thank the project management agency GRS (Gesellschaft für Anlagen-, und Reaktorsicherheit) and the University of Applied Sciences Kaiserslautern for the financial support in the procurement of laboratory infrastructure. The authors would also like to thank the companies Shimadzu Europe GmbH and EVIDENT for the support in technical equipment provision. Besides that, a data base of recent research projects were used within this publication. Therefore, the authors thank the German Research Foundation (Deutsche Forschungsgemeinschaft, DFG) for the financial support in different projects with the grant numbers STA 1133/6-1, STA 1133/10 and STA 1133/20-1.

Bibliography

[1] D. Radaj and M. Vormwald. *Ermüdungsfestigkeit*. Springer Berlin Heidelberg, 3 edition, 2007. doi:10.1007/978-3-540-71459-0.

[2] E. Haibach. *Betriebsfestigkeit*. Springer-Verlag, 3 edition, 2006. doi:10.1007/3-540-29364-7.

[3] S. Suresh. *Fatigue of Materials*. Cambridge University Press, October 1998. doi:10.1017/cbo9780511806575.

[4] L. Toth and S.Ya. Yarema. Formation of the science of fatigue of metals. *Material Science*, 42(1):1825–1870, September 2006. doi:10.1007/s11003-006-0132-3.

[5] H.J. Grover, S.A. Gordon, and Jackson L.R. *Fatigue of metals and structures*. Department of the Navy, 1960.

[6] J. Schijve. Fatigue of structures and materials in the 20th century and the state of the art. *International Journal of Fatigue*, 25:679–702, September 2003. doi:10.1016/S0142-1123(03)00051-3.

[7] W. J. M. Rankine. On the causes of the unexpected breakage of the journals of railway axles; and on the mean of preventing such accidents by observing the law of continuity in their construction. *Journal of the Franklin Institute*, 36(3):178–180, September 1843. doi:10.1016/s0016-0032(43)91062-2.

[8] W. A. J. Albert. *Die Bergwerks-Verwaltung des Hannoverschen Ober-Harzes in den Jahren 1831–1836*, chapter Über Treibseile am Harz. De Gruyter, 1837.

[9] W. Schütz. A history of fatigue. *Engineering Fracture Mechanics*, 54(2):263–300, May 1996. doi:10.1016/0013-7944(95)00178-6.

[10] J. A. Ewing. The crystalline structure of metals. *Phil. Trans., A*, 193, 1899.

[11] O. H. Basquin. The exponentional law of endurance tests. *Proc. ASTM.*, 10(2):625–630, 1910.

[12] A. Palmgren. Die lebensdauer von kugellagern (in german). *Verein Deutscher Ingenieure (in german)*, 68(14):339–341, 1924.

[13] M.A. Miner. Cumulative damage in fatigue. *Journal of Applied Mechanics*, 3:159–164, 1945.

[14] T. Sakai. Historical review and future prospect for researches on very high cycle fatigue of metallic materials. *Fatigue & Fracture of Engineering Materials & Structures*, 46(4):1217–1255, January 2023. doi:10.1111/ffe.13885.

[15] Din50100:2022-12 load controlled fatigue testing - execution and evaluation of cyclic tests at constant load amplitudes on metallic specimens and components, 2022.

[16] O.H. Basquin. The exponential law of endurance tests. In *American Society for Testing and Materials Proceedings*, volume 10, pages 625–630, 1910. URL: https://api.semanticscholar.org/CorpusID:222450133.

[17] S. S. Manson. Interfaces between fatigue, creep, and fracture. *International Journal of Fracture Mechanics*, 2(1):327–327, March 1966. doi:10.1007/bf00188825.

[18] S.S. Manson. Behavior of materials under conditions of thermal stress. In *Heat Transfer Symposium*, pages 9–75, 1953. URL: https://api.semanticscholar.org/CorpusID:4318976.

[19] L.F. Coffin. A study of the effects of cyclic thermal stresses on a ductile metal. *Journal of Fluids Engineering*, 76(6):931–949, August 1954. doi:10.1115/1.4015020.

[20] H.-J. Christ. *Wechselverformung von Metallen*. Springer Berlin Heidelberg, 1991. doi:10.1007/978-3-642-52345-8.

[21] P. Peralta and C. Laird. *Physical Metallurgy*, chapter 18. Elsevier, Amsterdam, 5 edition, 2014.

[22] S. Götz and K.-G. Eulitz. *Betriebsfestigkeit: Bauteile sicher auslegen!* Springer Fachmedien Wiesbaden, 2022. doi:10.1007/978-3-658-38511-8.

[23] H.-J. Christ, editor. *Ermüdungsverhalten metallischer Werkstoffe*, Weinheim, 2009. Wiley-VCH. Literaturangaben.

[24] C. Laird. *Plastic Deformation of Materials*, chapter Cyclic Deformation of Metals and Alloys. Elsevier, 1975.

[25] S. Zhao, R. Zhang, Y. Chong, X. Li, A. Abu-Odeh, E. Rothchild, D.C. Chrzan, M. Asta, J.W. Morris, and A.M. Minor. Defect reconfiguration in a ti–al alloy via electroplasticity. *Nature Materials*, 20(4):468–472, October 2020. doi:10.1038/s41563-020-00817-z.

[26] J. Polák and J. Man. Quantitative model of the surface relief formation in cyclic straining. *Acta Physica Polonica A*, 128(4):675–681, October 2015. doi:10.12693/aphyspola.128.675.

[27] Y. El-Madhoun, A. Mohamed, and M.N. Bassim. Cyclic stress–strain response and dislocation structures in polycrystalline aluminum. *Materials Science and Engineering: A*, 359(1–2):220–227, October 2003. doi:10.1016/s0921-5093(03)00347-2.

[28] N. Thompson and N.J. Wadsworth. Metal fatigue. *Advances in Physics*, 7(25):72–169, January 1958. doi:10.1080/00018735800101177.

[29] U. Krupp. *Fatigue Crack Propagation in Metals and Alloys: Microstructural Aspects and Modelling Concepts*. Wiley, February 2007. doi:10.1002/9783527610686.

[30] H. Mughrabi. Specific features and mechanisms of fatigue in the ultrahigh-cycle regime. *International Journal of Fatigue*, 28(11):1501–1508, November 2006. doi:10.1016/j.ijfatigue.2005.05.018.

[31] H. Mughrabi. Cyclic slip irreversibilities and the evolution of fatigue damage. *Metallurgical and Materials Transactions A*, 40(6):1257–1279, April 2009. doi:10.1007/s11661-009-9839-8.

[32] M.H. Loretto, editor. *Dislocations and properties of real materials*, number 323 in Book, London, 1985. The Institute of Metals. Literaturangaben.

[33] H. Mughrabi. Damage mechanisms and fatigue lives: From the low to the very high cycle regime. *Procedia Engineering*, 55:636–644, 2013. doi:10.1016/j.proeng.2013.03.307.

[34] J. Man, K. Obrtlík, and J. Polák. Extrusions and intrusions in fatigued metals. part 1. state of the art and history†. *Philosophical Magazine*, 89(16):1295–1336, June 2009. doi:10.1080/14786430902917616.

[35] S.-T. Tu and X.-C. Zhang. *Reference Module in Materials Science and Materials Engineering*, chapter Fatigue Crack Initiation Mechanisms. Elsevier, 2016.

[36] U. Holzwarth and U. Eßmann. The evolution of persistent slip bands in copper single crystals. *Applied Physics A Solids and Surfaces*, 57(2):131–141, August 1993. doi:10.1007/bf00331434.

[37] M.D. Sangid, H.-J. Maier, and H. Sehitoglu. The role of grain boundaries on fatigue crack initiation – an energy approach. *International Journal of Plasticity*, 27(5):801–821, May 2011. doi:10.1016/j.ijplas.2010.09.009.

[38] S. Kobayashi, T. Inomata, H. Kobayashi, S. Tsurekawa, and T. Watanabe. Effects of grain boundary- and triple junction-character on intergranular fatigue crack nucleation in polycrystalline aluminum. *Journal of Materials Science*, 43(11):3792–3799, June 2008. doi:10.1007/s10853-007-2236-z.

[39] Z.F. Zhang and Z.G. Wang. Comparison of fatigue cracking possibility along large- and low-angle grain boundaries. *Materials Science and Engineering: A*, 284(1–2):285–291, May 2000. doi:10.1016/s0921-5093(00)00796-6.

[40] Y. Guo, T.B. Britton, and A.J. Wilkinson. Slip band–grain boundary interactions in commercial-purity titanium. *Acta Materialia*, 76:1–12, September 2014. doi:10.1016/j.actamat.2014.05.015.

[41] K. Tanaka and T. Mura. A theory of fatigue crack initiation at inclusions. *Metallurgical Transactions A*, 13(1):117–123, January 1982. doi:10.1007/bf02642422.

[42] Y.Q. Chen, S.P. Pan, M.Z. Zhou, D.Q. Yi, D.Z. Xu, and Y.F. Xu. Effects of inclusions, grain boundaries and grain orientations on the fatigue crack initiation and propagation behavior of 2524-t3 al alloy. *Materials Science and Engineering: A*, 580:150–158, September 2013. doi:10.1016/j.msea.2013.05.053.

[43] C. Gu, Y.-P. Bao, P. Gan, M. Wang, and J.-S. He. Effect of main inclusions on crack initiation in bearing steel in the very high cycle fatigue regime. *International Journal of Minerals, Metallurgy, and Materials*, 25(6):623–629, May 2018. doi:10.1007/s12613-018-1609-4.

[44] K.S. Chan. Roles of microstructure in fatigue crack initiation. *International Journal of Fatigue*, 32(9):1428–1447, September 2010. doi:10.1016/j.ijfatigue.2009.10.005.

[45] Z. Xu, W. Wen, and T. Zhai. Effects of pore position in depth on stress/strain concentration and fatigue crack initiation. *Metallurgical and Materials Transactions A*, 43(8):2763–2770, November 2011. doi:10.1007/s11661-011-0947-x.

[46] J. Holmes and R.A. Queeney. Fatigue crack initiation in a porous steel. *Powder Metallurgy*, 28(4):231–235, January 1985. doi:10.1179/pom.1985.28.4.231.

[47] H. Neuber. Theory of stress concentration for shear-strained prismatical bodies with arbitrary nonlinear stress-strain law. *Journal of Applied Mechanics*, 28(4):544–550, December 1961. doi:10.1115/1.3641780.

[48] H. Neuber. *Kerbspannungslehre: Grundlagen für genaue Festigkeitsberechnung mit Berücksichtigung von Konstruktionsform und Werkstoff*. Springer Berlin Heidelberg, 1958. doi:10.1007/978-3-642-53069-2.

[49] D. Arola and M. Ramulu. An examination of the effects from surface texture on the strength of fiber reinforced plastics. *Journal of Composite Materials*, 33(2):102–123, January 1999. doi:10.1177/002199839903300201.

[50] D. Arola and C. Williams. Estimating the fatigue stress concentration factor of machined surfaces. *International Journal of Fatigue*, 24(9):923–930, September 2002. doi:10.1016/s0142-1123(02)00012-9.

[51] F. Quan, Z. Chen, H. Ye, C. Cui, and Y. Cui. Study of the effect of surface roughness on fatigue strength of gh4169 based on indirect evaluation of the notch root radius. *International Journal of Fatigue*, 152:106440, November 2021. doi:10.1016/j.ijfatigue.2021.106440.

[52] F. Weber, R. Acosta, T. Eyrisch, T. Hielscher, M. Magin, and P. Starke. Influence of processing parameters on the fatigue life time of specimens made from quenched and tempered steel sae 4140h. *Materials Testing*, 61(9):842–850, August 2019. doi:10.3139/120.111391.

[53] A. Javidi, U. Rieger, and W. Eichlseder. The effect of machining on the surface integrity and fatigue life. *International Journal of Fatigue*, 30(10–11):2050–2055, October 2008. doi:10.1016/j.ijfatigue.2008.01.005.

[54] R. Rennert, E. Kullig, M. Vormwald, A. Esderts, and M. Luke, editors. *Analytical strength assessment of components*. FKM Forschung im VDMA. VDMA Verlag GmbH, Frankfurt am Main, 7th revised edition 2020 edition, 2021.

[55] R. Rennert, M. Vormwald, and A. Esderts. Fkm-guideline "analytical strength assessment" – background and current developments. *International Journal of Fatigue*, 182:108165, May 2024. doi:10.1016/j.ijfatigue.2024.108165.

[56] Y. Murakami. *Metal Fatigue*. Elsevier, 2002. doi:10.1016/b978-0-08-044064-4.x5000-2.

[57] Y. Murakami, K. Tsutsumi, and M. Fujishima. Quantitative evaluation of effect of surface roughnesson fatigue strength. *Transactions of the Japan Society of Mechanical Engineers Series A*, 62(597):1124–1131, 1996. doi:10.1299/kikaia.62.1124.

[58] Y. Murakami and M. Endo. Effects of defects, inclusions and inhomogeneities on fatigue strength. *International Journal of Fatigue*, 16(3):163–182, April 1994. doi:10.1016/0142-1123(94)90001-9.

[59] H. Itoga. Effect of surface roughness on step-wise s–n characteristics in high strength steel. *International Journal of Fatigue*, 25(5):379–385, May 2003. doi:10.1016/s0142-1123(02)00166-4.

[60] J. Lai, H. Huang, and W. Buising. Effects of microstructure and surface roughness on the fatigue strength of high-strength steels. *Procedia Structural Integrity*, 2:1213–1220, 2016. doi:10.1016/j.prostr.2016.06.155.

[61] E. Bayraktar, R. Mora, I.-M. Garcia, and C. Bathias. Heat treatment, surface roughness and corrosion effects on the damage mechanism of mechanical components in the very high cycle fatigue regime. *International Journal of Fatigue*, 31(10):1532–1540, October 2009. doi:10.1016/j.ijfatigue.2009.04.017.

[62] S.A. McKelvey and A. Fatemi. Surface finish effect on fatigue behavior of forged steel. *International Journal of Fatigue*, 36(1):130–145, March 2012. doi:10.1016/j.ijfatigue.2011.08.008.

[63] S. Romano, P.D. Nezhadfar, N. Shamsaei, M. Seifi, and S. Beretta. High cycle fatigue behavior and life prediction for additively manufactured 17-4 ph stainless steel: Effect of sub-surface porosity and surface roughness. *Theoretical and Applied Fracture Mechanics*, 106:102477, April 2020. doi:10.1016/j.tafmec.2020.102477.

[64] S. Lee, J.W. Pegues, and N. Shamsaei. Fatigue behavior and modeling for additive manufactured 304l stainless steel: The effect of surface roughness. *International Journal of Fatigue*, 141:105856, December 2020. doi:10.1016/j.ijfatigue.2020.105856.

[65] S. Lee, B. Rasoolian, D.F. Silva, J.W. Pegues, and N. Shamsaei. Surface roughness parameter and modeling for fatigue behavior of additive manufactured parts: A non-destructive data-driven approach. *Additive Manufacturing*, 46:102094, October 2021. doi:10.1016/j.addma.2021.102094.

[66] C. Ye, C. Zhang, J. Zhao, and Y. Dong. Effects of post-processing on the surface finish, porosity, residual stresses, and fatigue performance of additive manufactured metals: A review. *Journal of Materials Engineering and Performance*, 30(9):6407–6425, July 2021. doi:10.1007/s11665-021-06021-7.

[67] T.D. Dinh, J. Vanwalleghem, H. Xiang, H. Erdelyi, T. Craeghs, and W. Van Paepegem. A unified approach to model the effect of porosity and high surface roughness on the fatigue properties of additively manufactured ti6-al4-v alloys. *Additive Manufacturing*, 33:101139, May 2020. doi:10.1016/j.addma.2020.101139.

[68] L. Denti and A. Sola. On the effectiveness of different surface finishing techniques on a357.0 parts produced by laser-based powder bed fusion: Surface roughness and fatigue strength. *Metals*, 9(12):1284, November 2019. doi:10.3390/met9121284.

[69] J. Pegues, M. Roach, R. Scott Williamson, and N. Shamsaei. Surface roughness effects on the fatigue strength of additively manufactured ti-6al-4v. *International Journal of Fatigue*, 116:543–552, November 2018. doi:10.1016/j.ijfatigue.2018.07.013.

[70] K. Solberg, S. Guan, N. Razavi, T. Welo, K.C. Chan, and F. Berto. Fatigue of additively manufactured 316l stainless steel: The influence of porosity and surface roughness. *Fatigue & Fracture of Engineering Materials & Structures*, 42(9):2043–2052, July 2019. doi:10.1111/ffe.13077.

[71] M. Nakatani, H. Masuo, Y. Tanaka, and Y. Murakami. Effect of surface roughness on fatigue strength of ti-6al-4v alloy manufactured by additive manufacturing. *Procedia Structural Integrity*, 19:294–301, 2019. doi:10.1016/j.prostr.2019.12.032.

[72] A. Yadollahi, M.J. Mahtabi, A. Khalili, H.R. Doude, and J.C. Newman. Fatigue life prediction of additively manufactured material: Effects of surface roughness, defect size, and shape.

Fatigue & Fracture of Engineering Materials & Structures, 41(7):1602–1614, March 2018. doi:10.1111/ffe.12799.

[73] J. Zhang and A. Fatemi. Surface roughness effect on multiaxial fatigue behavior of additive manufactured metals and its modeling. *Theoretical and Applied Fracture Mechanics*, 103:102260, October 2019. doi:10.1016/j.tafmec.2019.102260.

[74] D. Greitemeier, Dalle D.C., F. Syassen, J. Eufinger, and T. Melz. Effect of surface roughness on fatigue performance of additive manufactured ti–6al–4v. *Materials Science and Technology*, 32(7):629–634, May 2016. doi:10.1179/1743284715y.0000000053.

[75] N. Sanaei and A. Fatemi. Analysis of the effect of surface roughness on fatigue performance of powder bed fusion additive manufactured metals. *Theoretical and Applied Fracture Mechanics*, 108:102638, August 2020. doi:10.1016/j.tafmec.2020.102638.

[76] C. Li, W. Dai, F. Duan, Y. Zhang, and D. He. Fatigue life estimation of medium-carbon steel with different surface roughness. *Applied Sciences*, 7(4):338, March 2017. doi:10.3390/app7040338.

[77] K. Kethamukkala, C. Meng, J. Chen, and Y. Liu. Crack growth-based life prediction for additively manufactured metallic materials considering surface roughness. *International Journal of Fatigue*, 176:107914, November 2023. doi:10.1016/j.ijfatigue.2023.107914.

[78] J. Gockel, L. Sheridan, B. Koerper, and B. Whip. The influence of additive manufacturing processing parameters on surface roughness and fatigue life. *International Journal of Fatigue*, 124:380–388, July 2019. doi:10.1016/j.ijfatigue.2019.03.025.

[79] K.S. Stopka, M. Yaghoobi, J.E. Allison, and D.L. McDowell. Microstructure-sensitive modeling of surface roughness and notch effects on extreme value fatigue response. *International Journal of Fatigue*, 166:107295, January 2023. doi:10.1016/j.ijfatigue.2022.107295.

[80] Y. Hu, Y. Wang, J. Xi, A. Chen, and K. Nikbin. Numerical simulation of surface roughness effects on low-cycle fatigue properties of additively manufactured titanium alloys. *Engineering Failure Analysis*, 163:108407, September 2024. doi:10.1016/j.engfailanal.2024.108407.

[81] E. Natkowski, P. Sonnweber-Ribic, and S. Münstermann. Surface roughness influence in micromechanical fatigue lifetime prediction with crystal plasticity models for steel. *International Journal of Fatigue*, 159:106792, June 2022. doi:10.1016/j.ijfatigue.2022.106792.

[82] A. McMillan, R. Jones, D. Peng, and G.A. Chechkin. A computational study of the influence of surface roughness on material strength. *Meccanica*, 53(9):2411–2436, February 2018. doi:10.1007/s11012-018-0830-6.

[83] K. Singh, F. Sadeghi, M. Correns, and T. Blass. A microstructure based approach to model effects of surface roughness on tensile fatigue. *International Journal of Fatigue*, 129:105229, December 2019. doi:10.1016/j.ijfatigue.2019.105229.

[84] S.K. As, B. Skallerud, and B.W. Tveiten. Surface roughness characterization for fatigue life predictions using finite element analysis. *International Journal of Fatigue*, 30(12):2200–2209, December 2008. doi:10.1016/j.ijfatigue.2008.05.020.

[85] T.D. Dinh, S. Han, V. Yaghoubi, H. Xiang, H. Erdelyi, T. Craeghs, J. Segers, and W. Van Paepegem. Modeling detrimental effects of high surface roughness on the fa-

tigue behavior of additively manufactured ti-6al-4v alloys. *International Journal of Fatigue*, 144:106034, March 2021. doi:10.1016/j.ijfatigue.2020.106034.

[86] B. Vayssette, N. Saintier, C. Brugger, M. El May, and E. Pessard. Numerical modelling of surface roughness effect on the fatigue behavior of ti-6al-4v obtained by additive manufacturing. *International Journal of Fatigue*, 123:180–195, June 2019. doi:10.1016/j.ijfatigue.2019.02.014.

[87] G. Xu, Z. Qiao, S. Wu, T. Liu, M. Zhao, and G. Wang. Finite-element method for the analysis of surface stress concentration factor and relative stress gradient for machined surfaces. *Mechanical Sciences*, 14(2):451–461, October 2023. doi:10.5194/ms-14-451-2023.

[88] M. Suraratchai, J. Limido, C. Mabru, and R. Chieragatti. Modelling the influence of machined surface roughness on the fatigue life of aluminium alloy. *International Journal of Fatigue*, 30(12):2119–2126, December 2008. doi:10.1016/j.ijfatigue.2008.06.003.

[89] B. Zhao, J. Song, L. Xie, Z. Hu, and J. Chen. Surface roughness effect on fatigue strength of aluminum alloy using revised stress field intensity approach. *Scientific Reports*, 11(1), September 2021. doi:10.1038/s41598-021-98858-0.

[90] X. Zhu, Z. Dong, Y. Zhang, and Z. Cheng. Fatigue life prediction of machined specimens with the consideration of surface roughness. *Materials*, 14(18):5420, September 2021. doi:10.3390/ma14185420.

[91] P.S. Maiya. Geometrical characterization of surface roughness and its application to fatigue crack initiation. *Materials Science and Engineering*, 21:57–62, January 1975. doi:10.1016/0025-5416(75)90198-6.

[92] Y. Aono and H. Noguchi. Fatigue limit reliability of axisymmetric complex surface. *International Journal of Fracture*, 131(1):59–78, January 2005. doi:10.1007/s10704-004-3638-4.

[93] Z. Cheng, R. Liao, W. Lu, and D. Wang. Fatigue notch factors prediction of rough specimen by the theory of critical distance. *International Journal of Fatigue*, 104:195–205, November 2017. doi:10.1016/j.ijfatigue.2017.07.004.

[94] A. Niku-Lari, editor. *Advances in surface treatments*. Pergamon Press, Oxford, first edition edition, 1987. Includes bibliographical references and indexes.

[95] U. Wolfstieg and E. Macherauch. Ursachen und bewertung von eigenspannungen. *Chemie Ingenieur Technik*, 45(11):760–770, June 1973. doi:10.1002/cite.330451103.

[96] E. Macherauch and K.H. Kloos. Bewertung von eigenspannungen bei quasistatischer und schwingender werkstoffbeanspruchung. *Materialwissenschaft und Werkstofftechnik*, 20(1):1–13, January 1989. doi:10.1002/mawe.19890200104.

[97] S.O.A. El-Helieby and G.W. Rowe. Influences of surface roughness and residual stress on fatigue life of ground steel components. *Metals Technology*, 7(1):221–225, January 1980. doi:10.1179/030716980803286450.

[98] G.A. Webster and A.N. Ezeilo. Residual stress distributions and their influence on fatigue lifetimes. *International Journal of Fatigue*, 23:375–383, 2001. doi:10.1016/s0142-1123(01)00133-5.

[99] R. Sunder. *Advanced Materials*, chapter Why and How Residual Stress Affects Metal Fatigue. Springer International Publishing, 2015.

[100] A. Okamoto and H. Nakamura. The influence of residual stress on fatigue cracking. *Journal of Pressure Vessel Technology*, 112(3):199–203, August 1990. doi:10.1115/1.2928614.

[101] Y. Morikage, S. Igi, K. Oi, Y. Jo, K. Murakami, and K. Gotoh. Effect of compressive residual stress on fatigue crack propagation. *Procedia Engineering*, 130:1057–1065, 2015. doi:10.1016/j.proeng.2015.12.263.

[102] L. Zhu and M.-P. Jia. A new approach for the influence of residual stress on fatigue crack propagation. *Results in Physics*, 7:2204–2212, 2017. doi:10.1016/j.rinp.2017.06.039.

[103] T. Krug, K.-H. Lang, T. Fett, and D. Löhe. Influence of residual stresses and mean load on the fatigue strength of case-hardened notched specimens. *Materials Science and Engineering: A*, 468–470:158–163, November 2007. doi:10.1016/j.msea.2006.07.167.

[104] F. Ghanem, C. Braham, M.E. Fitzpatrick, and H. Sidhom. Effect of near-surface residual stress and microstructure modification from machining on the fatigue endurance of a tool steel. *Journal of Materials Engineering and Performance*, 11(6):631–639, December 2002. doi:10.1361/105994902770343629.

[105] C. Kanchanomai and W. Limtrakarn. Effect of residual stress on fatigue failure of carbonitrided low-carbon steel. *Journal of Materials Engineering and Performance*, 17(6):879–887, December 2008. doi:10.1007/s11665-008-9212-x.

[106] A. Chiocca, F. Frendo, and L. Bertini. Residual stresses influence on the fatigue strength of structural components. *Procedia Structural Integrity*, 38:447–456, 2022. doi:10.1016/j.prostr.2022.03.045.

[107] A. Chiocca, F. Frendo, F. Aiello, and L. Bertini. Influence of residual stresses on the fatigue life of welded joints. numerical simulation and experimental tests. *International Journal of Fatigue*, 162:106901, September 2022. doi:10.1016/j.ijfatigue.2022.106901.

[108] H. Sasahara. The effect on fatigue life of residual stress and surface hardness resulting from different cutting conditions of 0.45 *International Journal of Machine Tools and Manufacture*, 45(2):131–136, February 2005. doi:10.1016/j.ijmachtools.2004.08.002.

[109] R.M.N. Fleury and D. Nowell. Evaluating the influence of residual stresses and surface damage on fatigue life of nickel superalloys. *International Journal of Fatigue*, 105:27–33, December 2017. doi:10.1016/j.ijfatigue.2017.08.015.

[110] P. Pokorný, P. Dlhý, J. Poduška, R. Fajkoš, T. Vojtek, L. Náhlík, M. Grasso, and P. Hutař. Influence of heat treatment-induced residual stress on residual fatigue life of railway axles. *Theoretical and Applied Fracture Mechanics*, 109:102732, October 2020. doi:10.1016/j.tafmec.2020.102732.

[111] P.-A. Deschênes, J. Lanteigne, Y. Verreman, D. Paquet, J.-B. Lévesque, and M. Brochu. A new experimental method to study the influence of welding residual stresses on fatigue crack propagation. *International Journal of Fatigue*, 100:444–452, July 2017. doi:10.1016/j.ijfatigue.2017.01.031.

[112] Y. Choi. A study on the effects of machining-induced residual stress on rolling contact fatigue. *International Journal of Fatigue*, 31(10):1517–1523, October 2009. doi:10.1016/j.ijfatigue.2009.05.001.

[113] M.N. James, D.J. Hughes, Z. Chen, H. Lombard, D.G. Hattingh, D. Asquith, J.R. Yates, and P.J. Webster. Residual stresses and fatigue performance. *Engineering Failure Analysis*, 14(2):384–395, March 2007. doi:10.1016/j.engfailanal.2006.02.011.

[114] M.N. James. Residual stress influences on structural reliability. *Engineering Failure Analysis*, 18(8):1909–1920, December 2011. doi:10.1016/j.engfailanal.2011.06.005.

[115] M. Mlikota, S. Schmauder, K. Dogahe, and Ž. Božić. Influence of local residual stresses on fatigue crack initiation. *Procedia Structural Integrity*, 31:3–7, 2021. doi:10.1016/j.prostr.2021.03.002.

[116] F. Valiorgue, V. Zmelty, M. Dumas, V. Chomienne, C. Verdu, F. Lefebvre, and J. Rech. Influence of residual stress profile and surface microstructure on fatigue life of a 15-5ph. *Procedia Engineering*, 213:623–629, 2018. doi:10.1016/j.proeng.2018.02.058.

[117] J. Larue and S. Daniewicz. Predicting the effect of residual stress on fatigue crack growth. *International Journal of Fatigue*, 29(3):508–515, March 2007. doi:10.1016/j.ijfatigue.2006.05.008.

[118] D. Kumar, S. Idapalapati, and W. Wang. Influence of residual stress distribution and microstructural characteristics on fatigue failure mechanism in ni-based superalloy. *Fatigue & Fracture of Engineering Materials & Structures*, 44(6):1583–1601, March 2021. doi:10.1111/ffe.13454.

[119] R.C. McClung. A literature survey on the stability and significance of residual stresses during fatigue. *Fatigue & Fracture of Engineering Materials & Structures*, 30(3):173–205, March 2007. doi:10.1111/j.1460-2695.2007.01102.x.

[120] A. Fatemi and L. Yang. Cumulative fatigue damage and life prediction theories: a survey of the state of the art for homogeneous materials. *International Journal of Fatigue*, 20(1):9–34, January 1998. doi:10.1016/s0142-1123(97)00081-9.

[121] T. Bešter, M. Fajdiga, and M. Nagode. Application of constant amplitude dynamic tests for life prediction of air springs at various control parameters. *Strojniški vestnik – Journal of Mechanical Engineering*, 60(4):241–249, April 2014. doi:10.5545/sv-jme.2013.1348.

[122] Y. Lee. *Fatigue Testing and Analysis*, chapter Fatigue Damage Theories. Elsevier, 2005.

[123] B. Huang, S. Wang, S. Geng, and X. Liu. Improved numerical model for fatigue cumulative damage of mechanical structure considering load sequence and interaction. *Advances in Mechanical Engineering*, 13(2):168781402199530, February 2021. doi:10.1177/1687814021995309.

[124] K. Hectors and W. De Waele. Cumulative damage and life prediction models for high-cycle fatigue of metals: A review. *Metals*, 11(2):204, January 2021. doi:10.3390/met11020204.

[125] S. Schoenborn, H. Kaufmann, C.M. Sonsino, and R. Heim. Cumulative damage of high-strength cast iron alloys for automotive applications. *Procedia Engineering*, 101:440–449, 2015. doi:10.1016/j.proeng.2015.02.053.

[126] J. Bennett. A study of the damaging effect of fatigue stressing on sae x4130 steel. In *Research Paper RP1733*, volume 37, 1946.

[127] J. E. Inoma, D. G. Pavlou, and J. Zec. Implementation of linear, double-linear, and nonlinear fatigue damage accumulation rules for fatigue life prediction of offshore drilling top-drive tie-rods. *IOP Conference Series: Materials Science and Engineering*, 700(1):012025, November 2019. doi:10.1088/1757-899x/700/1/012025.

[128] D. Kujawski and F. Ellyin. On the concept of cumulative fatigue damage. *International Journal of Fracture*, 37(4):263–278, August 1988. doi:10.1007/bf00032533.

[129] S. Subramanyan. A cumulative damage rule based on the knee point of the s-n curve. *Journal of Engineering Materials and Technology*, 98(4):316–321, October 1976. doi:10.1115/1.3443383.

[130] S.P. Zhu, D. Liao, Q. Liu, J. Correia, and A. De Jesus. Nonlinear fatigue damage accumulation: Isodamage curve-based model and life prediction aspects. *International Journal of Fatigue*, 128:105185, November 2019. doi:10.1016/j.ijfatigue.2019.105185.

[131] S.P. Zhu, Y.Z. Hao, J. Correia, G. Lesiuk, and A. De Jesus. Nonlinear fatigue damage accumulation and life prediction of metals: A comparative study. *Fatigue & Fracture of Engineering Materials & Structures*, 42(6):1271–1282, November 2018. doi:10.1111/ffe.12937.

[132] Y Duyi. A new approach to low-cycle fatigue damage based on exhaustion of static toughness and dissipation of cyclic plastic strain energy during fatigue. *International Journal of Fatigue*, 23(8):679–687, September 2001. doi:10.1016/s0142-1123(01)00027-5.

[133] S. S. Manson and G. R. Halford. Practical implementation of the double linear damage rule and damage curve approach for treating cumulative fatigue damage. *International Journal of Fracture*, 17(2):169–192, April 1981. doi:10.1007/bf00053519.

[134] S. Benkabouche, H. Guechichi, A. Amrouche, and M. Benkhettab. A modified nonlinear fatigue damage accumulation model under multiaxial variable amplitude loading. *International Journal of Mechanical Sciences*, 100:180–194, September 2015. doi:10.1016/j.ijmecsci.2015.06.016.

[135] M. Roy, Y. Nadot, D.M. Maijer, and G. Benoit. Multiaxial fatigue behaviour of a356-t6. *Fatigue & Fracture of Engineering Materials & Structures*, 35(12):1148–1159, June 2012. doi:10.1111/j.1460-2695.2012.01702.x.

[136] G. Mesmacque, S. Garcia, A. Amrouche, and C. Rubio-gonzalez. Sequential law in multiaxial fatigue, a new damage indicator. *International Journal of Fatigue*, 27(4):461–467, April 2005. doi:10.1016/j.ijfatigue.2004.08.005.

[137] A. Yu, H.Z. Huang, Y.F. Li, W. Yang, and Z. Deng. A modified nonlinear fatigue damage accumulation model for life prediction of rolling bearing under variable loading conditions. *Fatigue & Fracture of Engineering Materials & Structures*, 45(3):852–864, January 2022. doi:10.1111/ffe.13641.

[138] A. Aeran, S.C. Siriwardane, O. Mikkelsen, and I. Langen. A new nonlinear fatigue damage model based only on s-n curve parameters. *International Journal of Fatigue*, 103:327–341, October 2017. doi:10.1016/j.ijfatigue.2017.06.017.

[139] T. Huang, R.C. Ding, Y.F. Li, J. Zhou, and H.Z. Huang. A modified model for nonlinear fatigue damage accumulation of turbine disc considering the load interaction effect. *Metals*, 9(9):919, August 2019. doi:10.3390/met9090919.

[140] H. Gao, H.Z. Huang, S.P. Zhu, Y.F. Li, and R. Yuan. A modified nonlinear damage accumulation model for fatigue life prediction considering load interaction effects. *The Scientific World Journal*, 2014:1–7, 2014. doi:10.1155/2014/164378.

[141] H.Y. Gao, F.J. Zuo, Z.Q. L, S.P. Zhu, and H.Z. Huang. Residual life prediction based on nonlinear fatigue damage accumulation model. *Journal of Shanghai Jiaotong University (Science)*, 20(4):449–453, July 2015. doi:10.1007/s12204-015-1647-2.

[142] Z. Fu, X. Hu, and J. Zhang. A new fatigue life prediction method based on nonlinear fatigue cumulative damage generalized expression. *Journal of Mechanical Science and Technology*, 36(1):205–212, January 2022. doi:10.1007/s12206-021-1219-3.

[143] Z. Li, D. Shi, S. Li, and X. Yang. Residual fatigue life prediction based on a novel damage accumulation model considering loading history. *Fatigue & Fracture of Engineering Materials & Structures*, 43(5):1005–1021, February 2020. doi:10.1111/ffe.13205.

[144] D Shang. A nonlinear damage cumulative model for uniaxial fatigue. *International Journal of Fatigue*, 21(2):187–194, February 1999. doi:10.1016/s0142-1123(98)00069-3.

[145] D. Zhu, W. Zhang, and Z. Ding. A modified fatigue damage model considering loading sequence effect. *International Journal of Damage Mechanics*, 31(7):1027–1056, March 2022. doi:10.1177/10567895221088029.

[146] S. Kwofie and N. Rahbar. A fatigue driving stress approach to damage and life prediction under variable amplitude loading. *International Journal of Damage Mechanics*, 22(3):393–404, July 2012. doi:10.1177/1056789512449638.

[147] F.J. Zuo, H.Z. Huang, S.P. Zhu, Z. Lv, and H. Gao. Fatigue life prediction under variable amplitude loading using a non-linear damage accumulation model. *International Journal of Damage Mechanics*, 24(5):767–784, September 2014. doi:10.1177/1056789514553042.

[148] A. Aeran, S.C. Siriwardane, O. Mikkelsen, and I. Langen. An accurate fatigue damage model for welded joints subjected to variable amplitude loading. *IOP Conference Series: Materials Science and Engineering*, 276:012038, December 2017. doi:10.1088/1757-899x/276/1/012038.

[149] Q. Liu, Y. Gao, Y. Li, and Q. Xue. Fatigue life prediction based on a novel improved version of the corten-dolan model considering load interaction effect. *Engineering Structures*, 221:111036, October 2020. doi:10.1016/j.engstruct.2020.111036.

[150] S. Giancane, R. Nobile, F.W. Panella, and V. Dattoma. Fatigue life prediction of notched components based on a new nonlinear continuum damage mechanics model. *Procedia Engineering*, 2(1):1317–1325, April 2010. doi:10.1016/j.proeng.2010.03.143.

[151] F. Bjørheim, D.G. Pavlou, and S.C. Siriwardane. Nonlinear fatigue life prediction model based on the theory of the s-n fatigue damage envelope. *Fatigue & Fracture of Engineering Materials & Structures*, 45(5):1480–1493, March 2022. doi:10.1111/ffe.13680.

[152] D.G. Pavlou. The theory of the s-n fatigue damage envelope: Generalization of linear, double-linear, and non-linear fatigue damage models. *International Journal of Fatigue*, 110:204–214, May 2018. doi:10.1016/j.ijfatigue.2018.01.023.

[153] K. Rege and D.G. Pavlou. A one-parameter nonlinear fatigue damage accumulation model. *International Journal of Fatigue*, 98:234–246, May 2017. doi:10.1016/j.ijfatigue.2017.01.039.

[154] F.L. Xia, S.P. Zhu, D. Liao, R. Dantas, J.. Correia, and A. De Jesus. Isodamage curve-based fatigue damage accumulation model considering the exhaustion of static toughness. *Engineering Failure Analysis*, 115:104575, September 2020. doi:10.1016/j.engfailanal.2020.104575.

[155] R.I. Stephens and H.O. Fuchs, editors. *Metal fatigue in engineering*. A Wiley-Interscience publication. Wiley, New York, 2. ed. edition, 2001. Includes bibliographical references and index.

[156] T. Erber, S.A. Guralnick, and S.C. Michels. Hysteresis and fatigue. *Annals of Physics*, 224(2):157–192, June 1993. doi:10.1006/aphy.1993.1043.

[157] W. Ramberg and W. Osgood. Description of stress-strain curves by three parameters. *National Advisery Committe for Aeronautics*, 1943.

[158] N. Mostaghel and R.A. Byrd. Inversion of ramberg–osgood equation and description of hysteresis loops. *International Journal of Non-Linear Mechanics*, 37(8):1319–1335, December 2002. doi:10.1016/s0020-7462(02)00025-2.

[159] B.P. Anatolyevich and G.N. Yakovlevna. Generalization of the ramberg–osgood model for elastoplastic materials. *Journal of Materials Engineering and Performance*, 28(12):7342–7346, December 2019. doi:10.1007/s11665-019-04422-3.

[160] R. Branco, R.F. Martins, J.A.F.O. Correia, Z. Marciniak, W. Macek, and J. Jesus. On the use of the cumulative strain energy density for fatigue life assessment in advanced high-strength steels. *International Journal of Fatigue*, 164:107121, November 2022. doi:10.1016/j.ijfatigue.2022.107121.

[161] Y.D. Hu, Z.Z. Hu, and S.Z. Cao. Theoretical study on manson-coffin equation for physically short cracks and lifetime prediction. *Science China Technological Sciences*, 55(1):34–42, September 2011. doi:10.1007/s11431-011-4581-z.

[162] Y.-J. Park and A.H.-S. Ang. Mechanistic seismic damage model for reinforced concrete. *Journal of Structural Engineering*, 111(4):722–739, April 1985. doi:10.1061/(asce)0733-9445(1985)111:4(722).

[163] H. Jiang, B. Fu, X. Lu, and L. Chen. Seismic damage assessment of rc members by a modified park-ang model. *Advances in Structural Engineering*, 18(3):353–364, March 2015. doi:10.1260/1369-4332.18.3.353.

[164] J. Guo, J.J. Wang, Y. Li, W.G. Zhao, and Y.L. Du. Three dimensional extension for park and ang damage model. *Structures*, 7:184–194, August 2016. doi:10.1016/j.istruc.2016.06.008.

[165] O. Scott-Emuakpor, T. George, C. Cross, and M.-H.H. Shen. Hysteresis-loop representation for strain energy calculation and fatigue assessment. *The Journal of Strain Analysis for Engineering Design*, 45(4):275–282, April 2010. doi:10.1243/03093247jsa602.

[166] D. Eifler and A. Piotrowski. Bewertung zyklischer verformungsvorgänge metallischer werkstoffe mit hilfe mechanischer, thermometrischer und elektrischer meßverfahren characterization of cyclic deformation behaviour by mechanical, thermometrical and electrical methods. *Materialwissenschaft und Werkstofftechnik*, 26(3):121–127, March 1995. doi:10.1002/mawe.19950260305.

[167] C. Lachowicz. Calculation of the elastic–plastic strain energy density under cyclic and random loading. *International Journal of Fatigue*, 23(7):643–652, August 2001. doi:10.1016/s0142-1123(00)00102-x.

[168] A. Chrysochoos, V. Huon, F. Jourdan, J.-M. Muracciole, R. Peyroux, and B. Wattrisse. Use of full-field digital image correlation and infrared thermography measurements for the thermomechanical analysis of material behaviour. *Strain*, 46(1):117–130, February 2010. doi:10.1111/j.1475-1305.2009.00635.x.

[169] T. Boulanger. Calorimetric analysis of dissipative and thermoelastic effects associated with the fatigue behavior of steels. *International Journal of Fatigue*, 26(3):221–229, March 2004. doi:10.1016/s0142-1123(03)00171-3.

[170] G. La Rosa. Thermographic methodology for rapid determination of the fatigue limit of materials and mechanical components. *International Journal of Fatigue*, 22(1):65–73, January 2000. doi:10.1016/s0142-1123(99)00088-2.

[171] M.P. Luong. Nondestructive evaluation of fatigue limit of metals using infrared thermography. *MRS Proceedings*, 503, 1997. doi:10.1557/proc-503-275.

[172] M.P. Luong. Fatigue limit evaluation of metals using an infrared thermographic technique. *Mechanics of Materials*, 28(1–4):155–163, July 1998. doi:10.1016/s0167-6636(97)00047-1.

[173] R. De Finis, D. Palumbo, F. Ancona, and U. Galietti. Fatigue limit evaluation of various martensitic stainless steels with new robust thermographic data analysis. *International Journal of Fatigue*, 74:88–96, May 2015. doi:10.1016/j.ijfatigue.2014.12.010.

[174] M. Liakat and M.M. Khonsari. Entropic characterization of metal fatigue with stress concentration. *International Journal of Fatigue*, 70:223–234, January 2015. doi:10.1016/j.ijfatigue.2014.09.014.

[175] M. Liakat and M.M. Khonsari. Rapid estimation of fatigue entropy and toughness in metals. *Materials & Design (1980-2015)*, 62:149–157, October 2014. doi:10.1016/j.matdes.2014.04.086.

[176] Z. Teng, H. Wu, C. Boller, and P. Starke. Thermodynamic entropy as a marker of high-cycle fatigue damage accumulation: Example for normalized sae 1045 steel. *Fatigue & Fracture of Engineering Materials & Structures*, 43(12):2854–2866, July 2020. doi:10.1111/ffe.13303.

[177] R.V. Prakash. Evaluation of fatigue damage in materials using indentation testing and infrared thermography. *Transactions of the Indian Institute of Metals*, 63(2–3):173–179, April 2010. doi:10.1007/s12666-010-0024-y.

[178] G. Meneghetti. Analysis of the fatigue strength of a stainless steel based on the energy dissipation. *International Journal of Fatigue*, 29(1):81–94, January 2007. doi:10.1016/j.ijfatigue.2006.02.043.

[179] M. Zaeimi, R. De Finis, D. Palumbo, and U. Galietti. Fatigue limit estimation of metals based on the thermographic methods: A comprehensive review. *Fatigue & Fracture of Engineering Materials & Structures*, 47(3):611–646, January 2024. doi:10.1111/ffe.14206.

[180] M. Ricotta, G. Meneghetti, B. Atzori, G. Risitano, and A. Risitano. Comparison of experimental thermal methods for the fatigue limit evaluation of a stainless steel. *Metals*, 9(6):677, June 2019. doi:10.3390/met9060677.

[181] D. Krewerth, T. Lippmann, A. Weidner, and H. Biermann. Application of full-surface view in situ thermography measurements during ultrasonic fatigue of cast steel g42crmo4. *International Journal of Fatigue*, 80:459–467, November 2015. doi:10.1016/j.ijfatigue.2015.07.013.

[182] K.P. Lijesh, M. Mehdizadeh, and M.M. Khonsari. Online monitoring of metal fatigue life. *Structural Health Monitoring*, 19(3):938–952, August 2019. doi:10.1177/1475921719871668.

[183] H. Wu, S.R. Raghuraman, J.A. Ziman, F. Weber, T. Hielscher, and P. Starke. Characterization of the fatigue behaviour of low carbon steels by means of temperature and micromagnetic measurements. *Metals*, 12(11):1838, October 2022. doi:10.3390/met12111838.

[184] A. Haghshenas, J.Y. Jang, and M.M. Khonsari. On the intrinsic dissipation and fracture fatigue entropy of metals. *Mechanics of Materials*, 155:103734, April 2021. doi:10.1016/j.mechmat.2020.103734.

[185] F. Schaefer, J. Rosar, H. Wu, P. Starke, and M. Marx. Obtaining a lower estimate of the fatigue limit of metals by a simplified quantitative thermometric approach in a low-cost one-specimen test. *International Journal of Fatigue*, 159:106729, June 2022. doi:10.1016/j.ijfatigue.2022.106729.

[186] K. Hayabusa, K. Inaba, H. Ikeda, and K. Kishimoto. Estimation of fatigue limits from temperature data measured by ir thermography. *Experimental Mechanics*, 57(2):185–194, October 2016. doi:10.1007/s11340-016-0221-7.

[187] B. Yang, P.K. Liaw, M. Morrison, C.T. Liu, R.A. Buchanan, J.Y. Huang, R.C. Kuo, J.G. Huang, and D.E. Fielden. Temperature evolution during fatigue damage. *Intermetallics*, 13(3–4):419–428, March 2005. doi:10.1016/j.intermet.2004.07.032.

[188] J. Medgenberg and T. Ummenhofer. Detection of localized fatigue damage in steel by thermography. In *Thermosense XXIX*. SPIE, April 2007. doi:10.1117/12.720166.

[189] P. Wang, T. Takagi, T. Takeno, and H. Miki. Early fatigue damage detecting sensors—a review and prospects. *Sensors and Actuators A: Physical*, 198:46–60, August 2013. doi:10.1016/j.sna.2013.03.025.

[190] D.R. Harting. The—s/n—fatigue-life gage: A direct means of measuring cumulative fatigue damage: Sensor generates an irreversible resistance change which is a continuous function of the fatigue experience of the structure to which it is attached. *Experimental Mechanics*, 6(2):19A–24A, February 1966. doi:10.1007/bf02326230.

[191] P. Charsley and B.A. Robins. Electrical resistance changes of cyclically deformed copper. *Materials Science and Engineering*, 14(2):189–196, May 1974. doi:10.1016/0025-5416(74)90012-3.

[192] R. Nobile and A. Saponaro. Electrical resistance measurements for fatigue damage prediction of aisi 316l stainless steel. *Procedia Structural Integrity*, 41:421–429, 2022. doi:10.1016/j.prostr.2022.05.048.

[193] R. Nobile and A. Saponaro. Real-time monitoring of fatigue damage by electrical resistance change method. *International Journal of Fatigue*, 151:106404, October 2021. doi:10.1016/j.ijfatigue.2021.106404.

[194] R. Nobile and A. Saponaro. In-situ measurements of fatigue damage evolution by electrical resistance method. *Procedia Structural Integrity*, 28:1321–1328, 2020. doi:10.1016/j.prostr.2020.10.103.

[195] H. Germann, P. Starke, and D. Eifler. Resistivity-based evaluation of the fatigue behavior of cast irons. *Metallurgical and Materials Transactions A*, 43(8):2792–2798, August 2011. doi:10.1007/s11661-011-0852-3.

[196] P. Starke, M. Klein, and D. Eifler. Resistivity – a characteristic fingerprint of fatigue induced changes in the microstructure of metallic materials. *Procedia Engineering*, 10:698–703, 2011. doi:10.1016/j.proeng.2011.04.116.

[197] B. Sun. High-cycle fatigue damage measurement based on electrical resistance change considering variable electrical resistivity and uneven damage. *International Journal of Fatigue*, 26(5):457–462, May 2004. doi:10.1016/j.ijfatigue.2003.10.004.

[198] M.A. Omari and I. Sevostianov. Evaluation of the growth of dislocations density in fatigue loading process via electrical resistivity measurements. *International Journal of Fracture*, 179(1–2):229–235, November 2012. doi:10.1007/s10704-012-9780-5.

[199] M.A. Omari and I. Sevostianov. Estimation of changes in the mechanical properties of stainless steel subjected to fatigue loading via electrical resistance monitoring. *International Journal of Engineering Science*, 65:40–48, April 2013. doi:10.1016/j.ijengsci.2013.02.006.

[200] P. Starke, F. Walther, and D. Eifler. Model-based correlation between change of electrical resistance and change of dislocation density of fatigued-loaded ice r7 wheel steel specimens. *Materials Testing*, 60(7–8):669–677, July 2018. doi:10.3139/120.111202.

[201] X. Wang and D.D.L. Chung. Real-time monitoring of fatigue damage and dynamic strain in carbon fiber polymer-matrix composite by electrical resistance measurement. *Smart Materials and Structures*, 6(4):504–508, August 1997. doi:10.1088/0964-1726/6/4/017.

[202] J. Gadomski and P. Pyrzanowski. Experimental investigation of fatigue destruction of cfrp using the electrical resistance change method. *Measurement*, 87:236–245, June 2016. doi:10.1016/j.measurement.2016.03.036.

[203] G. Biallas, A. Piotrowski, and D. Eifler. Cyclic stress-strain, stress-temperature and stress-electrical resistance response of nicumo alloyed sintered steel. *Fatigue & Fracture of Engineering Materials & Structures*, 18(5):605–615, May 1995. doi:10.1111/j.1460-2695.1995.tb01421.x.

[204] I. Sevostianov, A. Zagrai, W. A. Kruse, and H.C. Hardee. Connection between strength reduction, electric resistance and electro-mechanical impedance in materials with fatigue damage. *International Journal of Fracture*, 164(1):159–166, April 2010. doi:10.1007/s10704-010-9487-4.

[205] J. Cheng and Z. Li. An electrical resistance degradation model for thin film under fatigue loading. *Fatigue & Fracture of Engineering Materials & Structures*, 43(11):2582–2596, June 2020. doi:10.1111/ffe.13278.

[206] B. Sun, L. Yang, and Y. Guo. A high-cycle fatigue accumulation model based on electrical resistance for structural steels. *Fatigue & Fracture of Engineering Materials & Structures*, 30(11):1052–1062, October 2007. doi:10.1111/j.1460-2695.2007.01175.x.

[207] J. Gray and J. Henderson. The effects of mechanical stress on the electrical resistance of metals. *Proceedings of the Royal Society of London*, 54(326–330):283–300, December 1894. doi:10.1098/rspl.1893.0075.

[208] P.W. Bridgman. *Papers 32-58*, chapter The Effect of Tension on the Electrical Resistance of Certain Abnormal Metals. Harvard University Press, 1964.

[209] P.W. Bridgman. *Papers 94-121*, chapter The Effect of Homogeneous Mechanical Stress on the Electrical Resistance of Crystals. Harvard University Press, 1964.

[210] B.I. Stadnyk and V.P. Motalo. Electrical resistivity and mechanical stresses in metals. *Measurement Techniques*, 30(6):608–611, June 1987. doi:10.1007/bf00866867.

[211] M. Carballo, Z.J. Pu, and K.H. Wu. Variation of electrical resistance and the elastic modulus of shape memory alloys under different loading and temperature conditions. *Journal of Intelligent Material Systems and Structures*, 6(4):557–565, July 1995. doi:10.1177/1045389x9500600413.

[212] C.H. Gonzalez, N.F. de Quadros, C.J. de Araújo, M. Morin, and G. Guénin. Coupled stress-strain and electrical resistivity measurements on copper based shape memory single crystals. *Materials Research*, 7(2):305–311, June 2004. doi:10.1590/s1516-14392004000200014.

[213] W.-W. Maennig. Vergleichende untersuchung über die eignung der treppenstufen- methode zur berechnung der dauerschwingfestigkeit/ comparative study concerning the suitability of the stair-case method for fatigue strength evaluation/ etude comparative concernantl'aptitude de la méthode de l'escalier pour déterminer la résistance à la fatigue. *Materials Testing*, 13(1):6–11, January 1971. doi:10.1515/mt-1971-130103.

[214] W.J. Dixon and A.M. Mood. A method for obtaining and analyzing sensitivity data. *Journal of the American Statistical Association*, 43(241):109–126, March 1948. doi:10.1080/01621459.1948.10483254.

[215] J.T. Ransom and R.F. Mehl. *Symposium on Fatigue with Emphasis on Statistical Approach-II*, chapter The Statistical Nature of the Fatigue Properties of SAE 4340 Steel Forgings. ASTM International100 Barr Harbor Drive, PO Box C700, West Conshohocken, PA 19428-2959, 1953.

[216] M. Hück. Ein verbessertes verfahren für die auswertung von treppenstufenversuchen. *Materialwissenschaft und Werkstofftechnik*, 14(12):406–417, December 1983. doi:10.1002/mawe.19830141207.

[217] T. Thompson, J. Liu, and C. Hu. A comparative analysis of step loading and staircase testing for fatigue strength estimation of an engine component. *Fatigue & Fracture of Engineering Materials & Structures*, 46(2):667–681, November 2022. doi:10.1111/ffe.13898.

[218] R. Pollak, A. Palazotto, and T. Nicholas. A simulation-based investigation of the staircase method for fatigue strength testing. *Mechanics of Materials*, 38(12):1170–1181, December 2006. doi:10.1016/j.mechmat.2005.12.005.

[219] C. Müller, M. Wächter, R. Masendorf, and A. Esderts. Accuracy of fatigue limits estimated by the staircase method using different evaluation techniques. *International Journal of Fatigue*, 100:296–307, July 2017. doi:10.1016/j.ijfatigue.2017.03.030.

[220] D. Grove and F. Campean. A comparison of two methods of analysing staircase fatigue test data. *Quality and Reliability Engineering International*, 24(4):485–497, December 2007. doi:10.1002/qre.899.

[221] S. Lin. Evaluation of the staircase and the accelerated test methods for fatigue limit distributions. *International Journal of Fatigue*, 23(1):75–83, January 2001. doi:10.1016/s0142-1123(00)00039-6.

[222] I.M.W. Ekaputra, R.T. Dewa, G.D. Haryadi, and S.J. Kim. Fatigue strength analysis of s34mnv steel by accelerated staircase test. *Open Engineering*, 10(1):394–400, January 2020. doi:10.1515/eng-2020-0048.

[223] Y.X. Zhao, Y. Zhang, and H.W. He. Improved measurement on probabilistic fatigue limits/strengths by test data from staircase test method. *International Journal of Fatigue*, 94:58–80, January 2017. doi:10.1016/j.ijfatigue.2016.09.010.

[224] K.R.W. Wallin. Statistical uncertainty in the fatigue threshold staircase test method. *International Journal of Fatigue*, 33(3):354–362, March 2011. doi:10.1016/j.ijfatigue.2010.09.013.

[225] A. Martin, K. Hinkelmann, and A. Esderts. Zur auswertung von schwingfestigkeitsversuchen im zeitfestigkeitsbereich —: Teil 2: Wie zuverlässig kann die standardabweichung aus experimentellen daten geschätzt werden? *Materials Testing*, 53(9):513–521, September 2011. doi:10.3139/120.110256.

[226] J. Kim and H.-Y. Jeong. A study on the hysteresis, surface temperature change and fatigue life of sm490a, sm490a-weld and fc250 metal materials. *International Journal of Fatigue*, 32(7):1159–1166, July 2010. doi:10.1016/j.ijfatigue.2009.12.012.

[227] X. Wang, W. Zhang, T. Zhang, J. Gong, and M. Abdel Wahab. A new empirical life prediction model for 9–12 *Metals*, 9(2):183, February 2019. doi:10.3390/met9020183.

[228] A. Mehmanparast and A. Vidament. An accelerated corrosion-fatigue testing methodology for offshore wind applications. *Engineering Structures*, 240:112414, August 2021. doi:10.1016/j.engstruct.2021.112414.

[229] Q. Wu, X. Chen, Z. Fan, D. Nie, and R. Wei. Corrosion fatigue behavior of fv520b steel in water and salt-spray environments. *Engineering Failure Analysis*, 79:422–430, September 2017. doi:10.1016/j.engfailanal.2017.05.012.

[230] M. Amiri and M.M. Khonsari. Rapid determination of fatigue failure based on temperature evolution: Fully reversed bending load. *International Journal of Fatigue*, 32(2):382–389, February 2010. doi:10.1016/j.ijfatigue.2009.07.015.

[231] G. Fargione. Rapid determination of the fatigue curve by the thermographic method. *International Journal of Fatigue*, 24(1):11–19, January 2002. doi:10.1016/s0142-1123(01)00107-4.

[232] Z. Teng. Thermo-based fatigue life prediction: A review. *Fatigue & Fracture of Engineering Materials & Structures*, 46(9):3121–3144, June 2023. doi:10.1111/ffe.14079.

[233] P. Starke, F. Walther, and D. Eifler. Phybal—a new method for lifetime prediction based on strain, temperature and electrical measurements. *International Journal of Fatigue*, 28(9):1028–1036, September 2006. doi:10.1016/j.ijfatigue.2005.07.050.

[234] P. Starke and H. Wu. Use of non-destructive testing methods in a new one-specimen test strategy for the estimation of fatigue data. *International Journal of Fatigue*, 111:177–185, June 2018. doi:10.1016/j.ijfatigue.2018.02.011.

[235] H. Wu, A. Bäumchen, A. Engel, R. Acosta, C. Boller, and P. Starke. Steblife – a new short-time procedure for the evaluation of fatigue data. *International Journal of Fatigue*, 124:82–88, July 2019. doi:10.1016/j.ijfatigue.2019.02.049.

[236] R. Acosta, H. Wu, R. Sridaran Venkat, F. Weber, J. Tenkamp, F. Walther, and P. Starke. Steblife, a new approach for the accelerated generation of metallic materials' fatigue data. *Metals*, 10(6):798, June 2020. doi:10.3390/met10060798.

[237] R. Acosta, K. Heckmann, J. Sievers, T. Schopf, T. Bill, P. Starke, K. Donnerbauer, L. Lücker, F. Walther, and C. Boller. Microstructure-based lifetime assessment of austenitic steel aisi 347 in view of fatigue, environmental conditions and ndt. *Applied Sciences*, 11(23):11214, November 2021. doi:10.3390/app112311214.

[238] T. Bill, R. Acosta, C. Boller, K. Donnerbauer, L. Lücker, F. Walther, K. Heckmann, J. Sievers, T. Schopf, S. Weihe, and P. Starke. A short-time approach for fatigue life evaluation of aisi 347 steel for nuclear power energy applications. *Applied Sciences*, 11(23):11405, December 2021. doi:10.3390/app112311405.

[239] S Faust, I. Fleck, U. Jendrich, and R. Wenke. Forschungsvorhaben zum einfluss der herstellungsqualität auf die sicherheit von druckführenden komponenten. *GRS Abschlussberichte*, pages 1–163, January 2022. doi:10.1243/03093247jsa602.

[240] K.D. Haverkamp and K. Forch. Effect of heat treatment and precipitation state on toughness of heavy section mn-mo-ni-steel for nuclear power plants components. *Nuclear Engineering and Design*, 81(2):207–217, September 1984. doi:10.1016/0029-5493(84)90008-6.

[241] A. Das, S. Sunil, and R. Kapoor. Effect of cooling rate on the microstructure of a pressure vessel steel. *Metallography, Microstructure, and Analysis*, 8(6):795–805, December 2019. doi:10.1007/s13632-019-00585-6.

[242] Technical Commitee. Geometrical product specifications (gps) — indication of surface texture in technical product documentation. *DIN ISO 1302:2002*, 2002.

[243] J.D. Morrow. *Internal Friction, Damping, and Cyclic Plasticity*, chapter Cyclic Plastic Strain Energy and Fatigue of Metals. ASTM International, 1965.

[244] S. Schoenborn, H. Kaufmann, C.M. Sonsino, and R. Heim. Cumulative damage of high-strength cast iron alloys for automotive applications. *Procedia Engineering*, 101:440–449, 2015. doi:10.1016/j.proeng.2015.02.053.

[245] J. Polák. *Reference Module in Materials Science and Materials Engineering*, chapter Fatigue of Steels. Elsevier, 2016.

[246] A. Nieslony, C. Dsoki, H. Kaufmann, and P. Krug. New method for evaluation of the manson–coffin–basquin and ramberg–osgood equations with respect to compatibility. *International Journal of Fatigue*, 30(10–11):1967–1977, October 2008. doi:10.1016/j.ijfatigue.2008.01.012.

[247] S.S. Manson. Fatigue: A complex subject—some simple approximations: Both ends of the fatigue spectrum are covered in this lecture. on the one hand, the present state of understanding of the mechanism is reviewed and the complexity of the process observed. on the other hand, some approximations useful in design are outlined and their application illustrated. *Experimental Mechanics*, 5(4):193–226, July 1965. doi:10.1007/bf02321056.

[248] J. Park. Detailed evaluation of methods for estimation of fatigue properties. *International Journal of Fatigue*, 17(5):365–373, 1995. doi:10.1016/0142-1123(95)99737-u.

[249] C. Boller. *Materials data for cyclic loading*. Number B in Materials Data for Cyclic Loading. Elsevier, Amsterdam, Netherlands, 1987.

[250] K. lida. *Low Cycle Fatigue*, chapter Very Low Cycle Fatigue Life Influenced by Tensile or Compressive Prestrain. ASTM International100 Barr Harbor Drive, PO Box C700, West Conshohocken, PA 19428-2959, 1988.

[251] M.R. Mitchell and E.M. Caulfield. Fundamentals of modern fatigue analysis. *College of Engineering, University of Illinois*, 1978.

[252] U. Muralidharan and S.S. Manson. A modified universal slopes equation for estimation of fatigue characteristics of metals. *Journal of Engineering Materials and Technology*, 110(1):55–58, January 1988. doi:10.1115/1.3226010.

[253] M. Roessle. Strain-controlled fatigue properties of steels and some simple approximations. *International Journal of Fatigue*, 22(6):495–511, July 2000. doi:10.1016/s0142-1123(00)00026-8.

[254] E. Santecchia, A.M.S. Hamouda, F. Musharavati, E. Zalnezhad, M. Cabibbo, M. El Mehtedi, and S. Spigarelli. A review on fatigue life prediction methods for metals. *Advances in Materials Science and Engineering*, 2016:1–26, 2016. doi:10.1155/2016/9573524.

[255] K. Golos and F. Ellyin. A total strain energy density theory for cumulative fatigue damage. *Journal of Pressure Vessel Technology*, 110(1):36–41, February 1988. doi:10.1115/1.3265565.

[256] F. Ellyin. Fatigue life prediction under multiaxial stress conditions. *Dev. Eng. Mech.*, pages 133–158, 1987.

[257] F. Ellyin. An energy-based fatigue failure criterion. *Microstruct. Mech. Behav. Mater.*, 1986.

[258] P. Starke. Stresslifetc – ndt-related assessment of the fatigue life of metallic materials. *Materials Testing*, 61(4):297–303, March 2019. doi:10.3139/120.111319.

[259] F. Weber, H. Wu, and P. Starke. A new short-time procedure for fatigue life evaluation based on the linear damage accumulation by palmgren–miner. *International Journal of Fatigue*, 172:107653, July 2023. doi:10.1016/j.ijfatigue.2023.107653.

[260] R. Acosta, C. Boller, M. Doktor, H. Wu, H. Jost, F. Weber, and P. Starke. Evaluation of s-n curves including failure probabilities using short-time procedures. *Materials Testing*, 63(8):705–713, August 2021. doi:10.1515/mt-2020-0115.

[261] T. Ko and S.A. Cottrell. The formation of bainite. *J. Iron Steel Institude*, 172:307–313, 1972.

[262] M.F. Gallagher. Microstructure development in trip sheet steels containing si, al, or p [m.s. thesis, colorado school of mines, 2003]. *Advanced Steel Processing and Products Research Center*, pages 1–45, 2003.

[263] M.P. Luong. Infrared thermographic scanning of fatigue in metals. *Nuclear Engineering and Design*, 158(2–3):363–376, September 1995. doi:10.1016/0029-5493(95)01043-h.

[264] T.M.I. Fonseca-Junior and R. Magnabosco. Evaluation of methods for estimating fatigue properties applied to stainless steels and aluminum alloys. *Tecnologia em Metalurgia Materiais e Mineração*, 9(4):284–293, 2012. doi:10.4322/tmm.2012.040.

[265] R. Wagener and T. Melz. Fatigue life curve – a continuous wöhler curve from lcf to vhcf: Dedicated to professor dr.-ing. harald zenner on the occasion of his eightieth birthday. *Materials Testing*, 60(10):924–930, September 2018. doi:10.3139/120.111233.

[266] A. Aeran, R. Acosta, S.C. Siriwardane, P. Starke, O. Mikkelsen, I. Langen, and F. Walther. A nonlinear fatigue damage model: Comparison with experimental damage evolution of s355 (sae 1020) structural steel and application to offshore jacket structures. *International Journal of Fatigue*, 135:105568, June 2020. doi:10.1016/j.ijfatigue.2020.105568.

[267] A. Borgenstam, M. Hillert, and J. Agren. Metallographic evidence of carbon diffusion in the growth of bainite. *Acta Materialia*, 57(11):3242–3252, June 2009. doi:10.1016/j.actamat.2009.03.026.

[268] D. De-Castro, A. Eres-Castellanos, J. Vivas, F.G. Caballero, D. San-Martín, and C. Capdevila. Morphological and crystallographic features of granular and lath-like bainite in a low carbon microalloyed steel. *Materials Characterization*, 184:111703, February 2022. doi:10.1016/j.matchar.2021.111703.

[269] G.S. Cho, K. Choe, K.W. Lee, and A. Ikenaga. Effects of alloying elements on the microstructures and mechanical properties of heavy section ductile cast iron. *Journal of Material Science and Technology*, 23(1), 2007.

[270] M. Riebisch, B. Pustal, and A. Bührig-Polaczek. Influence of carbide-promoting elements on the microstructure of high-silicon ductile iron. *International Journal of Metalcasting*, 14(4):1152–1161, March 2020. doi:10.1007/s40962-020-00442-1.

[271] M.N. Ahmadabadi, E. Niyama, M. Tanino, T. Abe, and T. Ohide. Chemical composition and structural identification of eutectic carbide in 1 pct mn ductile iron. *Metallurgical and Materials Transactions A*, 25(5):911–918, May 1994. doi:10.1007/bf02652266.

[272] P. Starke, F.k Walther, and D. Eifler. New fatigue life calculation method for quenched and tempered steel sae 4140. *Materials Science and Engineering: A*, 523(1–2):246–252, October 2009. doi:10.1016/j.msea.2009.05.067.

[273] W.F. Wu, H.Y. Liou, and H.C. Tse. Estimation of fatigue damage and fatigue life of components under random loading. *International Journal of Pressure Vessels and Piping*, 72(3):243–249, August 1997. doi:10.1016/s0308-0161(97)00053-7.

[274] S. Stanzl, E. Tschegg, and H. Mayer. Lifetime measurements for random loading in the very high cycle fatigue range. *International Journal of Fatigue*, 8(4):195–200, October 1986. doi:10.1016/0142-1123(86)90021-6.

[275] M. Vormwald, P. Heuler, and T. Seeger. *Advances in Fatigue Lifetime Predictive Techniques*, chapter A Fracture Mechanics Based Model for Cumulative Damage Assessment as Part of Fatigue Life Prediction. ASTM International100 Barr Harbor Drive, PO Box C700, West Conshohocken, PA 19428-2959, 1992.

[276] K.N. Smith, P. Watson, and T Topper. A stress-strain function for the fatigue of metals. *Journal of Materials*, 5(4):767–778, 1970.

[277] A. Ince and G. Glinka. A modification of morrow and smith-watson-topper mean stress correction models. *Fatigue & Fracture of Engineering Materials & Structures*, 34(11):854–867, April 2011. doi:10.1111/j.1460-2695.2011.01577.x.

[278] B. Wolf. Characterization of the fatigue behaviour of the magnesium alloy az91d by means of mechanical hysteresis and temperature measurements. *International Journal of Fatigue*, 26(12):1357–1363, December 2004. doi:10.1016/j.ijfatigue.2004.04.005.

[279] S.S. Manson, J.C. Freche, and C.R. Ensign. *Fatigue Crack Propagation*, chapter Application of a Double Linear Damage Rule to Cumulative Fatigue. ASTM International100 Barr Harbor Drive, PO Box C700, West Conshohocken, PA 19428-2959, 1967.

[280] Z.n Peng, H.Z. Huang, J. Zhou, and Y.F. Li. A new cumulative fatigue damage rule based on dynamic residual s-n curve and material memory concept. *Metals*, 8(6):456, June 2018. doi:10.3390/met8060456.

[281] F. Mozafari, P. Thamburaja, A. Srinivasa, and S. Abdullah. Fatigue life prediction under variable amplitude loading using a microplasticity-based constitutive model. *International Journal of Fatigue*, 134:105477, May 2020. doi:10.1016/j.ijfatigue.2020.105477.

[282] M.M. Farag, R.M. El-Kady, and M.M.I. Hammouda. Cracking simulation-based cumulative fatigue damage assessment. *Fatigue & Fracture of Engineering Materials & Structures*, 44(8):2186–2201, May 2021. doi:10.1111/ffe.13487.

[283] R. Cappello, G. Meneghetti, M. Ricotta, and G. Pitarresi. On the correlation of temperature harmonic content with energy dissipation in c45 steel samples under fatigue loading. *Mechanics of Materials*, 168:104271, May 2022. doi:10.1016/j.mechmat.2022.104271.

[284] D. Shiozawa, T. Inagawa, T. Washio, and T. Sakagami. Accuracy improvement in dissipated energy measurement by using phase information. *Measurement Science and Technology*, 28(4):044004, February 2017. doi:10.1088/1361-6501/28/4/044004.

[285] D. Rigon, M. Ricotta, and G. Meneghetti. An analysis of the specific heat loss at the tip of severely notched stainless steel specimens to correlate the fatigue strength. *Theoretical and Applied Fracture Mechanics*, 92:240–251, December 2017. doi:10.1016/j.tafmec.2017.09.003.

[286] M. Liakat and M.M. Khonsari. On the anelasticity and fatigue fracture entropy in high-cycle metal fatigue. *Materials & Design*, 82:18–27, October 2015. doi:10.1016/j.matdes.2015.04.034.

[287] Q. Guo, X. Guo, J. Fan, R. Syed, and C. Wu. An energy method for rapid evaluation of high-cycle fatigue parameters based on intrinsic dissipation. *International Journal of Fatigue*, 80:136–144, November 2015. doi:10.1016/j.ijfatigue.2015.04.016.

[288] P. Corigliano, F. Cucinotta, E. Guglielmino, G. Risitano, and D. Santonocito. Fatigue assessment of a marine structural steel and comparison with thermographic method and static thermographic method. *Fatigue & Fracture of Engineering Materials & Structures*, 43(4):734–743, November 2019. doi:10.1111/ffe.13158.

[289] R. De Finis, D. Palumbo, L. M. Serio, L.A.C. De Filippis, and U. Galietti. Correlation between thermal behaviour of aa5754-h111 during fatigue loading and fatigue strength at fixed number of cycles. *Materials*, 11(5):719, May 2018. doi:10.3390/ma11050719.

[290] A. Chrysochoos, B. Berthel, F. Latourte, S. Pagano, B. Wattrisse, and B. Weber. Local energy approach to steel fatigue. *Strain*, 44(4):327–334, July 2008. doi:10.1111/j.1475-1305.2007.00381.x.

[291] A. Morabito, A. Chrysochoos, V. Dattoma, and U. Galietti. Analysis of heat sources accompanying the fatigue of 2024 t3 aluminium alloys. *International Journal of Fatigue*, 29(5):977–984, May 2007. doi:10.1016/j.ijfatigue.2006.06.015.

[292] H. Wu, J.A. Ziman, S.R. Raghuraman, J.-E. Nebel, and P. Weber, F.and Starke. Short-time fatigue life estimation for heat treated low carbon steels by applying electrical resistance and magnetic barkhausen noise. *Materials*, 16(1):32, December 2022. doi:10.3390/ma16010032.

[293] A. Todoroki, M. Ueda, and Y. Hirano. Strain and damage monitoring of cfrp laminates by means of electrical resistance measurement. *Journal of Solid Mechanics and Materials Engineering*, 1(8):947–974, 2007. doi:10.1299/jmmp.1.947.

[294] J.H. Hray and J.B. Henderson. The effects of mechanical stress on the electrical resistance of metals. *Proceedings of the Royal Society of London*, 53(321–325):76–78, December 1893. doi:10.1098/rspl.1893.0011.

[295] P.W. Bridgman. *Papers 32-58*, chapter The Effect of Tension on the Thermal and Electrical Conductivity of Metals. Harvard University Press, 1964.

[296] C.H. Gonzalez, M. Morin, and G. Guénin. Behaviour of electrical resistivity in single crystals of cu-zn-al and cu-al-be under stress. *Le Journal de Physique IV*, 11(PR8):Pr8–167–Pr8–172, November 2001. doi:10.1051/jp4:2001829.

[297] C. Rudolf, R. Goswami, W. Kang, and J. Thomas. Effects of electric current on the plastic deformation behavior of pure copper, iron, and titanium. *Acta Materialia*, 209:116776, May 2021. doi:10.1016/j.actamat.2021.116776.

[298] S. Saberi, M. Stockinger, C. Stoeckl, B. Buchmayr, H. Weiss, R. Afsharnia, and K. Hartl. A new development of four-point method to measure the electrical resistivity in situ during plastic deformation. *Measurement*, 180:109547, August 2021. doi:10.1016/j.measurement.2021.109547.

[299] F. Weber and P. Koziol, J.and Starke. Stresslife: A short-time approach for the determination of a trend s-n curve in and beyond the hcf regime for the steels 20mnmoni5-5 and sae 1045. *Materials*, 16(11):3914, May 2023. doi:10.3390/ma16113914.

[300] P. Starke, F. Walther, and D. Eifler. "phybal" a short-time procedure for a reliable fatigue life calculation. *Advanced Engineering Materials*, 12(4):276–282, April 2010. doi:10.1002/adem.200900344.

[301] S.I. Rokhlin, J.-Y. Kim, B. Xie, and B. Zoofan. Nondestructive sizing and localization of internal microcracks in fatigue samples. *NDT & E International*, 40(6):462–470, September 2007. doi:10.1016/j.ndteint.2007.02.001.

[302] K. Donnerbauer, R. Acosta, C. Boller, T. Bill, P. Starke, K. Heckmann, J. Sievers, T. Schopf, and F. Walther. Fatigue damage evaluation of stainless aisi 347 steel by advanced microstructure-sensitive ndt analysis. *Procedia Structural Integrity*, 42:738–744, 2022. doi:10.1016/j.prostr.2022.12.093.

[303] P. Starke, D. Eifler, and C. Boller. Fatigue assessment of metallic materials beyond strain measurement. *International Journal of Fatigue*, 82:274–279, January 2016. doi:10.1016/j.ijfatigue.2015.03.018.

[304] F. Bjørheim, S.C. Siriwardane, and D. Pavlou. A review of fatigue damage detection and measurement techniques. *International Journal of Fatigue*, 154:106556, January 2022. doi:10.1016/j.ijfatigue.2021.106556.

[305] B. Wisner, K. Mazur, and A. Kontsos. The use of nondestructive evaluation methods in fatigue: A review. *Fatigue & Fracture of Engineering Materials & Structures*, 43(5):859–878, February 2020. doi:10.1111/ffe.13208.

[306] S. Sagar, N. Parida, S. Das, G. Dobmann, and D. Bhattacharya. Magnetic barkhausen emission to evaluate fatigue damage in a low carbon structural steel. *International Journal of Fatigue*, 27(3):317–322, March 2005. doi:10.1016/j.ijfatigue.2004.06.015.

[307] E. Guglielmino, G. Risitano, and D. Santonocito. A new approach to the analysis of fatigue parameters by thermal variations during tensile tests on steel. *Procedia Structural Integrity*, 24:651–657, 2019. doi:10.1016/j.prostr.2020.02.057.

[308] A. Risitano and G. Risitano. Determining fatigue limits with thermal analysis of static traction tests. *Fatigue & Fracture of Engineering Materials & Structures*, 36(7):631–639, March 2013. doi:10.1111/ffe.12030.

[309] B. Atzori, G. Meneghetti, and M. Ricotta. Analysis of the fatigue strength under two load levels of a stainless steel based on energy dissipation. *EPJ Web of Conferences*, 6:38009, 2010. doi:10.1051/epjconf/20100638009.

[310] D. Shiozawa, T. Inagawa, T. Washio, and T. Sakagami. Fatigue limit estimation of stainless steels with new dissipated energy data analysis. *Procedia Structural Integrity*, 2:2091–2096, 2016. doi:10.1016/j.prostr.2016.06.262.

[311] F. Díaz. Some improvements in the analysis of fatigue cracks using thermoelasticity. *International Journal of Fatigue*, 26(4):365–376, April 2004. doi:10.1016/j.ijfatigue.2003.08.018.

[312] O.W. Dillon and T.R. Tauchert. The experimental technique for observing the temperatures due to the coupled thermoelastic effect. *International Journal of Solids and Structures*, 2(3):385–391, July 1966. doi:10.1016/0020-7683(66)90028-x.

[313] S. Vitzthum, J. Rebelo Kornmeier, M. Hofmann, M. Gruber, E. Maawad, A.C. Batista, C. Hartmann, and W. Volk. In-situ analysis of the thermoelastic effect and its relation to the onset of yielding of low carbon steel. *Materials & Design*, 219:110753, July 2022. doi:10.1016/j.matdes.2022.110753.

[314] U. Kleemann and H. Zenner. Bauteiloberfläche und schwingfestigkeit – untersuchungen zum einfluss der randschicht auf die dauerschwingfestigkeit von bauteilen aus stahl. *Materialwissenschaft und Werkstofftechnik*, 37(5):349–373, April 2006. doi:10.1002/mawe.200600995.

[315] G. Liu, C. Huang, B. Zhao, W. Wang, and S. Sun. Effect of machined surface integrity on fatigue performance of metal workpiece: A review. *Chinese Journal of Mechanical Engineering*, 34(1), December 2021. doi:10.1186/s10033-021-00631-x.

[316] M.R. Bayoumi and A.K. Abdellatif. Effect of surface finish on fatigue strength. *Engineering Fracture Mechanics*, 51(5):861–870, July 1995. doi:10.1016/0013-7944(94)00297-u.

[317] D. Taylor and O.M. Clancy. The fatigue performance of machined surfaces. *Fatigue & Fracture of Engineering Materials & Structures*, 14(2–3):329–336, February 1991. doi:10.1111/j.1460-2695.1991.tb00662.x.

[318] F. Weber, M. Maul, F. Juner, and P. Starke. A nonlinear lifetime prediction method for un- and low alloyed steels by damage determination based on non-destructive measurement techniques. *Fatigue & Fracture of Engineering Materials & Structures*, 47(5):1566–1583, February 2024. doi:10.1111/ffe.14252.

[319] Z. Cheng, R. Liao, and W. Lu. Surface stress concentration factor via fourier representation and its application for machined surfaces. *International Journal of Solids and Structures*, 113–114:108–117, May 2017. doi:10.1016/j.ijsolstr.2017.01.023.

[320] U. Essmann, U. Gösele, and H. Mughrabi. A model of extrusions and intrusions in fatigued metals i. point-defect production and the growth of extrusions. *Philosophical Magazine A*, 44(2):405–426, August 1981. doi:10.1080/01418618108239541.

[321] D. Görzen, P. Ostermayer, P. Lehner, B. Blinn, D. Eifler, and T. Beck. A new approach to estimate the fatigue limit of steels based on conventional and cyclic indentation testing. *Metals*, 12(7):1066, June 2022. doi:10.3390/met12071066.

[322] Y. Murakami. Material defects as the basis of fatigue design. *International Journal of Fatigue*, 41:2–10, August 2012. doi:10.1016/j.ijfatigue.2011.12.001.